Universita' degli Studi di Torino

Scuola di Dottorato in Scienze della Natura
e Tecnologie Innovative
Indirizzo in Fisica ed Astrofisica
XXX Ciclo

Prompt $\mathrm{D_s^+}$ meson production in pp, p-Pb and Pb-Pb collisions at LHC with ALICE

Author:
Anastasia Barbano

Supervisors:
Prof. Stefania Beolè
Dr. Francesco Prino

Examiners:
Dr. Ralf Averbeck
Dr. Patrick Robbe

January 16, 2018

Abstract

Prompt D_s^+ meson production in pp, p-Pb and Pb-Pb collisions at LHC with ALICE

The aim of this thesis is the study of the D_s^+-meson production in pp collisions at the centre-of-mass energy $\sqrt{s} = 7$ TeV and in p-Pb and Pb-Pb collisions at $\sqrt{s_{NN}} = 5.02$ TeV, with the ALICE detector at the CERN Large Hadron Collider. Heavy quarks provide an excellent way to investigate the properties of the Quark-Gluon Plasma (QGP) created in high-energy nucleus-nucleus collisions via the measurements of the nuclear modification factor (R_{AA}) and azimuthal anisotropy of hadrons originating from their hadronisation. At low and intermediate transverse momentum p_T, the study of the D_s^+ meson should also reveal information about the charm-quark hadronisation mechanism. If charm quarks hadronise by recombining with lighter quarks from the medium, the relative abundance of D_s^+ mesons with respect to non-strange D mesons is expected to be larger in Pb-Pb than in pp collisions, at low and intermediate p_T, due to the large abundance of strange quarks in the QGP. The analyses presented in this thesis are based on the full reconstruction of the $D_s^+ \to K^+K^-\pi^+$ decay, exploiting the displacement of the decay vertex from the interaction point. The p_T-differential cross-section of D_s^+ mesons and the relative yields of D_s^+ to non-strange D mesons were measured in pp and Pb-Pb collisions. In particular, the nuclear modification factors and, for the first time at LHC, the elliptic flow of D_s^+ mesons were measured in Pb-Pb collisions for central, semi-peripheral and peripheral collisions. The observed increase of strange particle yield relative to pion yield with increasing particle multiplicity in pp and p-Pb collisions suggested to investigate whether a similar enhancement is observed in the relative yield of D_s^+ mesons with respect to non-strange D mesons in high multiplicity p-Pb collisions. To this purpose, the relative ratios of D_s^+-meson and D^+-meson yields were measured in p-Pb collisions as a function of the event particle multiplicity in different p_T intervals.

In the first Chapter, the physics of heavy-ion collisions is introduced. The second Chapter is entirely dedicated to the role of heavy-flavour observables in the investigation of the QGP. A description of the main features of the ALICE apparatus and the detectors used in the analysis is illustrated in the third Chapter. The fourth, fifth and sixth Chapters present the work of this thesis, focusing on the strategy used in ALICE to reconstruct the D_s^+ mesons and discussing the results obtained in pp, Pb-Pb and p-Pb collisions, respectively.

The measurements presented in this thesis were approved by the ALICE Collaboration and presented in various conferences. The proton-proton analysis has already been published; the analysis of D_s^+ v_2 in Pb-Pb collisions is available on arXiv, waiting for a publication on a peer reviewed journal. The proton-nucleus and the other nucleus-nucleus results are still preliminary and will be published soon.

Abstract

Prompt D_s^+ meson production in pp, p-Pb and Pb-Pb collisions at LHC with ALICE

Il lavoro di questa tesi ha riguardato lo studio della produzione del mesone D_s^+ in collisioni pp alla energia del centro di massa di $\sqrt{s} = 7$ TeV e in collisioni p-Pb e Pb-Pb a $\sqrt{s_{NN}} = 5.02$ TeV, attraverso il rivelatore ALICE al Large Hadron Collider del CERN. I quark pesanti costituiscono una sonda eccellente per le proprietà del Plasma di Quark e Gluoni (QGP) che si crea in collisioni nucleo-nucleo ad alta energia, attraverso la misura del fattore di modificazione nucleare (R_{AA}) e dell'anisotropia azimutale degli adroni che originano dalla loro adronizzazione. A intermedio e basso momento trasverso p_T, lo studio del mesone D_s^+ dovrebbe inoltre rivelare informazioni riguardo il meccanismo di adronizzazione del quark charm all'interno del mezzo. Se il quark charm adronizza per coalescenza con i quark più leggeri presenti nel mezzo, l'abbondanza relativa di mesoni D_s^+ rispetto ai mesoni D non contenenti stranezza è attesa essere maggiore in collisioni Pb-Pb rispetto a collisioni pp, nella regione ad intermedio-basso p_T, grazie all'abbondanza di quark strani nel QGP. Le analisi presentate in questa tesi sono basate sulla ricostruzione completa della topologia di decadimento del canale $D_s^+ \to K^+K^-\pi^+$, sfruttando la distanza del vertice di decadimento dal vertice di interazione primario. La sezione d'urto differenziale in p_T per la produzione del mesone D_s^+ e i rapporti di produzione del mesone D_s^+ rispetto ai mesoni D non contenti stranezza sono stati misurati in collisioni pp e Pb-Pb. In particolare, l'analisi delle collisioni Pb-Pb ha portato alla misura del fattore di modificazione nucleare e, per la prima volta a LHC, del flow ellittico del mesone D_s^+ per collisioni centrali, semi periferiche e periferiche. L'osservazione dell'aumento della produzione di particelle contenenti stranezza rispetto alla produzione di pioni con l'aumentare della molteplicità di particelle prodotte in collisioni pp e p-Pb ha suggerito di investigare la presenza di un simile incremento nella produzione relativa del mesone D_s^+ rispetto ai mesoni D non contenenti stranezza in collisioni p-Pb ad alta molteplicità. A questo proposito, la misura del rapporto di produzione D_s^+/D^+ è stata effettuata in funzione della molteplicità di particelle in collisioni p-Pb in diversi intervalli di p_T.

Nel primo Capitolo verrà introdotta la fisica degli ioni pesanti. Il secondo Capitolo è invece interamente dedicato al ruolo delle osservabili per lo studio degli adroni pesanti nell'investigazione del QGP. Una descrizioni delle principali caratteristiche dell'esperimento ALICE e dei rivelatori utilizzati nelle analisi si può trovare nel terzo Capitolo. Nel quarto, quinto e sesto capitolo verrà presentato il lavoro di questa tesi, introducendo la strategia usata in ALICE per la ricostruzione del mesone D_s^+ e passando poi alla discussione dei risultati in collisioni pp, p-Pb e Pb-Pb rispettivamente.

Le misure presentate in questa tesi sono state approvate dalla Collaborazione ALICE e presentate in numerose conferenze. L'analisi dei dati in collisioni pp è stata pubblicata. L'analisi del v_2 del mesone D_s^+ disponibile su arXiv, con l'obiettivo di una rivista peer review. I risultati delle analisi in collisioni p-Pb e il resto dei risultati delle analisi in collisioni Pb-Pb sono ancora preliminari e saranno pubblicati a breve.

Contents

Chapter 1

Quark-Gluon Plasma

1.1 Strongly interacting matter

A deep insight into the matter which constituted the universe and its evolution starting from few second after the Big Bang has been achieved so far, in the past and recent years. From the decoupling of neutrinos and the nucleosynthesis, the evolution of the Universe is today quite well understood. Still, we have very little knowledge on what happened before. In the early Universe, after 10 μs after the Big Bang, matter was in a state very far away from the one described by Quantum Chromodynamics (QCD) at temperatures and energy densities of ordinary nuclear and hadronic matter. In QCD, the effective coupling between quarks and gluons depends on the squared transverse momentum q^2 exchanged in the interaction. In one loop calculation, the following relation for the strong coupling constant α_s can be found [257]:

$$\alpha_s(q^2) = \frac{\alpha_s(\mu^2)}{1 + \alpha_s(\mu^2)\frac{33-2n_f}{12\pi} ln(\frac{-q^2}{\mu^2})} \tag{1.1}$$

where μ is the momentum scale and n_f is the number of flavors considered. When exploring regions with $|q^2| \to 0$, which also correspond to distances larger than 1 fermi (hadron size), the strong coupling constant α_s becomes large. On the other hand, the coupling decreases with increasing q^2. This is the so-called *asymptotic freedom*, a general feature of non-Abelian gauge theories. Hence, interactions between quarks and gluons become weaker as their mutual distance decreases or as the exchanged momentum increases. Consequently, matter at very high temperatures or energy densities (or at high values of both of them) undergoes a phase transition from a state with quarks confined into hadrons into a new state of matter with on-shell quarks and gluons free to move over volumes larger than the hadron size. This deconfined state is called Quark-Gluon Plasma (QGP). In the primordial universe, quarks and gluons were expected to be in this plasma state, their interaction being dominated by the strong fundamental force. The temperature of the Universe at the time of the QGP was of hundreds of MeV. Right after some tens of microseconds, the cooling of this state down to a temperature $T \sim 150$ MeV (that corresponds to $\sim 10^{10}$ K: to give an idea, the temperature inside the Sun is around 11×10^6 K) lead to the creation of structures, irreversibly binding quarks together, inside colorless hadrons. The QCD matter phase diagram (Fig. 1.1) predicts the strongly-interacting matter to occur in different phases, depending on the temperature T and the baryo-chemical potential μ_B. [1] At low temperatures and for $\mu_B \sim 1$ GeV we are in the situation of the ordinary nuclei. By compressing or heating nuclear matter a state of hadronic gas is reached, nucleons can interact elastically and form resonances and other hadrons. At

[1] The baryo-chemical potential μ_B is defined as the energy needed to increase by one unit the net baryon number, $\mu_B = \partial \mathrm{E}/\partial N_B$, thus being directly related to the baryonic density.

extremely high values of temperature and energy density a transition to the Quark-Gluon Plasma is expected. These were the conditions of the primordial universe in the first micro-seconds after the Big Bang. The experimental research of this phase of matter started in the second half of the '80s, with the first fixed target experiments at the Super Proton Synchrotron (SPS) at CERN and at the Alternating Gradient Synchrotron (AGS) at Brookhaven National Laboratory (BNL). For the first time scientists tried to reproduce in the laboratory such a state of matter, initially through acceleration of light nuclei (Si and S respectively), then moving to heavier nuclei (Pb and Au).

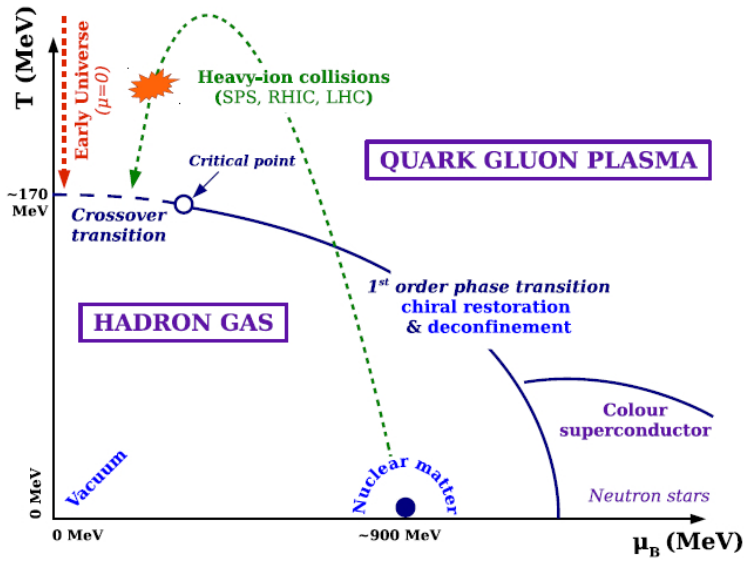

FIGURE 1.1: Phase diagram of strongly interacting matter.

Although the transformations in the early universe concerned the interactions among quarks, this phase transition would have never happened if not driven by macroscopic conditions, like the system temperature and energy density. The comprehension of the evolution of this state of matter has the promise to become accessible if we understand the thermodynamics laws of the QCD. It is not obvious indeed, nevertheless intriguing, to understand whether the QCD thermodynamics applies to the fireball created in the heavy-ion collisions in the laboratory, and whether the emitted hadrons keep a trace of the thermodynamics processes.

After the SPS, the Relativistic Heavy-Ion Collider (RHIC) at BNL has conducted experiments to create hot QCD matter through Au-Au collisions with the highest collision energy $\sqrt{s_{\mathrm{NN}}} = 200$ GeV per nucleon-nucleon collision, one order of magnitude above the top of SPS energy. The Large Hadron Collider (LHC) at CERN is conducting experiments along the same line with the highest achievable centre-of-mass energy of $\sqrt{s_{\mathrm{NN}}} = 5.02$ TeV per nucleon-nucleon collision.

1.2 Micro bang vs big bang: timescales of expansion, baryonic number

The system created in the laboratory by colliding relativistic nuclei presents many similarities with the matter of the primordial universe, but also some differences. A Hubble-like expansion drives the evolution of the system after the collisions in the laboratory and the fireball undergoes different phases (see Fig. 1.2):

- Pre-equilibrium phase: parton scatterings produce a large number of partons; they interact among each other leading the fireball to thermalise after a time of $\sim$ 0.6-1 fm/c;
- QGP phase: with high-energy collisions, if the temperature inside the fireball exceeds the critical temperature T_c, the system is in a deconfined phase with partonic degrees of freedom. While the phase of QGP in the early universe lasted tens of microseconds, due to the interplay of gravity and radiative pressure of the expanding matter, the plasma created in the laboratory has a lifetime of the order of 10^{-23} seconds. During this time, it rapidly expands and cools down, thus the size and local properties of the fireball change rapidly, contrary to what happened in the early universe.
- Hadronisation phase: while expanding, the temperature of the medium drops down and, when the critical temperature T_c is reached, quarks and gluons give rise to hadrons (confinement); the hadron gas continues the expansion and the temperature lowers further.
- Chemical freeze-out: inelastic processes cease and the relative abundances of the various hadron species are fixed;
- Kinetic freeze-out: even elastic collisions finish, fixing the momentum distribution of the produced particles.

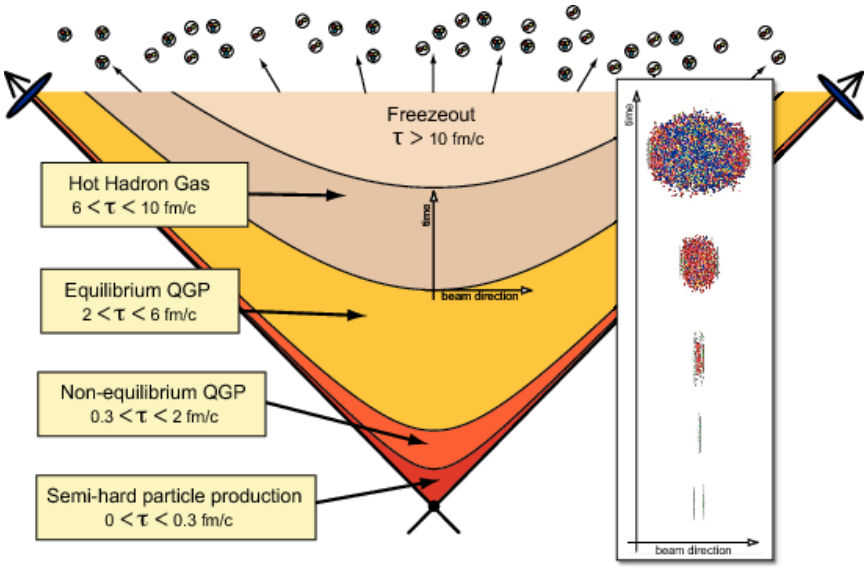

FIGURE 1.2: The space-time evolution of a heavy-ion collision [246].

Unlike in the early universe, we expect in the laboratory a significant matter-antimatter asymmetry in the particle abundance, at the lower centre-of-mass energies

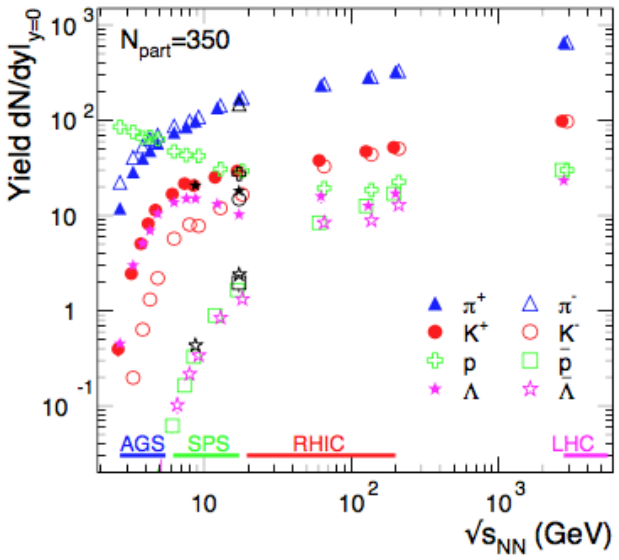

FIGURE 1.3: Collision energy dependence of the multiplicities (yield, dN/dy, at mid-rapidity) of pions, kaons, protons and lambda hyperons and their antiparticles, measured in central collisions (corresponding to an average number of 350 participant nucleons in the collision) of Au or Pb nuclei [85].

due to the stopping of the colliding nucleons. At the energies of AGS and SPS, colliding nuclei tend to stop each other, forming a dense, baryon-rich matter and hence a system with a large μ_B. At higher energies ($\sqrt{s_{\rm NN}} > 100{\rm GeV}/c$), they pass through each other leaving a nearly baryon-free matter in the region at central rapidity. In this case the system is closer to the conditions of zero baryo-chemical potential of the primordial universe. RICH experiments were the first to enter in the "baryon free" domain. Today, ALICE, CMS and ATLAS, thanks to unprecedentedly high energy beams at the LHC, are exploring this region with even smaller baryo-chemical potential. Figure 1.3 shows the measured yields of identified particles and anti-particles at mid-rapidity [2] as a function of the centre-of-mass energy of the collision, covering results by experiments at the AGS, SPS, RHIC and LHC [85]. The difference in the production of p and $\bar{\rm p}$ at low energies is a clear example of what discussed above. Because of the large stopping power in the low-$\sqrt{s_{\rm NN}}$ region, the quark content of the fireball is dominated by the quark content of the colliding nucleons. At LHC energies, yields of particles and anti-particles are the same, indicating the increasing transparency in the collision. The difference in the production of π^+ and π^- at low $\sqrt{s_{\rm NN}}$ is due to the isospin composition of the fireball. Finally, the difference between K^+ and K^- and between Λ and $\bar{\Lambda}$ is again due to their quark content, $K^+(u\bar{s})$, $K^-(\bar{u}s)$, $\Lambda(uds)$, $\bar{\Lambda}(\bar{u}\bar{d}\bar{s})$: like in the proton case, the quark content of the colliding nucleons drives the fireball content, in regimes of large stopping power. When the collision energies become high enough so that the we enter the "baryon free" domain and particle-to-antiparticle ratios ≈ 1, the baryo-chemical potential approaches ≈ 0 values.

[2] The rapidity y is defined as $y = 1/2\ \ln((E + p_L)/(E - p_L))$, where E is the particle energy and p_L its momentum longitudinal to the beam direction

1.3 What theory tells us

QCD is the widely accepted theory for the strong interaction. Phenomena at high energies, or equivalently, very short distances can be predicted via a perturbative approach, since the coupling constant is weak. How the quarks are bound in the hadrons, however, is controlled by the large-scale behaviour of the coupling, which increases with distance. For such reason, lattice calculation is an indispensable technique. Lattice QCD is a non-perturbative treatment of QCD formulated on a discrete grid or lattice of points in space and time [219]. Because of the non-perturbative nature of the theory, numerical simulations of Lattice QCD are the only tool allowing for calculations from first principles. The discretisation of the space-time continuum provides two main advantages: on one hand the problem of ultraviolet divergences typical of the perturbative approach is solved as the step of the lattice defines the shortest distance scale and hence a cut-off value for the momentum scale. On the other hand, we wish to describe a system of particles in a finite volume V, which is in thermal contact with a heat bath at temperature T. Associated with the particles, there may be a set of conserved charges N_i, with i=1, 2, ... (such as the particle number, electric charge, baryon number etc.). In quantum field theory, the most direct description is in terms of the grand canonical ensemble, defining a density operator ρ and a partition function Z of the system at a temperature T:

$$\rho = e^{-\frac{1}{T}(H-\mu_i N_i)}, \quad Z = Tr(e^{-\frac{1}{T}(H-\mu_i N_i)}) = \int dx \langle x|e^{-\frac{1}{T}(H-\mu_i N_i)}|x\rangle, \tag{1.2}$$

where μ_i are the chemical potentials for the conserved charges, and the quantum mechanical trace is a sum over all energy eigenstates $|x\rangle$ of the Hamiltonian H. From the partition function, all other thermodynamic equilibrium quantities are calculable. The basic idea behind lattice QCD is the possibility to express the grand canonical partition function using the path integral representation, going in the domain of imaginary time. Actually, the partition function has a very similar formulation to the propagator of a quantum mechanical system between two space-time points $\langle x_b|e^{-iH(t_b-t_a)}|x_a\rangle$. The path integral formulation allows the use of Monte-Carlo methods to find the equilibrium states of the system. With lattice discretisation, some "order parameters" can be defined, which are sensitive to certain processes and accessible from lattice calculations. From them, estimates of characteristics parameters, like the critical temperature T_c for the transition to a deconfined state, can be obtained. Among the order parameters, there are:

- **Polyakov loop,** defined as:

$$L(T) \sim \exp\{-V(r)/T\}, \tag{1.3}$$

  where $V(r)$ is the potential between a static quark-antiquark pair separated by a distance r. In pure gauge theory $V(r) \sim \sigma r$ where σ is the string tension [3]; hence V(∞) = ∞, and $L = 0$. In a deconfined medium, colour screening among the gluons leads to a melting of the string, which makes $V(r)$ finite at large r; hence L does not vanish. It thus becomes a parameter for estimating the state of deconfinement. Fig. 1.4 (left) shows lattice results for $L(T)$ and the corresponding susceptibility $\chi_L(T) \sim \langle T^2\rangle - \langle T\rangle^2$.

[3] Two colour sources in a confining gauge theory are bound together by a thin flux tube and this hypothesis is the core of the effective string description of confinement [126].

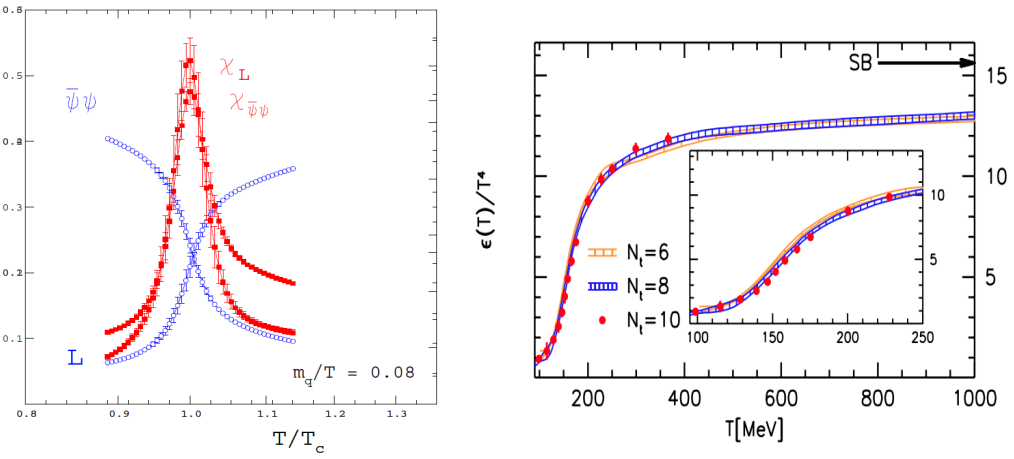

FIGURE 1.4: (Left) Chiral condensate $\langle\bar{\psi}\psi\rangle$ and free energy function L (blue) as function of temperature. Their susceptibilities are shown in red [178]. (Right) Lattice simulation of energy density as a function of temperature. The arrows indicate the position of the Stefan-Boltzmann limit [109].

- **Chiral condensate:** the effective quark mass is measured by the expectation value of the corresponding term in the Lagrangian, $\langle\bar{\psi}\psi\rangle(T)$. The chiral symmetry is the invariance of the Lagrangian under an axial transformation of the fermion field:

$$\Psi \rightarrow e^{-i\gamma_5 \frac{\vec{\tau}\cdot\vec{\theta}}{2}} \Psi \tag{1.4}$$

  where $\vec{\tau}$ are the three Pauli matrices and γ_5 is the chiral operator. In the limit of vanishing current quark masses, the Lagrangian becomes chirally symmetric. When confined into hadrons, the bare quarks "dress" themselves with gluons acquiring an effective constituent mass. After the transition to a deconfined phase, the quarks would recover the "bare" mass, and the chiral symmetry should be approximately restored. In the calculations, the order parameter for the transition is the effective quark mass, measured as the expectation value of the corresponding term in the Lagrangian, that is the chiral condensate $\langle\overline{\psi}\psi\rangle$. In Fig. 1.4 (left) the behaviour of the order parameter as a function of temperature is shown. Recent results provide a measure of the critical temperature T_c from the results for the chiral condensate, and it is estimated as $T_c = (154 \pm 9)$ MeV [217].

- **Energy density** ϵ at deconfinement: in Fig. 1.4 (right) it can be seen that ϵ/T^4 changes quickly at the critical temperature T_c, increasing from a low value typical of an hadron gas to a higher value closer to what expected for an ideal gas in the Stefan-Boltzmann limit of massless quarks and gluons. N_t is the number of points in the temporal direction of a hyper-cubic lattice [109]. The remarkable deviation of ϵ/T^4 from the Stefan-Boltzmann limit is a clear signal of surviving correlations in the deconfined phase. The rapid increase in energy density is expected to occur as consequence of the increased number of degrees of freedom in the phase transition.

1.4 Collision Geometry and the Glauber Model

In a collision of two nuclei, the impact parameter b, i.e. the distance between the centres of the nuclei in the transverse plane of the collision, can span values from 0 to about $R_1 + R_2$, where R_1 and R_2 are the radii of the two nuclei if approximated with hard spheres. Small values of b ($\lesssim 3.5$ fm) imply central collisions. The impact parameter can not be measured directly, yet it is possible to relate it to observables like the multiplicity of particles produced in the collision, the transverse energy or the number of spectator nucleons. The Glauber model is used to calculate the geometrical quantities that characterise the collision (such as the number of nucleons participating in the collisions, the number of spectator nucleons), and that can be correlated with some observables (such as multiplicity, transverse energy) to estimate the centrality of the collision [204]. The model provides a phenomenological description assuming that the nucleus-nucleus collision can be treated as a superposition of independent nucleon-nucleon collisions. Under the assumptions (optical limit) that, (i) at sufficiently high energies, the nucleons inside the nuclei are essentially undeflected after the collision, (ii) the nucleons are independent in the nucleus, (iii) protons and neutrons are indistinguishable and (iv) the radius of the nucleus is large compared to the extent of the nucleon-nucleon force, we can define the thickness functions of nuclei A, B for a certain value of impact parameter b (see Fig. 1.5):

$$T_i(\vec{s}) = \int \mathrm{d}z \rho_i(\vec{s}, z). \tag{1.5}$$

The thickness function is related to the nuclear density function ρ. The nuclear density is usually parameterised by a Woods-Saxon or 3-parameter Fermi distribution:

$$\rho(r) = \rho_0 \frac{1 + w(r/R)^2}{1 + \exp(\frac{r-R}{a})}, \tag{1.6}$$

where ρ_0 is the nuclear density in the center of the nucleus, $R = (6.62 \pm 0.06)$ fm is the radius parameter of the ^{208}Pb, $a = (0.546 \pm 0.010)$ fm is the skin thickness of the Pb nucleus and w characterizes deviations from a spherical shape ($w = 0$ for Pb).

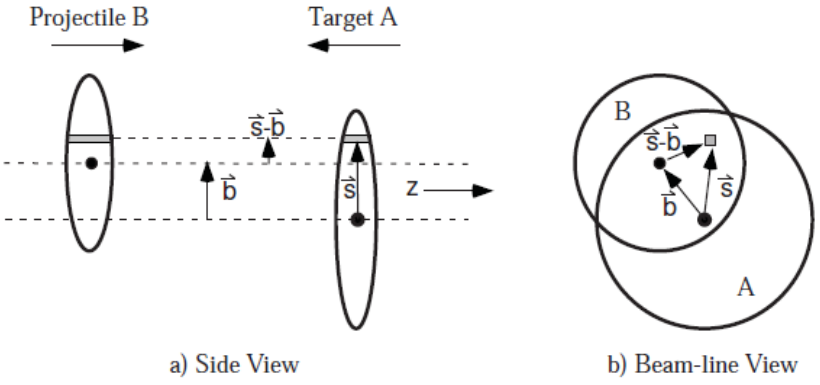

FIGURE 1.5: Schematic view of a nucleus-nucleus collision described in terms of the impact parameter b in the longitudinal (left) and transverse (right) plane.

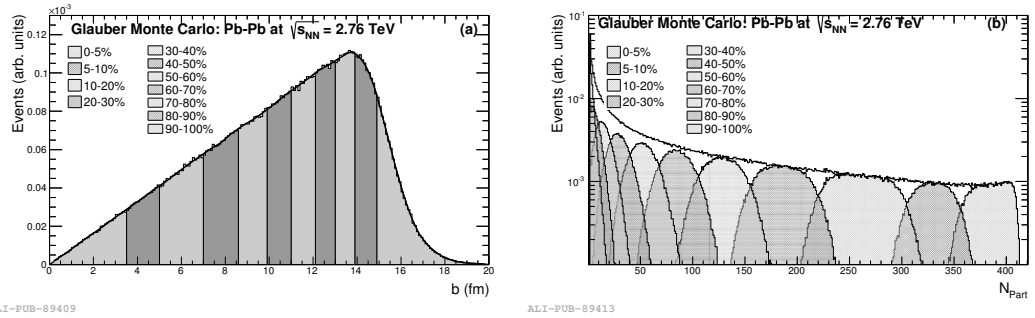

FIGURE 1.6: Left: impact parameter distribution obtained from Glauber MC simulations for Pb-Pb collisions at $\sqrt{s_{\rm NN}}$ = 2.76 TeV. Right: the corresponding $N_{\rm part}$ distributions for different intervals of centrality percentiles.

The nuclear overlap function is then defined as:

$$T_{\rm AB}(\vec{b}) = \int {\rm d}^2 s T_A(\vec{s}) T_B(\vec{s}-\vec{b}) \tag{1.7}$$

and it gives the probability for two incoming nucleons inside two nuclei colliding with impact parameter b to be in the same elementary area ${\rm d}^2 s$ in the transverse plane. By considering the mean of a binomial distribution, the average number of binary nucleon-nucleon collisions $\langle N_{\rm coll}\rangle$ as a function of the impact parameter b can then be written as [204]:

$$\langle N_{\rm coll}\rangle = AB \times T_{\rm AB}(b)\, \sigma_{\rm NN}^{\rm inel}, \tag{1.8}$$

where A and B are the mass numbers of the colliding nuclei and $\sigma_{\rm NN}^{\rm inel}$ is the inelastic interaction cross-section of the two nucleons. The average number of participant nucleons in the collisions (nucleons of target and projectile that interact) can be obtained as a function of the impact parameter b as:

$$\begin{aligned} N_{\rm part}(b) = &\int A\, T_A(\vec{s})[1-(1-\sigma_{\rm NN}^{\rm inel} T_B(\vec{b}-\vec{s}))^B]{\rm d}^2 s \\ &+ \int B\, T_B(\vec{b}-\vec{s})[1-(1-\sigma_{\rm NN}^{\rm inel} T_A(\vec{s}))^A]{\rm d}^2 s. \end{aligned} \tag{1.9}$$

The inelastic cross-section for a collision between two nuclei (A and B), in a certain centrality range ($0 < b < b_c$) can be expressed using the Glauber model geometry, as:

$$\sigma_{AB}(b_c) = \int_0^{b_c} 2\pi b\, {\rm d}b[1-(1-\sigma_{\rm NN}^{\rm inel} T_{\rm AB}(b))^{AB}]. \tag{1.10}$$

The centrality is usually expressed in terms of percentiles of the total nuclear interaction cross section σ_{AB} in Eq. 1.10. The percentile of the cross-section for collisions in a given impact parameter interval $b_{min} < b < b_{max}$ (see Fig. 1.6) is given by:

$$c = \frac{1}{\sigma_{AB}} \int_{b_{min}}^{b_{max}} \frac{{\rm d}\sigma_{AB}}{{\rm d}b'} {\rm d}b'. \tag{1.11}$$

A simple approach to use the Glauber Model formulation for the calculation of geometry related quantities like $N_{\rm part}$ and $N_{\rm coll}$ is a Monte Carlo implementation. Furthermore, it is possible to simulate experimental quantities like the charged particle multiplicity and to apply centrality cuts similar to those used in the analysis of real

data. In the simulation the nucleon distribution in the two colliding nuclei is randomly generated according to their nuclear density distributions. A random impact parameter b is also associated to the collision according to the distribution $\mathrm{d}\sigma/\mathrm{d}b \propto 2\pi b$. The nucleons travel along straight-line trajectories and the inelastic nucleon-nucleon cross-section is assumed to be independent of the number of collisions a nucleon underwent before. A nucleon-nucleon collision takes place if their distance d in the plane orthogonal to the beam axis satisfies the following condition:

$$d \leq \sqrt{\sigma_{\mathrm{NN}}^{\mathrm{inel}}/\pi}. \tag{1.12}$$

Optical Glauber and MC Glauber show good agreement when calculating simple geometric quantities like N_{part} and N_{coll} as a function of impact parameter. Some discrepancies appear at the highest values of the impact parameter. This is mainly due to the fact that in the Optical Approximation the incoming nucleon sees the incoming nucleus as a smooth density object and does not account for event-by-event density fluctuations [204].

In Chapter 3, more details will be given about the calculation of $\mathrm{N_{part}}$ and $\mathrm{N_{coll}}$ and about the centrality determination in the ALICE experiment.

1.5 Heavy-ion physics at the LHC

The SPS program, with its several experiments, was mainly aimed at understanding whether a new state of matter, with the characteristics of a Quark-Gluon Plasma, could actually be created in the laboratory. For a more quantitative study of the properties of this system, we had to wait for the following experiment era, at the RHIC and LHC colliders. However, the first results from the SPS revealed that Pb-Pb collisions were not simply a trivial superposition of elementary proton-proton (pp) collisions. First of all, it was possible to measure quantitatively the energy density and temperature of the fireball formed after collisions of two Pb nuclei. A formula derived by Bjorken [106] revealed the energy density of the system to be around 3 GeV/fm^3, slightly above the phase transition predicted by the Lattice QCD at about 0.5-0.6 GeV/fm^3 [168]. At that energy density, Lattice QCD gives a plasma temperature of about 210 MeV. The main experimental observations at the SPS showed an abundant production of hadrons containing strange quarks [233] ("strangeness enhancement"), the reduced production of the J/ψ mesons [40] ("anomalous J/ψ suppression") and the yields of low-mass lepton pairs [137] ("ρ melting"). They constituted the signals that a new state of matter had been found. Moreover, the NA49 experiment gave the first indications that the fireball medium could be described by QCD hydrodynamics, with the measurement of the elliptic flow of pion and proton in semi-peripheral Pb-Pb collisions at top SPS energy [73]. This observable, described in more detail in Sec. 1.5.4, is related with the initial spatial anisotropy of the overlapping area of the two colliding nuclei, that is then converted into a final momenta anisotropy. Such a process is only possible if the fireball is guided by collective motion effects in a liquid-like medium with small viscosity. The initial results from RICH confirmed the picture of an extremely strongly interacting and almost perfect liquid QGP, enough opaque to quench any fast parton travelling through it.
This effect and the experimental observations mentioned before will have a deeper insight in the LHC research program. In the following, a revision of some of the most important results and open points regarding heavy-ion physics at the higher LHC energies is reported.

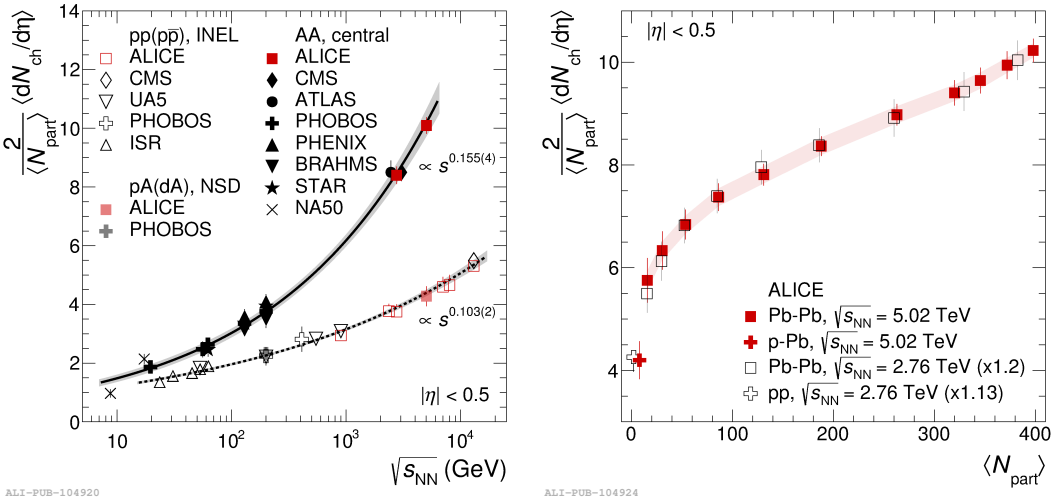

FIGURE 1.7: (Left) Charged particle pseudo-rapidity density per participant pair for pp and central AA collisions as a function of centre-of-mass energy per nucleon pair, measured in different colliding systems [49]. The fit to the power law is shown as solid (A-A) and dashed (pp) lines, together with the uncertainties on the dependence (shaded bands). (Right) Centrality dependence of $(\mathrm{d}N_{\mathrm{ch}}/\mathrm{d}\eta)/(\langle N_{\mathrm{part}}\rangle/2)$ for p-Pb and Pb-Pb collisions at $\sqrt{s_{\mathrm{NN}}} = 5.02$ TeV [32, 50], Pb-Pb collisions at $\sqrt{s_{\mathrm{NN}}} = 2.76$ TeV [16] and pp collisions at $\sqrt{s} = 7$ TeV measured with ALICE.

1.5.1 Particle multiplicity and energy density

The number of particles produced in the collision (multiplicity) is related to the density of the created medium. In fact particle multiplicity depends both on the centrality and on the energy of the collision. This observable is usually presented as a pseudo-rapidity ($\eta = -\ln(\tan(\theta/2))$ density of charged particles at mid-rapidity ($\mathrm{d}N_{\mathrm{ch}}/\mathrm{d}\eta|_{\eta=0}$). This is useful to compare experimental results with different acceptances. Furthermore, particle density is usually divided by the average number of nucleon pairs participating to the collision ($\langle N_{\mathrm{part}}\rangle/2$), to compare results of different colliding systems. The measurements by ALICE in the 5% most central Pb-Pb collisions at $\sqrt{s_{\mathrm{NN}}} = 5.02$ TeV showed a density of charged particles at mid-rapidity $\langle \mathrm{d}N_{\mathrm{ch}}/\mathrm{d}\eta\rangle = 1943 \pm 54$ and, normalised per participant pair, $(\mathrm{d}N_{\mathrm{ch}}/\mathrm{d}\eta)/(\langle N_{\mathrm{part}}\rangle/2) = 10.1 \pm 0.3$ [49]. The left panel of Fig. 1.7 presents $(\mathrm{d}N_{\mathrm{ch}}/\mathrm{d}\eta)/(\langle N_{\mathrm{part}}\rangle/2)$ as a function of the centre-of-mass energy per nucleon pair. The energy dependence of the charged multiplicity for central heavy-ion collisions can be fitted with a power law of the form as^b, where $b = 0.155\pm 0.004$ [49]. The rise is much stronger than in pp collisions where $b = 0.103 \pm 0.002$, obtained from a fit to the same function. It can also be noticed that the values of $(\mathrm{d}N_{\mathrm{ch}}/\mathrm{d}\eta)/(\langle N_{\mathrm{part}}\rangle/2)$ from p-Pb collisions are included in the figure and lay on the pp curve, showing that the strong rise in A-A collisions is not only due to the multiple interactions undergone by the participating nucleons, present in p-A collisions as well. The right panel of Fig. 1.7 shows the values of $(\mathrm{d}N_{\mathrm{ch}}/\mathrm{d}\eta)/(\langle N_{\mathrm{part}}\rangle/2)$ as a function of the average number of participant nucleons measured by ALICE in p-Pb [32] and Pb-Pb [49] collisions at $\sqrt{s_{\mathrm{NN}}} = 5.02$ TeV. The Pb-Pb measurements at $\sqrt{s_{\mathrm{NN}}} = 2.76$ TeV [16] are also shown, scaled by a factor of 1.2 (calculated from the observed $s^{0.155}$ dependence), as well as the pp measurements at $\sqrt{s} = 7$ TeV [50] scaled by a factor of 1.13. The charged particle density per participant pair shows a strong dependence on $\langle N_{\mathrm{part}}\rangle$, decreasing by a

factor of about 1.8 from most central collisions to peripheral ones. The measurement of particle production per participant pair can be used to constrain models describing particle production in heavy-ion collisions with different mechanisms. Among the others, theoretical calculations based on gluon saturation can give a good description of data (rcBK-MC [71], Kharzeev, Levin and Nardi [185] and Armesto, Salgado and Wiedemann [90]). These models assume the existence of a transverse momentum scale at which the gluon and quark phase space density saturates, thus limiting the number of produced partons and, hence, of particles. This results also in a centrality dependence of the multiplicity of heavy-ion collisions in the models, as observed in the experimental data.
The simplified Bjorken model [107] can be used to estimate the initial spatial energy density from the measured $\langle \mathrm{d}N_{\mathrm{ch}}/\mathrm{d}\eta \rangle$:

$$\epsilon_{Bj} = \frac{\langle m_T \rangle}{\tau_f A} \frac{\mathrm{d}N_{\mathrm{ch}}}{\mathrm{d}y} \tag{1.13}$$

where τ_f is the formation time of the secondary particles, A is the overlap area of the two colliding nuclei, $\langle m_T \rangle$ is the average transverse mass of the created particles defined as $m_{\mathrm{T}} = \sqrt{m^2 + p_{\mathrm{T}}^2}$ and y is the rapidity. Starting from the measured values of $\mathrm{d}N_{\mathrm{ch}}/\mathrm{d}\eta$, it is possible to estimate the energy density of the medium created in the collision. At top RICH energy (200 GeV), for the most central collisions, one obtains ~ 5 GeV/fm^3 at the conservative estimate for the formation time $\tau_f = 1$ fm/c [107], well above the critical value predicted by lattice QCD for the phase transition to QGP. For central Pb-Pb collisions at the LHC at $\sqrt{s_{\mathrm{NN}}} = 2.76$ TeV the value of ϵ_{Bj} is much higher and is around ~ 14 GeV/fm^3 [130].

1.5.2 Hadron multiplicities and chemical freeze-out

If we assume that a chemical and thermal equilibrium governs the medium when it undergoes chemical freeze-out, the thermal nature of the medium should be imprinted in the final hadron abundances. If these conditions occur, the behavior of the system at the equilibrium can be described via a statistical approach, using a description of the final particle yields in terms of thermodynamical quantities. Following the approach described in [113], we can introduce the partition function $\mathrm{Z}(T, V, \mu_Q)$, that allows for a quantitative description of the statistical properties of the equilibrated system, as a function of temperature T, volume V and chemical potentials μ_Q.

In the Grand Canonical (GC) ensemble describing a system in which energy and charges are on-average conserved within the full volume, the partition function is:

$$Z^{\mathrm{GC}}(T, V, \mu_Q) = \mathrm{Tr}[e^{-\beta(H - \sum_i \mu_{Q_i} Q_i)}], \tag{1.14}$$

where H is the Hamiltonian of the system, Q_i are the conserved charges, μ_{Q_i} are the chemical potentials needed to guarantee charges conservation on average in the whole system and $\beta = 1/T$ is the inverse temperature. At the leading order, the Hamiltonian of a non-interacting hadron-resonance gas contains all the degrees of freedom of a confined, strongly interacting medium. Further corrections can be added by introducing hadron repulsions, generally Van der Waals-like interactions. In the hadron-resonance gas a hadron mass spectrum containing mesons with masses below ~ 1.5 GeV/c^2 and baryons with masses below ~ 2 GeV/c^2 is considered. In this mass interval, the hadronic spectrum is well known as well as the decay channels of resonances and particles. With these assumptions, the maximum temperature for which the model can be considered trustable is ~ 200 MeV. The GC partition function

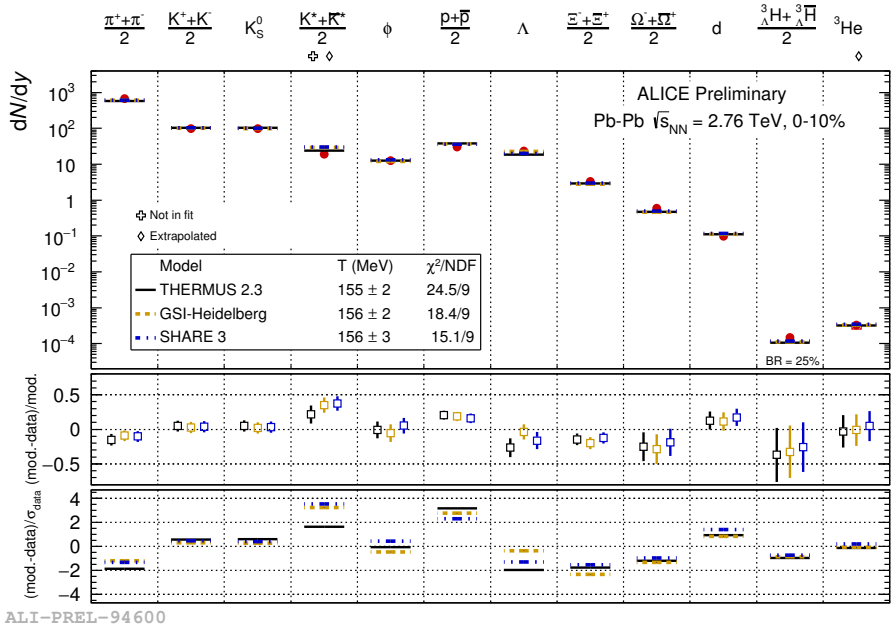

FIGURE 1.8: Grand Canonical thermal fit to ALICE 0-10% Pb-Pb data at $\sqrt{s_{\rm NN}} = 2.76$ TeV [152], with μ_B, γ_s, γ_c fixed to 1, 0 and 20 respectively.

of a non-interacting system, like that of our hypothesis, is given by the product of the independent partition functions of all the hadronic species. In the logarithmic form we write:

$$\ln Z(T, V\vec{\mu}) = \sum_i \ln Z_i(T, V, \vec{\mu}), \tag{1.15}$$

where $\vec{\mu} = (\mu_B, \mu_S, \mu_Q)$ are the chemical potentials related to the baryon number, strangeness and electric charge, and the sum is over all hadron species i. The density of particles of species i can be obtained from Eq. 1.15 as:

$$n_i(T, \vec{\mu}) = \frac{\langle N_i \rangle}{V} = \frac{1}{V}\frac{\partial(T \ln Z_i^{GC})}{\partial \mu_i} = \frac{T g_i}{2\pi^2} \sum_{k=1}^{\infty} \frac{(\pm 1)^{k+1}}{k} \lambda_i^k m_i^2 K_2(\frac{k m_i}{T}), \tag{1.16}$$

where (+) is for fermions and (-) for bosons, g_i is the spin-isospin degeneracy factor, $\lambda_i = e^{Q_i \mu_i}$ is the fugacity term and finally K_2 is the modified Bessel function. Further corrections to the particle density are necessary at high temperature ($\gtrsim 100$ MeV) or density, where the contribution to the particle yield N_i from resonance decays becomes dominant with respect to the thermal production of the species. Other deviations from the GC description can be taken into account by introducing parameters for strange, charm or light quarks (γ_S, γ_C and γ_q) production. For example, in case there is no thermalisation for the strangeness component in the medium, a factor $\gamma_s < 1$ is needed, usually whenever the size of system is small (i.e. pp collisions) or at low collision energies. The usage of γ_q is only applied in the so called non-equilibrium model SHARE [218]. This model describes an expanding, supercooled quark-gluon plasma which undergoes a sudden hadronization without further re-interactions. Among the five parameters of Eq. 1.16 ($T, V, \mu_B, \mu_S, \mu_Q$), up to three can be fixed with the knowledge of the conditions of the initial state. The other two parameters can be obtained by fitting the measured particle yields. In Fig. 1.8, a Grand-Canonical thermal fit with three different models using T and V as free

parameters is performed on the y-differential identified particle yields measured by ALICE in the 10% most central Pb-Pb collisions at $\sqrt{s_{\rm NN}} = 2.76$ TeV [152]. The fit quality is not fully satisfactory ($\chi^2/ndf \sim 2$), while it used to be of order 1 for RHIC energies [81]. The temperature, as parameter of the fit, results to be of the order of 155 MeV. The measured p and Ξ yields have a bad agreement with the fit (2.5 σ and 2 σ respectively). The measurements of resonances in central Pb-Pb collisions suggest elastic re-scattering in the late hadronic phases, that becomes quite important for pion production. If protons are excluded from the fits, the fit quality improves and the temperature goes up to ∼160 MeV (closer to RHIC results). Another possible interpretation is that inelastic processes during the hadronic phase may not be completely negligible, rather affecting baryon production. In particular, baryon annihilation in the hadronic phase should lead to a reduction of the proton yields [97, 98]. Other models suggest that a single freeze-out temperature for all particle species is not enough to describe the data [99], but temperature for lighter and heavier quarks could be different. So far, the production mechanism is not yet clearly understood as well as is not clear the way the temperature from the thermal fit relates to the QCD phase transition temperature.

1.5.3 Strangeness enhancement

The original idea of enhanced production of hadrons containing strange quarks as a signature of the quark deconfinement was proposed in 1980 by Rafelski and Hagedorn [228],[207]. As there are no strange quarks in the colliding nuclei, it follows that all strangeness must be created in the collision or in the QGP phase. Strange quarks are hard to produce at temperatures below T_c since their effective mass is larger than T_c when chiral symmetry is broken, but easy to produce at temperatures above T_c since the current mass of the strange quark is $m_s \sim 100$ MeV/c^2, due to chiral symmetry restoration (see Sec. 1.3). For $T > T_c$, also u and d quark masses decreases to $m_q \sim 0$

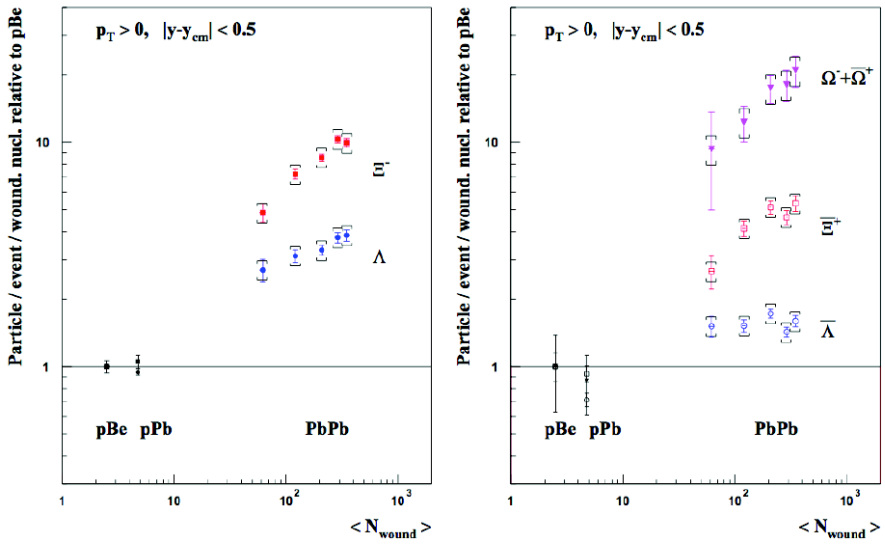

FIGURE 1.9: Hyperon enhancement as a function of the number of the wounded nucleons measured by the NA57 experiment in Pb-Pb collisions at $\sqrt{s_{\rm NN}} = 17.2$ GeV [233].

MeV/c^2, but the strange quark production becomes important. In a simple hadron gas, even if it is possible to produce strange particles from some inelastic scattering such as $\pi^0 + p \rightarrow K^+ + \Lambda$, it is less probable to produce multi-strange baryons, like

Ξ^- and Ω, as they are the result of more than one consecutive reactions. In presence of QGP, instead, it is expected an enhancement in the production of multi-strange baryons relative to pp reactions of about one order of magnitude. The abundant strangeness production in QGP is due to the large gluon density of the system, which favours gluon-fusion processes $gg \rightarrow s\bar{s}$. The Grand Canonical (GC) formulation is used whenever the conservation law of a quantum number, for example strangeness, can be on average implemented by using the corresponding chemical potential. This approach can be used in systems with a large number of produced particles. For smaller systems like pp or pA collisions, this is no longer valid and the Canonical (C) formulation must be used in turn. The canonical conservation of quantum numbers strictly reduces the phase space available for particle production [103], and this is usually referred to as canonical suppression [249]. This is the essence of the strangeness enhancement from pp to AA collisions.
In experiments the magnitude of strangeness production is usually estimated by measuring the enhancement factor, defined as the ratio of the yields of a given particle specie per participant nucleon in nucleus-nucleus collisions over the same ratio measured in smaller system (pp or pA). The first evidence of strangeness enhancement was measured by the NA57 and WA97 collaborations [233] in fixed-target Pb-Pb collisions at $\sqrt{s_{NN}}$= 17.2 GeV. The enhancement factor measured by NA57 is shown in Fig. 1.9 for Λ, Ξ^- (left) and their anti-particles (right) in p-Pb, p-Be and Pb-Pb collisions as a function of the number of participating nucleons. It is observed a hierarchy for these enhancement factors in Pb-Pb collisions, depending on the strangeness content of the particles and also on the collision centrality. In p-Be and in p-p there is no evidence of strangeness enhancement.

1.5.4 Collective flow and kinetic freeze-out

The "flow" of particles produced in the interaction is a collective phenomenon, which is observed as a collective motion pattern superimposed to the chaotic thermal motion of the particles inside the fireball. Its origin is related to the large pressure gradients generated when compressing and heating nuclear matter. It is possible to distinguish between different types of flow. In the following, the radial and the anisotropic flow in the transverse plane are discussed.

Radial flow

Regarding the particle production in pp collisions, following the approach in [236], we can treat the invariant yield of low p_{T} particles of a given species as radiated by a thermal source with temperature T, according to the Boltzmann distribution:

$$E\frac{\mathrm{d}^3n}{\mathrm{d}^3p} = \frac{\mathrm{d}n}{\mathrm{d}y\ m_{\mathrm{T}}\mathrm{d}m_T\ \mathrm{d}\varphi} = \frac{gV}{(2\pi)^3}E\ e^{-(E-\mu)/T}, \tag{1.17}$$

where g is the spin-isospin degeneracy factor for the considered particle species, μ is the grand canonical potential $\mu = n\mu_B + s\mu_S$, originating from the quantum numbers n and s for baryon and strangeness content, y is the rapidity, m_{T} the transverse mass and $\hbar = c = k_B = 1$. By integrating Eq. 1.17 over rapidity and φ, using the modified Bessel function K_1, we obtain the transverse mass distribution $\mathrm{d}n/(m_T\mathrm{d}m_T)$, which behaves asymptotically like a decreasing exponential for transverse masses larger than the source temperature:

$$\frac{\mathrm{d}N}{m_T\mathrm{d}m_T} = \frac{V}{2\pi^2}m_T K_1(\frac{m_T}{T}) \xrightarrow{m_T \gg T} V'\sqrt{m_T}e^{-m_T/T}. \tag{1.18}$$

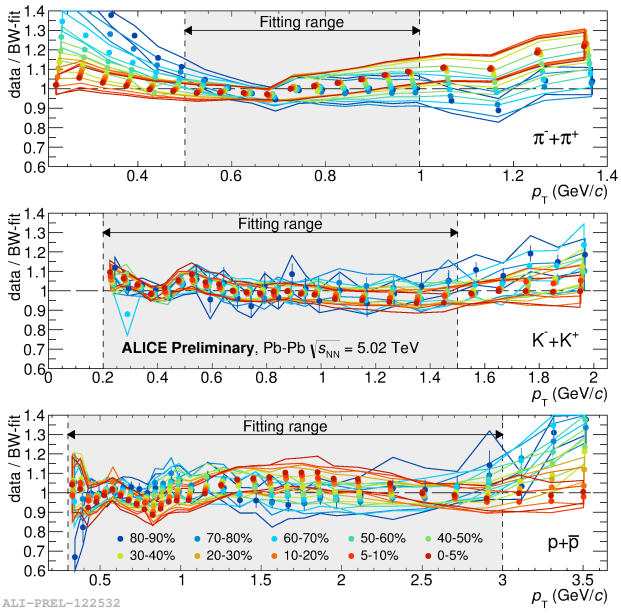

FIGURE 1.10: Ratio data to blast-wave fit for π, k, p spectra as a function of p_{T} in different centrality classes in Pb-Pb collisions at $\sqrt{s_{\mathrm{NN}}} = 5.02$ TeV [175], measured by ALICE.

It has been experimentally verified in pp collisions the universality, at low p_{T}, of the temperature T of the exponential slope of Eq. 1.18. In the low-p_{T} region ($\lesssim 1\,\mathrm{GeV}/c$), indeed, particles originate from soft processes and their production is governed by a Boltzmann exponential distribution. This law does not anymore describe production at higher p_{T}, where hard processes govern particle emission and the production spectra are better reproduced by power law functions. T_{slope} can be interpreted as the temperature of the particle emitting source. The universality of T_{slope} for different particle species is commonly referred to as m_{T}-scaling. When moving to nucleus-nucleus collisions, a breaking of the m_T-scaling occurs at low p_{T} and the slopes of the spectra are observed to decrease with increasing particle mass [88, 91]. The effect is present at all centralities, but it is stronger for central collisions. The slope of the exponential law, at low p_{T}, can be expressed as:

$$T_{\mathrm{slope}} = T_{\mathrm{fo}} + \frac{1}{2} m \beta_{\mathrm{T}}^2, \tag{1.19}$$

where the second term accounts for the dependence on the mass and the velocity is related to the radial flow, i.e. the collective velocity arising from the expansion of the fireball. The first term still accounts for the Brownian motion of the particles, present in Eq. 1.18. This is the idea developed within the Boltzmann-Gibbs blast-wave model [236], where the radial expansion velocity distribution $\beta_{\mathrm{T}}(r)$ in the region $0 \leq r \leq R$ is parametrized by relating it to the surface velocity β_s via:

$$\beta_{\mathrm{T}}(r) = \beta_s \left(\frac{r}{R} \right)^n, \tag{1.20}$$

where the exponent n is used to tune the shape of the spectra profile.

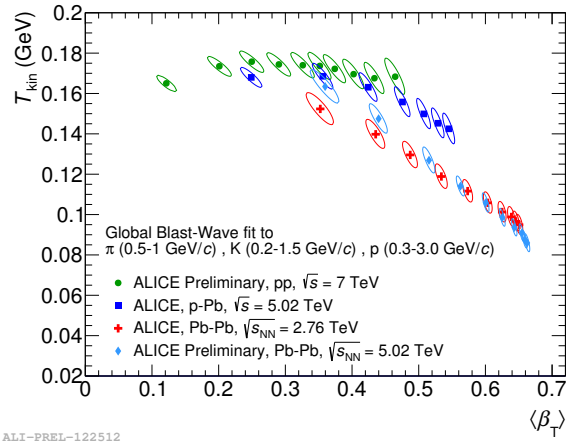

FIGURE 1.11: T_{kin} vs $\langle\beta_T\rangle$ from blast-wave fits for different colliding systems and energies [175].

The observed particle spectrum results from the sum of the spectra of individual thermal sources each boosted with the boost angle $\rho = \tanh^{-1}(\beta_{\mathrm{T}})$:

$$\frac{\mathrm{d}N}{p_{\mathrm{T}}\mathrm{d}p_{\mathrm{T}}\mathrm{d}\phi\mathrm{d}y} \propto \int_0^R r\mathrm{d}r\; m_{\mathrm{T}}\; K_1\left(\frac{m_{\mathrm{T}}\cosh(\rho(r))}{T_{\mathrm{fo}}}\right) I_0\left(\frac{p_{\mathrm{T}}\sinh(\rho(r))}{T_{\mathrm{fo}}}\right). \tag{1.21}$$

It is a three parameter $(T_{\mathrm{fo}}, \beta_s, n)$ simplified hydrodynamical model. The blast-wave fit to the measured spectra allows an estimate of the kinetic freeze-out temperature T_{fo} and radial velocity β_{T}. An example of data to blast-wave fit for the measured spectra of pions, kaons and protons in Pb-Pb collisions at $\sqrt{s_{\mathrm{NN}}} = 5.02$ TeV by ALICE is shown in Fig. 1.10, as a function of p_{T} (different centrality classes are in different colours).

Fig. 1.11 shows the ALICE results for the blast-wave parameters for different colliding systems and energies. Blast-wave parameters in Pb-Pb collisions at $\sqrt{s_{\mathrm{NN}}} = 5.02$ TeV follow the trends with collision centrality observed at lower energy ($\sqrt{s_{\mathrm{NN}}} = 2.76$ TeV). The largest expansion velocity is found for central Pb-Pb collisions, as well as the lowest temperature for the kinetic freeze-out.

Anisotropic flow

The anisotropic flow is characteristic of non-central collisions, where the finite impact parameter creates a fireball with a geometrical anisotropy. Due to particle re-scatterings during the system evolution, the initial spatial anisotropy is transferred to a final state momentum-space anisotropy. Absence of re-scatterings during the system evolution or any delays in time of such interactions would lead to null momentum anisotropy in the final state or to a decrease in the elliptic flow signal. Hence, the characterisation of anisotropic flow is important as it is sensitive to particle interactions occurring very early in the system evolution. Information of medium properties, such as Equation of State, sound velocity or shear viscosity can be extracted by a comparison of the measured anisotropic flow and hydrodynamic model calculations. In non-central heavy-ion collisions, an almond-shaped interaction volume is created in the overlap region (see Fig. 1.12). The reaction plane is defined by the collision impact parameter and the beam line (xz plane in Fig. 1.12). A pressure gradient larger in the reaction plane than in the plane perpendicular to it is expected. This generates an

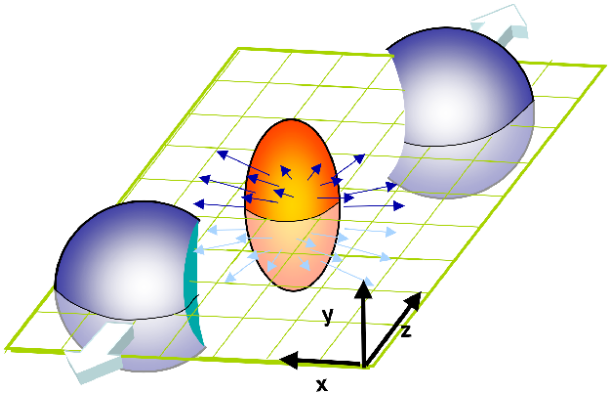

FIGURE 1.12: Picture of a semi-peripheral collision and the pressure gradients arising from a geometrical anisotropy.

anisotropy in azimuthal distributions of the particle momenta with respect to the reaction plane, which can be detected in the measured particle azimuthal distributions. This distribution can be parametrized through a Fourier series decomposition:

$$E\frac{\mathrm{d}^3N}{\mathrm{d}^3p} = \frac{1}{2\pi}\frac{\mathrm{d}^2N}{p_{\mathrm{T}}\mathrm{d}p_{\mathrm{T}}\mathrm{d}y}(1+\sum_{n=1}^{\infty}2v_n\cos(n(\varphi-\Psi_r))), \tag{1.22}$$

where φ is the azimuthal direction of the emitted particle and Ψ_r denotes the (true) reaction plane angle. In the formula, v_n are the Fourier coefficients, and they can be evaluated as $v_n = \langle cos(n(\varphi - \Psi_r))\rangle$, where $\langle\rangle$ indicates an average over all particles in all events with their azimuthal angle φ in a given rapidity and p_{T} momentum at a fixed centrality. The sine terms vanish due to the reflection simmetry with respect to the reaction plane. *Direct* and *elliptic flow* are common terms for the first and the second order Fourier coefficients respectively in the particle azimuthal distribution in Eq. 1.22, but coefficients up to at least 6^{th} order were measured at the LHC [2]. With the large amount of data provided by the LHC, in fact, we have the possibility to study not only the average anisotropies but also the initial space geometries fluctuations [3, 238], to which first-order and higher-order Fourier coefficients were indeed found to be sensitive. The positions of the nucleons in the overlap region of the colliding nuclei can fluctuate to create matter distributions asymmetries [247, 80, 77], which are converted into non-zero first-order and higher-order harmonic coefficients. Fig. 1.13 shows comparison to viscous hydrodynamics calculations [160] of the Fourier coefficients v_n up to 5^{th} order measured by ATLAS [2] (left panel) in Pb-Pb collisions at $\sqrt{s_{\mathrm{NN}}} = 2.76$ TeV and PHENIX [63] and STAR [212] (right panel) in Au-Au collisions at $\sqrt{s_{\mathrm{NN}}} = 200$ GeV. A value of the shear viscosity η/s of the medium equal to 0.12 allows a good parametrisation of hydro calculations for Au-Au collisions at top of RICH energy, while a value of 0.2 is found for Pb-Pb collisions at the LHC at $\sqrt{s_{\mathrm{NN}}} = 2.76$ TeV. This reveals a dependence of the shear viscosity on the temperature of the system. Fig. 1.14 shows the p_{T}-differential v_2 of $\pi^{\pm}, K^{\pm}, p(\bar{p})$ and Φ mesons for 10-20% (left) and 40-50% (right) collision centrality, measured by ALICE in Pb-Pb collisions at $\sqrt{s_{\mathrm{NN}}} = 5.02$ TeV [102]. For $p_{\mathrm{T}} < 2$ GeV/c, one can notice that the v_2 of the different species follows a mass ordering, which is expected for a hydrodynamically expanding source and is indicative of collective radial flow. For $3 < p_{\mathrm{T}} < 8$ GeV/c, particles are grouped according to the number of their valence quarks, rather than their mass, which supports the hypothesis of particle production via quark coalescence [205]. The non-zero v_2 at high p_{T} is attributed to path-length

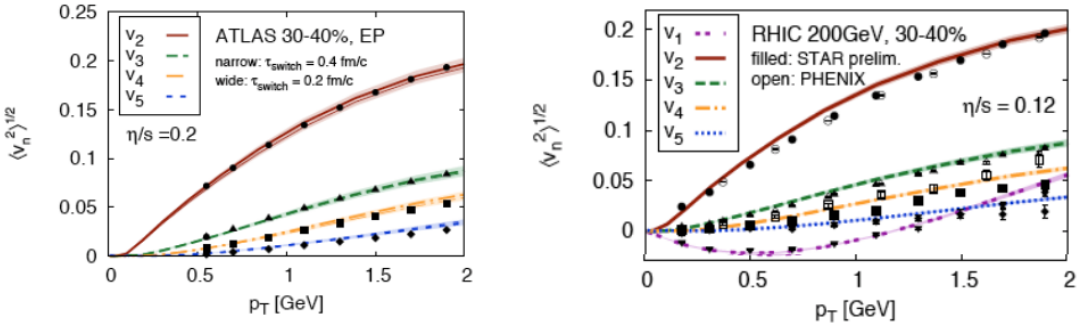

FIGURE 1.13: Fourier components of anisotropic transverse flow, $v_n(p_T)$, for Pb-Pb collisions at the LHC (left panel) and for Au-Au collisions at RICH (right panel), in comparison with viscous hydrodynamics calculations [160].

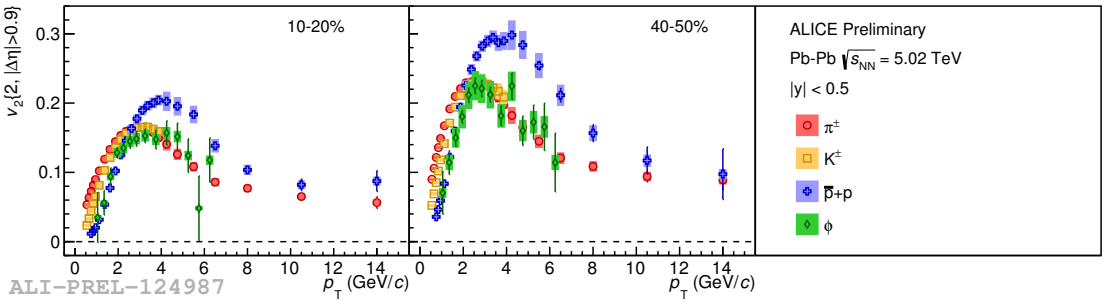

FIGURE 1.14: Elliptic flow coefficient v_2 of $\pi^{\pm}, K^{\pm}, p(\bar{p})$ and Φ meson for 10-20% (left) and 40-50% (right) collision centrality as function of p_T [102]. Statistical uncertainties are shown as bars and systematic uncertainties as boxes.

dependent in-medium energy loss which is discussed in the next section [166]. The ϕ meson, with its mass close to proton mass, is a very good probe of quark scaling and mass ordering. Indeed, the ϕ-meson v_2 follows proton v_2 at low p_T, but pion v_2 at intermediate p_T.

1.5.5 Chiral symmetry restoration

If, on one side, chiral symmetry restoration should play a role in the observed strangeness enhancement (see Sec. 1.5.3), on the other hand, signatures of this effect could also be found in the line shape of the invariant mass distribution of thermal low-mass (< 1 GeV/c^2) dileptons. Their production is in fact largely carried by light vector mesons ρ, ω and ϕ. For this reason their are ideal to investigate changes in the vector-meson mass distributions as the critical temperature for chiral restoration is approached and surpassed. Changes both in width and in mass of the mesons were originally advocated as signatures of the chiral transition [220]. Among light vector mesons, the ρ meson was used from the very beginning as the test particle for in-medium modifications, due to the abundant production of $\pi^+\pi^- \rightarrow \rho$ and subsequent decay $\rho \rightarrow \mu^+\mu^-$ with a lifetime of 1.3 fm/c, shorter than the time between hadronization and the thermal freeze-out. Fig. 1.15 shows NA60 measurement of the low-mass di-muon pair invariant mass distribution after subtracting the background

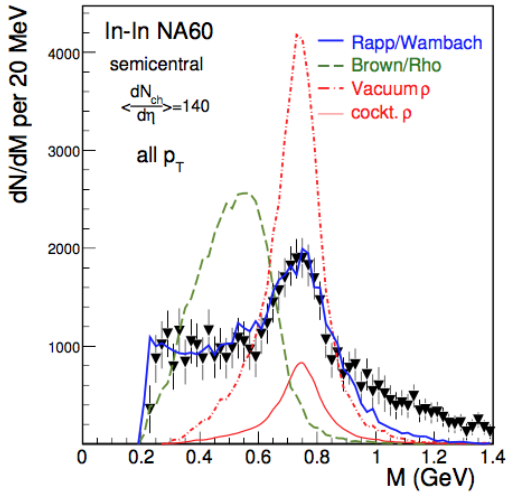

FIGURE 1.15: Di-muon pair invariant mass distribution after background subtraction to the ρ meson peak, for In-In collisions at $\mathrm{d}N_{ch}/\mathrm{d}\eta = 140$, compared to model predictions [230].

to the ρ meson peak, measured in In-In collisions at top SPS energy [137]. The ρ meson is clearly broadened in the medium as compared to the vacuum case, while no sign of mass shift is observed. The measurement was found to be in good agreement with models describing an in-medium broadening scenario (Rapp/Wambach [230]).

1.5.6 Jet quenching

Partons produced in the hard scattering processes occurring in the early stages of the collisions fragment into collimated cascades of hadrons, called jets. In heavy-ion collisions partons propagate inside the hot and dense QGP, and lose energy because of interactions with the colored medium (jet quenching), primarily via gluon radiation and, to smaller extent, elastic scattering [226]. The energy loss (ΔE) carries important information about transport coefficients of the QGP (different for radiative or collisional processes), because it is expected to be dependent on the opacity (associated to the medium density and the interaction strength) and on the path length L traversed by the parton inside the medium. Different models predict linear and quadratic dependences on L of the energy loss for elastic [248] and radiative [95] collisions respectively (a cubic dependence is predicted within the AdS/CFT framework). Furthermore, ΔE also depends on the color charge (different for quarks and gluons) and on the quark mass, as it will be discussed in Sec. 2.4 focusing in more detail on the heavy flavour quarks.

In perturbative QCD, the production cross-section for a hadron h from a process involving high-momentum transfer can be described using a factorisation approach as a convolution of the incoming parton distribution functions (PDFs) inside the nucleons, the hard partonic scattering cross-section and the final state fragmentation function (FFs):

$$\mathrm{d}\sigma_{pp\to hX} \approx \sum_{abjd} \int \mathrm{d}x_a \int \mathrm{d}x_b \int \mathrm{d}z_j f_{a/p}(x_a,\mu_f) \otimes f_{b/p}(x_b,\mu_f) \otimes \mathrm{d}\sigma_{ab\to jd}(\mu_f,\mu_F,\mu_R) \otimes D_{j\to h}(z_j,\mu_F), \tag{1.23}$$

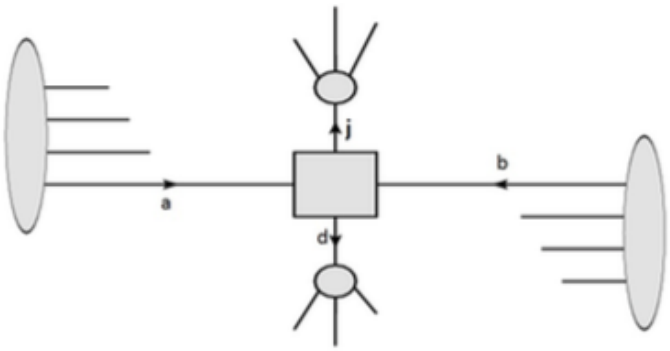

FIGURE 1.16: Schematic illustration of high p_{T} hadron production in high-energy nuclear collisions.

where x_a, x_b are the initial nucleon momentum fractions carried by the interacting partons, $z_j = p_h/p_j$ is the parton momentum fraction carried by the final observed hadron. Then, $f_{a/p}(x_a, \mu_f)$ and $f_{b/p}(x_b, \mu_f)$ are the parton distribution functions, $\mathrm{d}\sigma_{ab\to jd}(\mu_f, \mu_F, \mu_R)$ is the differential cross-section for parton scattering process and $D_{j\to h}(z_j, \mu_F)$ is the fragmentation function for parton j to hadron h, which represents the probability for a parton to hadronize into a hadron carrying a fraction z of the parton momentum. Finally, μ_f and μ_F are the factorisation scales and μ_R is the renormalisation scale. The PDFs are measured at a given Q^2 in experiments of deep inelastic scattering and evolved to different energy scales using DGLAP equations [76]. Fragmentation functions cannot be calculated with pQCD and are usually tuned on measurement in e^+e^- collisions.

The inelastic differential cross-section for nucleus-nucleus interaction, derived from Eq 1.10 under the assumption of the optical Glauber model, is:

$$\frac{\mathrm{d}\sigma_{\mathrm{AB}}^{\mathrm{inel}}}{\mathrm{d}\vec{b}} = 1 - [1 - T_{\mathrm{AB}}(\vec{b})\sigma_{\mathrm{NN}}^{\mathrm{inel}}]^{\mathrm{AB}}, \tag{1.24}$$

where $\sigma_{\mathrm{NN}}^{\mathrm{inel}}$ is the nucleon-nucleon inelastic interaction cross-section and T_{AB} is the nuclear overlap function of the two nuclei. For hard processes, for which the cross section is small, Eq. 1.24 can be approximated as:

$$\frac{\mathrm{d}\sigma_{\mathrm{AB}}^{\mathrm{hard}}}{\mathrm{d}\vec{b}} \simeq 1 - [1 - \mathrm{AB}\, T_{\mathrm{AB}}(\vec{b})\sigma_{\mathrm{NN}}^{\mathrm{hard}}] = \mathrm{AB}\, T_{\mathrm{AB}}(\vec{b})\sigma_{\mathrm{NN}}^{\mathrm{hard}} \propto \langle N_{\mathrm{coll}}\rangle \sigma_{\mathrm{NN}}^{\mathrm{hard}}, \tag{1.25}$$

where N_{coll} is the number of nucleon-nucleon collisions occurring in the nucleus-nucleus interactions. As a consequence, in case of particles produced in hard processes, the Glauber Model predicts that the production yield in heavy-ion collisions is governed by the N_{coll} scaling of the yield in pp collisions. One of the experimental observables used for the study of energy loss inside the QGP is the nuclear modification factor, defined as the ratio between the production of particles in nucleus-nucleus collisions and the one expected according to the binary scaling in nucleon-nucleon collisions:

$$R_{\mathrm{AA}}(p_{\mathrm{T}}, y) = \frac{1}{N_{\mathrm{coll}}} \frac{\mathrm{d}^2 N_{\mathrm{AA}}/p_{\mathrm{T}}\mathrm{d}y}{\mathrm{d}^2 N_{\mathrm{pp}}/p_{\mathrm{T}}\mathrm{d}y}. \tag{1.26}$$

R_{AA} is expected to be compatible with unity if no medium effects are present. A measurement significantly different from the unity implies modifications of the transverse momentum distributions of the produced hadrons, that can be related to in-medium

energy loss effects of quarks at high p_{T}. Other effects must be considered when studying the energy loss of partons inside the QGP, based on measurements of modification of momentum (energy) distribution of hadrons (jets) in A-A collisions relative to pp interactions. The first is that the PDFs of bounded nucleons are different from those of the free nucleons. In addition, other cold nuclear matter (CNM) effects could affect the measured distributions, such as k_{T} broadening due to multiple scattering of the parton in the nucleus, energy loss in CNM ... These effects will be discussed in Sec. 2.3.1. Finally, the parton travelling across the QGP experiences energy loss (hot nuclear matter effects) before fragmenting in the final state. Thus taking into account both cold and hot nuclear matter effects, Eq. 1.23 becomes:

$$\mathrm{d}\sigma_{AB\to hX} \approx \sum_{abjj\prime d} f_{a/A}(x_a) \otimes f_{b/B}(x_b) \otimes \mathrm{d}\sigma_{ab\to jd} \otimes P_{j\to j\prime} \otimes D_{h/j\prime}(z_{j\prime}), \qquad (1.27)$$

where the additional piece $P_{j\to j\prime}$ describes the effects of the hard parton j interacting with the colored medium before fragmenting into hadrons.

It is necessary to disentangle different contributions from cold and hot nuclear matter effects to have access to the medium transport properties via measurements of the R_{AA}. Some of the measurements of R_{AA} of high-p_{T} hadrons and jets at the LHC are presented below.

High-p_{T} hadrons

Measurements of the nuclear modification factors in central heavy-ion collisions at four different centre-of-mass energies, for neutral pions (π^0) (SPS [66, 139, 75], RHIC [64]), charged hadrons ($h^{\pm}$) (RHIC [60]), and charged particles (LHC [23, 1, 132]), compared to predictions of two models from [134, 258] are presented in Fig. 1.17. The LHC measurements at $\sqrt{s_{\mathrm{NN}}} = 2.76$ and 5.02 TeV show stronger suppression than SPS and RHIC measurements at intermediate p_{T}. CMS extended the measurement of the R_{AA} up to 300 GeV/c, and the suppression in the high-p_{T} region is found to be smaller with increasing p_{T}, demonstrating that even very energetic partons suffer energy loss in the medium. ALICE complements the picture down to $p_{\mathrm{T}} = 0$ GeV/c, showing a perfect agreement with CMS and ATLAS in the intermediate-p_{T} region. ALICE also measured the nuclear modification factor of identified particle species, that can further constrain the models. In Fig. 1.18 the R_{AA} of pions, kaons and protons measured in Pb-Pb collisions at $\sqrt{s_{\mathrm{NN}}} = 5.02$ TeV is shown, for different centrality classes. First, it has to be noticed that the suppression has a clear dependence on the collision centrality. It becomes stronger in more central events, where the medium is more spatially extended, hotter and denser. A second observation from results in Fig. 1.18 is that there is a mass ordering at low p_{T} that is a direct consequence of the radial flow. In fact, in the low-p_{T} region, where the particle yields in A-A collisions are not governed by the N_{coll} scaling of the yields in pp collisions, the particle spectra are harder in A-A than in pp collisions due to the radial flow, which is present at all centralities, but is stronger for central collisions and is more pronounced for massive particles. At high p_{T} instead, the suppression is similar for the three species. Different model calculations were compared to the R_{AA} measured in different centrality classes by CMS [132] and ALICE [23] and allowed for an extraction of the transport coefficient [95] $\hat{q} \approx 1.7 - 1.9$ GeV^2/c illustrated in [117, 195].

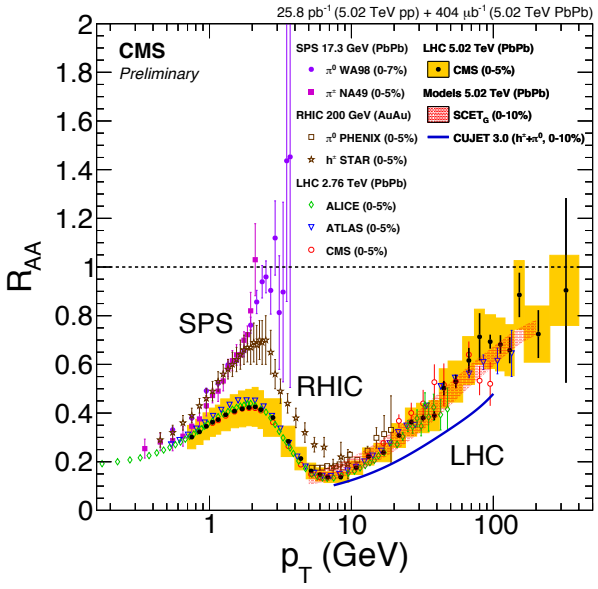

FIGURE 1.17: Measurements of the nuclear modification factors in central heavy-ion collisions at four different center-of-mass energies at SPS [66, 139, 75], RHIC [64, 60], and LHC [23, 1, 132], compared to predictions of two models from [134, 258].

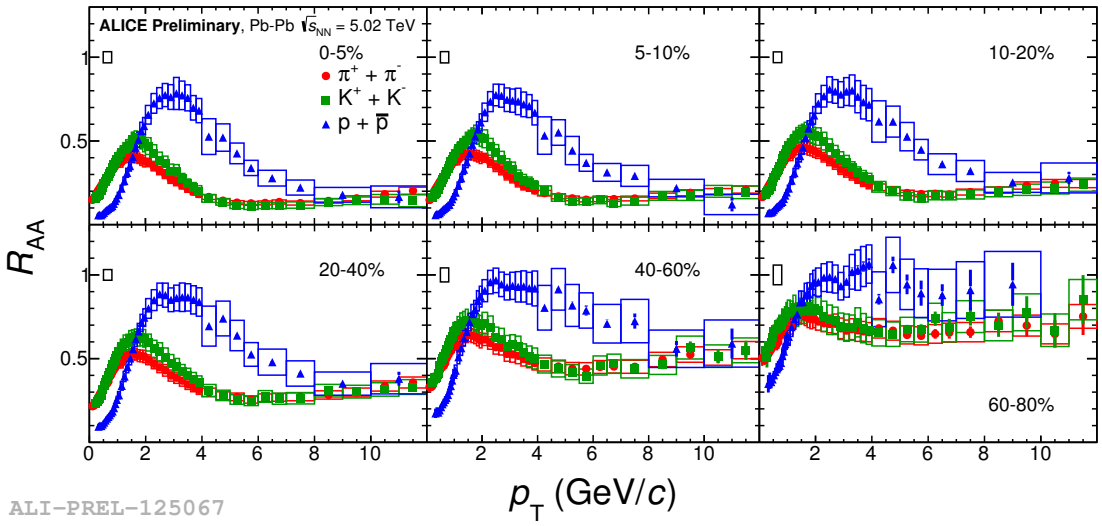

FIGURE 1.18: Nuclear modification factor of pions, kaons and protons measured by ALICE in Pb-Pb collisions at $\sqrt{s_{\mathrm{NN}}} = 5.02$ TeV in different centrality classes [175].

Jets

The interest in jet measurement with respect to single hadrons is that the kinematics of the leading parton becomes accessible and we are less sensitive to fragmentation effects. Therefore jets are expected to put more stringent constraints on assumptions in models for parton energy loss. Experimental techniques are now able to clearly identify jets even in the huge background of high-energy heavy-ion collisions. The interaction of the high-p_{T} partons with the color field of the medium induces the radiation of (mostly) soft ($\omega \ll E_L$, E_L being the energy of leading parton) and collinear

($k_\perp \ll \omega$, $k_\perp$ being the transverse component of the radiated gluon momentum) gluons. The modeling of a jet emerging from the medium is more complex than that of single hadron, since not only the energy loss of the leading parton has to be kept into account, but also the radiated gluons can further re-scatter in the medium inside the jet cone. Thus the total energy inside the jet cone of radius R at the time t_f is:

$$E_{jet}(t_f, R) = E_L(t_f) + E_g(t_f, R), \tag{1.28}$$

where E_g is the energy of the radiated gluons, that is defined as:

$$E_g(t_f, R) = \int_R d\omega dk_\perp^2 \omega f_g(\omega, k_\perp^2, t_f), \tag{1.29}$$

where $f_g(\omega, k_\perp, t)$ is the double differential distribution of the accompanying gluons of the leading parton. It can be obtained after solving the following transport equation for the distribution of radiated gluons [226]:

$$\frac{df_g(w, k_\perp, t)}{dt} = -\hat{e}\frac{\partial f_g}{\partial \omega} + \frac{1}{4}\hat{q}\nabla_{k_\perp}^2 f_g + \frac{dN_g^{rad}}{d\omega dk_\perp^2 dt}. \tag{1.30}$$

The first and the second term in the right-hand side of Eq. 1.30 describe the evolution of radiated gluons which can transfer energy into the medium via collisional processes (controlled by coefficient $\hat{e}$) and accumulate transverse momentum $k_\perp$ (coefficient $\hat{q}$). The last term accounts for additional gluon radiation coming from emission of the leading parton.

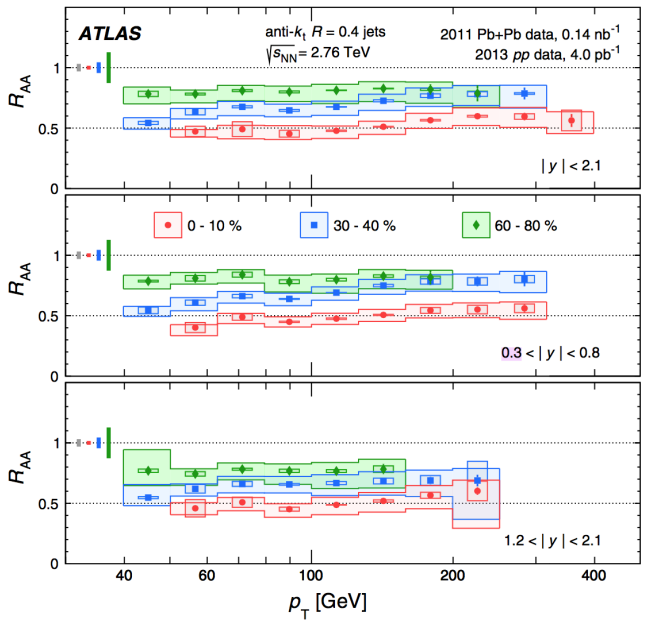

FIGURE 1.19: Jet R_{AA} as a function of p_{T} in different centrality intervals in Pb-Pb collisions at $\sqrt{s_{\mathrm{NN}}} = 2.76$ TeV [4]. Each panel shows a different range in $|y|$.

Fig. 1.19 shows the jet R_{AA} measured by ATLAS as a function of p_{T} in different centrality classes and different rapidity selections for the three panels [4]. The suppression has a clear dependence on the event centrality, while is quite flat as a function of p_{T} in the analysed range from 40 to 400 GeV/c. This result confirms the strong

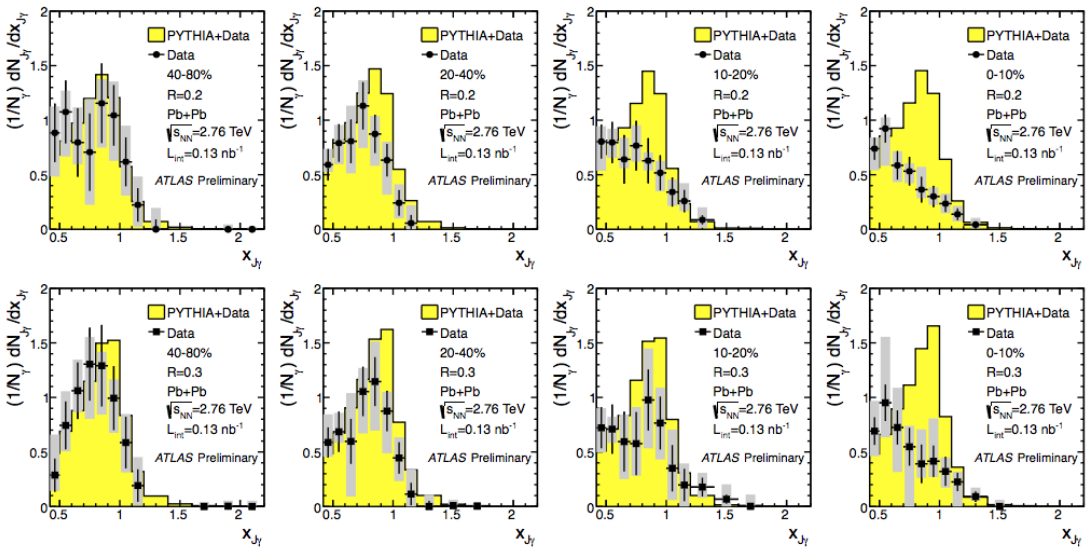

FIGURE 1.20: $\frac{1}{N}\frac{dN}{dx_J}$ distribution for reconstructed photon-jet events in Pb-Pb collisions at $\sqrt{s_{\rm NN}} = 2.76$ TeV compared to PYTHIA calculations (x_J is defined in the text) [202]. Different centrality classes are shown in each column, while the rows show results for two jet radii, R = 0.2 and R = 0.3.

suppression observed for high-$p_{\rm T}$ charged hadron yield in Pb-Pb relative to pp collisions at LHC energies and reveals that the medium is so opaque to quench even the most energetic jets. The azimuthal correlations of transverse energy of back-to-back jets constitute an other interesting observable to characterize the effect of jet-medium interaction. At LHC energies, a large number of dijet from back-to-back partons is observed to have an asymmetry in the energy of the two reconstructed jets, that can be quantified by $x_J = p_{\rm T}^{jet1}/p_{\rm T}^{jet2}$. In general, measurements of inclusive jets and dijet suffer from the fact that leading jets experience themselves some energy loss, thus the energy of the jet is not fully defined. Using weak bosons (Z or W) or photons, that do not interact with the medium, to replace one of the two jets allows us to fully calibrate the initial energy of the jet, as explained in [256]. Fig. 1.20 shows the $\frac{1}{N}\frac{dN}{dx_J}$ distribution for reconstructed photon-jet events in Pb-Pb collisions at $\sqrt{s_{\rm NN}} = 2.76$ TeV compared to PYTHIA calculations [202]. Each column corresponds to different centrality classes, while the rows show results for two jet radii, R = 0.2 and R = 0.3. In more peripheral collisions the x_J distribution is peaked towards 1, thus meaning that higher $p_{\rm T}$ dijets tend to be balanced in momentum. Moving towards more central events, the x_J distribution appears flatter around $0.5 < x_J < 1$, to eventually become peaked around $x_J \sim 0.5$ in the 10% more central events. This is understood in terms of different path lengths that the parton and the photon have to traverse in the medium.

1.5.7 Quarkonium production

Quarkonium, the bound state of a $c\bar{c}$ (charmonium) or $b\bar{b}$ (bottomonium) pair, was proposed from the very beginning as one of the most powerful signatures of the QGP formation. The signature given by the J/ψ vector meson production yield is of particular interest to access information about the formation of a deconfined medium. The J/ψ mesons, and more in general the charmonium states, are formed

by a $c\bar{c}$ quark pair, that can only be produced (due to their large mass) in the initial hard parton scatterings, occurring before the formation of the Quark-Gluon Plasma. Theoretical calculations based on lattice QCD predict a J/ψ suppression to be induced by the screening of the color force in a deconfined medium, due to the presence of free color charges, which becomes stronger as the temperature increases [40, 200]. J/ψ suppression was first observed at the SPS in Pb-Pb collisions, by the NA38 and NA50 experiments [40]. The ratios between the observed J/ψ yield and the expected one based on the so-called "ordinary nuclear absorption" measured in p-A collisions are shown in Fig. 1.21 as a function of the energy density ϵ of the medium traversed by the charmonium state. The results showed that for energy densities up to $\epsilon \lesssim 2$ GeV/fm^3, the yield of the J/ψ meson is compatible with measurements in pp and p-A collisions, in which only ordinary nuclear absorption is present. In Pb-Pb collisions, instead, where ϵ becomes larger, there is a clear deviation from unity of the ratio measured/expected, which was interpreted as a first indication of charmonium suppression due to colour screening in the QGP [40]. Charmonium

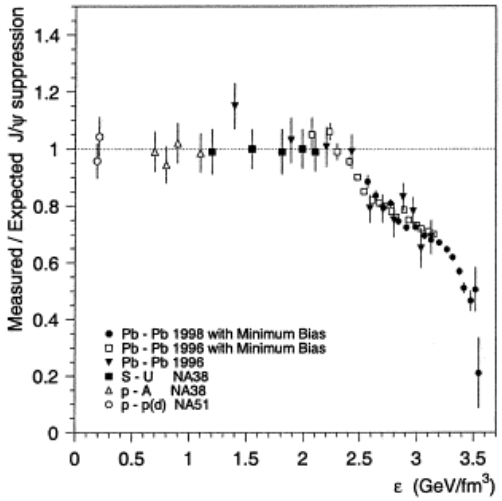

FIGURE 1.21: Ratio between measured J/ψ production and expected one in pp, p-A and A-A collisions as function of the energy density of the medium [40].

states were also expected to melt at different temperatures of the plasma, accordingly to their binding energy, giving rise to a sequential melting scenario [145, 140]. When data at higher collision energies became available at RICH [62, 61], results showed unexpectedly that J/ψ suppression had the same magnitude as the one observed at the SPS [239]. At LHC energies, a reduced suppression as compared to lower collision energies was observed [33]. In Fig. 1.22 the ALICE measurements of J/ψ $R_{\rm AA}$ in Pb-Pb collisions at $\sqrt{s_{\rm NN}} = 2.76$ TeV [33] and at $\sqrt{s_{\rm NN}} = 5.02$ TeV [53] are compared to measurements at RHIC [62] for Au-Au collisions at $\sqrt{s_{\rm NN}} = 200$ GeV. In the left panel of Fig. 1.22 the $R_{\rm AA}$ is presented as a function of the centrality and shows smaller J/ψ suppression at the higher energies, where the measurement is for J/ψ with $p_{\rm T} < 8\,{\rm GeV}/c$. The centrality dependence is similar at the two LHC energies. In the right panel of the same figure, the dependence on $p_{\rm T}$ reveals that the different suppression at different $\sqrt{s_{\rm NN}}$ is mostly in the low-$p_{\rm T}$ region. CMS measured the J/ψ $R_{\rm AA}$ in the high $p_{\rm T}$ region, up to $p_{\rm T} = 30$ GeV/c, confirming a stronger suppression ($R_{\rm AA} \approx 0.3$ for most central events) with respect to low $p_{\rm T}$ [183]. All these observations can be explained by a (re)generation effect of uncorrelated c and $\bar{c}$ quarks, relevant at LHC energies due to the large production cross-section of

$c\bar{c}$ quark pairs. Another observable sensitive to the J/ψ production mechanism is the elliptic flow v_2. If we assume that the J/ψ is produced by coalescence of charm quarks, and that the charm thermalises in the medium, the J/ψ should inherit the flow of the quarks and show a positive v_2. Nevertheless, a non-zero v_2 could also be observed due to the path-length dependence of the charmonium in-medium energy loss, thus the final v_2 may be an interplay of multiple effects. Fig. 1.23 presents recent measurements by ALICE of J/ψ v_2 at forward and mid-rapidity in Pb-Pb collisions at $\sqrt{s_{\rm NN}} = 5.02$ TeV for semi-central events (20-40% centrality class) [42], compared with some of the available theoretical models. At forward rapidity, the maximum v_2 is reached in $4 < p_{\rm T} < 6$ GeV/c, with a significance for non-zero v_2 larger than 6.6σ. Model calculations including (re)combination of thermalised charm and beauty quarks as source of J/ψ production, together with a path-length dependent in-medium energy loss can describe the data at low $p_{\rm T}$, but fail in reproducing the measured shape at higher $p_{\rm T}$, suggesting a missing mechanism in the model (*Du et al.* in Fig. 1.23 [145]). The model by *Zhou et al.* [265] includes, in addition to the cited components, a contribution from the modification of quarkonium production in the presence of a strong magnetic field in the early stage of the heavy-ion collision [165]. The v_2 resulting from the different in-plane and out-of-plane survival probabilities of primordial J/ψ is shown as dashed red and dash-dotted orange lines. At LHC energies also the bottomonium states have been measured, opening the way to precision studies for the $\Upsilon(n\mathrm{S})$ family. Due to smaller production cross-section of b quarks compared to c quarks, effects of coalescence are expected to have a smaller impact with respect to charmonium [83]. A sequential suppression pattern is expected also for $b\bar{b}$ states, due to different binding energies of the bottomonium states. CMS measured the $R_{\rm AA}$ of Υ(1S), Υ(2S) and Υ(3S) as a function of the centrality in Pb-Pb collisions, computed as the average number of participating nucleons, at $\sqrt{s_{\rm NN}} = 2.76$ TeV [184] (Fig. 1.23, right) and at $\sqrt{s_{\rm NN}} = 5.02$ TeV [242]. The $R_{\rm AA}$ in the right panel of Fig. 1.23 shows a suppression for the Υ(2S) state, that is larger with respect to the Υ(1S) state at all centralities, while for the Υ(3S) only an upper limit could be determined. The measured suppression of the three Υ states is compatible with theoretical models of a sequential melting of quarkonium states in a hot medium [184].

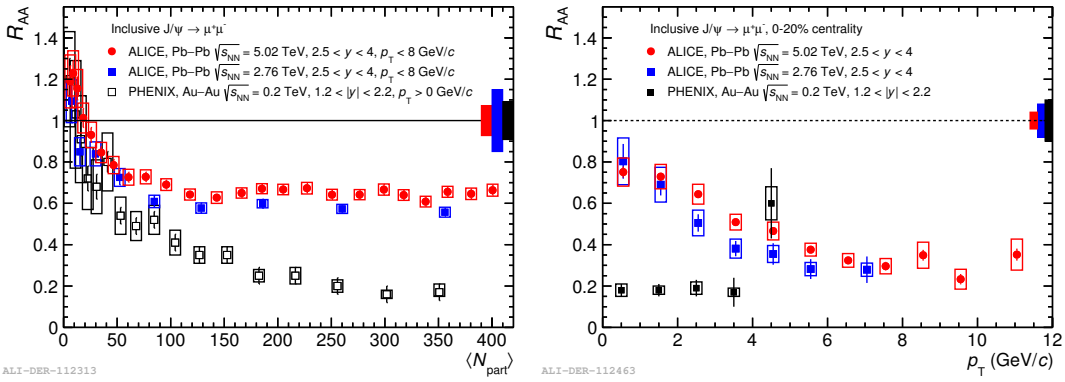

FIGURE 1.22: Centrality (left) and transverse momentum (right) dependence of the J/ψ $R_{\rm AA}$ measured by ALICE in Pb-Pb collisions at $\sqrt{s_{\rm NN}} = 2.76$ TeV [33] (blue) and at $\sqrt{s_{\rm NN}} = 5.02$ TeV [53] (red) compared to PHENIX [62] results Au-Au collisions at $\sqrt{s_{\rm NN}} = 200$ GeV.

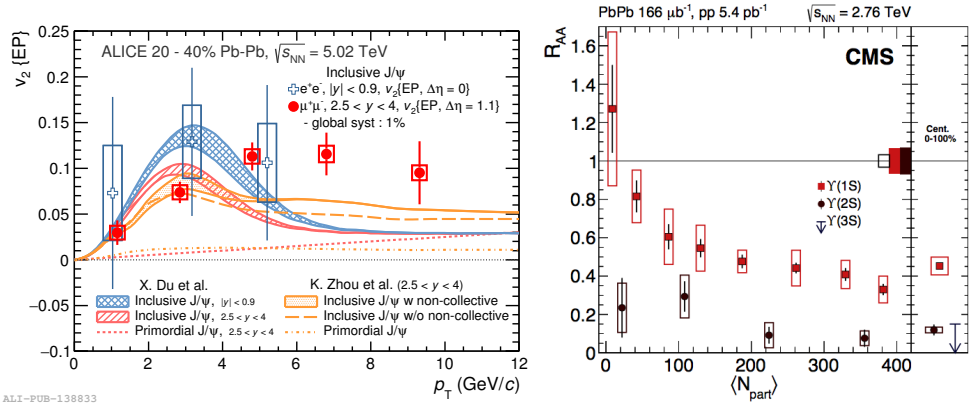

FIGURE 1.23: Left: inclusive J/ψ $v_2(p_T)$ at forward and mid-rapidity for semi-central (20-40%) Pb-Pb collisions at $\sqrt{s_{NN}} = 5.02$ TeV [42]. Calculations from transports model from Refs. [145] and [265] are also shown. Right: nuclear modification factors of Υ(1S) and Υ(2S) meson production in Pb-Pb collisions at $\sqrt{s_{NN}} = 2.76$ TeV measured by CMS, as a function of centrality. The upper limit derived on the nuclear modification factor for Υ(3S) is represented with an arrow in the centrality integrated panel on the right [184].

1.5.8 Latest discoveries in small systems

In 2010 CMS discovered first signals of long-range rapidity correlations in high-multiplicity pp collisions at $\sqrt{s} = 7$ TeV [182], a quite unexpected effect in small systems. Such correlations were already observed in Au-Au collisions at RICH [79, 78, 21] and naturally explained in terms of collective expansion of the medium formed in the collisions. This observation paved the way to searching further signals of collective behaviours in small systems. The interest in the angular correlations among particles lays in the possibility to reveal the underlying mechanisms of particle production. In [182], CMS studied the two-dimensional $\Delta\eta$-$\Delta\phi$ correlation function, where $\Delta\eta$ is the difference in pseudo-rapidity between two particles and $\Delta\phi$ is the difference in their azimuthal angle ϕ. The p_T-inclusive two-particle correlation, as a function of $\Delta\eta$ and $\Delta\phi$ is defined as:

$$R(\Delta\eta, \Delta\phi) = \Big\langle (\langle N \rangle - 1)\Big(\frac{S_N(\Delta\eta, \Delta\phi)}{B_N(\Delta\eta, \Delta\phi)} - 1\Big)\Big\rangle, \tag{1.31}$$

where (i) $S_N(\Delta\eta, \Delta\phi)$ is the correlation function for the signal distribution, determined by counting all particle pairs in each event within a multiplicity bin, (ii) $B_N(\Delta\eta, \Delta\phi)$ is the correlation function for the background distribution, determined by correlating each charged particle of one event with every particle from a different event within the same multiplicity bin, (iii) the average is made over all the multiplicity bins of the analysis. By using the ratio of $S_N(\Delta\eta, \Delta\phi)$ and $B_N(\Delta\eta, \Delta\phi)$, detector effects such as tracking inefficiencies, non-uniform acceptances, etc, are automatically corrected for. In Fig. 1.24, $R(\Delta\eta, \Delta\phi)$ is plotted for high-multiplicity events ($N_{tracks} > 110$) in pp collisions at $\sqrt{s} = 7$ TeV, selecting tracks with $1 < p_T < 3$ GeV/c. Several correlation structures are present. The narrow peak at $(\Delta\eta, \Delta\phi) \approx (0, 0)$ is the contribution from jet-like particle production (near-side peak). The broad ridge around $\Delta\phi \approx \pi$ is due to the fragmentation of back-to-back jets (away-side ridge). The ridge-like structure that appears around $\Delta\phi \approx 0$ was unexpected, indeed never observed in two-particle correlations in pp data. Event

generators, such as PYTHIA, did not reproduce the observed structure, that seems to resemble hydrodynamic behaviours of heavy-ion collisions [79, 78, 21], and the physical origin is still not clear. From this first observation, many studies have been

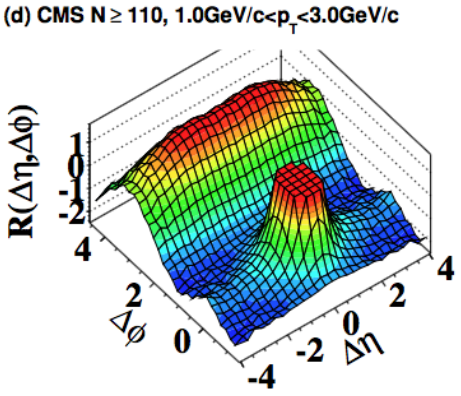

FIGURE 1.24: Two-particle correlation functions in $\Delta\eta$-$\Delta\phi$ for 7 TeV pp collisions, in high multiplicity events ($N_{trk} > 110$), with $1 < p_{\mathrm{T}} < 3\,\mathrm{GeV}/c$ [182].

done to unravel the nature of the long-range near-side peak. Correlations among several produced particles have been explored, since this allows to further suppress short-range particle correlations, such as jets or resonance decays, in order to further investigate the collective nature of the observed azimuthal correlations. One of the most used methods is the Q-cumulants method. Following the approach in [105], the correlations of two, four and six particles are evaluated as:

$$\begin{aligned}
\langle\langle 2\rangle\rangle &= \langle\langle e^{in(\phi_1-\phi_2)}\rangle\rangle \\
\langle\langle 4\rangle\rangle &= \langle\langle e^{in(\phi_1+\phi_2-\phi_3-\phi_4)}\rangle\rangle \\
\langle\langle 6\rangle\rangle &= \langle\langle e^{in(\phi_1+\phi_2+\phi_3-\phi_4-\phi_5-\phi_6))}\rangle\rangle,
\end{aligned} \tag{1.32}$$

where ϕ_i are the azimuthal angles of the correlated particles in an event, n is the harmonic number and $\langle\langle ...\rangle\rangle$ indicates the average over all combinations from all events in a given multiplicity range. The cumulants are obtained as follows:

$$\begin{aligned}
c_n\{4\} &= \langle\langle 4\rangle\rangle - 2 \times \langle\langle 2\rangle\rangle^2 \\
c_n\{6\} &= \langle\langle 6\rangle\rangle - 9 \times \langle\langle 4\rangle\rangle\langle\langle 2\rangle\rangle + 12 \times \langle\langle 2\rangle\rangle^3.
\end{aligned} \tag{1.33}$$

Finally the Fourier harmonics v_n coefficients are obtained from cumulants in Eq. 1.33 as:

$$\begin{aligned}
v_n\{4\} &= \sqrt[4]{-c_n\{4\}} \\
v_n\{6\} &= \sqrt[6]{\frac{1}{4}c_n\{6\}}.
\end{aligned} \tag{1.34}$$

In the left panel of Fig. 1.25, the $v_2\{4\}$, $v_2\{6\}$ measured by CMS in pp collisions at $\sqrt{s} = 13$ TeV are shown as a function of the particle multiplicity, in the interval $0.3 < p_{\mathrm{T}} < 3$ GeV/c and $|\eta| < 2.4$. In the middle and right panels of the same figure, also the $v_2\{8\}$ and $v_2\{\mathrm{LYZ}\}$ (from Lee-Yang zeros method [104]) coefficients are shown, for p-Pb and Pb-Pb collisions at $\sqrt{s_{\mathrm{NN}}} = 5$ TeV and $\sqrt{s_{\mathrm{NN}}} = 2.76$ TeV respectively. $v_2\{8\}$ and $v_2\{\mathrm{LYZ}\}$ are less affected by non-flow correlations, thus are expected to give the cleanest values of the genuine collective flow. The values of

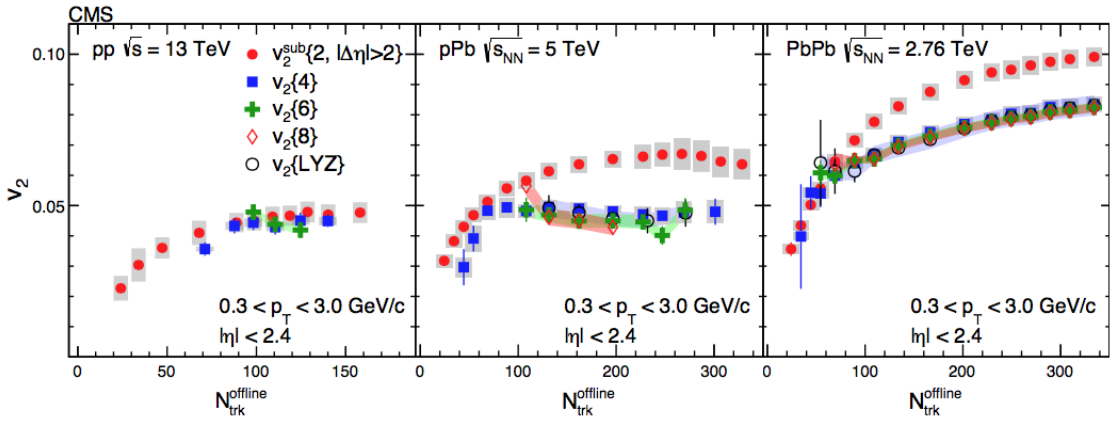

FIGURE 1.25: $v_2^{sub}\{2, |\Delta\eta| > 2\}$, $v_2\{4\}$, $v_2\{6\}$, $v_2\{8\}$ and $v_2\{LYZ\}$ as a function of the multiplicity, in the interval $0.3 < p_{\rm T} < 3\,{\rm GeV}/c$ and $|\eta| < 2.4$ [180] measured by CMS, in pp, p-Pb and Pb-Pb collisions.

$v_2\{4\}$, $v_2\{6\}$ and of $v_2\{8\}$ and $v_2\{\rm LYZ\}$, where present, are compatible among them in each of the three colliding systems. This supports the idea of a collective behaviour behind the long-range correlations observed in pp collisions. In alternative to the classical scenario of position-space anisotropy that must be transposed into final observed momentum-space anisotropies, other theoretical calculations, such as the color glass condensate glasma model [234], interpret the collective behaviour as due to momentum space-anisotropies. These are already present before the collision via initial interactions of gluons inside the projectile proton or nucleus. Besides, in Fig. 1.25 the $v_2^{sub}\{2, |\Delta\eta| > 2\}$, defined from two-particle $\Delta\eta$, $\Delta\phi$ correlation after subtraction of jet correlations from low-multiplicity events, is also shown. Some hydrodynamical models interpret the similar magnitude of $v_2\{4\}$ and $v_2^{sub}\{2, |\Delta\eta| > 2\}$ in pp collisions as the consequence of smaller number of initial fluctuating source than in p-Pb and Pb-Pb collisions [262].

Recently, ALICE reported about the first observation of strangeness production enhancement in high-multiplicity pp collisions [52]. As anticipated in 1.5.3, strangeness enhancement was originally proposed as a signature of the Quark-Gluon Plasma and verified to be even more pronounced for multi-strange baryons. The production of strange hadrons in heavy-ion collisions can be described using a grand-canonical statistical model and does not show a significant dependence on the collision centrality, if one excludes the very peripheral events. For the latter, the relative yield of strange particles to pions becomes very similar to what observed in pp and in p-Pb [35, 57] collisions, and this is understood in terms of canonical suppression [249]. In [52], ALICE presented the measurement of the production of primary strange (K^0_S, Λ, $\bar{\Lambda}$) and multi-strange (Ξ^-, Ξ^+, Ω^-, Ω^+) hadrons in pp collisions at $\sqrt{s} = 7$ TeV. Fig. 1.26 (left panel) shows the $p_{\rm T}$-differential yields of K^0_S, $\Lambda + \bar{\Lambda}$, $\Xi^- + \Xi^+$, $\Omega^- + \Omega^+$ at mid-rapidity, for a selection of classes of events with progressively lower multiplicity, indicated by roman numbers in bracket in the figure. It can be noticed that the $p_{\rm T}$ spectra become harder as the multiplicity increases, and the hardening becomes stronger with increasing particle mass. This is a feature already observed in p-Pb collisions [35] and typically characterizing Pb-Pb collisions, where they are described in terms of relativistic hydrodynamical expansion. A simultaneous fit with the blast-wave model to all $p_{\rm T}$ spectra in the common highest multiplicity class (I in Fig. 1.26 left) and in defined $p_{\rm T}$ ranges allowed the extraction of the chemical freeze-out temperature $T_{\rm fo} = 163 \pm 10$ MeV and the transverse velocity of the bulk

$\langle\beta_\perp\rangle = 0.49 \pm 0.02$. The p_{T} distributions were then fitted in their full p_{T} range using a Tsallis-Lèvy function to obtain the p_{T}-integrated yields. Finally, the right panel of Fig. 1.26 shows the ratio of p_{T}-integrated hadron yields to the pion yields, as a function of the charged-particle multiplicity, together with the measurements in p-Pb ($\sqrt{s_{\mathrm{NN}}} = 5.02$ TeV) and Pb-Pb ($\sqrt{s_{\mathrm{NN}}} = 2.76$ TeV) collisions. Despite the different energy of the collisions, the ratios show a smooth increase from pp to most central Pb-Pb collisions, with the highest multiplicity points in pp being fully compatible with the magnitude of the enhancement in p-Pb at same multiplicity values or in most peripheral Pb-Pb collisions. At higher multiplicities, the ratios in Pb-Pb collisions do not show particular dependence on the collision centrality. This suggests that the mechanism of strangeness enhancement is rather related with the characteristics of the final state produced in the collisions, than the characteristics of the collision itself. Still, the physical mechanism remains unclear, since the available models fail in reproducing at the same time both the ratios in Fig. 1.26 and the p_{T}-integrated proton to pion ratios at mid-rapidity [52].

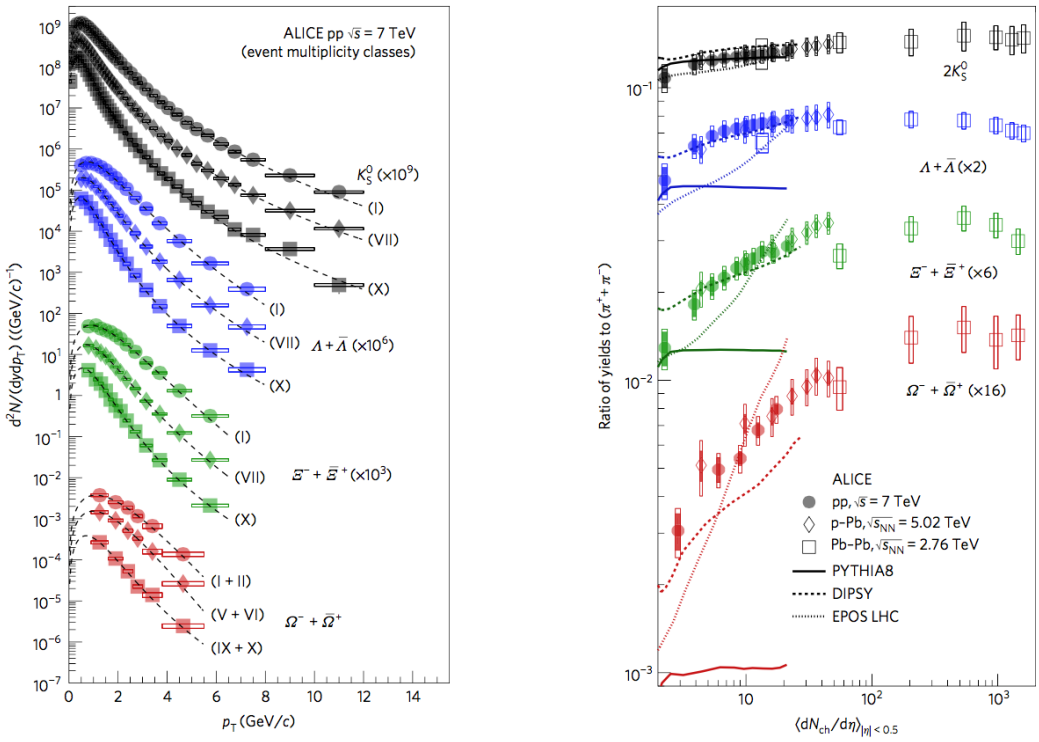

FIGURE 1.26: Left: p_{T}-differential yields of K^0_S, $\Lambda+\bar{\Lambda}, \Xi^-+\Xi^+$, $\Omega^-+\Omega^+$ at mid-rapidity, for a selection of classes of events with progressively lower multiplicity. The Tsallis-Lèvy fit is shown as dashed line. Right: p_{T}-integrated ratios of K^0_S, $\Lambda+\bar{\Lambda}$, $\Xi^-+\Xi^+$, $\Omega^-+\Omega^+$ to pion yield $(\pi^- + \pi^+)$ as a function of $\langle \mathrm{d}N_{\mathrm{ch}}/\mathrm{d}\eta \rangle$ at mid-rapidity [52].

Chapter 2

Heavy flavours

2.1 The importance of being heavy

Hadrons carrying heavy flavour (charm or beauty quarks) constitute a powerful probe to study the properties of the Quark-Gluon Plasma created in high-energy heavy-ion collisions. Heavy quarks are produced in initial hard parton-scattering processes of the nucleon-nucleon collisions and on short time scales ($\sim$ 0.1 and 0.02 fm/c for charm and beauty, respectively) compared to the QGP formation time, which is about 0.3-1.5 fm/c at Large Hadron Collider (LHC) energies [194]. Furthermore, in contrast with light quarks and gluons, that can be produced or annihilated during QGP evolution, heavy quarks have negligible annihilation rate [112] and secondary "thermal" charm and beauty production from processes like $gg \rightarrow c\overline{c}$ is expected to be negligible in the QGP [263], unless the initial QGP temperatures happen to be much larger than those currently reachable at colliders. Therefore, heavy quarks preserve their identity when traversing the fireball and can be used as a probe to study the interaction with the medium constituents, in particular getting access to the transport coefficients of the QGP.
There are different ways to experimentally detect hadrons containing heavy flavours:

- full reconstruction of exclusive decay channels, like $\mathrm{D}^0 \rightarrow \mathrm{K}^-\pi^+$ or $B^0 \rightarrow J/\psi K^0_S$;
- detection of leptons from heavy-flavour hadron decays, for example $D, B \rightarrow e, \mu + X$;
- selection of semi-inclusive decays, for example J/ψ mesons displaced from the primary vertex (thus, coming from beauty decay) or Λ_c and Ξ_c reconstruction from $e\,\Lambda$ and $e\,\Xi$ pairs;
- reconstruction of $c-$ and $b-$jets.

2.2 Heavy-quark production in pp collisions

The study of heavy flavours in pp collisions is an important benchmark of perturbative QCD calculations. The large mass of these quarks acts as a cut off; it prevents indeed from divergencies in the calculation that arise from collinear gluon radiation and that are suppressed in case of massive quarks due to the so-called dead-cone effect [143]. For this reason, perturbative calculations are applicable down to low p_{T} as well as for the computation of the total cross-section. The two processes responsible for heavy-quark production at the leading order in perturbative theory are $q\overline{q} \rightarrow Q\overline{Q}$ and $gg \rightarrow Q\overline{Q}$, whose corresponding diagrams are shown in Fig. 2.1. The relative

production rates for heavy quarks of mass m_1 and m_2 behave, at high energy, as [198]:

$$\begin{aligned} \frac{\sigma(gg \to Q_1\overline{Q}_1)}{\sigma(gg \to Q_2\overline{Q}_2)} &\to 1 - \frac{\log(m_1^2/m_2^2)}{\log(s/m_2^2)}, \\ \frac{\sigma(q\overline{q} \to Q_1\overline{Q}_1)}{\sigma(q\overline{q} \to Q_2\overline{Q}_2)} &\to 1 - \mathcal{O}(m_1^4/s^2), \end{aligned} \tag{2.1}$$

hence, at large centre-of-mass energy s, the $q\overline{q} \to Q\overline{Q}$ process vanishes more quickly. In the left panel of Fig. 2.2 the inclusive production cross-section in pp collisions, as a function of centre-of-mass energy, for charm, bottom, top quark pairs is shown [198]. Analytic calculations that provide a description for inclusive heavy-hadron production

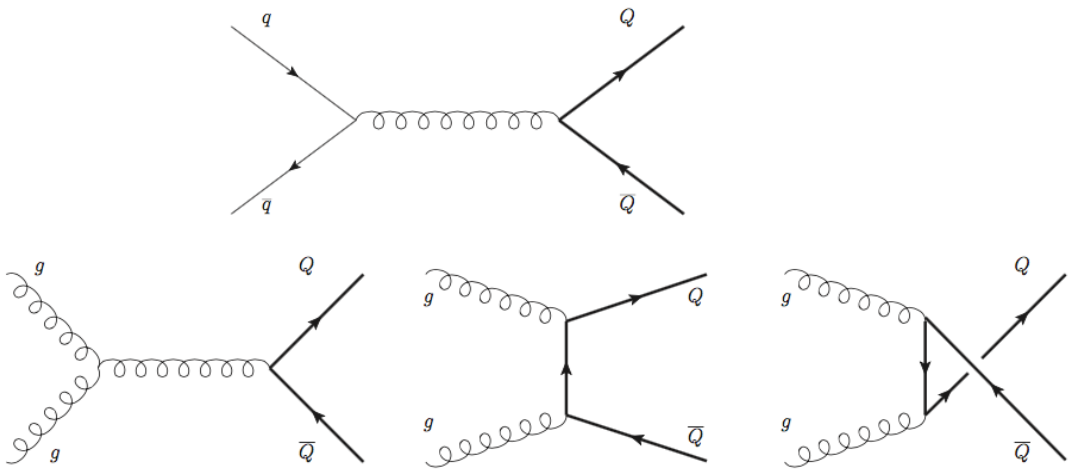

FIGURE 2.1: Leading-order diagrams for heavy-quark pair production.

or their decay products in pp collisions utilising the collinear factorisation approach are FONLL [120, 119] and GM-VFNS [189]. FONLL is a Fixed-Order calculation with Next-to-Leading-Logarithms resummation and provides calculations in the full kinematic range ($p_{\mathrm{T}} \ll m_q, p_{\mathrm{T}} \sim m_q, p_{\mathrm{T}} \gg m_q$), giving description of bottom and charm production at Tevatron, RHIC and LHC. GM-VFNS was originally performed in the massless limit and subsequently improved with finite mass terms. Within both approaches, the single inclusive distribution of a heavy-flavour hadron H_q is obtained as a convolution of a perturbative cross section $d\sigma$ at the partonic level with parton distribution functions $f(x, Q^2)$ and non-perturbative fragmentation function $D^{NP}_{q->H_q}$. Possibly a decay function $g^{weak}_{H_q \to l}$ describing, for instance, the hadron weak decay into a lepton can be included:

$$d\sigma_l = f(x, Q^2) \otimes d\sigma_q \otimes D^{NP}_{q->H_q} \otimes g^{weak}_{H_q \to l}. \tag{2.2}$$

The functional form of the non-perturbative fragmentation function (FF) $D^{NP}_{q->H_q}$ is generally chosen as result of fit on e^+e^- data for heavy-hadron production. For example, FONLL uses a Kartvelishvili et al. distribution [179] for the FF of bottom quarks:

$$D^{NP}_{b->H_b} = (\alpha + 1)(\alpha + 2)z^{\alpha}(1 - z), \tag{2.3}$$

where the fragmentation parameter α was chosen as a result of the fit on the LEP data concerning production of a mixture of b-hadrons [122, 174, 17], since no data are available for individual hadrons like B^0 or B^+. For charm quarks, experimental data

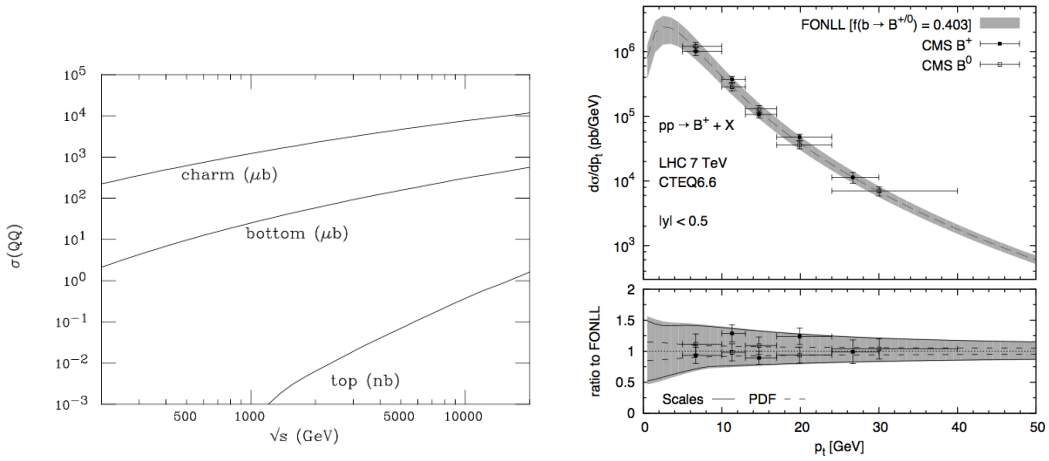

FIGURE 2.2: Left: total production cross-sections for charm, bottom and top quark pairs, in pp collisions as a function of the center-of-mass energy [198]. Right: FONLL calculation and systematic uncertainty band [123] for beauty-hadron production, rescaled to the $|y| < 0.5$ region, and comparison with CMS data [181, 128].

for individual D-meson species exist. Since from the theoretical point of view some differences are expected in the quark fragmentation into pseudo-scalar (D^0, D^+) and vector (D^{*+}) mesons, one needs to define two different FF. The functional forms used for the FF of charm quarks in FONLL are taken from [121] and have one single non-perturbative parameter common to the pseudo-scalar and vector FF. This parameter is adjusted on ALEPH data [96] for D^{*+} production. Fig. 2.2 (right) shows the CMS measurement of p_T-differential cross-section for B^+ and B^0 mesons as a function of p_T in the rapidity interval $|y| < 0.5$ in pp collision at $\sqrt{s} = 7$ TeV [181, 128], compared to FONLL predictions. The FONLL uncertainty band is obtained from variations of renormalisation scale μ and common factorisation scale μ_f as well as of the heavy-quark mass. Similar comparison, but for charmed hadrons, is shown in Fig. 2.3 for D^0-meson production in pp collision at $\sqrt{s} = 7$ TeV measured by ALICE [43], as a function of p_T. FONLL predictions are displayed in the left panel and GM-VFNS in the right one. Calculations are in agreement with bottom and charm production at the LHC, within their uncertainties. FONLL central values tend to underestimate charm production, that systematically lays on the upper edge of FONLL uncertainty band, whereas GM-VFNS tends to slightly overestimate the production at high p_T but agrees very well at intermediate-low p_T.

In contrast to FONLL and GM-VFNS, that are based on NLO pQCD calculations and are limited to inclusive production of heavy quarks and mesons, general-purpose Monte Carlo generators, such as PYTHIA [243], provide a more complete description of the final state, including decay kinematics. They simulate the final states of high-energy collisions in full detail, including hard and soft interactions, parton distributions, initial- and final-state parton showers, multiple parton interactions, fragmentation and decay. They contain a large list of hard Standard Model and Beyond Standard Model processes, which are interfaced with parton emission, different models of hadronisation and particle decays. The processes are treated at leading order (LO). The higher order calculations are included only in an approximate approach. However, the next-to-leading order (NLO) is needed to compare results with experimental data. The PYTHIA generator, for example, contains theoretical perturbative

QCD calculations that are exact only at leading order, where only the pair creation processes $q\overline{q} \rightarrow Q\overline{Q}$ and $gg \rightarrow Q\overline{Q}$ are included. Higher-order contributions at the NLO to account for flavour excitation processes like $qQ \rightarrow qQ$, $gQ \rightarrow gQ$ and gluon splitting $g \rightarrow Q\overline{Q}$ are also accounted. The cross-section of these processes diverges as the transverse momentum of the outgoing quarks of the hard interaction (p_{T}^{hard}) goes to zero. The divergences can be controlled by a lower cut on the value of p_{T}^{hard}, that has a large influence in the heavy-flavour production in the low-p_{T} region, which is of the prime interest for ALICE. To compare PYTHIA to data, p_{T}^{hard} and other PYTHIA parameters must be tuned to reproduce as well as possible NLO predictions. The first generator of heavy-quark production that did the effort of matching NLO calculations with LO calculations was MC@NLO [155]. It performed a matching to the general-purpose Monte Carlo generator HERWIG [135], proposing a first solution to the otherwise double counting of NLO events, by subtracting the approximated NLO cross sections (which were implemented in HERWIG) from the exact NLO cross section. The NLO calculations for the hard processes in heavy-flavour production are obtained with the POWHEG [154] (Positive Weight Hardest Emission Generator) generator, that interfaces with PYTHIA and HERWIG parton showers.

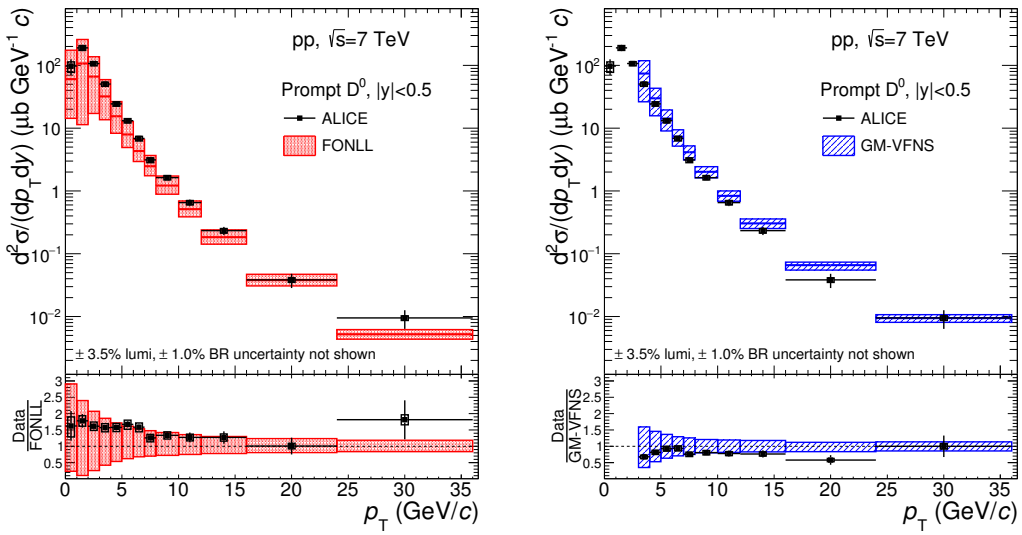

FIGURE 2.3: p_{T}-differential production cross section of prompt D^0 mesons with $|y| < 0.5$ in the interval $0 < p_{\mathrm{T}} < 36$ GeV/c, in pp collisions at $\sqrt{s} = 7$ TeV [43]. The cross section is compared to pQCD calculations: FONLL [120, 119] (left panel) and GM-VFNS [189] (right panel).

2.3 Heavy quarks in p-A collisions

2.3.1 Cold nuclear matter effects

The importance of studying heavy-flavour production in p-A collisions relies on the possibility to characterise a class of phenomena that are expected to break the binary scaling in nucleus-nucleus collisions but are not a consequence of the presence of a deconfined plasma. Such effects can in fact be present both in p-A and in A-A collisions and their origin is mainly related to modification of the PDFs for nucleons bound in nuclei and multiple soft scatterings of the partons in the nuclei prior to

the hard interaction energy loss in cold nuclear matter. They are usually called Cold Nuclear Matter (CNM) effects and can affect the partons that undergo the hard scattering process (initial-state effects) as well as the produced heavy quarks and hadrons (final-state effects). Furthermore, recent interest in p-A collisions is focused on revealing possible effects that could indicate the formation of a QGP droplet in small collision systems [101, 110, 118].

2.3.2 Nuclear Parton Distribution Functions

One can quantify the nuclear modification of the parton distribution function via the ratio:

$$R_i^A(x, Q^2) = f_{i/A}(x, Q^2)/f_{i/p}(x, Q^2) \tag{2.4}$$

where $f_{i/A}(x, Q^2)$ and $f_{i/p}(x, Q^2)$ are the parton distribution functions in the nucleus

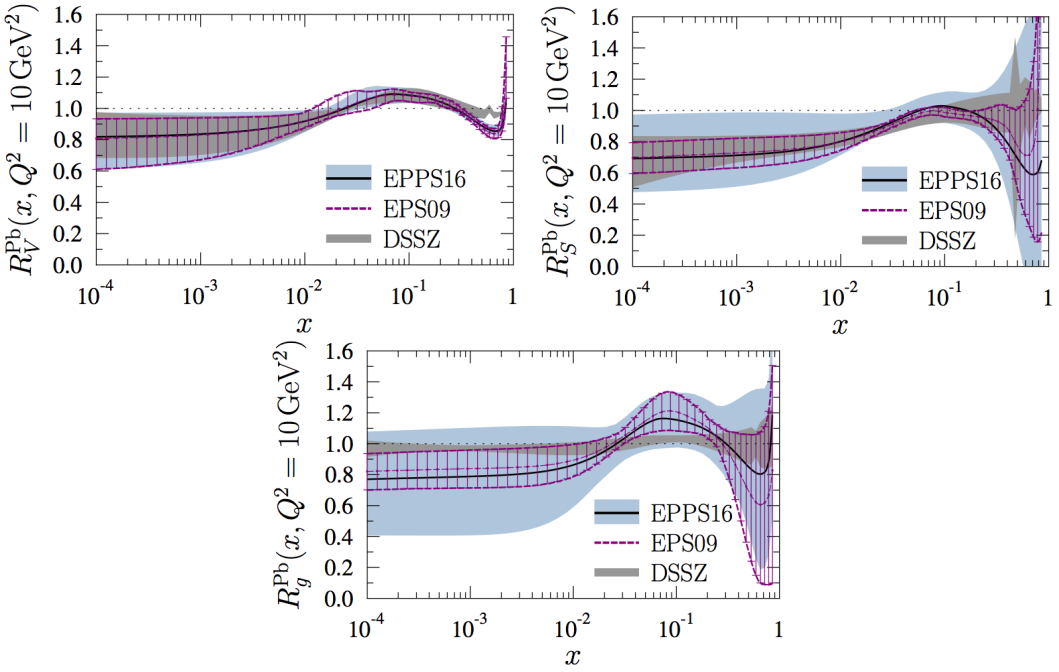

FIGURE 2.4: The nuclear modifications $R_i^A(x, Q^2)$ (Eq. 2.4) in a Pb nucleus for three different flavours as given by the EPS09 [147], EPPS16 [148] and DSSZ [151] nPDF parameterisations.

and in the proton respectively, and the variable x represents the fraction of the nucleon momentum carried by a parton. Figure 2.4 shows the ratios $R_i^A(x, Q^2)$ for the valence quarks, sea quarks and gluons inside a Pb nucleus as obtained from global DGLAP calculations with next-to-leading order EPS09 [147], EPPS16 [148] and DSSZ [151] parameterisations of the nuclear PDFs which are tuned on measurements of DIS, Drell-Yan and hadron and dijet production in p-A collisions. In general, four different regions are visible in the trend of $R_i^A(x, Q^2)$ versus x, which correspond to four x-regimes in which different effects influence the PDFs of bound nucleons:

- **Fermi motion:** this effect is due to the thermal momentum that nucleons have inside the nucleus. Thus the structure function $F_2^A(x)$ of the bound nucleons is the convolution of the structure function of the free nucleon $F_2^N(x/z)$ (where z is the momentum fraction of the nucleons times the atomic number of the nucleus) with the momentum distribution of nucleons $f_N(z)$ inside the nucleus: $F_2^A(x) = \int_x^A dz f_N(z) F_2^N(x/z)$. This is the dominant effect for $x > 0.7$.

- **EMC effect:** first observed in 1982 by the EMC collaboration [92], this effect appears as $R_i^A(x, Q^2) < 1$, especially affecting the region of valence quarks $0.2 < x < 1$. Figure 2.5 shows the ratio of the structure functions of iron $F_2^{iron}(x)$ and deuterium $F_2^D(x)$, that one would expect to be at 1 (except for some corrections at high x from Fermi motion). From further experimental investigations, it was clear that the effect is almost independent from the squared momentum transfer, it increases with nuclear mass number A and scales approximately with the average nuclear density. Many phenomenological models tried to explain such behaviour. In the Q^2-rescaling models, quarks in nuclei move in a larger confinement volume and, because of the uncertainty principle, they carry less momentum than quarks in free nucleons. Some models proposed that quarks in nuclei move in quark bags with n quarks, other proposed an enhancement of pion-cloud effects and a nuclear pionic field, but no models so far are universally accepted.

- **Nuclear shadowing and anti-shadowing:** a second depletion region is observed in the ratio of parton distribution functions $f_{i/A}(x, Q^2)/f_{i/p}(x, Q^2)$ at very low $x < 0.01$ (typical region of sea quarks). This is commonly denoted by shadowing region and is accompanied by an anti-shadowing region at $0.01 < x < 0.2$ in which the ratio $R_i^A(x, Q^2)$ is above unity. Different models were proposed to explain the nuclear shadowing. Some models are based on virtual photon fluctuations into vector meson states (GVMD); others invoke superposition ad fusion of partons of different nucleons at very low x, that should deplete the region, thus favouring the population of the anti-shadowing region.

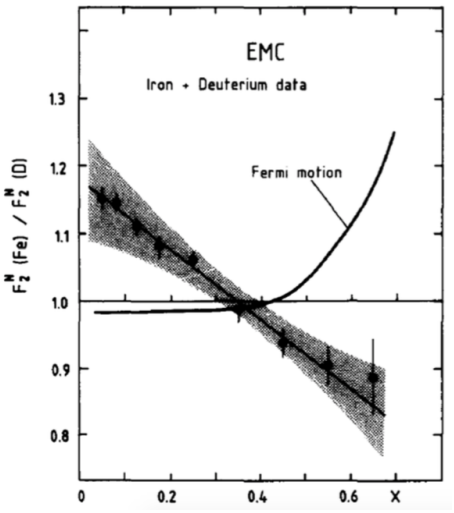

FIGURE 2.5: Ratio of iron $F_2^{iron}(x)$ and deuterium $F_2^D(x)$ structure function as a function of Bjorken-x [92].

An other CNM effect is the so-called Cronin Effect [136], discovered in the '70s at FermiLab. It consists in an observed enhancement in the nuclear modification factor for p_{T} values between 2 and 5 GeV/c. This is commonly understood as due to the fact that, in p-A collisions, the partons of the projectile nucleon undergo several elastic scatterings with the partons of the target nucleus before the hard scattering process occurs. The multiple scatterings give the parton an extra momentum component in the transverse plane (k_{T} broadening), which causes a broadening of the p_{T} spectra of the heavy quarks produced in the hard scattering processes, resulting

in an enhancement of the nuclear modification factor at low and intermediate p_{T}. Going towards larger values of transverse momentum, the extra-k_{T} from the elastic collisions becomes negligible and the nuclear modification factor gets close to unity.

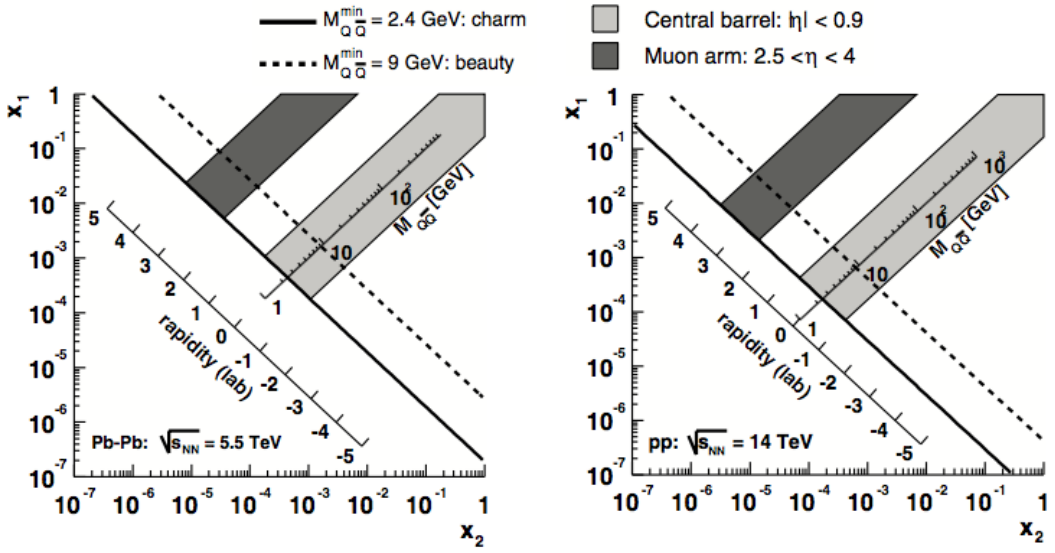

FIGURE 2.6: ALICE acceptance in the (x_1, x_2) plane for heavy flavours in Pb-Pb at $\sqrt{s_{\mathrm{NN}}} = 5$ TeV on the left panel and pp collisions at $\sqrt{s} = 14$ TeV on the right [149].

It is important to understand which are the ranges of Bjorken x at play when producing $c\overline{c}$ and $b\overline{b}$ pairs at the LHC. The probed x value depends on the centre-of-mass energy of the collision, on the invariant mass $M_{Q\overline{Q}}$ of the $Q\overline{Q}$ pair produced in the hard scattering and on its rapidity $y_{Q\overline{Q}}$. Under the hypothesis that the transverse momentum of the parton in the nucleon is negligible, the four-momenta of the two incoming gluons are $(x_1, 0, 0, x_1) \cdot (Z_1/A_1)\sqrt{s_{\mathrm{pp}}}/2$ and $(x_2, 0, 0, -x_2) \cdot (Z_2/A_2)\sqrt{s_{\mathrm{pp}}}/2$, where x_1 and x_2 are the momentum fractions carried by the gluons, and $\sqrt{s_{\mathrm{pp}}}$ is the c.m.s. energy for pp collisions. The c.m.s $\sqrt{s_{\mathrm{NN}}}$ energy of nucleon-nucleon collisions is obtainable as $\sqrt{s_{\mathrm{NN}}} = Z/A\sqrt{s_{\mathrm{pp}}}$. The square of the invariant mass of the produced $Q\overline{Q}$ pair is given by:

$$M^2_{Q\overline{Q}} = x_1 x_2 s_{\mathrm{NN}} = x_1 \frac{Z_1}{A_1} x_2 \frac{Z_2}{A_2} s_{\mathrm{pp}}, \tag{2.5}$$

and the rapidity in the laboratory is:

$$y_{Q\overline{Q}} = \frac{1}{2}\ln\left[\frac{E + p_z}{E - p_z}\right] = \frac{1}{2}\ln\left[\frac{x_1}{x_2} \cdot \frac{Z_1 A_2}{Z_2 A_1}\right]. \tag{2.6}$$

From Eq. 2.5 and 2.6 and for a symmetric colliding system ($A_1 = A_2, Z_1 = Z_2$) one obtains:

$$x_1 = \frac{M_{Q\overline{Q}}}{\sqrt{s_{\mathrm{NN}}}}\exp(+y_{Q\overline{Q}}), \qquad x_2 = \frac{M_{Q\overline{Q}}}{\sqrt{s_{\mathrm{NN}}}}\exp(-y_{Q\overline{Q}}). \tag{2.7}$$

Because of its lower mass, charm allows to probe lower x values than beauty. The x regime relevant for charm production at the LHC ($\approx 10^{-4}$) is about 2 orders of

magnitude lower than at RHIC and 3 orders of magnitude lower than at the SPS. Measurements of charm and beauty particles in the forward (or backward) rapidity region ($|y| \sim 4$) gives access to x regimes about 2 orders of magnitude lower, down to $x \approx 10^{-6}$. Figure 2.6 [149] shows the (x_1, x_2) plane for charm and bottom production at the LHC covered by the ALICE acceptance, for Pb-Pb collisions at $\sqrt{s_{\rm NN}} = 5$ TeV on the left panel and pp collisions at $\sqrt{s} = 14$ TeV on the right. The shadowed regions correspond to the rapidity region covered by the ALICE central barrel ($|\eta| < 0.9$) and by the muon arm ($2.5 < \eta < 4$). The points with equal invariant mass (solid and dashed lines for $c\bar{c}$ and $b\bar{b}$ pairs respectively) lie on hyperbolae (straight lines in the log-log scale).

2.3.3 Experimental results in p-A collisions

The nuclear modification of the PDFs can significantly affect final hadrons yields, especially at low $p_{\rm T}$ due to shadowing, which is the most relevant effect at LHC energies. One can define the nuclear modification factor for p-Pb collisions as:

$$R_{\rm pPb} = \frac{1}{A} \frac{d^2\sigma^{\rm promptD}_{pPb}/dp_{\rm T}dy}{d^2\sigma^{\rm promptD}_{pp}/dp_{\rm T}dy}, \tag{2.8}$$

where A is the Pb mass number $A = 208$.

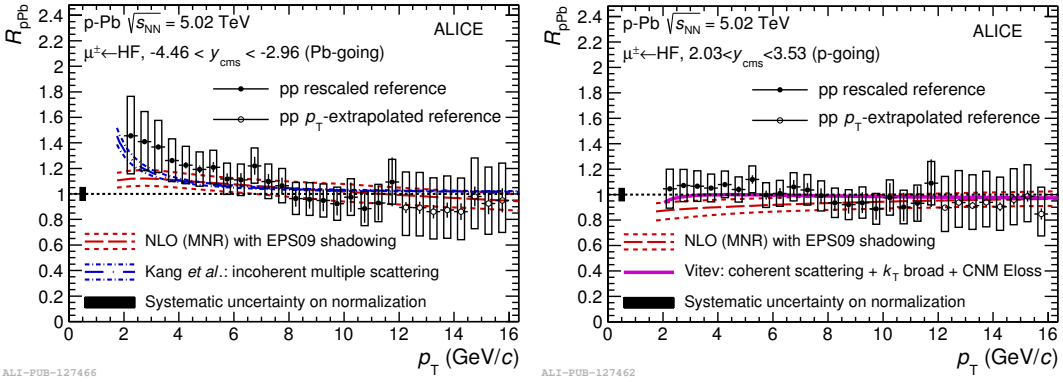

FIGURE 2.7: Nuclear modification factor of muons from heavy-flavour hadron decays as a function of $p_{\rm T}$ for p-Pb collisions at $\sqrt{s_{\rm NN}} = 5.02$ TeV at backward rapidity ($-4.46 < y_{\rm cms} < -2.96$, left) and forward rapidity ($2.03 < y_{\rm cms} < 3.53$, right) [44] compared to model predictions [177, 199].

ALICE measured the $p_{\rm T}$-differential nuclear modification factor $R_{\rm pPb}$ of muons from heavy-flavour hadron decays in p-Pb collisions at $\sqrt{s_{\rm NN}} = 5.02$ TeV at forward and backward rapidity [44] (Fig. 2.7). At backward rapidity, the Bjorken-x values are expected to vary from about 10^{-3} to 10^{-1}, while at forward rapidity they are located in the range from about $5{\cdot}10^{-6}$ to 10^{-2}. While at forward rapidity muon $R_{\rm pPb}$ is compatible with unity in the full $p_{\rm T}$ range ($2 < p_{\rm T} < 16\,{\rm GeV}/c$) in which the measurement was carried out, at backward rapidity, it is larger than unity at low $p_{\rm T}$ with a maximum deviation of $R_{\rm pPb} = 1$ of 2.2σ of the combined statistical and systematic uncertainties in the interval $2.5 < p_{\rm T} < 3.5$ GeV/c. At higher $p_{\rm T}$, it is compatible with unity. The results indicate that CNM effects are small and that the strong suppression of the yields of muons from heavy-flavour hadron decays observed

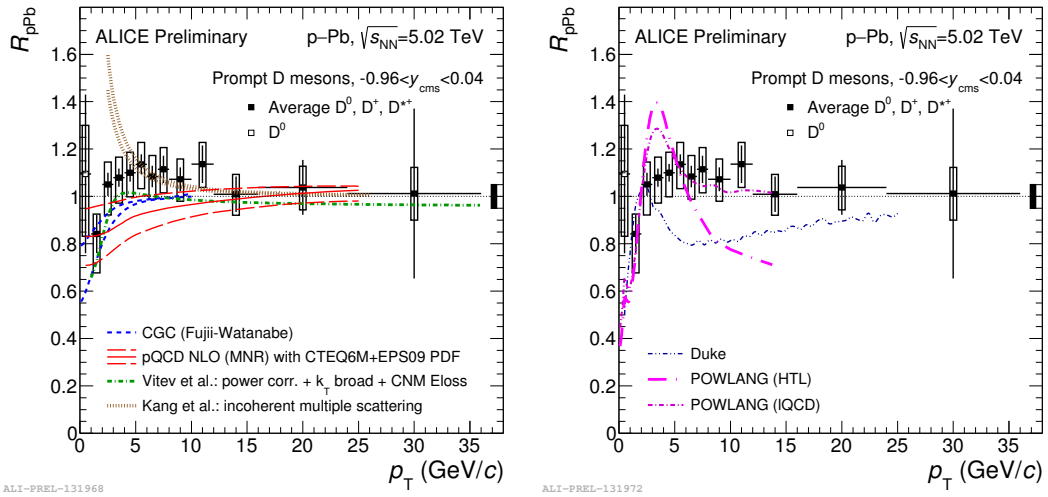

FIGURE 2.8: Left: nuclear modification factor $R_{\rm pPb}$ of prompt D mesons in p-Pb collisions at $\sqrt{s_{\rm NN}} = 5.02$ TeV. Data are compared with results of theoretical calculations including only CNM effects [158, 123, 148, 240, 177]. Right: the results of the Duke [260] and POWLANG [101] transport models are compared with the measured D-meson $R_{\rm pPb}$.

in the 10% most central Pb-Pb collisions [31] should result from final-state effects, i.e. the heavy-quark in-medium energy loss. ALICE also measured the $R_{\rm pPb}$ of prompt D mesons in p-Pb collisions at $\sqrt{s_{\rm NN}} = 5.02$ TeV as a function of $p_{\rm T}$ and the results are shown in Fig. 2.8 (left panel) [223]. Data are compared to theoretical models that include CNM effects: a calculation based on the Color Glass Condensate formalism [157, 158], a FONLL calculation [123] with CTEQ6M PDFs [225] and EPPS16 NLO nuclear modification [148], a LO pQCD calculation with intrinsic $k_{\rm T}$ broadening, nuclear shadowing and energy loss of the charm quarks in cold nuclear matter (Vitev et al.) [240], and a higher-twist calculation based on incoherent multiple scatterings (Kang et al.) [177]. The three former calculations describe the data within uncertainties in the entire $p_{\rm T}$ range, although for the CGC calculation the compatibility with the data in 3-12 GeV/c is at the limit of the uncertainties of the data and of the calculations. The calculation by Kang et al., which has a different trend with respect to the others, is disfavoured by the data for $p_{\rm T} < 3$–4 GeV/c. CNM effects are expected to be largest for small $p_{\rm T}$, where, in addition, the predictions of the different theoretical approaches differ and the statistical uncertainty of the present measurement for the lowest $p_{\rm T}$ interval is about 30% and does not discriminate the different models. In the right-hand panel of Fig. 2.8, the data are compared with the results of two transport model calculations, Duke [260] and POWLANG [101], both of them assuming that a Quark–Gluon Plasma is formed in p–Pb collisions. Both models are based on the Langevin approach for the transport of heavy quarks through an expanding deconfined medium described by relativistic viscous hydrodynamics. In both the Duke and POWLANG results the D-meson nuclear modification factor shows a structure with a maximum at $p_{\rm T} \approx 2.5$ GeV/c and $p_{\rm T} \approx 3-4$ GeV/c respectively, followed by a moderate (< 20-30%) suppression at higher $p_{\rm T}$, resulting from the interplay of CNM effects and interactions of charm quarks with the radially expanding medium. The trend predicted by these models is disfavoured by the data, which in particular disfavour a suppression larger than 10-15% in the interval $3 < p_{\rm T} < 12$ GeV/c.

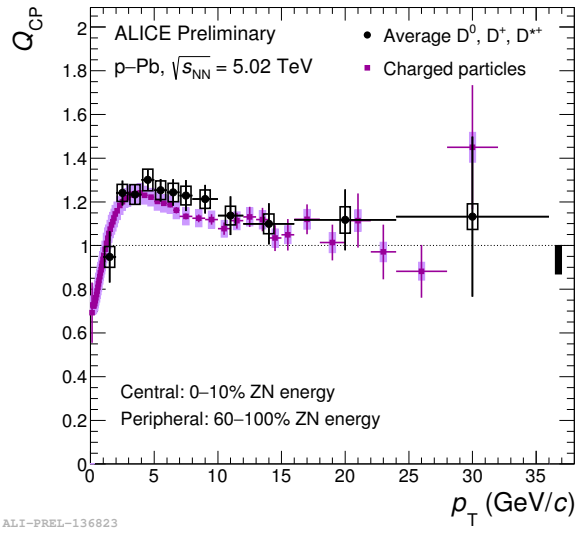

FIGURE 2.9: D-meson (black) and charged-particle (magenta) central-to-peripheral nuclear modification factor [223].

The nuclear modification factor in p-Pb collisions can be also measured in given centrality classes. Its definition is:

$$Q_{\mathrm{pPb}}^{\mathrm{mult}} = \frac{(\mathrm{d}^2N/\mathrm{d}p_{\mathrm{T}}\mathrm{d}y)_{\mathrm{pPb}}^{\mathrm{mult}}}{\langle T_{\mathrm{pPb}}\rangle^{\mathrm{mult}}(\mathrm{d}^2\sigma_{pp}/\mathrm{d}p_{\mathrm{T}}\mathrm{d}y)}, \tag{2.9}$$

where $(\mathrm{d}^2N/\mathrm{d}p_{\mathrm{T}}\mathrm{d}y)_{\mathrm{pPb}}^{\mathrm{mult}}$ is the yield of a given species in p-Pb collisions in a given centrality class, and $\langle T_{\mathrm{pPb}}\rangle^{\mathrm{mult}}$ is the average nuclear overlap function in the same centrality class. In order to achieve better precision on the yields, the ratio of the nuclear modification factor in central to peripheral events, Q_{CP}, can be defined as:

$$Q_{\mathrm{CP}} = \frac{(\mathrm{d}^2N/\mathrm{d}p_{\mathrm{T}}\mathrm{d}y)_{\mathrm{pPb}}^{\mathrm{central}}/\langle T_{\mathrm{pPb}}\rangle^{\mathrm{central}}}{(\mathrm{d}^2N/\mathrm{d}p_{\mathrm{T}}\mathrm{d}y)_{\mathrm{pPb}}^{\mathrm{peripheral}}/\langle T_{\mathrm{pPb}}\rangle^{\mathrm{peripheral}}}. \tag{2.10}$$

The Q_{CP} of D mesons in the 0-10% and 60-80% centrality classes was measured by ALICE [223] (Fig. 2.9) and it increases in the interval 1-4 GeV/c, up to values of about 1.25 and then tends to decrease. The average value of the D-meson Q_{CP} in the interval $3 < p_{\mathrm{T}} < 8$ GeV/c is larger than unity by 1.5 standard deviations of the combined statistical and systematic uncertainty. It is an open question whether the observed bump of Q_{CP}, whose magnitude is similar for D mesons and charged particles, is related to initial state effects or to collectivity effects in the final state.

2.4 Heavy quarks in A-A collisions

High-momentum partons traversing the QGP are expected to lose energy because of interactions with the medium constituents. One of the experimental observables used for the study of energy loss is the nuclear modification factor, defined in Sec. 1.5.6. The possibility to disentangle effects of cold nuclear matter from the ones related to in-medium energy loss paves the way to characterise the hot and dense medium properties. In fact, the magnitude of energy lost in the medium is determined by the

properties of the fireball like the transport coefficients, that encode the momentum transfers with the medium, or the mean free path, closely related to the medium density ρ and the cross section σ of the parton-medium interaction. A colour charge can lose energy in a plasma at a temperature T by two mechanisms: radiative and collisional energy losses, which originate, respectively, from elastic and inelastic interactions with the medium constituents.

2.4.1 Collisional processes

Collisional processes are $2 \to 2$ elastic scatterings off thermal gluons (Fig. 2.10, first to third diagrams) and quarks (Fig. 2.10, fourth diagram). It is possible to calculate, in the limit $E \gg M^2/T$, the heavy-quark collisional energy loss $\mathrm{d}E/\mathrm{d}x$ in a QGP, by summing all contributions of Fig. 2.10 [215]:

$$\frac{\mathrm{d}E}{\mathrm{d}x} = \frac{4\pi T^2}{3}\,\alpha_s(m_D^2)\,\alpha_s(ET)\Big[\Big(1+\frac{n_f}{6}\Big)\ln\frac{ET}{m_D^2} + \frac{2}{9}\frac{\alpha_s(M^2)}{\alpha_s(m_D^2)} \times \ln\frac{ET}{M^2} + c(n_f) + \mathcal{O}\Big(\alpha_s(m_D^2)\,\ln\frac{ET}{m_D^2}\Big)\Big], \tag{2.11}$$

where α_s is the QCD running coupling constant, n_f is the number of flavours considered in the scattering diagrams of Fig. 2.10, m_D is the Debye screening mass of the plasma $m_D = 4\pi\alpha_s T^2(1+n_f/6)$ and $c(n_f) \sim \mathcal{O}(1)$ is a constant.

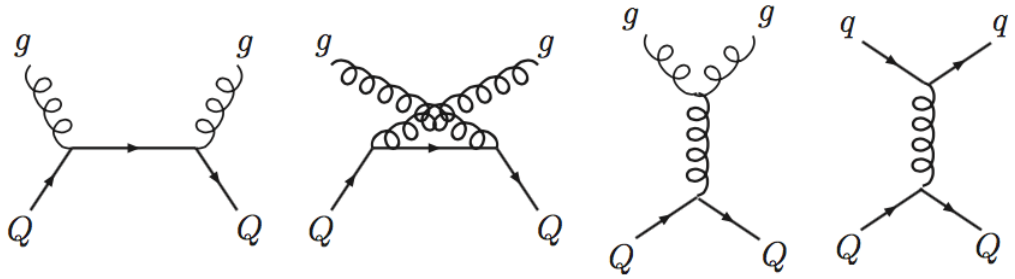

FIGURE 2.10: Feynman diagrams for leading-order perturbative HQ scattering off light partons.

The multiple scatterings of the heavy quark with the medium partons can also be treated as Brownian motion and typically be described by the Boltzmann equation. In the limit of small momentum transfer, the latter can be reduced to the Fokker-Planck equation, which is often further reduced into the Langevin equation. These partial-differential equations can be used as transport equations, to describe the evolution of the momentum distribution of heavy quarks along time. The Langevin equation for heavy-quark collisional energy loss presents itself as [124]:

$$\frac{\mathrm{d}\vec{p}}{\mathrm{d}t} = -\eta_D(p)\vec{p} + \vec{\xi}. \tag{2.12}$$

In Eq. 2.12, the first right-hand side term is the deterministic friction force, while the second one ($\vec{\xi}$) is the thermal random noise, satisfying the properties:

$$\langle \xi^i(p_\mathrm{T})\xi^j(p_{\mathrm{T}'})\rangle = b^{ij}(p_\mathrm{T})\frac{\delta_{tt'}}{\mathrm{d}t}, \quad b^{ij}(p_\mathrm{T}) = k_\parallel(p)\hat{p}^i\hat{p}^j + k_\perp(\delta^{ij} - \hat{p}^i\hat{p}^j). \tag{2.13}$$

In Eq. 2.13, k represents the momentum-space diffusion coefficient of heavy quarks; the coefficient η_D of Eq. 2.13 is involved in the definition of the spatial diffusion

coefficient D_s, which is related to the momentum-space diffusion coefficient via:

$$D_s = \frac{T}{M\eta_D} = \frac{2T^2}{k}. \tag{2.14}$$

To simulate the evolution of heavy quarks, one needs to discretise terms and calculate the increment $\vec{p}(t + \Delta t) - \vec{p}(t)$ at a given time t.

2.4.2 Gluon-radiation processes

While a parton is traversing the medium, it picks up some transverse momentum $k_\perp$ due to multiple scatterings. If we consider a gluon in the hard parton wave function, when the accumulated $k_\perp$ is enough, it can decohere from the partonic projectile and be emitted. These are $1 \to 2$ processes, like $Q \to g\,Q$, where Q is the heavy quark and g the gluon. The average phase ϕ of the gluon emitted with frequency ω on a distance Δz is approximately:

$$\phi = \left\langle \frac{k_\perp^2}{2\omega}\Delta z \right\rangle \sim \frac{\hat{q}L}{2\omega}L = \frac{\omega_c}{\omega}, \tag{2.15}$$

where $\hat{q}$ is the transport coefficient of the medium, defined as the average squared transverse momentum transferred to the projectile per average unit path length L: $\hat{q} = \langle k_\perp^2 \rangle / L$ [232]. Hence, gluons are emitted from the parton traversing a finite path length L with a characteristic gluon frequency ω_c:

$$\omega_c = \frac{1}{2}\hat{q}L^2. \tag{2.16}$$

The distribution of energy ω of the radiated gluons, for small energies $\omega < \omega_c$ is of the form:

$$\omega\frac{\mathrm{d}I}{\mathrm{d}\omega} \sim \frac{2\alpha_s C_R}{\pi}\sqrt{\frac{\omega_c}{2\omega}}, \tag{2.17}$$

where C_R is the Casimir factor for the QCD coupling, equal to 4/3 for quark-gluon coupling and to 3 for gluon-gluon coupling. The ω-integrated average parton energy loss results then (BDMPS formalism [232]):

$$\langle \Delta E \rangle \propto \alpha_s\, C_R\, \hat{q}\, L^2. \tag{2.18}$$

We can then summarise the main properties of average parton energy loss via radiative processes:

- it grows with the path length like: $\Delta E \propto L^2$;
- it is proportional to $\alpha_s C_R$, thus it is larger by a factor $9/4 = 2.25$ for a gluon traversing the medium than for a quark;
- it is independent of the initial parton energy E.

Furthermore, while in the limit of massless partons the probability of gluon emission is maximum for collinear radiation, in the massive limit the soft-gluon emission probability, for small emission angles $\Theta \ll 1$, is [143]:

$$\mathrm{d}\sigma_{Q\to gQ} \sim \frac{\Theta^2 \mathrm{d}\Theta^2}{[\Theta^2 + \Theta_0^2]}\frac{\mathrm{d}\omega}{\omega}, \tag{2.19}$$

with $\Theta_0 = M_Q/E_Q$. Therefore, in the kinematical region $\Theta < \Theta_0$ the yield of radiated gluons in the forward direction provides a small contribution to the total multiplicity of emitted gluons. The depleted forward region is called the *dead cone* [143]. Since $\Theta_0 = M_Q/E_Q$, the effect is expected to be more relevant with increasing parton mass. A hierarchy in the energy loss is hence expected:

$$\Delta E_{gluon} > \Delta E_{light\,quark} > \Delta E_{heavy\,quark}, \tag{2.20}$$

where the first inequality comes from the different couplings in gg and gq processes due to the Casimir factor in Eq. 2.17 and the second from the dead-cone effect. The hierarchy, if present, should consequently affect the $R_{\rm AA}$ values of hadrons originating from gluon, light and heavy-quark fragmentation.

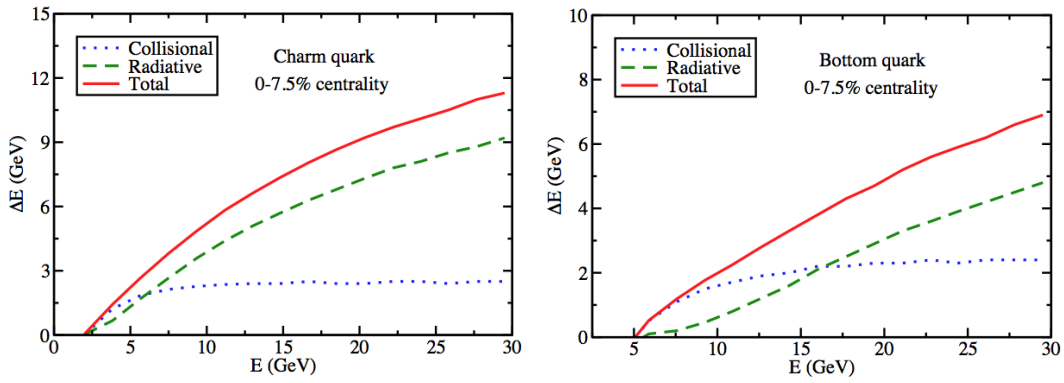

FIGURE 2.11: Comparison of radiative and collisional energy losses for charm (left) and for bottom (right) quarks as a function of the quark energy from calculations in [124].

In Fig. 2.11, an example of calculations from [124] for the energy loss of charm (left) and beauty (right) quarks in central Pb-Pb collisions at the LHC is shown as a function of the initial energy of the quark. In the model [124], quarks evolve in a static medium at a temperature $T = 300$ MeV according to a Langevin equation (like that in Eq. 2.12) with an additional term for radiative contribution. Both the contributions from collisional and radiative energy loss are displayed in Fig. 2.11. Elastic interactions dominate the low-$p_{\rm T}$ region, up to ~ 6 GeV/c for charm and ~ 16 GeV/c for beauty quarks. At higher $p_{\rm T}$, the contribution from radiative processes is the dominant one and must be considered when performing calculations at LHC energies. It is also interesting to look at Fig. 2.12 (left), always from the same calculations [124], that shows the thermalisation process of charm quarks in the medium as a function of time. The initial energy of the charm quarks is 10 GeV. Depending on the different implementation for energy loss, the thermalisation of the charm quarks occurs at different times.

2.4.3 Heavy flavour hadronisation in the medium

The final hadron yields and momentum distributions not only depend on the energy loss mechanisms of the partons inside the medium, but also on the way parton hadronisation occurs. There are basically two mechanisms for heavy quarks to produce heavy-flavour hadrons: fragmentation of a heavy quark into a jet of lower-momentum hadrons, or coalescence (re-combination) of low-momentum quarks with partons from

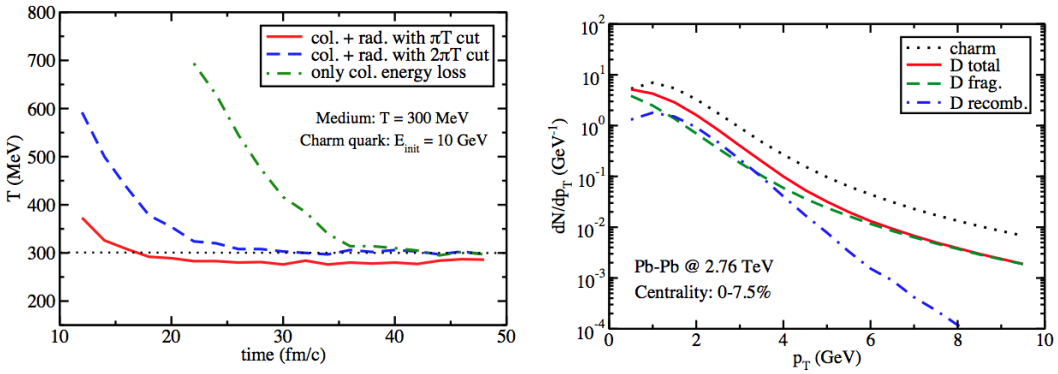

FIGURE 2.12: Left: thermalisation process of charm quarks in a static medium [124]. Right: relative contributions from different hadronisation mechanisms to D-meson production from charm quarks, as a function of the transverse momentum, from calculations in [124].

the medium. Figure 2.12 (right) illustrates the contributions of coalescence and fragmentation mechanisms into the final D-meson yields from charm-quark hadronisation in central Pb-Pb collisions at the LHC. The recombination mechanism gives an important contribution at low p_{T}, while the independent fragmentation dominates at higher p_{T}. Since the coalescence with partons from the medium gives rise to a hadron with momentum larger than that of the heavy quark, the p_{T} distribution of the final hadrons produced via coalescence will be slightly harder than that of the initial quarks, i.e. shifted towards higher momenta. A remarkable example for the study of heavy-quark hadronisation processes and the role of coalescence is the production of J/ψ meson, discussed in Sec. 1.5.7.

The measurement of $\mathrm{D_s}$-meson production in A-A collisions can provide crucial additional information to understand the interactions of charm quarks with the strongly-interacting medium formed in heavy-ion collisions at high energies. In particular, the $\mathrm{D_s}$-meson yield is sensitive to strangeness production and to the hadronisation mechanism of charm quarks. The enhancement of strange particle production in presence of QGP was already discussed in Sec. 1.5.3 and a pattern of strangeness enhancement increasing with the hadron strangeness content when going from pp to p-A and then to heavy-ion collisions was observed at the SPS [86, 87, 65, 74], at RHIC [38] and at the LHC [52]. This strangeness enhancement effect could also affect the production of charmed hadrons if the dominant mechanism for D-meson formation at low and intermediate momenta is in-medium hadronisation of charm quarks via recombination with light quarks. Under these conditions, the relative yield of $\mathrm{D_s}$ mesons with respect to non-strange charmed mesons at low p_{T} is predicted to be enhanced in nucleus-nucleus collisions as compared to pp interactions [84, 191, 172]. The comparison of the p_{T}-differential production yields of non-strange D mesons and of $\mathrm{D_s}$ mesons in A-A and pp collisions is therefore sensitive to the role of recombination in charm-quark hadronisation. Figure 2.13 shows D- and $\mathrm{D_s}$-meson R_{AA} (left-hand panel) and v_2 (right), in semi-central Au-Au collisions at RHIC, from the TAMU model calculations [173], also compared to STAR measurements of $\mathrm{D^0}$-meson R_{AA} in 0-80% Au-Au collisions [264]. The model predicts the maximum R_{AA} to be more pronounced for the $\mathrm{D_s}$, reaching values larger than 1.5 due to c-quark coalescence with the enhanced strangeness in Au-Au. In the calculations of the model, the elliptic flow coefficient results to be sensitive both to the collectivity of the medium and to hadronisation.

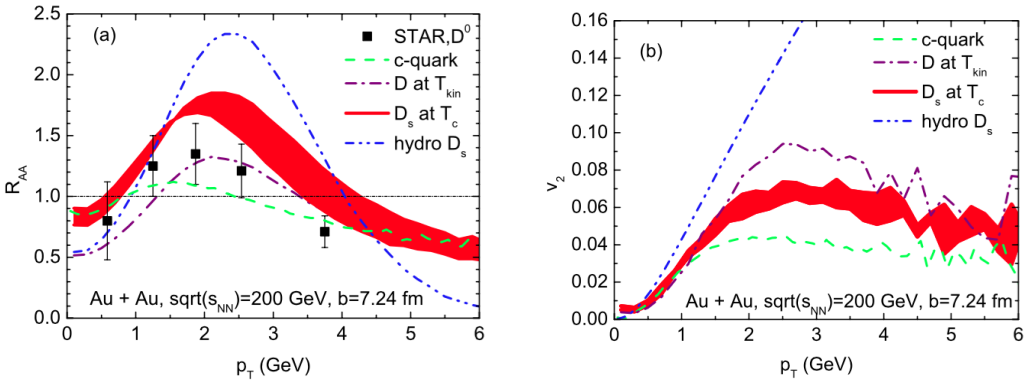

FIGURE 2.13: Results for the $R_{\rm AA}$ (left panel) and v_2 (right) of $\rm D_s$ (red bands) and D (purple dashed-dotted lines) mesons in semi-central Au-Au collisions at RHIC [173]. Results for charm quarks at pseudo-critical temperature T_c (green dashed lines), the equilibrium limit for $\rm D_s$ meson in the hydrodynamic medium at T_c (blue dashed-double-dotted line) and STAR data for the $\rm D^0$-meson $R_{\rm AA}$ in in 0-80% Au-Au collisions are also reported [264].

Thanks to the coalescence of charm quarks with thermal light and strange quarks, the flow coefficients of non-strange D and $\rm D_s$ mesons reach values larger by ∼50% than the v_2 of charm quarks. Furthermore, interactions of non-strange D mesons with the medium constituents during the hadronic phase create a further 30% difference between strange and non-strange D-meson v_2.

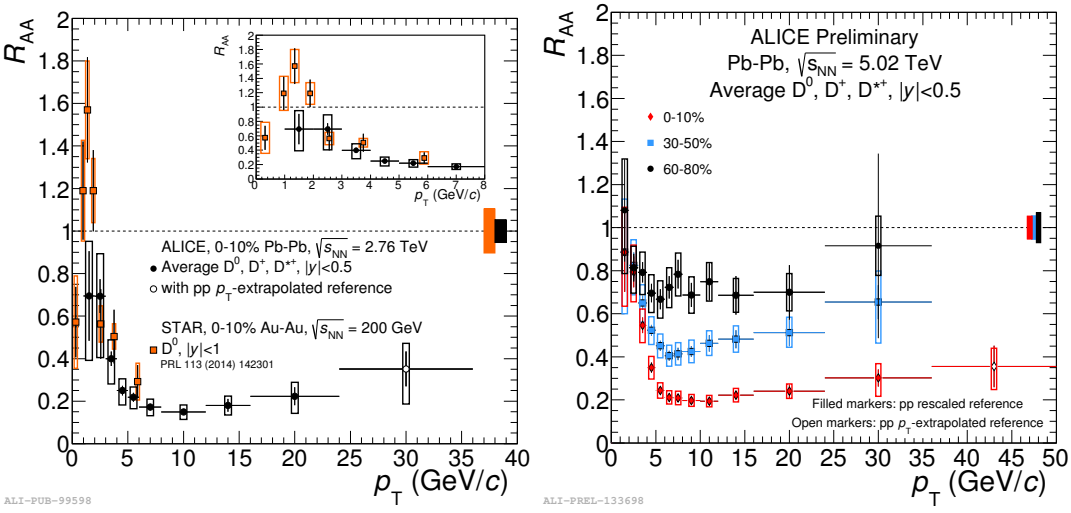

FIGURE 2.14: Left: average non-strange D-meson $R_{\rm AA}$ as a function of $p_{\rm T}$ in the 10% most central Pb-Pb collisions at $\sqrt{s_{\rm NN}} = 2.76$ TeV measured by ALICE [58], compared to $\rm D^0$ $R_{\rm AA}$ measured by the STAR Collaboration in 0-10% Au-Au collisions at RHIC at $\sqrt{s_{\rm NN}} = 200$ GeV [59]. A zoomed-in plot of the interval $0 < p_{\rm T} < 8\,{\rm GeV}/c$ is shown in the inset. Right: average $R_{\rm AA}$ of prompt $\rm D^0$, $\rm D^+$ and $\rm D^{*+}$ mesons in the 0–10% (red), 30–50% (blue) and 60–80% (black) centrality classes at $\sqrt{s_{\rm NN}} = 5.02$ TeV [222].

2.4.4 Experimental results in A-A collisions

In the left-hand panel of Fig. 2.14, the average D-meson $R_{\rm AA}$ for the 10% most central Pb-Pb collisions at $\sqrt{s_{\rm NN}} = 2.76$ TeV measured by ALICE [58] is compared to the $\rm D^0$ nuclear modification factor measured by the STAR Collaboration for the 10% most central Au-Au collisions at $\sqrt{s_{\rm NN}} = 200$ GeV [59]. The nuclear modification factors measured at the two energies are compatible within uncertainties for $p_{\rm T} > 2\,{\rm GeV}/c$. Similar $R_{\rm AA}$ of D mesons for $p_{\rm T} > 5\,{\rm GeV}/c$ does not necessarily imply a similar charm-quark energy loss at the two collision energies. A combined effect of a denser medium and of the harder $p_{\rm T}$ spectra at the LHC could result in similar values of $R_{\rm AA}$ at lower collision energies [94]. In the interval $1 < p_{\rm T} < 2\,{\rm GeV}/c$, the $R_{\rm AA}$ measured by STAR shows a maximum. This effect can be described by models including parton energy loss, collective radial flow and the contribution of the recombination mechanism to charm-quark hadronisation [22]. The ALICE results at higher energy do not show a maximum. Several effects can explain differences at the two energies, due to the different role of initial-state effects or of radial flow at the two collision energies. In the initial state, the modification of the parton distribution functions in a nuclear environment is predicted to lead to a stronger suppression of the heavy-quark production yields at low $p_{\rm T}$ with increasing $\sqrt{s_{\rm NN}}$ [147], because of the smaller values of Bjorken-x probed and therefore more shadowing is expected. In addition, the $k_{\rm T}$-broadening effect, which gives rise to an enhancement of the $R_{\rm AA}$ at low-intermediate $p_{\rm T}$ (Cronin peak), is known to be more pronounced at lower collision energies [254, 253]. In the final state, in addition to energy loss, the collective expansion of the medium is also predicted to affect the momentum distribution of charmed hadrons in heavy-ion collisions. This effect could be enhanced by hadronisation via recombination. The stronger radial flow (see Sec. 1.5.4) at the LHC than at RHIC [39, 24, 30] does not necessarily give rise to a more pronounced bump-like structure in the $R_{\rm AA}$ at low $p_{\rm T}$ with increasing collision energy. Its effect can in fact be counterbalanced by the different shape of the momentum spectra in pp collisions at different energies. Reduced uncertainties on the measurements are needed to draw firmer conclusions. Preliminaries results of the average nuclear modification factors of $\rm D^0$, $\rm D^+$ and $\rm D^{*+}$ as a function of $p_{\rm T}$ measured in Pb-Pb collisions at $\sqrt{s_{\rm NN}} = 5.02$ TeV are shown in Fig. 2.14 (left), for the 0–10%, 30–50% and 60–80% centrality classes [222]. The D-meson nuclear modification factors at $\sqrt{s_{\rm NN}} = 5.02$ TeV exhibit a suppression which is compatible within uncertainties with that measured at lower energy $\sqrt{s_{\rm NN}} = 2.76$ TeV [58]. The suppression is maximal at $p_{\rm T} = 6$–10 GeV/c for central and semi-central events, where a reduction of the yields by a factor of about 5 and 2.5 with respect to the binary-scaled pp reference is observed in the two centrality classes, respectively. The suppression decreases with decreasing $p_{\rm T}$ for $p_{\rm T} < 6$ GeV/c, and $R_{\rm AA}$ is compatible with unity in the interval $1 < p_{\rm T} < 3$ GeV/c. The average $R_{\rm AA}$ in the 60–80% centrality class shows a suppression by about 20–30%, without a pronounced dependence on $p_{\rm T}$. Recent studies proposed that event selections and geometry determination of the collision can bias the $R_{\rm AA}$, causing an artificial suppression for $R_{\rm AA}$ in peripheral collisions even in absence of jet quenching and shadowing [196].

The $R_{\rm AA}$ of prompt $\rm D_s$ mesons in the 10% most central Pb-Pb collisions at $\sqrt{s_{\rm NN}} = 2.76$ TeV is compared in the left-hand panel of Fig. 2.15 to the average nuclear modification factor of $\rm D^0$, $\rm D^+$ and $\rm D^{*+}$ mesons measured in the same centrality class [58]. This comparison is meant to address the expected effect of hadronisation via quark recombination in the partonic medium on the relative abundances of strange and non-strange D-meson species. In the three $p_{\rm T}$ intervals, the values of the

D_s-meson R_{AA} are higher than those of non-strange D mesons, although compatible within the large uncertainties. More precise measurements are expected with the data sample from LHC Run 2 at $\sqrt{s_{NN}} = 5.02$ TeV and are the subject of this thesis.

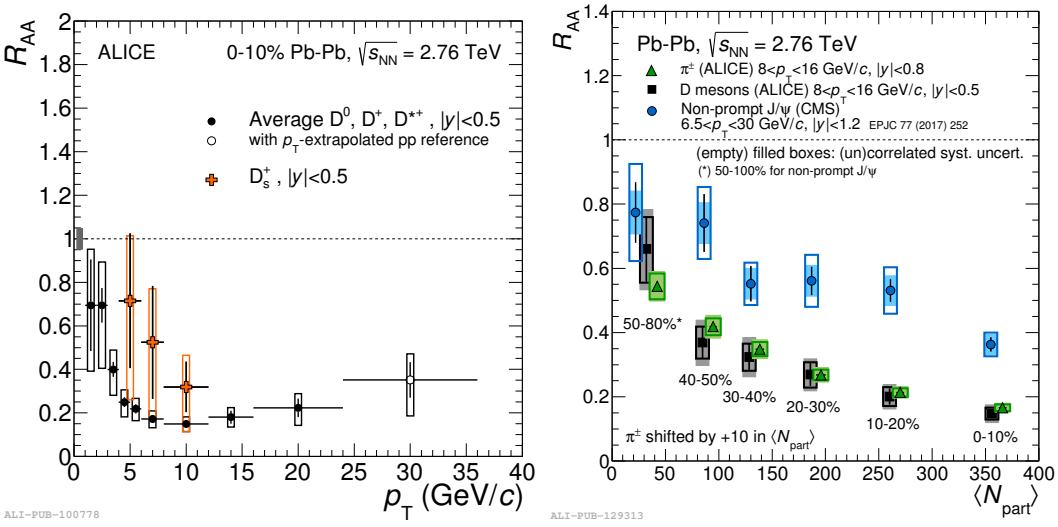

FIGURE 2.15: Left: R_{AA} of prompt D_s mesons [54] compared to non-strange D mesons [58] in the 0-10% centrality class at $\sqrt{s_{NN}} = 2.76$ TeV. Right: Comparison of the D-meson [48] and charged-pion [37] R_{AA} as a function of centrality expressed in terms of $\langle N_{part} \rangle$ in $8 < p_T < 16$ GeV/c measured by ALICE [48], and of the R_{AA} of non-prompt J/ψ mesons in $6.5 < p_T < 30$ GeV/c measured by CMS [183].

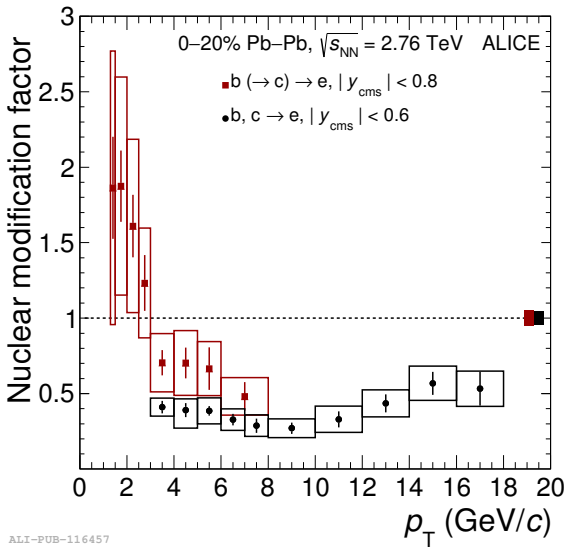

FIGURE 2.16: Right: R_{AA} of electrons from beauty-hadron decays as a function of p_T together with the corresponding result for beauty- and charm-hadron decays [56] for the 20% most central Pb-Pb collisions at $\sqrt{s_{NN}} = 2.76$ TeV.

Figure 2.15 (right) shows the average of the D^0, D^+ and D^{*+} nuclear modification factors as a function of centrality measured by ALICE in Pb-Pb collisions at $\sqrt{s_{NN}} = 2.76$ TeV, for the interval $8 < p_T < 16$ GeV/c in $|y| < 0.5$ [48], compared to

the R_{AA} of charged pions [37] in $|y| < 0.8$ for the same p_{T} interval, and to non-prompt J/ψ meson R_{AA} measured by the CMS Collaboration for $6.5 < p_{\mathrm{T}} < 30$ GeV/c in $|y| < 1.2$ [183]. The different width of the rapidity interval for D and non-prompt J/ψ mesons ($|y| < 0.5$ and $|y| < 1.2$, respectively) is not expected to play a big role, since the intervals are partially overlapping and there is no significant y dependence of the R_{AA} of non-prompt J/ψ mesons in $|y| < 1.2$ [183]. The p_{T} interval 8-16 GeV/c for D mesons was chosen in order to obtain a significant overlap with the p_{T} distribution of B mesons decaying to J/ψ particles with $6.5 < p_{\mathrm{T}} < 30\,\mathrm{GeV}/c$. The nuclear modification factors of charged pions and D mesons are compatible within uncertainties in all centrality classes. A possible interpretation of the similar R_{AA} of D mesons and pions is related to a mixture of competitive effects which affect the nuclear modification factor in addition to the parton in-medium energy loss. In particular, in the presence of a colour-charge and quark-mass dependent energy loss, the harder p_{T} distribution and the harder fragmentation function of charm quarks compared to those of light quarks and gluons could lead to similar values of D-meson and pion R_{AA}, as discussed in [141]. The value of the D-meson R_{AA} in all the centrality classes, except the most peripheral one, is lower than that of non-prompt J/ψ mesons. The R_{AA} of electrons from beauty-hadron decays [55] is compared with the one of heavy-flavour decay electrons, i.e. originating from both charm- and beauty-hadron decays, in Fig. 2.16 for the 20% most central Pb-Pb collisions [56]. The measurements agree within uncertainties at high p_{T}, while, in the p_{T} interval $3 < p_{\mathrm{T}} < 6$ GeV/c, the R_{AA} of electrons from beauty-hadron decays is about 1.2σ higher than that of heavy-flavour decay electrons. The observation of different suppression for particles originating from charm or beauty quarks like those presented in Fig. 2.15 (right) and 2.16 is consistent with a scenario of decreasing in-medium parton energy loss with increasing quark mass.

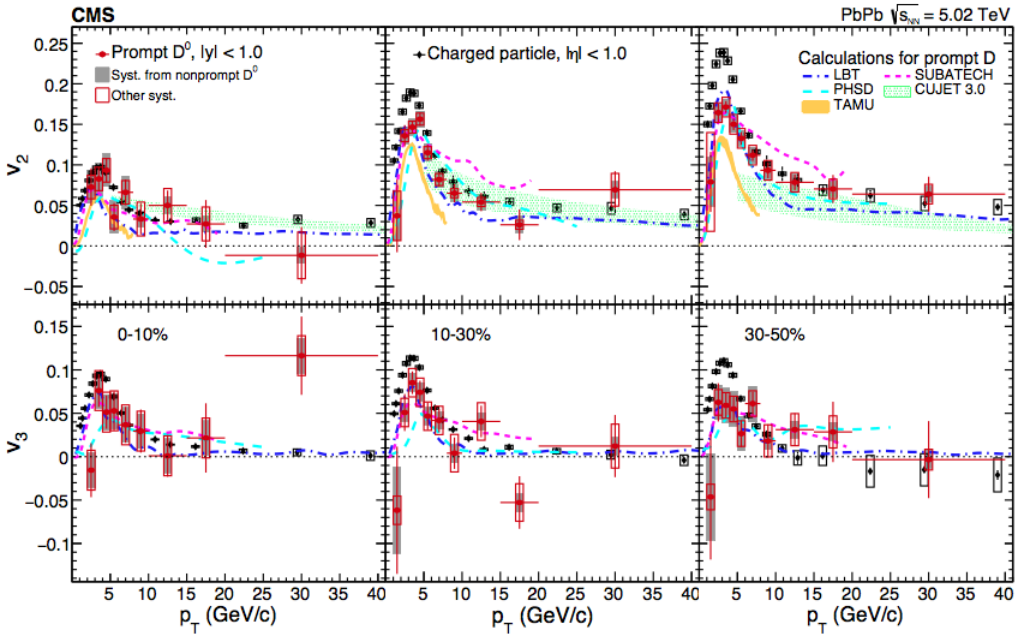

FIGURE 2.17: Prompt D^0 meson v_2 (upper) and v_3 (lower) coefficients as a function of p_{T} at midrapidity ($|y| < 1.0$) for the centrality classes 0-10% (left), 10-30% (middle), and 30-50% (right) [241].

The measurement of the elliptic flow v_2 provides further insight into the interactions of charm quarks with the medium. At low $p_{\rm T}$, D-meson v_2 offers the unique opportunity to test whether also charm quarks participate in the collective expansion dynamics and possibly thermalise in the medium [164, 211]. At low and intermediate $p_{\rm T}$, the elliptic flow is also expected to be sensitive to the hadronization mechanism [164], while at high $p_{\rm T}$, it can constrain the path-length dependence of parton energy loss [166]. First measurements of a positive D-meson v_2 were done by ALICE in Pb-Pb collisions at $\sqrt{s_{\rm NN}} = 2.76$ TeV [18]. The v_2 and v_3 of prompt $\rm D^0$ meson measured by CMS in Pb-Pb collisions at $\sqrt{s_{\rm NN}} = 5.02$ TeV are presented in Fig. 2.17, for the 0-10%, 10-30% and 30-50% centrality classes [241]. The measured v_2 and v_3 are larger than 0 at low $p_{\rm T}$ and then decrease at higher $p_{\rm T}$. The elliptic flow v_2 reaches its maximum value in the 30-50% centrality class, due to the initial geometrical anisotropy of the fireball. The result suggests that charm quarks take part in the collective motion of the medium and that collisional processes as well as quark recombination may contribute to the observed elliptic flow. For $p_{\rm T} > 6\,{\rm GeV}/c$, the $\rm D^0$ meson $v_2 > 0$ suggests a path-length dependence of the charm-quark energy loss. The path-length effect is more evident for semi-peripheral collisions, where the difference of in-plane and out-of-plane path-lengths is maximum.

The simultaneous comparison of $R_{\rm AA}$ and elliptic flow v_2 measurements with theoretical calculations can provide more stringent constraints to the charm-quark in-medium interactions and hadronisation processes. Fig. 2.18 shows the D-meson $R_{\rm AA}$ [222] measured by ALICE in Pb-Pb collisions at $\sqrt{s_{\rm NN}} = 5.02$ TeV, in the 0-10%, 30-50% and 60-80% centrality classes and Fig. 2.19 shows the D-meson v_2 [41] in the 30-50% centrality class. Transport models in Fig. 2.18 and 2.19 include: POWLANG [100] and TAMU [170], in which the interactions only include collisional processes; BAMPS-el+rad [250], LBT [125] and PHSD [245], in which also energy loss from medium-induced gluon radiation is considered, in addition to collisional process. Models based on perturbative QCD calculations of parton energy loss are: CUJET3.0 [258], Djordjevic [142] and MC@sHQ+EPOS2 [208], that include both radiative and collisional energy loss processes, and SCET [176] model, that includes medium-induced gluon radiation and a mechanism of formation and dissociation of heavy-flavour hadrons in the QGP. All models, with the exception of BAMPS and CUJET3.0, include a nuclear modification of the parton distribution functions. The LBT, MC@sHQ, PHSD, POWLANG and TAMU models include a contribution of hadronisation via quark recombination, in addition to independent fragmentation. Most of the models provide a fair description of the measured $R_{\rm AA}$ in the region $p_{\rm T} < 10$ GeV/c in central collisions, but many of them (LBT, PHSD, POWLANG and SCET) provide a worse description of non-central collisions. The CUJET3.0 and Djordjevic models provide a fair description of the $R_{\rm AA}$ in all three centrality classes for $p_{\rm T} > 5 - 10$ GeV/c, where radiative energy loss is expected to be the dominant interaction mechanism, suggesting that the dependence of radiative energy loss on the path length of charm quarks in the hot and dense medium is well understood. The TAMU model overestimates $R_{\rm AA}$ at high $p_{\rm T}$ in central events and describes the magnitude of the elliptic flow, but fails in reproducing the shape. This may be due to missing radiative term for the energy loss. BAMPS-el overestimates the v_2 at low $p_{\rm T}$ while underestimating the suppression at high $p_{\rm T}$. The radiative term in BAMPS-el+rad improves the description of the $R_{\rm AA}$ but gives a smaller than observed low $p_{\rm T}$ v_2. POWLANG overestimates suppression at hight $p_{\rm T}$ in all the centrality classes, while gives a good description of the v_2. PHSD, LBT and MC@sHQ provide instead a fair description of both v_2 magnitude and shape as well as of energy loss. The

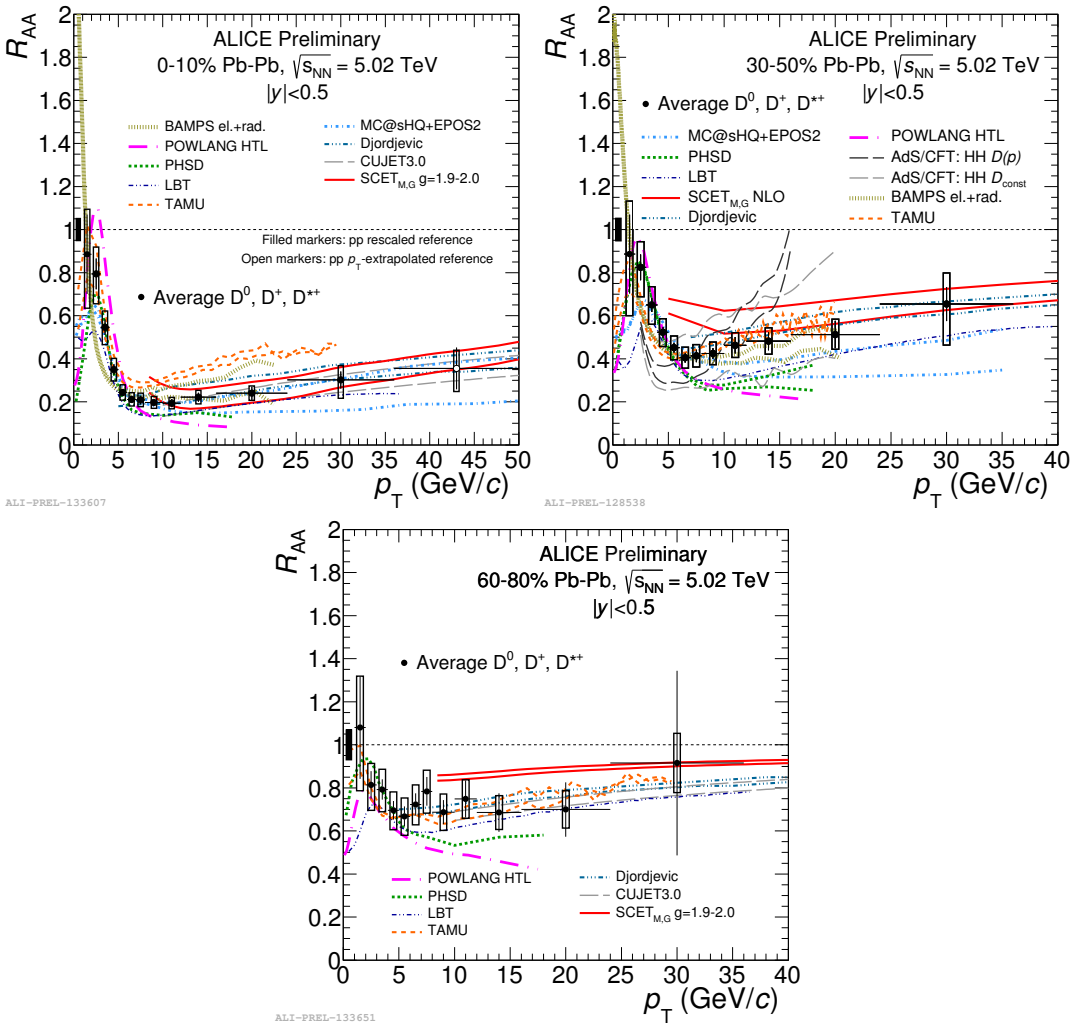

FIGURE 2.18: Average D-meson $R_{\rm AA}$ [222] in 0-10%, 30-50% and 60-80% centrality classes as a function of $p_{\rm T}$ at $\sqrt{s_{\rm NN}}$ = 5.02 TeV, compared with models.

calculations that describe the v_2 data with $\chi^2/\mathrm{ndf} < 1$ use values of the charm quark diffusion coefficient $2\pi\,T\,D_s$ in the range 1.5–7 at $T_{\rm c}$. The corresponding thermalisation time [206] for charm quarks is $\tau_{\rm charm} = \frac{m_{\rm charm}}{T} D_s \approx 3$–$14$ fm/c with $T = T_{\rm c}$ and $m_{\rm charm} = 1.5$ GeV/c^2. These values are comparable to the estimated decoupling time of the high-density system [15].

More quantitative comparisons between measurements and model calculations towards an estimate of the heavy-quark transport coefficients was proposed in a recent Bayesian model-to-data analysis [259]. The dependence of $2\pi T D_s(T)$ on the temperature (see Fig. 2.20) was extracted. The spacial diffusion coefficient is better constrained in the region (1.3 - 1.5) T_c, that is indeed a temperature range where charm quarks spend most of their time in the medium. Furthermore, the coefficient, extracted from model-to-data comparison, is found to be compatible to lattice QCD calculations and some results from the latter are displayed in Fig. 2.20.

The larger data samples that will be collected during Run 3 and Run 4 at the LHC will allow to substantially reduce the measurement uncertainties, providing further

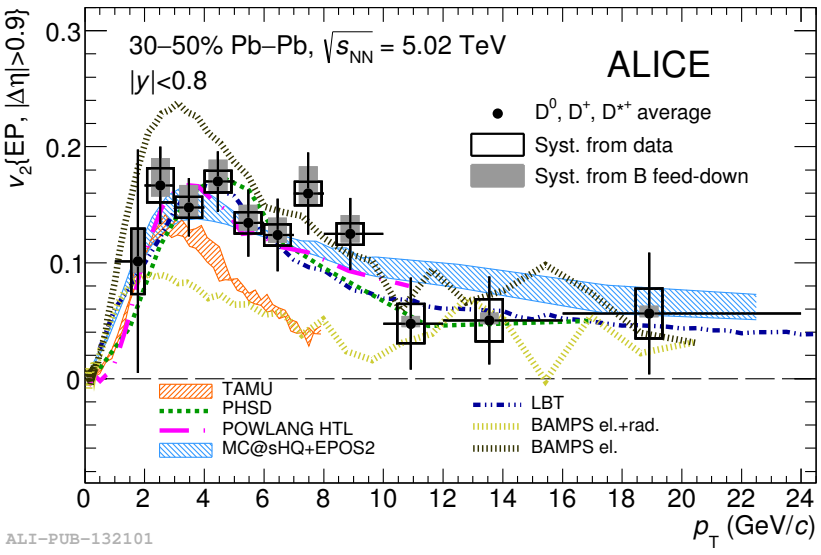

FIGURE 2.19: Average D-meson v_2 [41] in the 30-50% centrality class as a function of p_T at $\sqrt{s_{NN}} = 5.02$ TeV, compared with models.

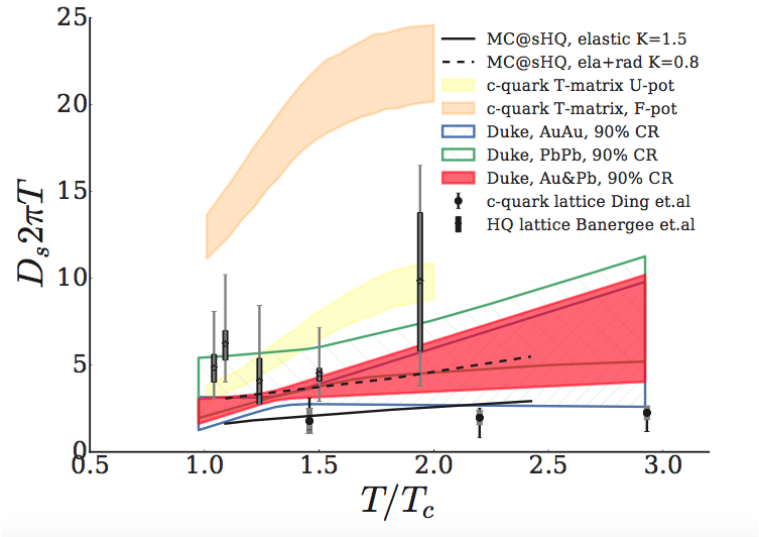

FIGURE 2.20: Estimated temperature dependence of the spatial diffusion coefficient $2\pi T D_s(T/T_c)$, compared with other models calculations.

constraints to models and constraining the values of the QGP transport coefficients.

Chapter 3

The ALICE experiment at the LHC

3.1 The Large Hadron Collider

The Large Hadron Collider (LHC), with a circumference of 27 km, is the world largest and most powerful particle collider, built by the European Organisation for Nuclear Research (CERN) from 1998 to 2008. It is placed in the tunnel of the previous Large Electron Positron collider, at a depth between 50 and 175 m underground. The LHC accelerator chain is shown in Fig. 3.1. The first stage of the acceleration takes place on the Linac2, a linear accelerator with an output proton energy of 50 MeV. The proton-booster synchrotron (PSB) increases the energy to 1.4 GeV, injecting into the proton synchrotron (PS). This accelerates the beam to 26 GeV and injects it into the super proton synchrotron (SPS), out of which 450 GeV protons are eventually injected into the LHC for the start of the ramp up to the energy of 7 TeV. At the nominal configuration, LHC accelerates protons grouped in 2808 bunches per beam, each bunch containing up to 1.15^{11} protons. The beam is bent along the circular LHC path by 1232 superconducting dipoles and controlled and focused by other 600 smaller magnets. The design and construction of the dipoles was the most technologically challenging part of the accelerator. To achieve the required bending power, the dipole field should be on average B $\sim$ 8.3 Tesla. The coils are made of NiTi superconducting cable, kept at T = 1.9 K by superfluid liquid He. They are 15 m long, weigh 35 tonnes and store in their magnetic field 7 MJ of energy, for a total of 10 GJ in the full ring.
The nominal instantaneous luminosity for pp collisions, with a bunch crossing every 25 ns, is of $10^{34}\mathrm{s}^{-1}\mathrm{cm}^{-2}$; for Pb-Pb collisions it is about $10^{27}\mathrm{s}^{-1}\mathrm{cm}^{-2}$. Since September 2008, the four main experiments (ALICE, ATLAS, CMS and LHCb) collected data with pp collisions at $\sqrt{s} = 900, 2.36, 2.76, 5, 7, 8$ and 13 TeV, Pb-Pb collisions at $\sqrt{s_{\mathrm{NN}}} = 2.76$ and 5.02 TeV, Xe-Xe collisions at $\sqrt{s_{\mathrm{NN}}} = 5.44$ TeV and p-Pb collisions at $\sqrt{s_{\mathrm{NN}}} = 5.02$ TeV.

3.2 The ALICE experiment

ALICE (A Large Ion Collider Experiment) [36] is an experiment at the LHC optimised for the study of QCD matter created in high-energy collisions between heavy nuclei. The aim of ALICE is the study of the behaviour of matter at high densities and temperatures and at nearly zero baryo-chemical potential. The major challenge that the detector project had faced was the large number of particles created in Pb-Pb collisions. Moreover, the study of the QGP requires to reconstruct tracks down

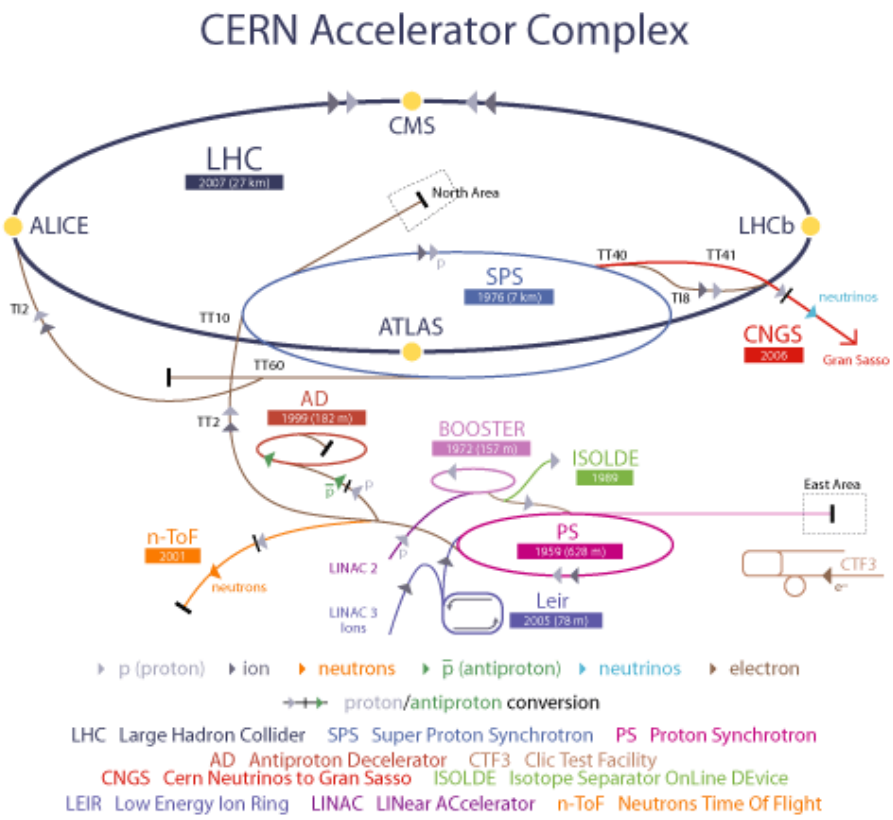

FIGURE 3.1: Layout of the full CERN accelerator complex, including all elements of the LHC injector chain.

to low momenta and identify them on a wide momentum range. For this reason, ALICE detectors were designed to have a high granularity, a low transverse momentum threshold $p_{\mathrm{T}}^{\mathrm{min}} \sim 0.15$ GeV/c and good particle identification capabilities up to 20 GeV/c. The apparatus consists of three main parts:

- **central barrel**, contained within the large magnet producing a moderate solenoidal field of B = 0.5 T in nominal running conditions and composed of detectors devoted to the reconstruction of charged particles, photons and jets and covering the pseudo-rapidity range -0.9 $< \eta <$ 0.9 over the full azimuth. They are the Inner Tracking System (ITS), optimised for vertex reconstruction and tracking; a cylindrical Time Projection Chamber (TPC), surrounding the ITS, that is the main detector for tracking and provides also particle identification; a Transition Radiation Detector (TRD), designed for electron identification; a Time Of Flight (TOF) detector, that provides pion, proton and kaon identification; a Photon Spectrometer (PHOS); an Electromagnetic Calorimeter (EMCal) and a Di-Jet Calorimeter (DCal), a High-Momentum Particle IDentification (HMPID) and the ALICE Cosmic Ray Detector (ACORDE);

- **forward muon spectrometer**, dedicated to the study of muons in the pseudo-rapidity range 2.5 $< \eta <$ 4.0;

- **the forward detectors**, which include the Photon Multiplicity Detector (PMD) and the silicon Forward Multiplicity Detector (FMD), dedicated to the measurement of photons and charged particles around $|\eta| \sim 3$, respectively; the quartz Cherenkov T0 detector, which delivers the time and the longitudinal position

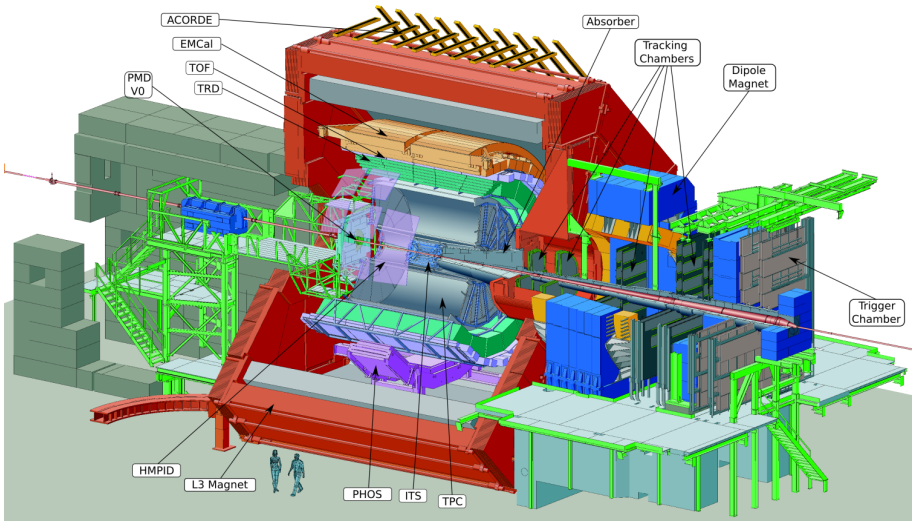

FIGURE 3.2: Picture of the ALICE experiment detectors.

of the interaction; the plastic scintillator V0 detector, which measures charged particles at -3.7 $< \eta <$ -1.7 and 2.8 $< \eta <$ 5.1, and is mainly used for triggering and for the determination of centrality and event plane angle in Pb-Pb collisions; the Zero Degree Calorimeter (ZDC) also used for determination of centrality.

The layout of ALICE set-up is shown in Fig. 3.2. ALICE apparatus has overall dimensions of 16 x 16 x 26 m^3 and a total weight of ∼10000 t. The maximum pp interaction rate at which all ALICE detectors can be safely operated is around 700 kHz. Typical luminosity values for the ALICE pp data taking range from $L \sim 10^{29}s^{-1}cm^{-2}$ to $L \sim 10^{31}s^{-1}cm^{-2}$. In the following sections, the detectors of ALICE used in the analyses presented in this thesis and their performance will be described. For information on the other detectors more details can be found in [14].

3.2.1 Magnet

The magnet used in ALICE was constructed for the L3 experiment at LEP and it produces a moderate solenoidal magnetic field (B $<$ 0.5 T). In the choice of the magnetic field two aspects must be considered: the magnet has to be intense enough to bend the particle trajectory and allow a good track-momentum resolution, but has to permit the reconstruction of low momentum particles. The lower momentum that allows reconstruction of the track with the ALICE magnet is given by $p_{\mathrm{cutoff}} = 0.3\,\mathrm{B}\,\mathrm{R} \sim 0.2\,\mathrm{GeV}/c$, where B is the magnetic field in Tesla and R is the minimum radius for a particle to traverse the entire TPC, whose external radius is $\mathrm{R_{ext}} = 2.5$ m. Tracks with lower momentum can be reconstructed using the Inner tracking System, as discussed in the next sections.

3.2.2 Inner Tracking System (ITS)

The Inner Tracking System is one of the central barrel detectors used for track reconstruction, primary and secondary vertex finding and Particle Identification (PID). It is composed by six cylindrical layers of silicon detectors placed coaxially around the beam vacuum tube (Fig. 3.3). The layers are located at radii between 39 mm and 430 mm and cover the pseudo-rapidity range $|\eta| < 0.9$. The two innermost layers are made of Silicon Pixel Detectors (SPD). The pseudo-rapidity coverage of the SPD

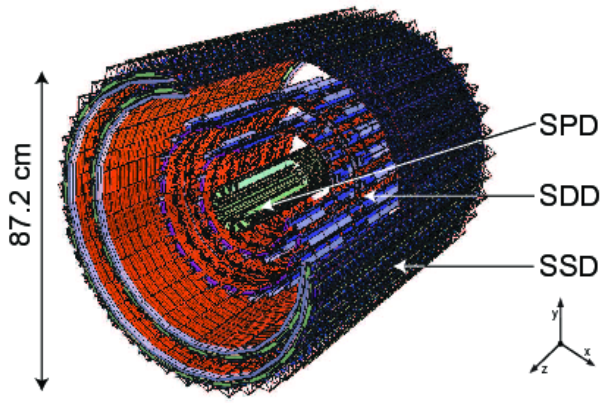

FIGURE 3.3: View of the six silicon layers of the Inner Tracking System

inner layer is $|\eta| < 1.95$ for particles produced at $z_{\rm vtx} = 0$. The two middle layers are made of Silicon Drift Detectors (SDD) and two outer layers of Silicon micro-Strip Detectors (SSD). Its basic functions are [72]:

- determination with high precision of primary vertex position (interaction point) and reconstruction of secondary vertices of charm, beauty and hyperon decays,
- improvement of the momentum and angle measurements of the TPC,
- recover particles that are not tracked in the TPC due to acceptance limitation (very low momentum particles not reaching the TPC and high momentum particles crossing the inactive areas between adjacent TPC chambers).

All the ITS detectors were carefully optimised to minimise their radiation length, achieving 1.1% per layer, the lowest value among all the current LHC experiments [72]. The resolution of the track impact parameter is determined by the spatial resolution of the ITS detectors. The ITS detectors have a spatial resolution of a few tens of μm in the $r\varphi$ plane, with the best precision (12 μm) for the innermost detectors equipped with SPD. The left and the right panels of Fig. 3.12, that will be discussed in Sec. 3.6, show respectively the resolution on the final vertex position in transverse coordinates and on the impact parameter in the transverse plane.

The four outer layers provide analogue read-out and for this reason they can be used for particle identification (PID) via $\mathrm{d}E/\mathrm{d}x$ measurements for low-$p_{\rm T}$ particles. The measured cluster charge in each of the four layers with PID capabilities is normalised to the path length in the silicon active volume, which is calculated from the reconstructed track parameters, to obtain a $\mathrm{d}E/\mathrm{d}x$ value for each layer. A single $\mathrm{d}E/\mathrm{d}x$ value is then calculated with a truncated mean of the values from the four layers, to assure that the $\mathrm{d}E/\mathrm{d}x$ peak shape is Gaussian. The resolution σ on the $\mathrm{d}E/x$ is of about 10% and it provides kaon-pion separation at 1σ level for $p_{\rm T} \lesssim 0.7\,\mathrm{GeV}/c$ and proton/pion separation for $p_{\rm T} \lesssim 1.2\,\mathrm{GeV}/c$. An example of the distribution of the measured truncated mean values of energy loss per path unit as a function of track momentum in the ITS is shown in Fig. 3.4.

3.2.3 Time Projection Chamber (TPC)

The TPC is the only device which can provide good tracking performance up to track densities of 8000 charged particles per unit of rapidity, which were foreseen to be

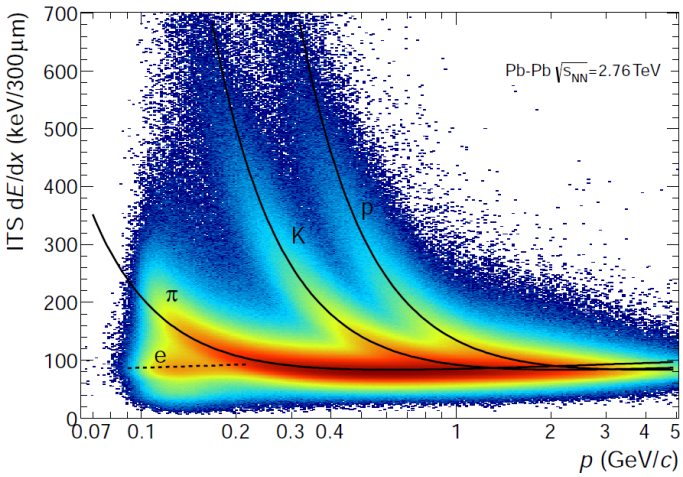

FIGURE 3.4: Distribution of the energy-loss signal in the ITS as a function of momentum. The lines show the parameterisations of the expected mean energy loss.

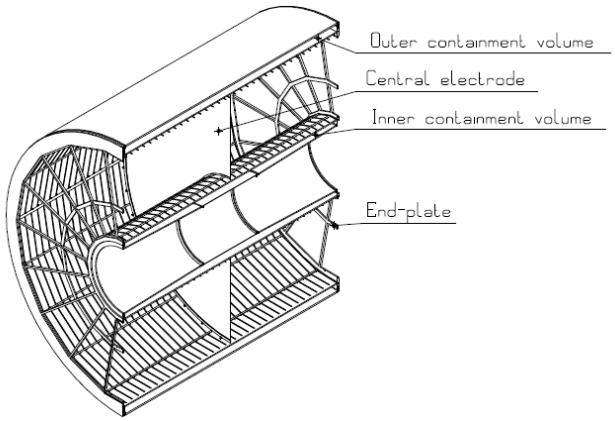

FIGURE 3.5: A view of the ALICE Time-Projection Chamber detector.

produced in Pb-Pb collisions at the LHC at the time when ALICE was designed [70]. It has a cylindrical shape with inner and outer radius of 80 and 250 cm, respectively, and an overall length in the beam direction of 500 cm. The minimum inner radius of the TPC was determined by the maximum acceptable hit density. The outer radius was defined by the minimum length required for a $\mathrm{d}E/\mathrm{d}x$ resolution better than 10%. At smaller radii (and larger track densities), tracking is taken over by the ITS. The TPC covers an acceptance of $|\eta| < 0.9$. The TPC is a chamber full of high-purity gas to transport ionisation electrons over long distances (2.5 m) towards the read-out end-plates. It is composed by a central high-voltage (HV) electrode which divides the gas volume into two symmetric drift regions, and two opposite axial potential degraders to create a highly uniform electrostatic field of up to 400 V/cm (Fig. 3.5). Charged particles traversing the gas form a ionisation trace that will move at constant velocity towards one of the two end-plates. The density of ionisation depends on the velocity and mass of the particle. Once on the end-plate, readout chambers allow to amplify and register the signals of particle tracks. The end-plates are segmented into 18 trapezoidal sectors and equipped with multi-wire proportional chambers covering an overall active area of 32.5 m^2. The original mixture of gas was composed by 90%

Ne, 10% CO_2; successively a further 5% of N_2 was added. During 2015-2016, the Ar replaced the Ne in the mixture. The TPC is the main detector for track reconstruc-

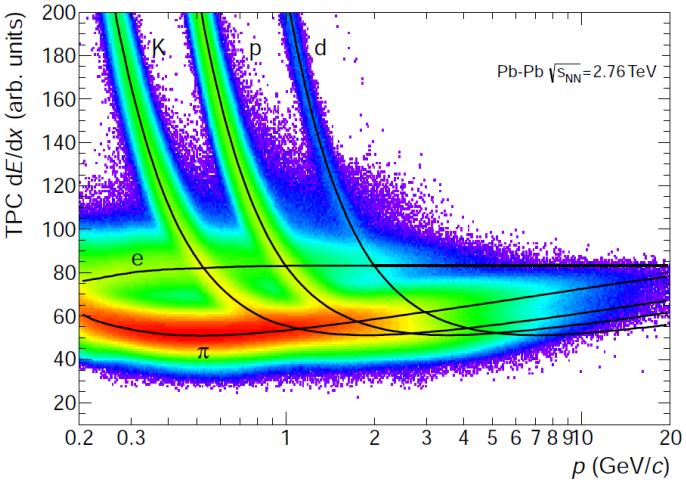

FIGURE 3.6: Distribution of the energy-loss signal in the TPC as a function of momentum. The lines show the parameterisations of the expected mean energy loss.

tion (see Sec. 3.6). It is used for measurements of the charged-particle momenta, with a resolution better than 2.5% for electrons with momentum of about 4 GeV/c, and for particle identification via dE/dx.

Particle Identification is performed over a wide momentum range. It is made by simultaneously measuring the specific energy loss, the charge and the momentum of the particles traversing the detector gas. The maximum number of clusters associated to a track in the TPC is 159 and the dE/dx value of the track is determined using a truncated mean. The dE/dx, described by the Bethe Block formula, is parameterised by a function proposed by ALEPH Collaboration [108]:

$$f(\beta_\gamma) = \frac{P_1}{\beta^{P_4}}\left(P_2 - \beta^{P_4} - \ln\left(P_3 + \frac{1}{(\beta_\gamma)^{P_5}}\right)\right), \tag{3.1}$$

where β is the particle velocity, γ is the Lorentz factor, and P_{1-5} are fit parameters. The measured dE/dx as a function of the track momentum measured in TPC is shown in Fig. 3.6. The lines correspond to the parametrisation. A clear separation among the different particle species is observed for $p_{\mathrm{T}} \lesssim 1\,\mathrm{GeV}/c$, which allows for a PID on a track-by-track basis. At higher p_{T} the separation of the species is still feasible on a statistical basis via multi-Gaussian fits. The PID resolution is about 5.2% in pp collisions and 6.5% in the 5% most central Pb-Pb collisions. Thanks to the dE/dx resolution, particle ratios can be measured in the relativistic rise region at p_{T} up to $\approx 20\,\mathrm{GeV}/c$.

3.2.4 Time-Of-Flight (TOF)

The TOF detector is a large area array of Multigap Resistive Plate Chambers (MRPC), positioned at radial distance of 370-399 cm from the beam axis. It has a cylindrical shape, covering polar angles between 45 and 135 degrees over the full azimuth. The TOF has a modular structure with 18 sectors in φ (Fig. 3.7); each of these sectors is divided into 5 modules along the beam direction. This detector is entirely devoted

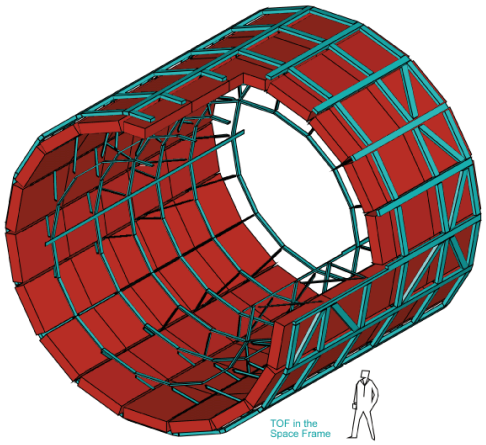

FIGURE 3.7: A view of the ALICE Time-Of-Flight detector.

to particle identification. The ionisation produced by any particle crossing the MRPCs starts a gas avalanche which generates the observed signal. The TOF identifies the particle species via a measure of the time of flight inside the chambers. Let us consider the following relation:

$$m = p\sqrt{\frac{t_{\mathrm{TOF}}^2}{L^2} - 1}$$

where m is the mass of the particle, p the momentum, t_{TOF} the time-of-flight and L the track length. It can be shown that the σ_m/m resolution, at relatively high momenta, it is influenced much more by the errors on the time-of-flight and track length measurements than by error on the momentum determination. The time of collision, which constitutes the start time for the time-of-flight measurement, is obtained on an event-by-event basis either using the particle arrival times at the TOF, or the information from the T0 detector, or a combination of the two [51]. The T0 detector is composed by two arrays of Cherenkov counters, T0A and T0C, located at apposite sides of the interaction point at $-3.28 < \eta < -2.97$ and $4.61 < \eta < 4.92$. It has a time resolution of 20-25 ps in Pb-Pb collisions and ~ 40 ps in pp collisions. The TOF resolution is 80 ps for pions with a momentum around 1 GeV/c, in 0-70% Pb-Pb collisions. This values includes the detector resolution, the contribution from electronics and the uncertainty on the start time of the event. It provides PID in the intermediate momentum range, allowing for pion/kaon separation at 3σ level up to $p_{\mathrm{T}} \approx 2.5\,\mathrm{GeV}/c$ and kaon/pion separation up to $p_{\mathrm{T}} \approx 4\,\mathrm{GeV}/c$. Figure 3.8 shows the distribution of the measured velocity β as a function of momentum (measured by TPC). The background is due to tracks that are incorrectly matched to TOF hits in high-multiplicity Pb-Pb collisions.

3.2.5 V0 Detector

The V0 detector is made of two arrays of scintillator counters, V0A and V0C, positioned on both sides of the interaction point. The V0A detector is located at 340 cm distance from the nominal interaction point position, along the beam axis, on the side opposite to the muon spectrometer, whereas V0C is fixed to the front face of the hadronic absorber, 90 cm from the nominal interaction point. They cover the pseudo-rapidity ranges $2.8 < \eta < 5.1$ (V0A) and $-3.7 < \eta < -1.7$ (V0C) and are

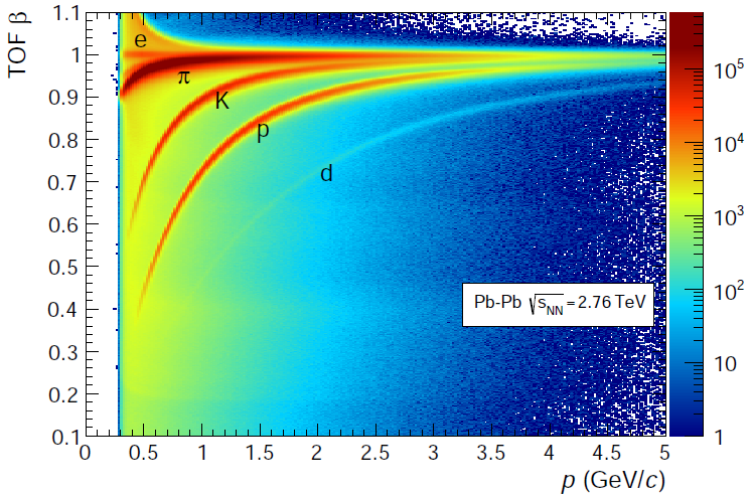

FIGURE 3.8: Distribution of β velocity measured by the TOF detector as a function of momentum for particles reaching the TOF in Pb-Pb interactions.

segmented into 32 individual counters each distributed in four radial rings and 8 azimuthal sectors. The V0 provides a minimum bias trigger as well as high-multiplicity triggers for the central barrel detectors and can be used to estimate the centrality of the collision based on the energy deposited in the V0 scintillator tiles. Furthermore, it is used for beam-gas background rejection (see Sec. 3.4).

3.2.6 Zero Degree Calorimeter (ZDC) Detector

The ZDC provides a measure of the energy carried in the forward direction (at 0° relative to the beam direction) by non-interacting (spectator) nucleons. This quantity is useful to estimate the centrality of the event. Typically the beams are deflected by means of two separation dipoles located at about 65 m distance from the interaction point (IP). These magnets will also deflect the spectator protons, separating them from the spectator neutrons, which fly away at 0°. Two sets of ZDCs are placed at about 115 m distance from the interaction point on both sides of the interaction point. Each set is constituted by one calorimeter for neutron detection (ZN), positioned between the two beam vacuum tubes to intercept the spectator neutrons, and one for proton detection (ZP), placed externally to the outgoing beam, to collect the spectator protons. The hadronic ZDCs are quartz-fibre sampling calorimeters. The shower generated by incident particles in a dense absorber (tungsten for ZN and brass for ZP) produces Cherenkov radiation in quartz fibres (the active material) interspersed in the absorber. The two sets of ZDCs are complemented by the information of two small electromagnetic calorimeters (ZEM), located at 7.5 m from the interaction point, to detect the energy of particles emitted at forward rapidity (mainly photons generated from π^0 decays).

3.3 The ALICE Trigger System and Data Aquisition

ALICE has a two-layer trigger architecture [150]. The low-level trigger is a hardware trigger called Central Trigger Processor (CTP). The High-Level trigger (HLT) is implemented as a pure software trigger. The ALICE Central Trigger Processor (CTP) is designed to combine and synchronise information from all the triggering detectors

in ALICE and informations about the LHC filling scheme and bunch crossing, and to send the correct sequences of trigger signals to all detectors. Since the ALICE experiment has to collect data in pp (p-Pb) and Pb-Pb collisions, the trigger system was optimised for these two types of collisions. The HLT allows the implementation of sophisticated logic for the triggering. While the CTP governs the readout of the sub-detectors, the HLT receives a copy of the data read out from the sub-detectors and processes it.

3.3.1 The Central Trigger Processor (CTP)

The hardware trigger combines informations from sub-detectors to decide whether or not to write an event on disk. The CTP evaluates trigger inputs from the trigger detectors every machine clock cycle ($\sim$ 25 ns).

The trigger inputs are divided into three different levels:

- L0 level: the Level 0 trigger decision (L0) is made $\sim 0.9\,\mu$s after the collision using V0, T0, EMCal, PHOS, and MTR. The trigger requirement can be simply the input of one detector or a logical condition based on the trigger inputs of different trigger detectors.

- L1 level: the events accepted at L0 are further evaluated by the Level 1 (L1) trigger algorithm in the CTP. The L1 trigger decision is made $\sim 6.5\,\mu$s after L0. The latency is caused by the computation time (TRD and EMCal) and propagation times (ZDC, 113 m from IP2). The L0 and L1 decisions, delivered to the detectors with a latency of about 300 ns, trigger the buffering of the event data in the detector front-end electronics.

- L2 level: the Level 2 (L2) decision, taken after about 100 μs corresponding to the drift time of the TPC, triggers the sending of the event data to DAQ and, in parallel, to the High Level Trigger system (HLT). L2 can be used to reject events with multiple collisions (pile-up) in different bunch crossings occurring in the TPC readout time.

Information about the LHC bunch filling scheme is used by CTP to suppress the background. The information about the bunch crossing, regarding the arrival of bunches from both A-side and C-side, or one of them, or neither, is provided to the CTP by the bunch crossing mask at a resolution of 25 ns. The beam-gas interaction background, can be studied by triggering on bunches without a collision partner, and can be subtracted from the physics data taken with the requirement of the presence of both bunches. ALICE operates with minimum-bias (MB) triggers, mainly based on V0 and SPD, and with rare triggers that are optimised to select particular classes of events such as events containing jets or muons or high-multiplicity events. By definition MB triggers have the highest rate of inputs signals, while the rare triggers have much lower rate. In general, several types of triggers during the data taking at the same time keep busy a very large fraction of the total data acquisition bandwidth. To prevent losing precious events due to the fact that no space is available on the temporary memory, the trigger system follows an event prioritisation scheme. In the case that the utilisation of the temporary storage is above a certain value, only rare triggers are accepted. This scheme significantly increases the acceptance of rare events.

3.3.2 The Data AcQuisition System (DAQ)

The DAQ manages the data flow from the sub-detector electronics to the archiving on tape. Once the CTP decides to register a specific event, raw data are sent to the Local Data Concentrators (LDCs) via the optical Detector Data Links (DDLs). LDCs are sets of computers that perform sub-event reconstruction. In this step of the acquisition, raw data are processed. The size of a single central event processed by LDCs can be ≈70 MB. In order to optimise the usage of the recording bandwidth available, an additional event selection and compression is done by the High-Level Trigger (HLT). The events processed by LDCs are then transferred to a second layer of computers, the Global Data Collectors (GDCs), which perform the event building.

3.3.3 The High Level Trigger (HLT)

The ALICE software trigger, called HLT, is a farm of multiprocessor computers. It is composed by about 1000 PCs processing the data in parallel allowing an online analysis of the events. The HLT receives a copy of the raw data for events passing the L2 trigger level and performs per-detector reconstructions. The trigger decision is based on the global reconstructed event, hence from a much more complete information than that available for the hardware trigger. Therefore, the HLT allows for more sophisticated triggers. Examples include triggers on high-energy jets or on muon pairs. Data rate reduction is achieved by reducing the event rate by selecting interesting events (software trigger) and by reducing the event size by selecting sub-events (e.g. pile-up removal in pp interactions) and by advanced data compression. In particular, the data volume produced by the TPC is reduced via the HLT by reconstructing clusters or hits and by storing cluster information instead of the raw data. The trigger decision, partial readout information, compressed data, and the reconstruction output is sent to LDCs and subsequently processed by the DAQ.

3.4 Machine-induced background

The operation of detectors at the LHC can be affected by machine-induced background (MIB), that scales with the beam intensity. The sources of this background can be: (i) beam-gas interactions, caused by nucleons in the beams interacting with residual gas in the beam pipe; (ii) interactions of the beam halo with mechanical structures in the machine; (iii) collisions of bunches in the main radio-frequency buckets with satellite bunches located at short distance from the main bunches. The background from sources (i) and (ii) can be rejected by exploiting the arrival time of the signal in the two V0 module detectors. The background caused by one of the LHC beams produces in fact an early signal on one of the two V0 (depending on the side from where the beam arrives) compared to the collision time at the nominal interaction point. The difference between the expected beam and background signals is about 22.6 ns in the A side and 6 ns in the C side. As shown in the left panel of Fig. 3.9, background events accumulate mainly in two peaks at (-14.3 ns, -8.3 ns) and at (14.3 ns, 8.3 ns) in the V0 time sum-difference plane, well separated from the main (collision) peak at (8.3 ns, 14.3 ns). The V0 time information is used to set the trigger conditions on collision or background events. The collected events are further selected offline to remove any residual contamination from MIB and satellite collisions. The V0 trigger logic is re-applied at the offline level using a V0 arrival time computed offline as a weighted average of all detector elements. For pp collisions, an additional selection on the correlation between number of hits and track segments (tracklets) in

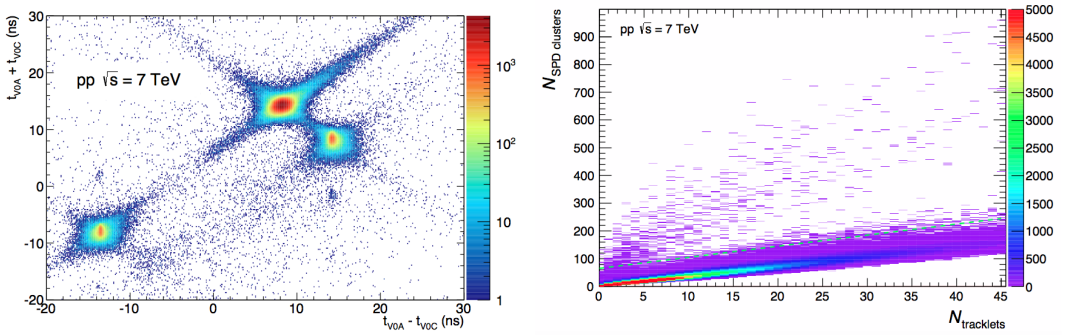

FIGURE 3.9: Left: correlation between the sum and difference of signal times in V0A and V0C. Right: correlation between reconstructed SPD clusters and tracklets. The green dashed line is used to separate the populations of collisions and MIB.

SPD detector is used. In fact, background particles usually cross the pixel layers in a direction parallel to the beam axis, producing hits that are not associated to any tracklet in the reconstruction (right panel of Fig. 3.9). The dashed green line represents the cut used in the offline selection: events lying in the region above the line are tagged as background and rejected. The fraction of background events that survives the above cuts was determined by control triggers with only one of the beams crossing the ALICE interaction point and was found to be about 0.3% in the pp data taking during the 2010 run, but it strongly depends on the running conditions and on the specific trigger configuration under study. In Pb-Pb collisions the fraction was found to be smaller than 0.02%. Collisions of main bunches and satellite bunches located at short distance from the main bunch are also a source of background. They are rejected using the correlation between the sum and the difference of times measured in the ZDC, as shown in Fig. 3.10 for Pb-Pb collisions. The large cluster in the middle corresponds to collisions between ions in the main bunches, while the small clusters along the diagonals (spaced by 2.5 ns in time difference) correspond to collisions in which one of the ions belongs to satellite bunches.

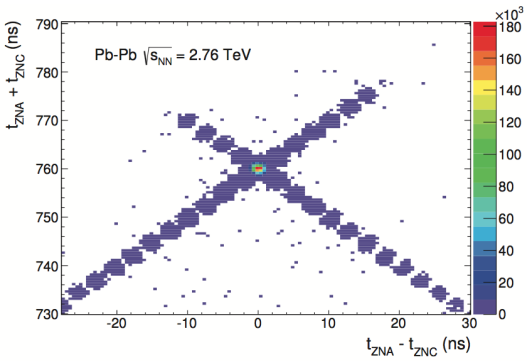

FIGURE 3.10: Correlation between the sum and the difference of times recorded by the neutron ZDCs on either side (ZNA and ZNC) in Pb-Pb collisions.

3.5 Electromagnetic interactions

The study of the properties of QGP requires to focus on the hadronic interactions in heavy-ion collisions. At LHC energies, the cross sections for electromagnetic (EM)

processes are very large ($\mathcal{O}$(kbarn)). They are due to ultra-peripheral collisions between the EM clouds of the two colliding ions that can occur via (i) ultra-peripheral $\gamma\gamma$ collisions, (ii) photo-nuclear interactions. The first process generally results in the creation of an e^+e^- pair. Photo-nuclear interactions are generated by one photon from the EM field of one of the nuclei that interacts with the other nucleus, possibly fluctuating into a vector meson. In particular, among photo-nuclear processes, there is the electromagnetic dissociation (EMD), in which the sudden EM pulse produced by the crossing ions leads to the dissociation of one (single) or both (mutual) nuclei with the emission of at least one nucleon (neutron). The single EMD events can be rejected by correlating the response of ZNA and ZNC. In general, the selection of events with multiplicity larger than a certain threshold (see Sec. 3.9) allows the rejection of EM processes.

3.6 Track and vertex reconstruction

The track reconstruction and vertex finding are performed offline using information of the central barrel detectors (ITS and TPC). The track reconstruction is based on the Kalman filter [156], which performs simultaneously the track recognition (track finding) and reconstruction (track fitting). The main steps are described below.

- **Clusterisation step:** the detector data are converted into "clusters" (i.e. groups of hits produced by the same particle crossing the considered detector element) characterised by positions, signal amplitudes, signal times, etc., and their associated errors. The clusterisation is performed separately for each detector.

- **First interaction vertex reconstruction with SPD:** the clusters found in the SPD detector are used to determine the tracklets, i.e. segments of tracks build by associating pairs of reconstructed points close in azimuthal angle ($\Delta\varphi <$ 0.01 rad) and pseudo-rapidity in the two SPD layers. The preliminary vertex is defined as a space point where the maximum number of tracklets converge. In pp collisions, where interaction pileup is expected, the algorithm is repeated several times, discarding at each iteration those clusters which contributed to already-found vertices. When a primary vertex is not found (particularly in low-multiplicity events) or in Pb-Pb collisions, the algorithm performs a one-dimensional search in the z-distribution of the points of closest approach of tracklets to the nominal beam axis.

- **TPC track finding and inward propagation:** track finding and fitting is performed in three stages, following an inward-outward-inward scheme. The first inward stage starts with track finding in the TPC. The TPC can produce a maximum of 159 clusters per track (corresponding to its 159 tangential pad rows). The track finding procedure starts at large TPC radius. Track seeds are built with two TPC clusters and the interaction point reconstructed from the SPD tracklets, then with three clusters and without the vertex constraint. The track seeds are propagated inward with the Kalman filter algorithm and, at each step, the nearest cluster is added. A special algorithm is used to reject tracks with a fraction of common clusters larger than a certain limit (between 20% and 50%). Only tracks that have at least 20 clusters (out of the maximum 159) and that miss no more than 50% of the clusters expected for a given track position are accepted. The contamination from tracks with more than 10% wrongly associated clusters does not exceed 3% even in most central Pb-Pb

collisions. The efficiency of tracking in TPC is defined as the ratio between the reconstructed tracks and the generated primary particles in the simulation, and is shown in Fig. 3.11 (left) as a function of the transverse momentum of the track. The tracking efficiency steeply drops below $p_{\mathrm{T}} \sim 0.5\,\mathrm{GeV}/c$ due to the interaction of the particles with the detector material. The efficiency is almost independent of the occupancy in the detector.

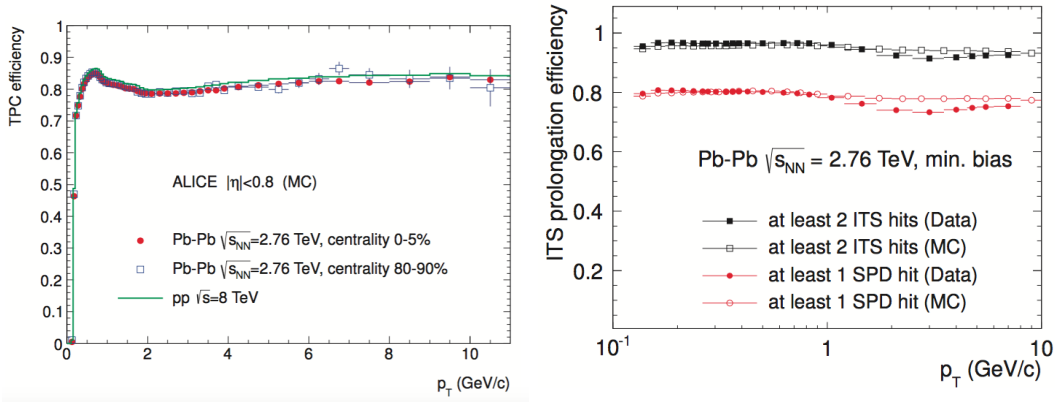

FIGURE 3.11: Left: TPC track finding efficiency for primary particles in pp collisions at $\sqrt{s} = 8$ TeV and Pb-Pb collisions at $\sqrt{s_{\mathrm{NN}}} = 2.76$ TeV(simulation) [36]. Right: track prolongation efficiency from TPC to ITS as a function of p_{T} for data and Monte Carlo in Pb-Pb collisions at $\sqrt{s_{\mathrm{NN}}} = 2.76$ TeV [36].

- **Track inward propagation to ITS:** the reconstructed tracks in the TPC are propagated inward towards the ITS, matching them to clusters in the outermost ITS layers. They are then propagated inwards and updated at each ITS layer attaching all clusters that satisfy a proximity cut. Each TPC track is hence associated to a tree of tracks in the ITS. The track candidates in ITS are then selected with quality cuts (reduced χ^2 and number of shared clusters with other tracks). The tracks are then extrapolated to their point of closest approach to the IP reconstructed with SPD tracklets. The track prolongation efficiency from TPC to ITS, also called matching efficiency, in Pb-Pb collisions is shown in Fig. 3.11 (right), as a function of p_{T} of the tracks for different requests on ITS points. The prolongation efficiencies from data and Monte Carlo (MC) simulations are shown by solid and open symbols, respectively.

- **Standalone ITS track finding:** since the track efficiency in TPC allows to reconstruct tracks down to $p_{\mathrm{T}} \sim 200$ MeV/c for pions and $p_{\mathrm{T}} \sim 400$ MeV/c for protons, a standalone ITS reconstruction is performed with those clusters that were not used in the ITS-TPC tracks. The used algorithm allows to track low-momentum particles down to e.g. $p_{\mathrm{T}} \sim 80$ MeV/c for pions. The standalone ITS tracking allows also to recover high-p_{T} particles crossing the TPC in the active regions between adjacent chambers.

- **Track outward propagation:** the Kalman filter is used to propagate the tracks in the outward direction using the clusters found at the previous stage. The tracks are matched to TRD tracklets in each of the six TRD layers, if possible, and to TOF clusters. The track length integral and the time of flight expected for various particle species are updated for subsequent particle identification with TOF. The matching with outer detectors (EMCal, PHOS and

HMPID) is also attempted. Only the TPC and the ITS points are used to update the measured track kinematics.

- **Final inward propagation (refit):** in the last step of the track reconstruction procedure, the tracks are propagated inwards starting from the outer radius of the TPC. The tracks are refitted in TPC and ITS with the previously found clusters and finally are propagated to their distance of closest approach to the interaction point determined from SPD tracklets. The position, direction, curvature of the track (proportional to the inverse of transverse momentum) and its associated covariance matrix are determined.

- **Interaction vertex reconstruction with tracks:** ITS-TPC tracks are used to find the interaction vertex position with a higher precision than with SPD tracklets. The resolution on the transverse (x, y) position of the interaction vertices found with SPD and with global tracks are shown in the left panel of Fig. 3.12. Both resolutions scale with the square root of the number of contributing tracks (tracklets). The resolution of the distance of closest approach to the primary vertex in the transverse plane for charged-particle ITS-TPC tracks in pp, p-Pb and Pb-Pb collisions is shown in Fig. 3.12 (right). The resolution improves in heavier systems thanks to large multiplicities that allow a more precise determination of the primary vertex. The relative transverse-momentum resolution of the tracks is related to the resolution on the track curvature via:

$$\frac{\sigma_{p_{\mathrm{T}}}}{p_{\mathrm{T}}} = p_{\mathrm{T}}\, \sigma_{1/p_{\mathrm{T}}}. \tag{3.2}$$

The inverse-p_{T} resolution for TPC standalone tracks and ITS-TPC combined tracks is shown in Fig. 3.13 (left), for p-Pb collisions as a function of the inverse p_{T}. In central Pb-Pb collisions, the p_{T} resolution deteriorates by $\sim 10 - 15\%$ at high p_{T}.

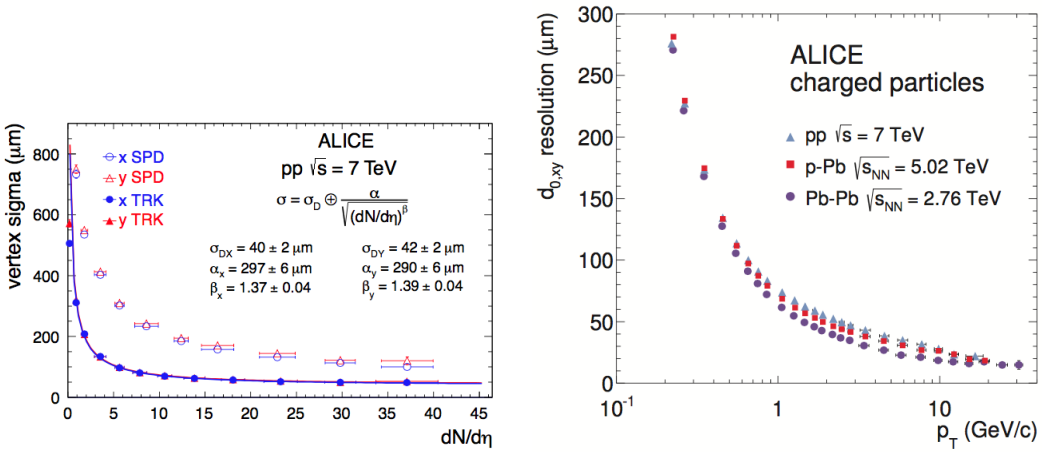

FIGURE 3.12: Left: resolution on the transverse coordinate of the vertex position from tracks (solid points) and SPD tracklets (open points) as a function of multiplicity [36]. Right: resolution of the distance of closest approach to the primary vertex in the transverse plane for charged ITS-TPC tracks. The contribution from the vertex resolution is not subtracted [36].

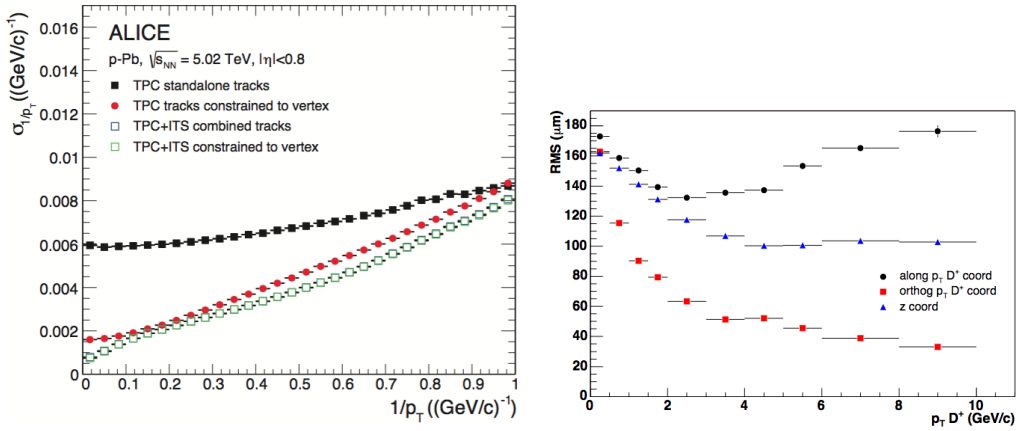

FIGURE 3.13: Left: p_{T} resolution for TPC standalone and ITS-TPC tracks with and without the constraint to the vertex [36]. Right: resolution of the position of the reconstructed secondary vertex of $\mathrm{D}^+ \to \mathrm{K}^-\pi^+\pi^+$ decays along D^+ p_{T} direction (black), orthogonal to D^+ p_{T} direction (red), and along z-axis (blue).

3.7 Secondary vertex reconstruction

For the reconstruction of heavy-flavour hadron decays, the reconstruction of decay vertices is done during the analysis phase. Tracks are grouped in pairs (e.g. for the $\mathrm{D}^0 \to \mathrm{K}^-\pi^+$ decays) or in triplets (for the D^+ and D_s^+ cases), defining objects called "candidates". The algorithm used for the secondary vertex reconstruction is based on a straight line approximation of the tracks (which are helices) in the vicinity of the primary vertex, by calculating the tangent line. The algorithm finds the point of minimum distance between the two (or three) tracks by minimising the quantity:

$$D^2 = \sum_{i=1}^{N} d_i^2, \tag{3.3}$$

where N is the number of decay particles (3 in case of $\mathrm{D}_\mathrm{s}^+ \to \mathrm{K}^+\mathrm{K}^-\pi^+$ decays) and d_i is the distance between the track i and the vertex (x_0, y_0, z_0), weighted with the errors from the track covariance matrix:

$$d_i^2 = \left(\frac{x_i - x_0}{\sigma_{x_i}}\right)^2 + \left(\frac{y_i - y_0}{\sigma_{y_i}}\right)^2 + \left(\frac{z_i - z_0}{\sigma_{z_i}}\right)^2. \tag{3.4}$$

The resolution of the reconstructed secondary vertex is shown in Fig. 3.13 (right) (right) as example for the $\mathrm{D}^+ \to \mathrm{K}^-\pi^+\pi^+$ meson. The resolution improves with increasing D^+ meson p_{T} and is better in the plane perpendicular to the D^+ p_{T} direction. The resolution of the secondary vertex for the $\mathrm{D}_\mathrm{s}^+ \to \mathrm{K}^+\mathrm{K}^-\pi^+$ meson is similar to that of D^+. Resolutions of about 100 μm allow to resolve the D_s decay vertices, which are displaced from the interaction point by $\approx 150 - 300\,\mu$m.

3.8 Simulations

Simulations are used in the analysis to calculate the reconstructed efficiencies and to study the detector performance. Event generators are used to simulate pp, p-Pb and Pb-Pb collisions. In particular, PYTHIA 6 and PYHTIA 8 were used for

pp collisions, DPMJET, HIJING and EPOS-LHC for Pb-Pb and p-Pb collisions for the studies presented in this thesis. The physics processes at partonic level and informations such as type, momentum, charge, mother/daughter relationships... are stored in the kinematics tree. The GEANT package is then used to simulate the transport of the particles through the detectors. During the transport, the energy deposition in the various detectors is stored as "hits". The hits are subsequently converted into "digits", which represent the real detector response and take into account instrumental effects, such as the presence of inactive channels, the noise due to the front-end electronics ... The digits correspond to the raw data coming from the Data Acquisition System in a real data taking. The same reconstruction procedure used for real data is applied to the simulated digits.

3.9 Centrality determination

The geometrical Glauber model [204] introduced in Sec. 1.4 describes nuclear collisions as a superposition of binary nucleon-nucleon interactions. A participant nucleon of one nucleus is defined as a nucleon that undergoes one or more collisions with nucleons of the other nucleus. The number of participants nucleons $N_{\rm part}$ can be calculated as a function of the impact parameter b of the collision using the Glauber model, the nucleon-nucleon inelastic cross section and the nucleon density profiles of the projectile and target nucleus. The number of spectator nucleons can be computed from the number of participant nucleons $N_{\rm part}$ as $N_{\rm spec} = A_{\rm proj} + A_{\rm target}$ - $N_{\rm part}$, where $A_{\rm proj}$ and $A_{\rm target}$ are the mass numbers of the colliding nuclei. The number of binary collisions $N_{\rm coll}$ can be calculated for a given value of the impact parameter. The impact parameter b and other geometry-related quantities ($N_{\rm part}$, $N_{\rm spec}$, $N_{\rm coll}$) are not directly measurable. The determination of the collision centrality is based measurements of multiplicity (energy) produced in the collision, which can be described utilising the Glauber model convoluted with a model for particle production based on a negative binomial distribution (NBD):

$$P_{\mu,k}(n) = \frac{\Gamma(n+k)}{\Gamma(n+1)\Gamma(k)} \frac{(\mu/k)^n}{(\mu/k+1)^{n+k}}, \tag{3.5}$$

which gives the probability of measuring n hits per independent emitting source of particles (called ancestor), where μ is the mean multiplicity per ancestor and k controls the width of the distribution. The number of ancestors is parameterised as: $N_{\rm ancestors} = fN_{\rm part} + (1-f)N_{\rm coll}$. This is inspired by two-component models [138, 185], which decompose particle production in nucleus-nucleus collisions into the contributions due to soft and hard interactions, where the soft interactions produce particles with an average multiplicity proportional to $N_{\rm part}$, and the probability for hard interactions to occur is proportional to $N_{\rm coll}$. With the Glauber Monte Carlo approach, the collision processes are simulated and the $N_{\rm part}$, $N_{\rm coll}$ and the number of ancestors are computed event by event. This allows to extract multiplicity distributions which can be compared to the measured ones and to extract the values of the parameters μ, n and k. The standard method typically used in ALICE is to define the centrality classes in Pb-Pb collisions based on the NBD-Glauber fit to the sum of V0A and V0C amplitudes. Other methods are used to asses the systematic uncertainty on the centrality determination [25]. In Fig. 3.14 (left panel) the distribution of the V0 amplitudes for Pb-Pb collisions at $\sqrt{s_{\rm NN}} = 2.76$ TeV [25] is shown. The events were triggered with a signal in both V0A and V0C and at least two hits in the outer SPD layer. The beam background was removed, as well as part of the EM

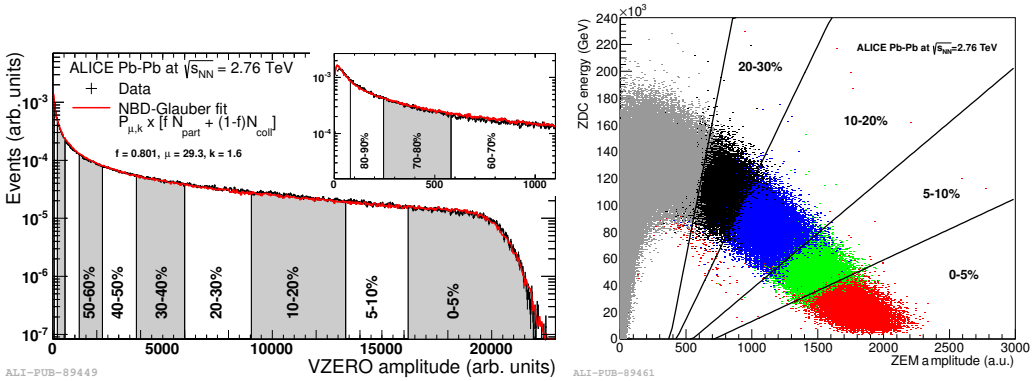

FIGURE 3.14: Left: distribution of the sum of amplitudes in the V0 scintillators for events in Pb-Pb collisions at $\sqrt{s_{\rm NN}} = 2.76$ TeV [25]. The distribution is fitted with the NBD-Glauber fit, shown as a red line. The centrality classes used in the analysis are indicated in the figure. The inset shows a zoom of the most peripheral region. Right: spectator energy deposited in the ZDC calorimeters as a function of ZEM amplitude [25]. The lines are a fit to the boundaries of the centrality classes with linear functions.

background with a ZDC cut and a z-vertex cut ($|z_{\rm vtx}| < 10$ cm). The V0 amplitude obtained with the NBD-Glauber model fitted to the data is shown as a red curve in Fig. 3.14 (left). The centrality is expressed as a percentage of the total nuclear interaction cross section σ obtained by integrating the V0 amplitude distribution. The normalisation is performed utilising the integral up to a threshold value $\mathrm{V0_{THR}}$ (anchor point), which corresponds to the 90% of the total hadronic cross section. For example, if we define V as the VZERO amplitude, the top 10% central class is defined by the boundary $\mathrm{V0_{10}}$ which satisfies:

$$\frac{\int_{\mathrm{V0_{10}}}^{\infty}(\mathrm{d}N_{\rm ev}/\mathrm{d}V)\mathrm{d}V}{\int_{\mathrm{V0_{THR}}}^{\infty}(\mathrm{d}N_{\rm ev}/\mathrm{d}V)\mathrm{d}V} = \frac{1}{9}. \tag{3.6}$$

Events with lower multiplicity than that of the anchor point suffer from contamination of EM background and trigger inefficiencies, therefore are not used in the determination of the centrality percentiles. The experimental distribution can be divided into classes by defining intervals on the measured distribution, which correspond to defined percentile intervals of the hadronic cross section. Another detector that can be used to determine the centrality of an event is the ZDC. The energy deposited by the spectator nucleons in the ZDC has a monotonic dependence on the multiplicity only for relatively small impact parameter values. For peripheral collisions, in particular, it is possible that the nuclei fragments resulting from the collision have a magnetic rigidity (ratio of their charge and mass) similar to that of beam particles, thus they are not bent away from the beam vacuum tube by the magnets and their energy is not collected by the ZDCs. For this reason, the ZDC information needs to be correlated with the signals measured by the two EM calorimeters (ZEM), as shown in the right panel of Fig. 3.14 [25]. The centrality classes previously determined by using the V0 are used to individuate the centrality classes in the ZDC-ZEM plane, since the ZEM amplitude has unknown dependence on $N_{\rm part}$ and $N_{\rm coll}$. Then, the centrality classes are defined by cutting the plane into regions defined by straight lines from linear fits to the boundary regions between two adjacent classes. This allows to define centrality intervals up to the 30% of the hadronic cross section, but not for more peripheral

collisions.

3.10 The ALICE Offline Software Framework

In ALICE, pp and Pb-Pb events recorded with MB trigger have an average size of about 1.1MB and 13.75 MB respectively. For the Pb-Pb data sample at $\sqrt{s_{\mathrm{NN}}} = 5.02$ TeV in 2015, a total raw data volume of 2.4 PB was collected; volumes of 500 TB and 2.7 PB of raw data were collected for the p-Pb (2016, $\sqrt{s_{\mathrm{NN}}} = 5.02$ TeV) and pp (2017, $\sqrt{s} = 13$ TeV) data samples, respectively. The processing and analysis of these data necessitate unprecedented amount of computing and storage resources. Grid computing provides the answer to these needs. Grid computing consists of a coordinated use of large sets of different, geographically distributed resources in order to allow high-performance computation. It is organised in different levels or Tiers. Data coming from LHC experiments are stored in the CERN computing centre, the Tier-0. Copies of the collected data are then replicated in large regional computing centres (Tier-1), which also contribute in the event reconstruction and Monte Carlo simulation. Tier-2 centres are computing centres located in different institutions which do not have large storage capabilities but provide a large fraction of the computing resources for Monte Carlo simulations and data analysis. ALICE uses the ALICE Environment (AliEn) system [231] as a user interface to connect to a Grid composed of ALICE specific services that are part of the AliEn framework and basic services of the Grid middleware installed at the different sites.

3.10.1 The AliRoot Framework

The ALICE offline framework, AliRoot [14] is based on Object-Oriented techniques for programming and, as a supporting framework, on the ROOT system [114], complemented by the AliEn system which gives access to the computing Grid. The AliRoot framework was developed as an extension of ROOT and is used for simulation, alignment, calibration, reconstruction, visualisation and analysis of the experimental data. The AliRoot framework is schematically shown in Fig. 3.15. The STEER module

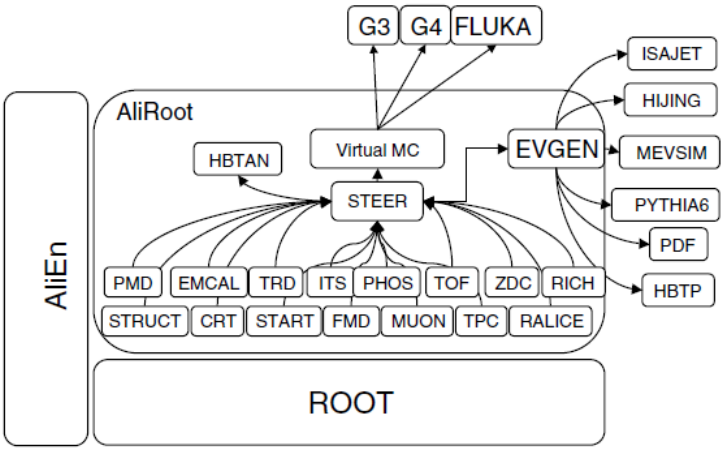

FIGURE 3.15: Schematic view of the AliRoot framework.

provides steering, run management, interface classes, and base classes. The detector related software is divided in independent modules that contain the code for simulation and reconstruction. Detector response simulation can be performed via different

transport packages like GEANT3 [116] written in FORTRAN and GEANT4 [67] written in C++. In these packages the detector material budget is simulated in detail, including support structures and the beam pipe. The transport code can hence simulate the decays of unstable particles and the trajectory of the daughter particles, the interactions of the particles with the detectors material and the production of secondary particles. The reconstruction results are stored in ESDs (Event Summary Data), from which the AODs (Analysis Object Data) are extracted. The AODs contain the relevant information for physics analyses. Additional information, used only for some specific analysis, is stored in additional files, usually called delta-AODs. For example, specific AOD are produced for the reconstruction of open-charm meson with two or three body decays. The analysis code, which contain the tasks utilised by the user to read the AOD files on the GRID and to produce quantities, histograms and trees for final analysis, calculations of efficiencies and quality and stability checks, is contained in the AliPhysics framework, which is built on the AliRoot and ROOT frameworks and is progressively developed by the data analysis groups.

Chapter 4

$\mathrm{D_S^+}$ production in pp collisions at $\sqrt{s}$ = 7 TeV

In this Chapter, the p_{T}-differential cross section of prompt charm-strange $\mathrm{D_s^+}$ meson measured in the rapidity range $|y|$ <0.5 in pp collisions at $\sqrt{s}$ = 7 TeV with the ALICE detector will be discussed. The sample of pp collisions at $\sqrt{s}$ = 7 TeV is the one providing up to now the most precise reference for the nuclear modification factors R_{AA} and R_{pPb}. Furthermore, the measurement of D-meson cross-section in pp collisions constitutes a benchmark for pQCD calculations at this energy. In comparison to previous ALICE publications based on the same data sample [19, 26, 45], the present results, which have been published in [43], have total (statistical and systematic) uncertainties reduced by a factor of about two. This improvement has several sources:

- changes in the detector calibration, alignment and track reconstruction algorithm, which resulted in better p_{T} resolution, thus higher signal-to-background ratio;
- a data sample with 20% larger integrated luminosity.
- optimization of the $\mathrm{D_s}$-meson selection procedure;
- refinements in the estimation of the systematic uncertainties, which is now more data-driven;

4.1 Event selection

The analysis was performed on 370M of events, which passed the physics selection cuts described in this Section and were thus selected for the analysis. The larger data sample of the current reconstruction (the number of events was 300M for the previous reconstruction) was obtained thanks to improvements in the reconstruction and detector alignments. A minimum-bias (MB) trigger was used to collect the data sample, by requiring at least one hit in either of the V0 counters or in the SPD. This trigger was estimated to be sensitive to about 87% of the pp inelastic cross section [159]. Contamination from machine-induced background was rejected offline using the timing information from the V0 and the correlation between the number of hits and tracklets in the SPD detector (see Sec. 3.4). The SPD detector can also be used to identify the presence of multiple interaction vertices in pp collisions (pile-up vertices). Since the readout time of the SPD is 300 ns, several bunch crossings are expected to occur in one SPD event. The algorithm of pile-up identification runs the vertex finding algorithm on the SPD tracklets not associated to the main vertex, which is the one with largest associated multiplicity. A vertex is tagged pile-up if there is a

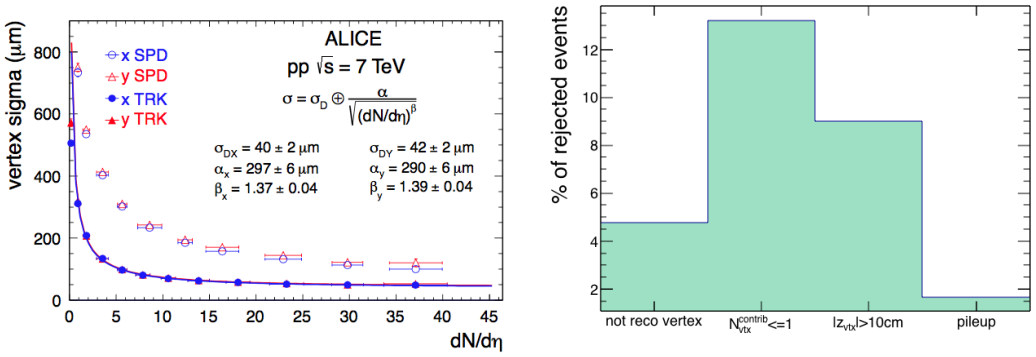

FIGURE 4.1: Left: resolutions of x- and y- vertices reconstructed with SPD tracklets or global tracks as a function of the event multiplicity. Right: fractions of events rejected during vertex and physics selection.

minimum number of tracklets associated to it (N_{min}^{trkl}) and if the z-separation between primary and pile-up vertex (Δz) is larger than a certain value. In this analysis, $N_{min}^{trkl} > 3$ and $\Delta z > 0.6$ cm were used. A further selection was applied on the event, requiring a primary vertex reconstructed from at least two ITS+TPC tracks (global tracks). In general, the vertex can be reconstructed by using only SPD tracklets. The reconstruction of the vertex with only SPD has higher efficiency due to the wider η coverage of the SPD and due to the less stringent request applied to tracklets w.r.t. tracks in the vertex calculations. The efficiency of vertex reconstruction with tracklets is $\epsilon_{SPD}^{vtx} \approx 96\%$ while that with global tracks is $\epsilon_{TRK}^{vtx} \approx 81\%$. On the other hand, global tracks allow to reach better resolution on the vertex, as shown in Fig. 4.1 left. Since the reconstruction of the decay topology requires a good resolution on the position of primary and secondary vertices, in this analysis events were required to have a vertex reconstructed with global tracks. Furthermore, the requirement for the z-vertex coordinate to be $|z_{RecoVert}| < 10$ cm selects tracks within $\eta < 0.9$, which is the acceptance region of ITS and TPC, and contributes to reject satellite collisions (see Sec. 3.4) that mostly occur at positions well outside the fiducial vertex region. The percentage of events rejected during the vertex and physics selection is shown in Fig. 4.1 (right panel). The most important contribution comes from the vertex selections.

4.2 D_s^+ reconstruction and strategy

The D_s^+ mesons can not be directly detected because of their mean proper decay length $c\tau = 150 \pm 2$ μm [213] that prevents them from reaching the detectors. Hence, the analysis is based on the reconstruction of the decay products. D_s^+ mesons and their antiparticles were reconstructed in the decay channel $D_s^+ \to \phi\pi^+$ (and its charge conjugate) followed by $\phi \to K^+K^-$ (Fig. 4.2). The branching ratio (BR) of this decay channel is 2.27 ± 0.08 % [213]. Other D_s^+ decay channels can give rise to the same final products $K^+K^-\pi^+$, such as $D_s^+ \to K^{*0}K^+$ and $D_s^+ \to f_o(980)\pi^+$ with BR 2.63 ± 0.13 % and 1.16 ± 0.32 %, respectively. It was verified that the selection efficiency for these decay modes is strongly suppressed by the cuts applied to select the signal candidates of $D_s^+ \to \phi\pi^+ \to K^-K^+\pi^+$, that include a selection on the mass of the intermediate resonant state. Since the width of the ϕ peak is narrower than those of the K^{*0} and the $f_o(980)$, the decay channel through the ϕ resonance, being the one that provides the best discrimination between signal and background, was used in this analysis.

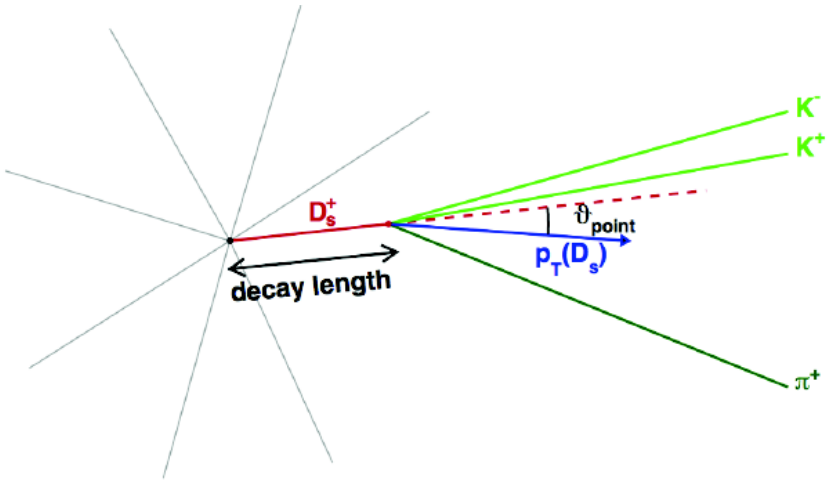

FIGURE 4.2: Schematic view of the $D_s^+ \to \phi\pi^+ \to K^+K^-\pi^+$ decay.

The D_s^+ signal is extracted from the invariant-mass[1] distribution of the candidates, which are obtained by combinatorial association of three reconstructed tracks with the correct charge-sign combination. Hence, the invariant-mass distribution will have a contribution from real D_s^+ decays ($D_s^+ \to K^+K^-\pi^+$) and another from background candidates. In order to improve the signal-to-background ratio, specific cuts were applied on the decay topology, on the invariant mass of K^+K^- pair and on the particle identification, as explained in the following sections. In particular, the selections based in the decay topology exploit the fact that the D_s^+ meson mean proper decay length of $\sim 150\,\mu$m makes it possible to separate its decay vertex from the primary vertex of the pp interaction. Before the candidates go through specific selections on the decay topology and particle identification, they have to pass single-track quality cuts. In the following, details of each selection step will be illustrated.

4.3 Single-track selections

Reconstructed tracks were selected by requiring:

- successful fit with the Kalman filter in TPC and ITS (see Sec. 3.6)
- pseudo-rapidity $|\eta| < 0.8$
- $p_{\mathrm{T}} > 0.3$ GeV/c
- at least 70 (out of a maximum of 159) associated space points in the TPC
- ratio of crossed rows (total number of hit TPC pad rows, i.e. corrected for pad rows with missing signal) over findable clusters (pad rows which, based on the geometry of the track, are possible clusters) in the TPC larger than 0.8

[1]The invariant mass is defined as:

$$m^2 = E^2 - \vec{p}^{\,2} = (E_1 + E_2)^2 - (\vec{p_1} + \vec{p_2})^2$$
$$m^2 = m_1^2 + m_2^2 + 2(E_1E_2 - p_1p_2\cos\theta)$$

- $\chi^2/\text{ndf} < 2$ for the track-momentum fit in the TPC (where ndf is the number of degrees of freedom involved in the tracking procedure)
- at least two (out of six) hits in the ITS, out of which at least one in either of the two SPD layers

For tracks that satisfy the above selection criteria, the transverse momentum resolution is better than 1% at $p_T = 1\,\text{GeV}/c$ and about 2% at $p_T = 10\,\text{GeV}/c$. The resolution on the track impact parameter, which is the distance of closest approach of the track to the primary vertex, is better than 75 μm for $p_T > 1$ GeV/c for the projection on the bending plane ($r\phi$, normal to the beam direction) in pp collisions. In order to have unbiased determination of the primary vertex, for each D_s^+ candidate the interaction point was recalculated from the reconstructed tracks after excluding the candidate decay tracks.

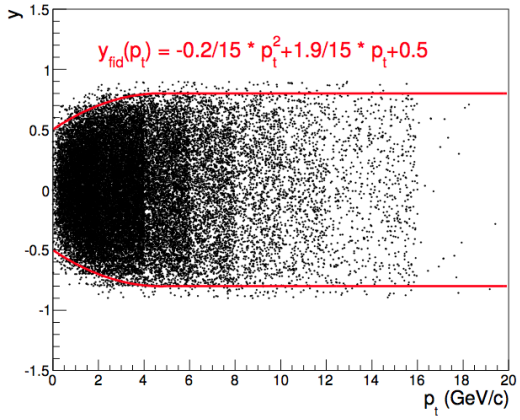

FIGURE 4.3: Rapidity versus p_T distribution of the reconstructed D_s^+ mesons. The fiducial acceptance region is defined by $|y| < y_{fid}(p_T)$.

The single-track selection criteria reduce the D_s^+-meson acceptance in the rapidity-transverse momentum plane. The acceptance drops steeply to zero for $|y| > 0.5$ at low p_T and for $|y| > 0.8$ at $p_T > 5$ GeV/c. A p_T-dependent fiducial acceptance region was therefore defined as $|y| < y_{fid}(p_T)$, with $y_{fid}(p_T)$ increasing from 0.5 to 0.8 in the transverse momentum range $0 < p_T < 5$ GeV/c according to a second-order polynomial function, and $y_{fid} = 0.8$ for $p_T > 5$ GeV/c (see Fig. 4.3):

$$y_{fid}(p_T) = -\frac{0.2}{15}p_T^2 + \frac{1.9}{15}p_T + 0.5. \tag{4.1}$$

4.4 Decay-chain and topology selection

The $D_s^\pm$ candidates are built from combinatorial association of three candidate tracks passing the selection criteria described in Sec. 4.3, with the correct combination of charge signs. In this way, a large number of candidates is created, most of them being combinatorial background. Strict selections are therefore needed to increase the signal-to-background ratio and the statistical significance of the signal, by applying cuts on variables that have the potential to discriminate D_s^+ signal (i.e. corresponding to real $D_s^\pm$ decays) from background candidates. To give an idea, there are about 885M D_s candidates in the 370M analysed events, after a preliminary filtering selections with very loose cuts. Candidates are thus selected by applying geometrical cuts on the displaced decay vertex topology, which are tuned as a function of the

D-meson p_{T}. The main feature of the $\mathrm{D_s^+}$-decay topology is the presence of three tracks displaced from the primary vertex and compatible with the hypothesis of being originated from a common point. The variable that allows one to evaluate the displacement of a track from the interaction point is its impact parameter, whose resolution is mostly determined by the hits in the two SPD inner layers of the Inner Tracking System.
The request of a minimum $p_{\mathrm{T}} = 0.3$ GeV/c of the daughter tracks contributes to the background rejection exploiting the harder p_{T} distribution of the $\mathrm{D_s}$ decay products with respect to the background tracks. The other selections are applied by exploiting the secondary vertex which is reconstructed from the three tracks that compose the $\mathrm{D_s}$ candidate. The topological cuts used for $\mathrm{D_s^\pm}$ signal selection are explained in detail below. Fig. 4.4, 4.5 and 4.6 complement the description, showing distributions of some of the below listed variables for prompt signal (in red) and background (in blue) candidates, in the interval $2 < p_{\mathrm{T}} < 16\,\mathrm{GeV}/c$, extracted from Monte Carlo production (PYTHIA [243]) and data, respectively. The distributions in data are obtained from candidate triplets with very loose selections on the topological variables, thus the contribution from the signal is negligible. The beauty feed-down component (also obtained from MC) is shown in green curve for those variables whose distributions for prompt signal from charm decays and for feed-down signal from beauty decays are different. Below the list of the variables on which the cuts are applied.

- **Decay length** D_{len}, defined as the distance between primary and secondary vertex. $\mathrm{D_s^\pm}$ decay vertices are displaced by a few hundred μm from the interaction vertex ($c\tau \approx 150\,\mu$m). Since real $\mathrm{D_s^\pm}$ decay vertices have, on average, larger values of decay length than the background, as it can be seen in Fig. 4.4 (left), this allows one to discriminate signal from background. Likely cut values are $D_{len} > 300 - 400\,\mu$m. To be noted that $\mathrm{D_s}$ mesons coming from weak decays of beauty hadrons have larger D_{len} with respect to prompt $\mathrm{D_s}$ from charm decay, due to more displaced decay vertices.

- **Normalised decay length** $\mathbf{NDL_{xy}}$, defined as the decay length in the transverse plane (xy) divided by its uncertainty (Fig. 4.4 right). Typical values of cuts on this variable are around 2.

- **Cos**θ_{point}, where θ_{point} is the angle between the momentum of the reconstructed $\mathrm{D_s^\pm}$ meson and the $\mathrm{D_s^\pm}$ flight line (line connecting primary and secondary vertex, see left panel in Fig. 4.5). The pointing angle is expected to be small for signal candidates, resulting in a distribution of $\cos\theta_{point}$ peaking at 1 for signal and being broader for background candidates. Hence, cuts like $\cos\theta_{point} > 0.93$ or tighter were usually applied to reject background.

- **Track dispersion** σ_{vtx} around the decay vertex, defined as:

$$\sigma_{vtx} = \sqrt{d_1^2 + d_2^2 + d_3^2}$$

  where d_i is the distance of minimal approach between the decay track i and the decay vertex. All tracks should originate from the secondary vertex, and σ_{vtx} should be ~ 0; in real cases, as a consequence of the tracking and vertex finding resolution, the σ_{vtx} differs from 0 and an upper cut is needed to exclude vertices made of random combination of tracks. Typical cut values on the track dispersion were between $0.02 < \sigma_{vtx} < 0.05$ cm (see Fig. 4.5 right).

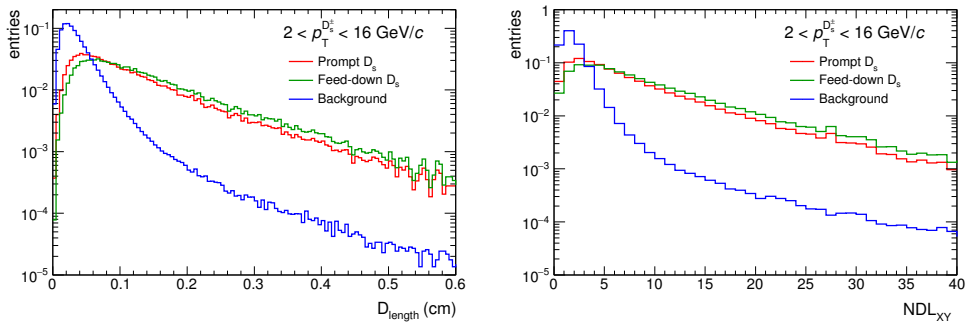

FIGURE 4.4: Left: distributions of decay length for prompt (red), feed-down (green) signal and background (blue) D_s candidates. Right: distributions of normalised decay length in the transverse plane signal (red) and background (blue) D_s candidates.

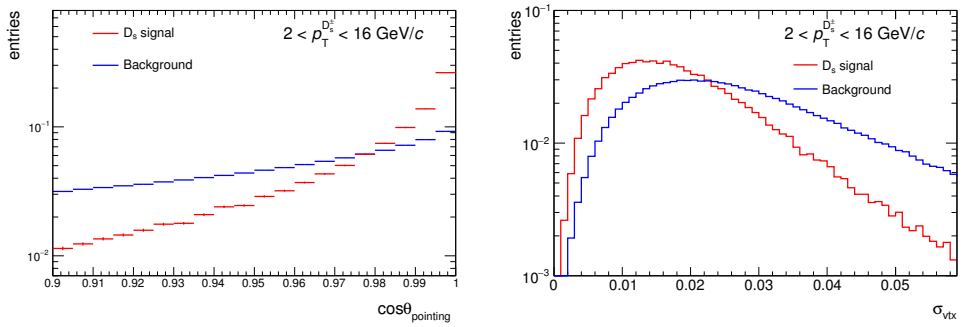

FIGURE 4.5: Distributions of $\cos\theta_{point}$ (left) and track dispersion around secondary vertex σ_{vtx} (right) for signal (red) and background (blue) D_s candidates.

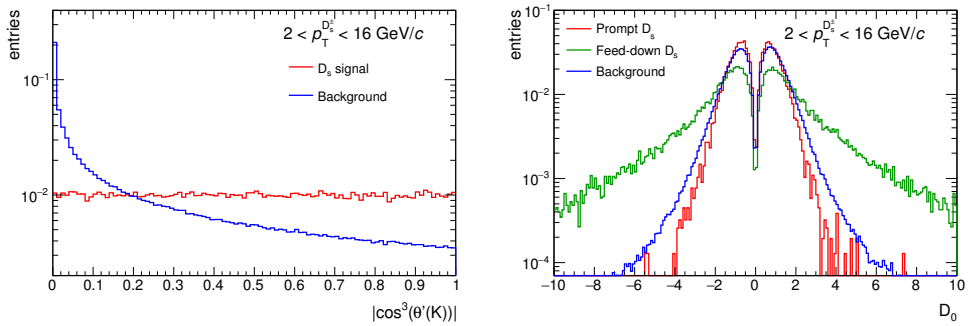

FIGURE 4.6: Left: distributions of $|\cos^3(\theta'(K))|$ for signal (red) and background (blue) D_s candidates. Right: distributions of maximum normalised single-track impact parameter among the three D_s daughters, in the transverse plane, for prompt (red), feed-down (green) signal and background (blue) D_s candidates.

- $\theta^*(\pi)$ **angle**, it is the angle between the pion in the KKπ rest frame and the KKπ flight line. Cuts were applied on the distribution of the $\cos\theta^*(\pi)$, with typical values between $0.95 < \cos\theta^*(\pi) < 1.0$.

- θ'**(K) angle**, it is defined as the angle between one of the kaons and the pion in the KK rest frame. Cuts were applied on the distribution of the $|\cos^3(\theta'(K))|$

(Fig. 4.6, left), with typical values between $0.0 < |\cos^3(\theta'(K))| < 0.05$. The selections on $\theta^*(\pi)$ and θ'(K) angles have already been used in various experiments which measured $\mathrm{D_s^+}$ production like ZEUS [133] and ATLAS [201] as well as in previous ALICE analyses [19, 26, 45, 54] and are based on kinematical considerations on the decay chain with a ϕ in the intermediate state.

- **Single-track normalised impact parameter residual** D_0 : it is defined as the difference between the expected impact parameter value $d^{exp}_{0,r,\phi} \approx D^{xy}_{len} \cdot \sin(\theta_{xy})$ (D^{xy}_{len} is the decay length on xy plane and θ_{xy} is the angle between the reconstructed D-meson momentum and the i-th daughter track on xy plane) and the reconstructed one $d^{reco}_{0,r,\phi}$ for the i-th daughter track. The difference $d_0^{reco} - d_0^{exp}$ is normalised by its uncertainty calculated as the sum in quadrature of the uncertainties on d_0^{reco} and d_0^{exp}. In Fig. 4.6 (right) the distributions of the $D_0 = max[d_0^{reco} - d_0^{exp}/\sigma]$ among the three daughter tracks of $\mathrm{D_s}$ candidates are shown, in different colours for background and signal candidates, distinguished between prompt and beauty feed-down components. Since the distributions of D_0 are quite different for prompt and feed-down D mesons, a selection based on this variable can reduce the feed-down D-meson contribution with respect to that of prompt D mesons. In this analysis selections on the $D_0 \sim 2$ were applied.

New topological variables were introduced with respect to the previous analysis of this sample. They are the projections of the cosine of the Pointing angle and of the (normalised) decay length in the xy plane and the single-track normalised impact parameter residual. The projections of the variables in the xy plane are justified by the better resolution of the impact parameter resolution with respect to z-direction.

A further selection which allowed to reduce the background is the requirement that the **invariant mass of the reconstructed** K^+K^- **pair** is compatible with the ϕ-meson mass. This is not a topological cut (i.e. a cut exploiting the displacement of the decay vertex), but a selection on the decay chain. It is required that at least one of the two pairs of tracks with opposite charge has an invariant mass compatible with the ϕ mass when the kaon mass is assigned to the two tracks. The selection is done on the absolute value of the difference between the ϕ invariant mass from PDG ($\sim 1.019\,\mathrm{GeV}/c$) and the reconstructed one:

$$\Delta M = |M^{inv}_{rec} - M_\phi|.$$

Typical values for cuts on ΔM are between $3 < \Delta M < 15$ MeV/c^2, thus always preserving more than 85% of the signal.

4.5 Particle identification

The Particle IDentification (PID) selection is based on the specific energy loss $\mathrm{d}E/\mathrm{d}x$ in the TPC and the time-of-flight from the interaction vertex to the TOF detector. This is used in the D-meson analysis to reduce the background, and it is essential for $\mathrm{D_s^+}$ studies because of the low values of signal-over-background ratios (S/B). A track is considered compatible with a certain particle species (π, K or p) if the measured signal has a difference within $n\sigma$ from the expected one for the corresponding mass hypothesis:

$$|S_{meas} - S^{\pi,k,p}_{expected}| < n^{\pi,k,p}\sigma,$$

where σ is the resolution on the energy-loss or time-of-flight signals for each species and $S^{\pi,k,p}_{expected}$ is the expected signal in TPC or TOF calculated respectively with Bethe-Bloch or time-of-flight equations for a given mass hypothesis (see Sec. 3.2.3 and 3.2.4). Candidate triplets were required to have two tracks compatible with the kaon hypothesis and one with the pion hypothesis. In addition, since the decay particle with opposite charge sign with respect to the D_s^+ mother particle in the $D_s^+ \to K^+K^-\pi^+$ chain has to be a kaon, a triplet was rejected if the opposite-sign track was not compatible with the kaon hypothesis. The criterion used to classify tracks on the basis of their PID information in TPC and TOF detectors is illustrated in Fig. 4.7, where $n\sigma^{\mathrm{max,TPC}} = 1$ for $0.6 < p_T < 0.8\,\mathrm{GeV}/c$ and 2 elsewhere and $n\sigma^{\mathrm{max,TOF}} = 3$ at all p_T. A response value of -1, 0 or 1 (green values in Fig. 4.7) is assigned to the PID signal in each detector. For both detectors, a final response value of -1 is assigned if the PID signal of the track is different from the expected one by more than 3σ. In cases where the TPC or TOF information is not available, a response value of 0 is assigned to the detector. This holds in particular for tracks at low momentum that may not reach the TOF. To combine PID information in the two detectors, the response values in TPC and TOF are summed together and the track is considered compatible with a species hypothesis if the combined response value is 1 or 2. This PID selection preserves ~85-90% of the signal depending on the p_T.

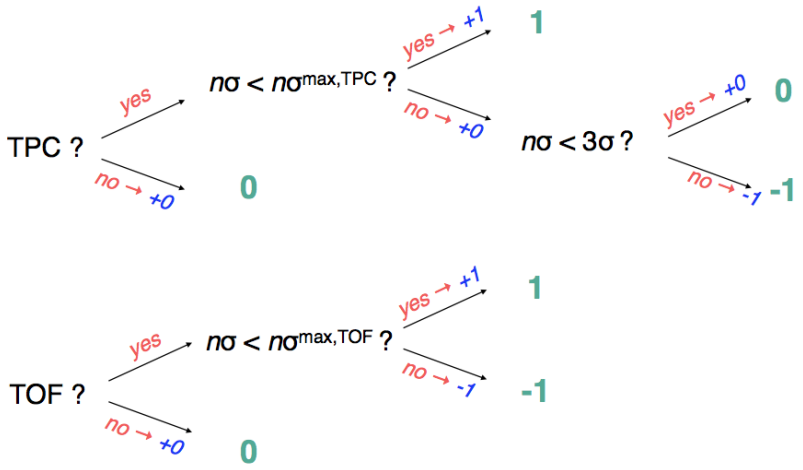

FIGURE 4.7: PID selection criteria in TPC and TOF for a specific mass hypothesis.

4.6 Invariant mass spectra, cut optimisation and signal extraction

For each candidate, two values of invariant mass can be computed, corresponding to the two possible assignments of the kaon and the pion mass to the two same-sign tracks. Considering the D_s^+ decay, the charge configuration of the tracks (+, -, +) can be interpreted both as to (K^+, K^-, π^+) and (π^+, K^-, K^+) mass assignments. Candidates were rejected if none of the two pairs of opposite-charged tracks had an invariant mass compatible with the PDG world average for the ϕ mass. Signal candidates with wrong mass assignment to the same-sign tracks would give rise to a contribution to the invariant mass distributions that could introduce a bias in the extraction of the

raw yield of D_s^+ mesons. It was verified, both in data and in simulations, that the particle identification and the requirement on the invariant mass of the two tracks identified as kaons to be compatible with the ϕ PDG mass reduce the bias contribution to a negligible level. D_s^+ candidates that pass all the selections are used to fill invariant mass histograms in different intervals of candidate p_T. The histograms are fitted by a function consisting of a sum of a Gaussian and an exponential function to describe the signal peak and the background shape respectively:

$$f(x) = Ae^{-B\cdot x} + Ce^{-\frac{(x-\mu)^2}{2\sigma^2}}. \tag{4.2}$$

The selection criteria used in the analysis as "central cuts" were tuned to preserve high selection efficiency and high statistical significance for the D meson signal, defined as:

$$Signif = \frac{\mathrm{S}}{\sqrt{\mathrm{S}+\mathrm{B}}},$$

where S and B are the extracted signal and background obtained from the fit procedure integrated within 3σ around the peak of the Gaussian (σ being the Gaussian width of the peak from the fit). The statistical significance is related to the relative statistical uncertainty on the extracted signal, so higher significance means lower statistical uncertainty on the raw yield. A third variable which is considered in the cut optimisation procedure is the signal-over-background ratio S/B. It was also required that the position and the width of the Gaussian peak were compatible with the values obtained in simulated events, with the same selection strategy. The selection values depend on the p_T of the D_s-meson candidate, since the number of background candidates depends on p_T as well. At low momentum, where the contribution from the combinatorial background is dominant, tighter selections are needed but, due to less displaced vertices with respect to the higher p_T candidates which are more boosted, too strong selections on the decay topology (e.g. decay length) are not allowed. The cuts used in the analysis are detailed in Table 4.1. The number of D_s candidates per event, after all the selections described above, is of the order of $\sim 10^{-7}$. In Fig. 4.8 the

D_s meson	pt interval (GeV/c)			
	2–4	4–6	6–8	8–12
Decay length (μm)	>300	>350	>350	>400
Decay length XY (μm)	>0	>200	>200	>200
Norm Decay length XY	>2.0	>0.0	>2.0	>2.0
Cosine pointing	>0.94	>0.95	>0.94	>0.94
σ_{vtx} (cm)	<0.02	<0.03	<0.03	<0.06
ΔM (MeV/c^2)	<8.0	<10.0	<4.5	<9.0
$\cos\theta^*(\pi)$	<1.0	<1.0	<1.0	<0.95
$\lvert\cos^3\theta'(\mathrm{K})\rvert$	>0.10	>0.05	>0.05	>0.05
Norm. IP residual Kaon	<2.5	<2.0	<2.0	<2.0
Norm. IP residual Pion	<2.5	<2.0	<2.0	<2.0

TABLE 4.1: Selections used for the $D_s^\pm$ meson in the four transverse momentum intervals considered.

invariant mass distributions of $D_s^\pm$ mesons in four p_T intervals from 2 to 12 GeV/c are shown and the values of S/B, statistical significance and extracted yields with their statistical uncertainties are reported in Table 4.2.

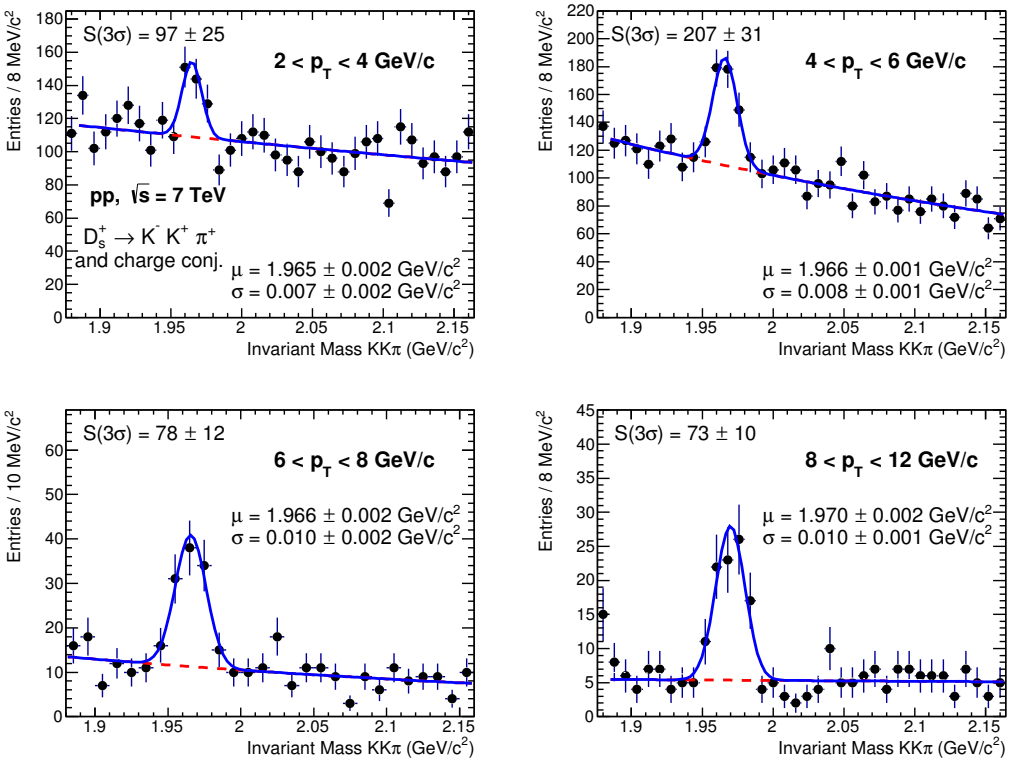

FIGURE 4.8: Invariant mass distributions of D_s^+ candidates and charge conjugates in the four considered p_T intervals.

p_T (GeV/c)	S/B	Signif.	S(3σ)
2-4	0.18	3.8	97 ± 25
4-6	0.30	6.9	207 ± 31
6-8	1.10	6.4	78 ± 12
8-12	1.78	6.8	73 ± 10

TABLE 4.2: S/B, statistical significance and yield for $D_s^\pm$ signal peak in the four transverse momentum intervals considered.

An indication of the improved resolution provided by the new reconstruction of the sample is visible in the left panel of Fig. 4.10, that shows an improvement by ∼25-30% on the values of the Gaussian sigmas of the simulated signal peak in the current reconstruction with respect to those in the old one. In the right panel of the same figure, the Gaussian widths of D_s peak are shown as a function of p_T for the current reconstruction in data (solid points) and in MC (dashed) and the values agree within uncertainties.

4.7 Corrections

The $D_s^\pm$ raw yields (sum of particle and anti-particle) extracted from the fits to the invariant-mass distributions were corrected to obtain the p_T-differential production

cross sections of prompt $\mathrm{D_s^+}$ mesons. The production cross section was calculated as:

$$\left.\frac{\mathrm{d}\sigma^{\mathrm{D_s^+}}}{\mathrm{d}p_{\mathrm{T}}}\right|_{|y|<0.5} = \frac{1}{\Delta p_{\mathrm{T}}}\frac{1}{\mathrm{BR}\cdot L_{\mathrm{int}}}\frac{f_{\mathrm{prompt}}(p_{\mathrm{T}})\cdot\frac{1}{2}N^{\mathrm{D_s^\pm\ raw}}(p_{\mathrm{T}})\Big|_{|y|<y_{\mathrm{fid}}}}{C_{\Delta y}\,(\mathrm{Acc}\times\epsilon)_{\mathrm{prompt}}(p_{\mathrm{T}})}\,, \tag{4.3}$$

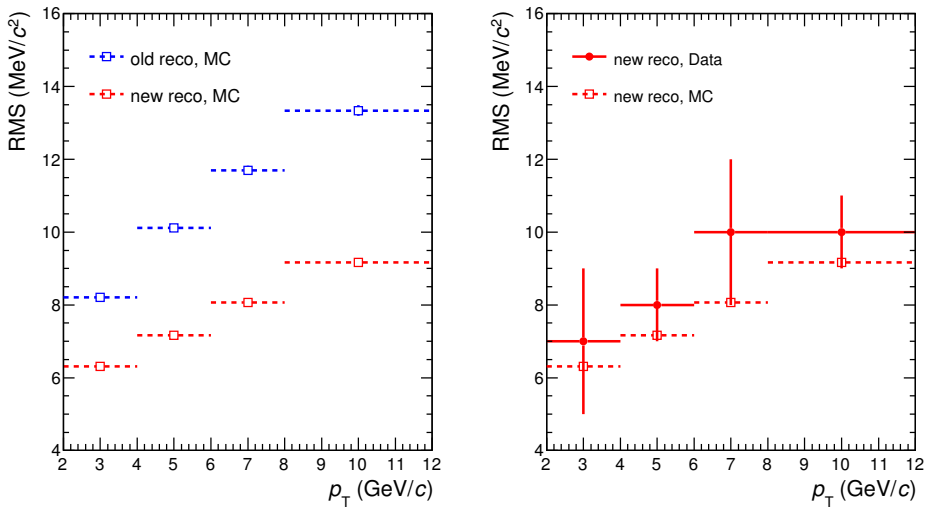

FIGURE 4.9: Left: MC Gaussian widths of $\mathrm{D_s}$ peak as a function of p_{T}, for current (red) and previous (blue) reconstruction. Right: Gaussian widths of $\mathrm{D_s}$ peak as a function of p_{T} for current reconstruction in data (solid) and MC (dashed).

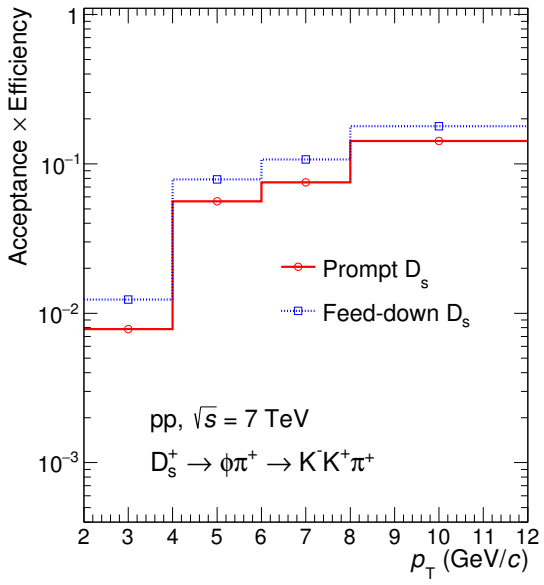

FIGURE 4.10: Acceptance-times-efficiency of prompt and feed-down $\mathrm{D_s}$ mesons as a function of $\mathrm{D_s}$ p_{T}.

where $N^{D_s^\pm \text{ raw}}(p_T)$ is the value of the raw yield (sum of particles and antiparticles), which needs to be corrected for the B-meson decay feed-down contribution (i.e. multiplied by the prompt fraction f_{prompt}), divided by the acceptance-times-efficiency of prompt D_s mesons $(\text{Acc} \times \epsilon)_{\text{prompt}}$, and divided by a factor of two to obtain the charge (particle and antiparticle) averaged yields. The corrected yields were further divided by the decay channel branching ratio (BR), the p_T interval width (Δp_T), the rapidity coverage ($C_{\Delta y} = 2y_{\text{fid}}$) and the integrated luminosity L_{int}. The rapidity acceptance correction factor $C_{\Delta y}$ was computed with the PYTHIA 6.4.21 event generator with Perugia-0 tune as the ratio between the generated D-meson yield in $\Delta y = 2y_{\text{fid}}$, (with y_{fid} varying from 0.5 at low p_T to 0.8 at high p_T) and that in $|y| < 0.5$. It was checked that calculations of the $C_{\Delta y}$ correction factor based on FONLL pQCD calculations or on the assumption of uniform D-meson rapidity distribution in $|y| < y_{\text{fid}}$ would give the same result, because both in PYTHIA and in FONLL the D-meson yield is uniform within 1% in the range $|y| < 0.8$. The integrated luminosity $L_{\text{int}} = (6.0 \pm 0.2)\,\text{nb}^{-1}$ was computed as $L_{\text{int}} = N_{\text{ev}}/\sigma_{\text{pp,MB}}$, where N_{ev} is the number of analysed events and $\sigma_{\text{pp,MB}} = 62.2$ mb [28] is the cross-section for the minimum-bias trigger condition, derived from a van der Meer scan measurement [203].

4.7.1 Reconstruction and selection efficiency

The acceptance-times-efficiency correction factor, $(\text{Acc} \times \epsilon)$, was determined for the D_s-meson hadronic decay considered in this analysis using Monte Carlo simulations of pp collisions generated with the PYTHIA 6.4.21 event generator [243] with the Perugia-0 tune [244] and particle transport through the apparatus using GEANT3 [115]. The luminous region distribution and the conditions (active channels, gain, noise level and alignment) of all the ALICE detectors were included in the simulations, considering also their evolution over time during the 2010 LHC data taking period. In the production, only events containing a $c\bar{c}$ or a $b\bar{b}$ pair were transported through the apparatus and reconstructed, and D mesons were forced to decay hadronically via the decay channels relevant to the specific analyses. The efficiency was extracted separately for prompt and feed-down D-mesons and is shown in Fig. 4.10, for the selection criteria reported in Tab. 4.2. D mesons from beauty-hadron decays have higher efficiency than the prompt ones in all the p_T intervals, due to the larger average displacement of their decay vertices from interaction point. The efficiency increases with p_T because at higher p_T the background is less dominant and looser selections are allowed. In general, with the chosen topological selections, efficiencies in this analysis are on average 15% lower than those used in the previously published analysis [26]. The present analysis uses more powerful selection variables (projections on xy plane and impact parameter residual) that enhance the signal-over-background ratio for D_s meson by a factor from 2 to 5 depending on the p_T interval, with a slight reduction of the global efficiency. Large signal-over-background ratios are indeed essential to assure a good stability of the extracted yield.

4.7.2 Beauty feed-down subtraction

The f_{prompt} fraction was calculated using the beauty production cross sections from FONLL calculations [120, 119], the $B \to D + X$ decay kinematics from the EvtGen

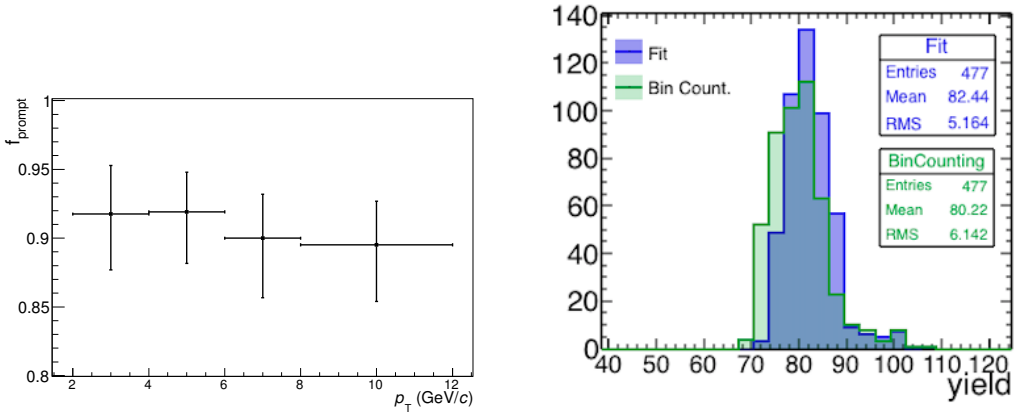

FIGURE 4.11: Left: prompt fraction values for D_s meson with the final selections as a function of p_T in pp collisions at $\sqrt{s} = 7$ TeV. Right: multiple-trial raw yield distribution from fit and bin counting extraction in different colours, as an example for the interval $6 < p_T < 8\,\mathrm{GeV}/c$.

package [192] and the efficiencies for feed-down D mesons reported in Fig. 4.10:

$$f_{\mathrm{prompt}} = 1 - \frac{N_{\mathrm{raw}}^{\mathrm{D\ feed\text{-}down}}}{N_{\mathrm{raw}}^{\mathrm{D}}} = 1 - \left(\frac{\mathrm{d}^2\sigma}{\mathrm{d}p_{\mathrm{T}}\mathrm{d}y}\right)_{\text{feed-down}}^{\mathrm{FONLL}} \cdot \frac{(\mathrm{Acc}\times\epsilon)_{\text{feed-down}} \cdot C_{\Delta y}\Delta p_{\mathrm{T}} \cdot \mathrm{BR} \cdot L_{\mathrm{int}}}{N^{\mathrm{D}+\overline{\mathrm{D}},\mathrm{raw}}/2}, \tag{4.4}$$

where the p_T dependence of f_{prompt}, $N^{\mathrm{D}+\overline{\mathrm{D}},\mathrm{raw}}$ and $(\mathrm{Acc}\times\epsilon)_{\text{feed-down}}$ is omitted for brevity. The values of f_{prompt} of D_s meson vary between 0.89 and 0.92 as a function of p_T and are shown in Fig. 4.11 (left). The prompt fraction decreases with p_T due to topological cuts, such as the decay length, that are more efficient in selecting D_s meson from beauty decays. The values of f_{prompt} are compatible with those obtained in the analysis of the first reconstruction of the sample [26].

4.8 Systematic uncertainties

In this section the studies carried out to estimate the systematic uncertainties on the measurement of the D_s^+ cross section as a function of p_T are presented. The contributions to the systematic uncertainty from the different sources were studied separately and are described in the following.

4.8.1 Raw yield extraction

The value extracted for the yield depends on the configuration of the invariant-mass fit. In order to estimate the systematic uncertainty on the raw yield, a possible approach is to explore all the possible fit configurations and build a distribution of the yields, via a multiple-trial approach. The fits to the invariant-mass distributions were repeated several times varying i) the lower and upper limits of the fit, ii) the background fit function (3 cases: exponential, linear and second order polynomial), iii) the Gaussian mean and width of the signal line shape, which were left free or fixed to MC values. The fits which did not converge or had $\chi^2/\mathrm{ndf} > 2.0$ were rejected

and not considered in the evaluation of the systematic uncertainty. It was verified that the yields extracted with the default fit parameters had compatible values to the mean of the distribution of yields from the multiple-trial approach. An example of the distribution of yields from multiple-trial approach applied on fit and on bin counting is shown in the right panel of Fig. 4.11, for the interval $6 < p_T < 8\,\mathrm{GeV}/c$. In the blue distribution, the signal extraction is done via a fit of the invariant mass, while in the green distribution it is estimated from the counting of the entries in the invariant-mass histogram after subtracting the background counts calculated from the background fit function. The values of the mean and the RMS of both the distributions are reported in the plot. The RMS of the distribution of the multiple trials on fit was used as an estimator of the systematic uncertainty on the raw yield extraction. With the above selection criteria, the value resulted to be ∼6% in all p_T intervals. The relative difference between the means of the yield distributions for the extraction via fit and via bin counting resulted to be smaller than 6% at all p_T and therefore no additional uncertainty was assigned from this check. The assigned uncertainty is reduced by a factor 3-4 with respect to the analysis with the old reconstruction, where it was around 15-20% depending on the p_T interval. To further investigate whether the systematic uncertainty estimated with this approach is not too much conservative, a slightly different approach was tested. We assumed that the systematic uncertainty on the yield extraction via the fit procedure arises only from variations in the line shape of the signal and in the fitting function for the background. Let us examine these two contributions separately.

Signal line shape The uncertainty from signal line shape was calculated by considering the combinations among these fit configurations: (i) free Gaussian width parameter, (ii) width parameter fixed to MC value, (iii) Gaussian width varied by 20% with respect to MC value (to account for the maximum difference of width values between data and MC), (iv) free peak position, (v) peak position fixed to MC value. The uncertainty was estimated as the maximum error (max. value - min. value) divided by $\sqrt{12}$, considering the distribution uniform. It resulted to be ∼5% in all the p_T intervals.

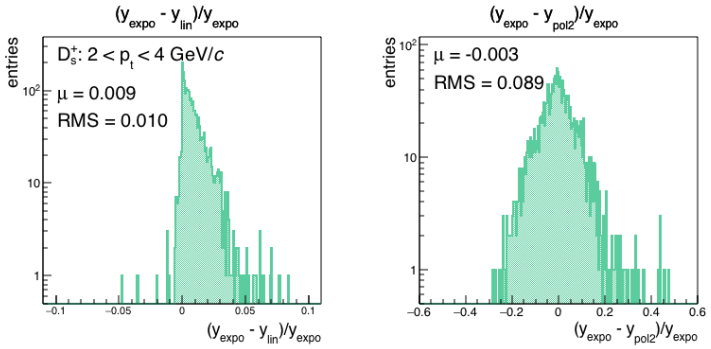

FIGURE 4.12: Relative difference of signal yield with exponential and first (left) and second (right) order polynomial functions for background, in $2 < p_T < 4$ GeV/c.

Background fit function Using different functions to fit the background introduces some systematic differences in the extracted yields. The default shape used for the central value of raw yield is an exponential function, but first and second order polynomial shapes were also tested to estimate the systematic uncertainty. In Table 4.3 the

values of reduced chi square referred to the compatibility of the background function with data (excluding the region within 3σ from the peak) are reported. One can see

	p_{T} interval (GeV/c)	Exponential	Linear	Pol2
χ^2/ndf	2–4	1.21	1.21	1.09
	4–6	1.15	1.18	1.16
	6–8	1.03	1.02	1.03
	8–12	0.99	0.99	1.03

TABLE 4.3: Reduced χ^2 values for the fit of the background (peak region excluded) in the considered p_{T} intervals of the $\mathrm{D_s}$ meson.

that all the three shapes give a good description of data, but in general no improvements are visible when adding more parameters in the fit with respect to exponential shape, so the latter confirms itself as a good choice. Nevertheless, it is important to look also at the values of the extracted yield to assess possible biases. In order to do this, 50 simulated samples were generated via Poissonian smearing of the fit function with the exponential background. For each sample, the yields extracted utilising a fit function with exponential background were compared with those obtained using linear and polynomial functions with the same configuration for the parameters of the Gaussian peak, mass range and bin width. The difference of the yields with linear and parabolic backgrounds relative to the yield extracted using a fit with exponential background was used to fill a histogram. The procedure was repeated for different configurations of lower and upper limits for the fit and invariant-mass bin widths for each of the 50 samples. A potential shift from zero of the mean of the resulting distribution should reveal the bias from the change of background. The spread of the distribution is related to statistical fluctuations. In Fig. 4.12 an example of the above described distribution is presented, in the interval $2 < p_{\mathrm{T}} < 4\,\mathrm{GeV}/c$. Left and right panels show respectively the distribution of the difference of yields extracted with first or second order polynomial shapes to those extracted with exponential background. The shift in the distribution is not statistically significant since $\mu < 3\,\mathrm{RMS}$. Hence, no bias arises from the change of background and the main systematic effect from this approach comes from the function used for the signal peak, resulting in a 5% uncertainty that is consistent with the 6% quoted from the first approach.

4.8.2 Selection efficiency

The systematic uncertainty on the selection efficiency accounts for possible imperfections in the MC description of the variables used to select the signal, which could introduce a bias in the efficiency. A possible test to quantify the effect of any discrepancy in the description of topological variables between data and MC is to exploit different sets of cuts that have different selection efficiencies and to compare the cross sections. In this analysis, twelve sets of cuts were compared, their respective efficiencies spanning a variation up to a factor of $\sim$6 with respect the default efficiency, depending on the p_{T} interval. Only the cuts that provided medium-high statistical significance and good S/B ratios of the extracted yields were taken into account for the final systematics. Fig. 4.13 shows the ratios of raw yields (top left panel) and efficiencies (top right) extracted with the different sets of cuts with respect to the

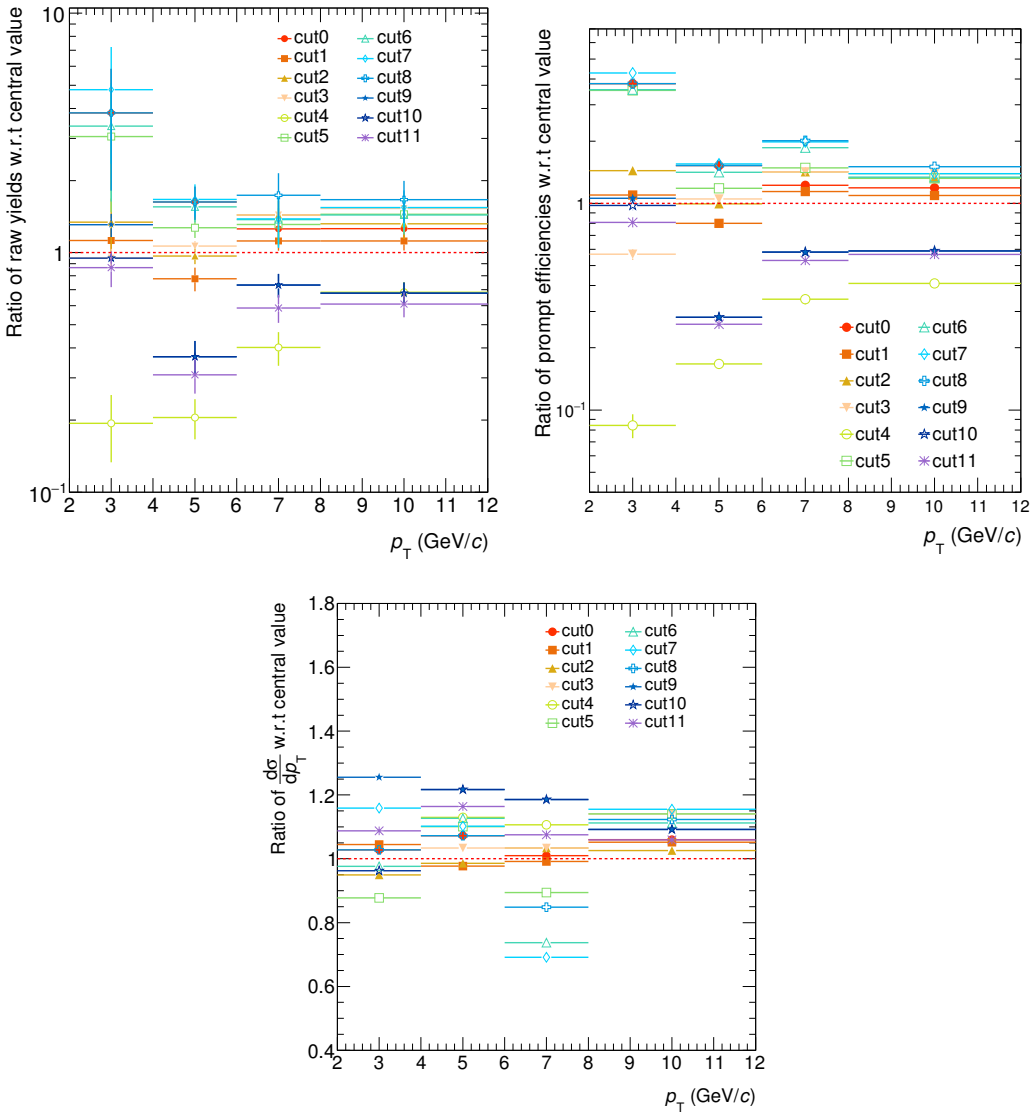

FIGURE 4.13: Ratios of D_s raw yields (top left), selection efficiencies (top right) and cross sections (bottom) with different sets of cuts with respect to their respective values with the default selections, as a function of p_T.

reference values with the default selections as a function of p_T. To find several sets of cuts that provide a good signal stability, more than one variables need to be varied at the same time. It is very likely that, while the selection on some variables needs to be released, the selection on others requires to be tightened. For this reason, the extracted yields with lower selection efficiency are in general not simply sub-samples of those with higher efficiency, thus making not straightforward the calculation of the error on the ratios of raw yields and hence, of the cross sections in order to estimate the systematic uncertainty. The ratios of the different cross sections to the default one are shown in the bottom panel of the same Fig. 4.13. We took the RMS of the their distributions in each p_T interval as an estimator of the systematic uncertainty. The uncertainty resulted to be 7% in all p_T bins. In particular, the effect of possible imperfections in the description of the residual misalignment in the simulations was

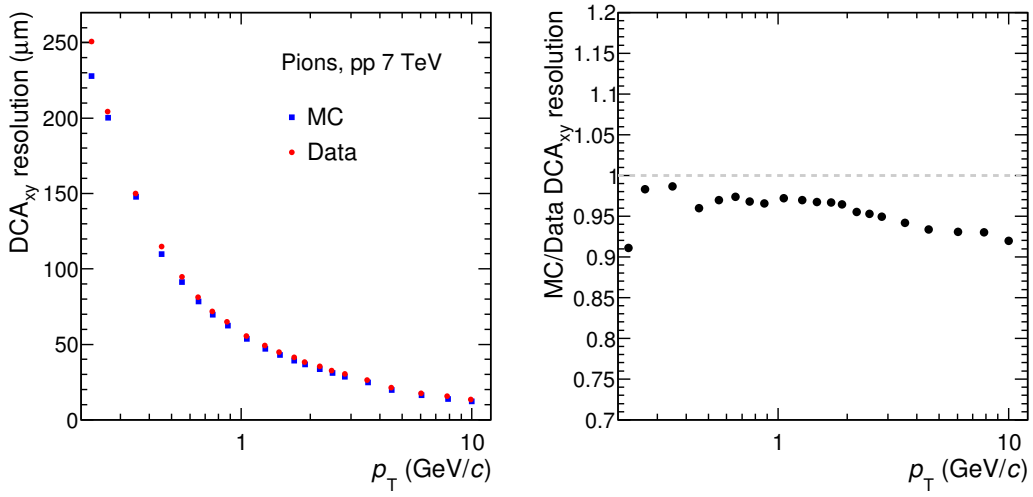

FIGURE 4.14: DCA_{xy} resolution curves of pion tracks as a function of p_T in data and in MC (left panel) and their ratio (right panel) in pp collisions at $\sqrt{s} = 7$ TeV.

studied separately starting from the differences observed on the impact parameter resolution in data and in the simulation. Fig. 4.14 (left) shows, as an example for pion tracks, distributions of DCA_{xy} resolution as a function of p_T in data and in simulation in pp collisions at $\sqrt{s} = 7$ TeV. The values were extracted via fits to the DCA_{xy} distributions of tracks in data and in MC, in different p_T intervals. The right panel of the Fig. 4.14 shows the MC-to-data ratio of the DCA_{xy} resolutions. The agreement is overall good. To estimate the effect of the residual discrepancy, the resolution values in the MC were reduced by 10% and the DCA_{xy} of tracks in MC smeared according to the new resolution. The variation of the efficiencies was less than 3%, lower than the 7% from the cut variation study, which includes this contribution.

4.8.3 PID efficiency

To test the efficiency correction of PID efficiency, looser PID selection criteria were used with respect to the default selection described in Sec. 4.5. In fact, in the D_s case, the rare signal and the large background do not allow for a reliable signal extraction without particle identification. The looser PID selection accepts those cases reported in Fig. 4.7 where combined response values from TPC and TOF detectors are 0, 1 or 2, which correspond to a 3σ cut on the dE/dx and time-of-flight signals. The tighter standard selection only accepts as final response values of the tracks 1 or 2. In Fig. 4.15 the ratio of the corrected yields obtained with looser-to-default PID selection is shown, for the twelve different sets of cuts discussed in Sec. 4.8.2. The evaluation of the systematic uncertainty, estimated as the RMS of the distributions in each p_T interval, was made considering only the region $p_T > 4\,\mathrm{GeV}/c$, since with looser PID we could not obtain a stable extraction of the raw yield for most of the different sets of cuts, whose statistical significance values were < 3 and the S/B was about few percent. The RMS of the corrected yield distributions for the considered p_T intervals is about 7% and this value is assigned as uncertainty in all p_T intervals.

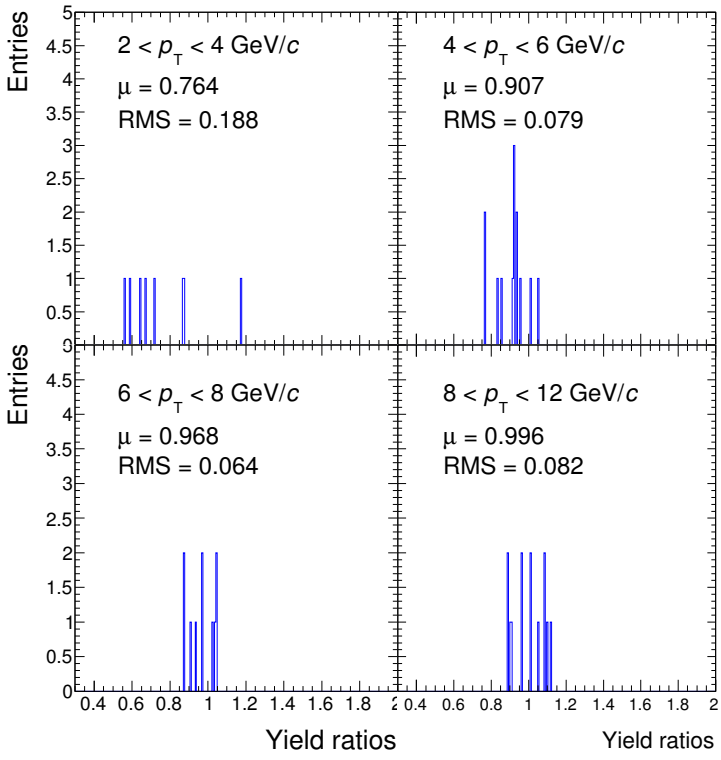

FIGURE 4.15: Ratio of D_s corrected yields with looser and default PID selections (for twelve different sets of topological selections).

4.8.4 Track reconstruction efficiency

The systematic uncertainty related to the tracking efficiency includes the effects arising from track finding in the TPC, from track prolongation from the TPC to the ITS, and from track quality selections. It was estimated with the following tests:

- comparison of the D-meson cross sections obtained with different track selection cuts;
- comparison of the TPC-ITS track matching efficiency in data and simulations.

These checks are discussed in the following subsections.

Variation of track selections

For this purpose, cases with higher statistical significance, such as D^0 and D^+ mesons, were used to estimate the systematic uncertainty. The D-meson raw yields and efficiencies were evaluated with different sets of track selection cuts. The following selections were tested:

1. additional cut on number TPC crossed rows > 120-[5 (GeV/c)/p_T] (not used in the default selections);
2. additional number of TPC clusters > 0.65× number of TPC crossed rows (not used in the default selections);

3. tighter selection on the ratio of crossed rows over findable clusters in the TPC (> 0.9 instead of 0.8).

The systematic uncertainty was assigned based on the observed variation of the prompt D^0 and D^+ cross sections with respect to the default selections. Based on this check, systematic uncertainties of 2% and 3% independent of D-meson p_T were respectively estimated for D^0 (two-body decay) and D^+ (three-body decay). The values are consistent with a 1% per-track systematic uncertainty, that was inherited for the D_s-meson analysis.

ITS-TPC matching efficiency

The matching efficiency, i.e. efficiency of track prolongation from TPC to ITS, is defined as the fraction of tracks successfully prolonged from TPC to ITS (having at least one cluster in the SPD layers) over the number of tracks reconstructed in TPC. Systematic uncertainty on its determination arises from discrepancies in the tracking performance between data and Monte Carlo. Primary particles are defined as prompt particles produced in the collision, including decay products, except those from weak decays of strange particles. Matching efficiency for primary tracks is higher than for secondary tracks (originating from strange-hadron decays, thus with secondary vertices likely to be outside the SPD layers or for particles produced in interactions with material). If the fractions of primary and secondary tracks are different in data and in Monte Carlo, this could lead to a discrepancy in the matching efficiency which is not due to the tracking performance and therefore it should not be accounted for in the systematic uncertainty on tracking. Hence, data-driven corrections for primary and secondary fractions were used to re-weight the MC and obtain a corrected inclusive MC efficiency, which is then used in the comparison to data, to estimate the systematic uncertainty.
The steps in the procedure are:

- extract the matching efficiencies for different particle types: $\mathrm{Eff}^{\mathrm{MC}}_{\mathrm{primaries}}$, $\mathrm{Eff}^{\mathrm{MC}}_{\mathrm{secondaries}}$, $\mathrm{Eff}^{\mathrm{Data}}_{\mathrm{inclusive}}$
- extract the fraction of primary tracks in data: $\mathrm{f'}_{\mathrm{primaries}}$
- compute a corrected MC-inclusive efficiency: $\mathrm{Eff}^{\mathrm{MC}}_{\mathrm{inclusive}} = \mathrm{f'}_{\mathrm{primaries}}$ x $\mathrm{Eff}^{\mathrm{MC}}_{\mathrm{primaries}}$ + (1- $\mathrm{f'}_{\mathrm{primaries}}$) x $\mathrm{Eff}^{\mathrm{MC}}_{\mathrm{secondaries}}$
- estimate the relative systematic uncertainty: $(\mathrm{Eff}^{\mathrm{Data}}_{\mathrm{inclusive}} - \mathrm{Eff}^{\mathrm{MC}}_{\mathrm{inclusive}})/\mathrm{Eff}^{\mathrm{Data}}_{\mathrm{inclusive}}$.

A minimum-bias Monte Carlo production (with the PYTHIA 6 event generator and GEANT 3 for particle transport through the apparatus) anchored to 2010 pp data taking at $\sqrt{s} = 7$ TeV was used for this study. Charm-enriched productions were not used in this study since the shape of DCA distribution of tracks (used to extract data-driven primary track fraction) is affected by the heavy-flavour particle enhancement and may bias the fit. Efficiency was studied as a function of:

- p_T, from 0.5 to 15 GeV/c
- ϕ, between (0,2π)
- η, between (-0.8,0.8)

Let us examine below more in detail the steps needed to calculate the systematic uncertainty.

1. **ITS-TPC matching efficiency:** it is calculated separately for primary and secondary tracks in MC, inclusively on data. For the numerator of the matching efficiency, tracks were selected requiring to have a successful fit with the Kalman filter in the TPC and ITS, a hit in one of the two SPD layers, |DCAxy| < 2.4 cm and |DCAz| < 3.2 cm.

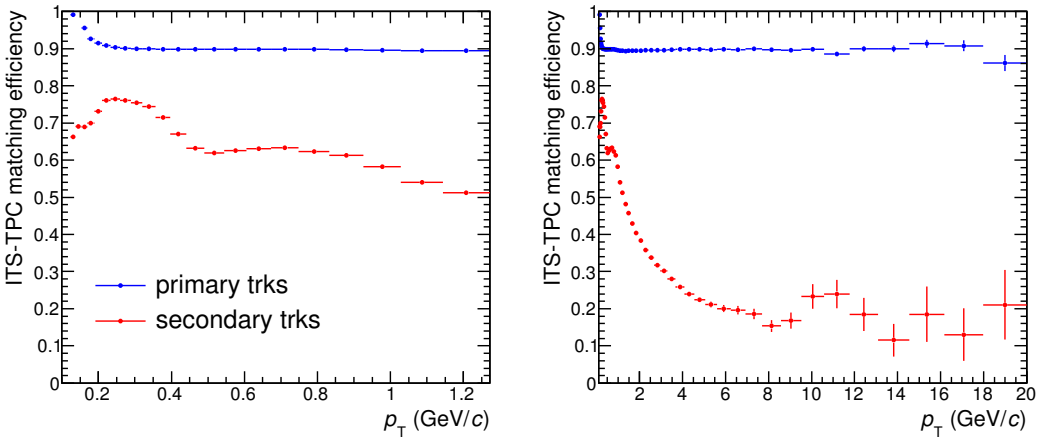

FIGURE 4.16: Matching efficiency for primary and secondary tracks as a function of p_T in MC for p_T interval from 0.1 to 1 GeV/c (left) and up to 20 GeV/c (righ).

In Fig. 4.16, ITS-TPC matching efficiency of charged tracks in MC as a function of p_T is shown. The left panel is referred to the low p_T region (0.1-1 GeV/c), the right one extends the p_T interval up to 20 GeV/c. The difference between matching efficiency of primary and secondary tracks is large and increases with p_T.

2. **Fractions of primary tracks:** these are extracted with a data-driven technique based on a fit to the measured track impact parameter distribution using MC templates for DCA_{xy} distributions of primary and secondary tracks, in different p_T, η and φ intervals. The ROOT TFractionFitter package was used to perform the fit. The fit was configured using three templates describing primary tracks, secondaries tracks from strange-hadron decays and tracks produced in interactions in the material. A selection on tracks requiring at least one hit in either of the two SPD layers was used, to assure good enough resolution to distinguish primary and secondary DCA_{xy} distributions. Fits were performed on the DCA_{xy} distributions of charged particles from data in the range [-1,1] cm, in different intervals of p_T, φ, η and constraining the three fractions in the TFractionFitter class within reasonable minimum and maximum values. The fractions were then calculated by integrating the histogram resulting from the fit in the range $|DCA_{xy}| < 2.4$ cm, for consistency with what done for the matching efficiency calculation. As a closure test, it was verified that the MC values for the fractions of primary and secondary tracks were in agreement with the values extracted when performing the fit with TFractionFitter on the inclusive MC distribution, with the three MC templates. In Fig. 4.17 the distributions of DCA_{xy} in data and in MC for the different components are shown in different colours, in p_T intervals from 0.5 to 15 GeV/c. In Fig. 4.18 the ratio of DCA_{xy} distributions in data to the distribution resulting from the fit (obtained

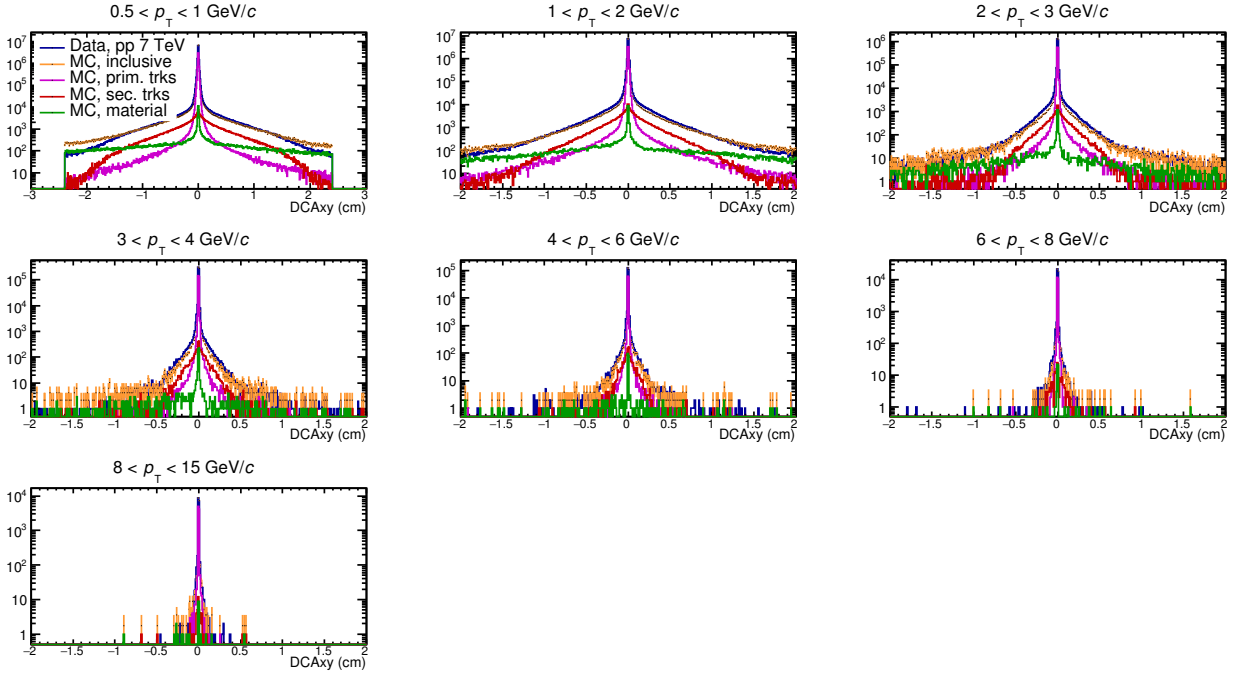

FIGURE 4.17: DCA_{xy} distributions in data and in MC for primary and secondary tracks in different colours, in p_T intervals from 0.5 to 15 GeV/c.

as output of TFractionFitter class) are plotted. At low p_T, where the statistics allows a good performance of the fit, the values of the bin-per-bin ratios stay

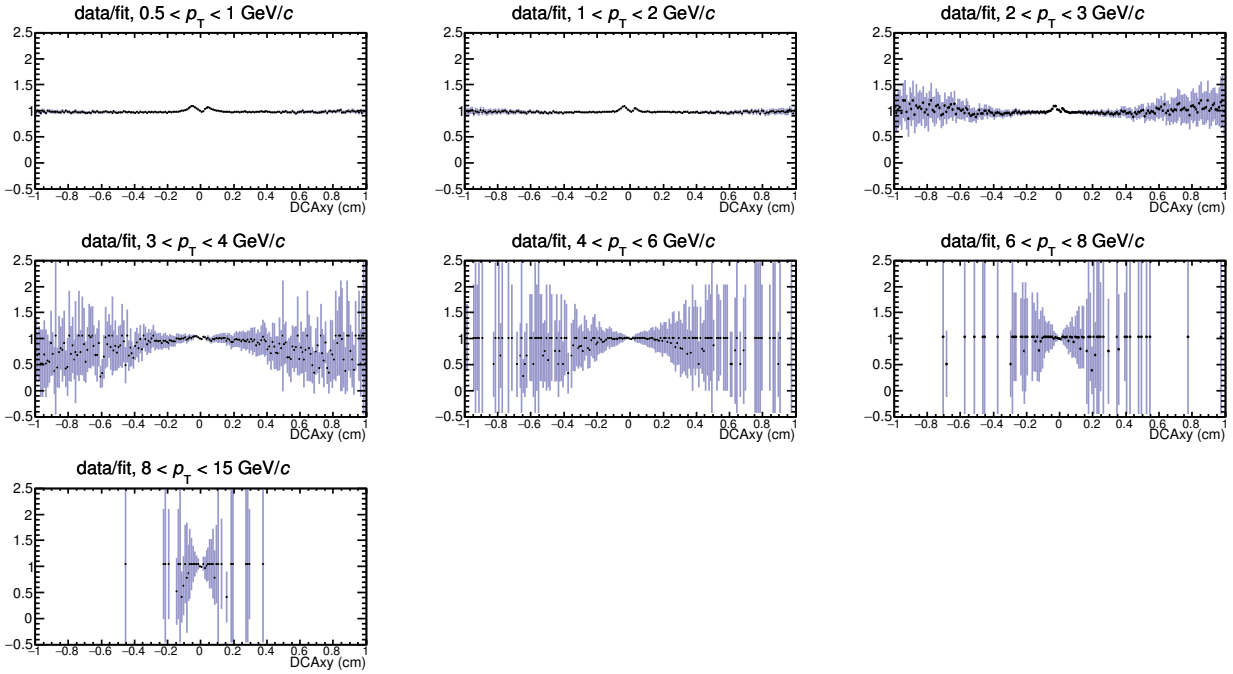

FIGURE 4.18: Ratio of DCA_{xy} distributions in data and in the fit result histograms, in p_T intervals from 0.5 to 15 GeV/c.

within 10% variation. At higher p_T, the agreement gets slightly worse but the values of the ratios always stay around unity. Furthermore, the smooth values of the data-driven fractions obtained from the fits as a function of p_T, η and φ are an indication of the reliability of the fit. In Fig. 4.19, the data-driven values of primary and secondary fractions are shown and compared to the ones from the PYTHIA + GEANT 3 simulation (empty markers). The fraction of secondaries in the figure already includes the contributions from material. We conclude that the fraction of secondaries is underestimated in the simulations.

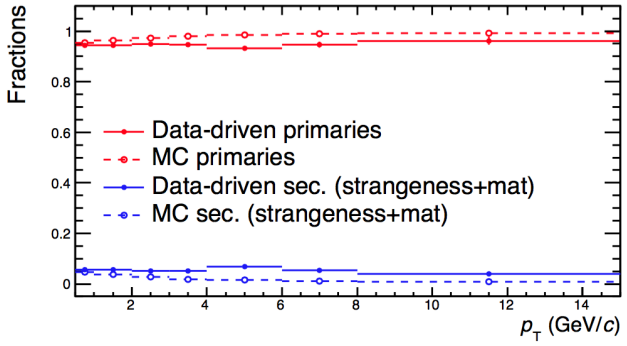

FIGURE 4.19: Data-driven (solid lines) and MC (dashed lines) fractions of primary (red) and secondary (blue) tracks as a function of p_T in pp collisions at $\sqrt{s} = 7$ TeV.

3. **Correction to the primary fraction:** since the fraction of primary particles was calculated using tracks with the request of a hit in one of the SPD layers, the primary fraction estimated for this sample of tracks needs to be rescaled to the primary fraction of the sample of tracks reconstructed in the TPC. The reason for this correction is that the primary fraction is then used to (re)-weight the matching efficiency, that is normalised to the number of tracks in the TPC only. The fractions of primary tracks are expected to be different in ITS and TPC due to their different amount of secondary tracks from strangeness decays, whose secondary vertices are likely to be outside the SPD layers and therefore do not contribute to the number of tracks in the ITS. The correction factor is based on MC information and obtained as the ratio of the fraction of primary tracks in TPC to the fraction of primary tracks with TPC-ITS matching and one point in the SPD. The final fraction of primary tracks is hence f'$_{\rm primaries}$ = f$_{\rm primaries}$ x correction factor, where f$_{\rm primaries}$ is the fraction obtained at step 2. Typical values of correction factor for primary tracks are around $\sim$ 0.95-0.98 as a function of p_T. In Fig. 4.20 an example of fractions of primary and secondary tracks in MC requiring ITS-TPC matching or points in the TPC detector only are shown in different colours as a function of p_T.

4. **ITS-TPC corrected matching efficiency:** it is calculated as Eff$^{\rm MC}_{\rm inclusive}$ = f'$_{\rm primaries}$ x Eff$^{\rm MC}_{\rm primaries}$ + (1- f'$_{\rm primaries}$) x Eff$^{\rm MC}_{\rm secondaries}$. The corrected matching efficiency is shown in Fig. 4.21, 4.23 (left) and 4.24 (left) as a function of p_T, ϕ, η respectively, for kaons and pions (selected with a 3σ PID cut on dE/dx in TPC). It was verified that no substantial changes are obtained if considering all the species (π, K, p, e,μ). The drops in efficiency in some ϕ regions are due to SPD inactive modules during the data taking. Finally, the ratios of MC inclusive (i.e. including primary and secondary tracks) matching efficiencies to efficiency

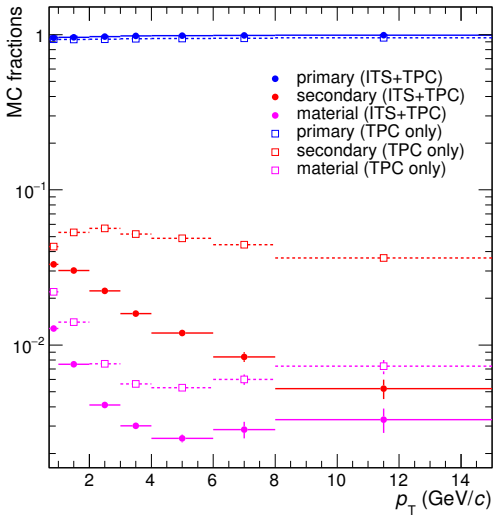

FIGURE 4.20: Example of fractions of primary and secondary tracks in MC requiring ITS-TPC and one point in SPD layers or TPC only selections in different colours as a function of p_T.

in data are shown in Fig. 4.22, 4.23 (right) and 4.24 (right) as a function of p_T, ϕ, η respectively. The data driven weighting procedure in MC allows to obtain better description of the data and a reduced systematic uncertainty as compared to the one obtained using the uncorrected MC. This per-track uncertainty is

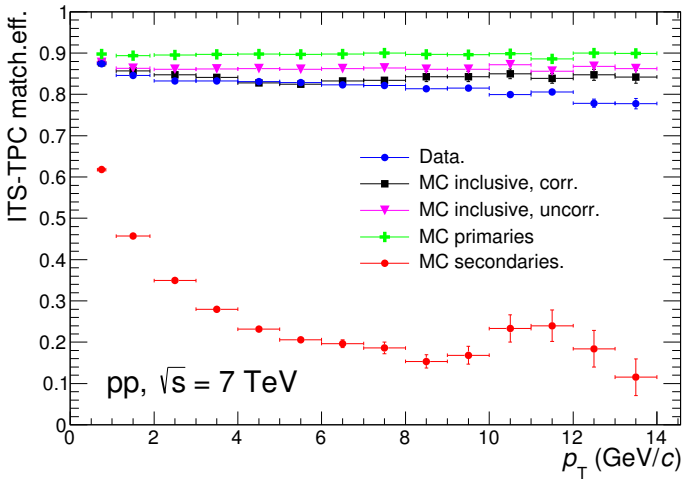

FIGURE 4.21: ITS-TPC matching efficiency as a function of p_T for 2010 pp data taking at $\sqrt{s} = 7$ TeV. The matching efficiency is shown for data (blu), for MC primary (green) and secondary (from strangeness decay and material interaction, in red) tracks, for inclusive MC tracks with (black) and without (magenta) data-driven correction.

then summed in quadrature with the 1% per-track systematic uncertainty on track selection discussed in the previous section.

Finally, the information from the simulations was used to propagate the uncertainty

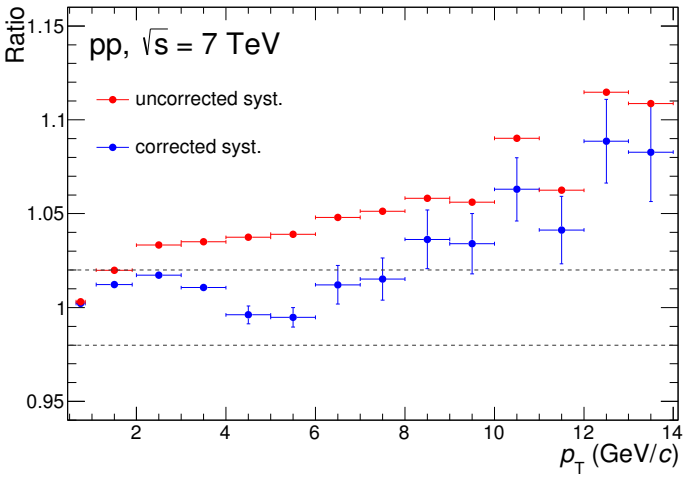

FIGURE 4.22: Ratio of ITS-TPC matching efficiencies in data and MC as a function of p_T before (red) and after (blue) data-driven correction.

at the track level to the D-meson level through the decay kinematics. The tracking uncertainties of the three daughter tracks were assumed to be fully correlated and were summed linearly. In the simulation the same topological and PID cuts used in data were applied. In the left panel of Fig. 4.25, the scatter plot of p_T of daughter tracks versus D_s-meson p_T is presented, and the mean p_T profile is also shown. The right panel shows the final systematic uncertainty of tracking efficiency for the 3-prong D_s-meson decay as a function of Ds-meson p_T, as obtained with this MC-based procedure. The estimated uncertainty in the previous analysis of this sample was 4% per track, which resulted in 12% for the three-body decay of D_s^+ mesons. This study allowed a reduction of the systematic uncertainty on tracking by a factor of 2÷3.5, depending on p_T, for D_s meson.

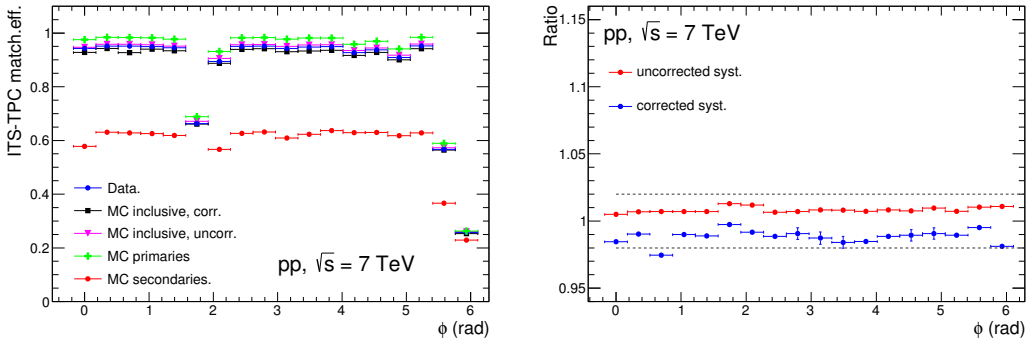

FIGURE 4.23: Left: ITS-TPC matching efficiency as a function of ϕ for 2010 pp data taking at $\sqrt{s} = 7$ TeV. The p_T of the tracks is $0.5 < p_T < 14\,\mathrm{GeV}/c$. The matching efficiency is shown for data (blu), for MC primary (green) and secondary (from strangeness decay and material interaction, in red) tracks, for inclusive MC tracks with (black) and without (magenta) data-driven correction. Right: ratio of ITS-TPC matching efficiencies in data and MC as a function of ϕ before (red) and after (blue) data-driven correction.

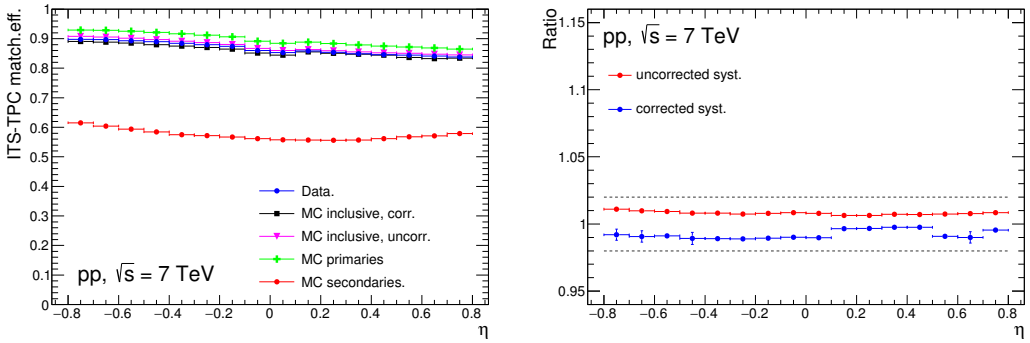

FIGURE 4.24: Left: ITS-TPC matching efficiency as a function of η for 2010 pp data taking at $\sqrt{s} = 7$ TeV. The p_{T} of the tracks is $0.5 < p_{\mathrm{T}} < 14\,\mathrm{GeV}/c$. The matching efficiency is shown for data (blu), for MC primary (green) and secondary (from strangeness decay and material interaction, in red) tracks, for inclusive MC tracks with (black) and without (magenta) data-driven correction. Right: ratio of ITS-TPC matching efficiency in data and MC as a function of η before (red) and after (blue) data-driven correction.

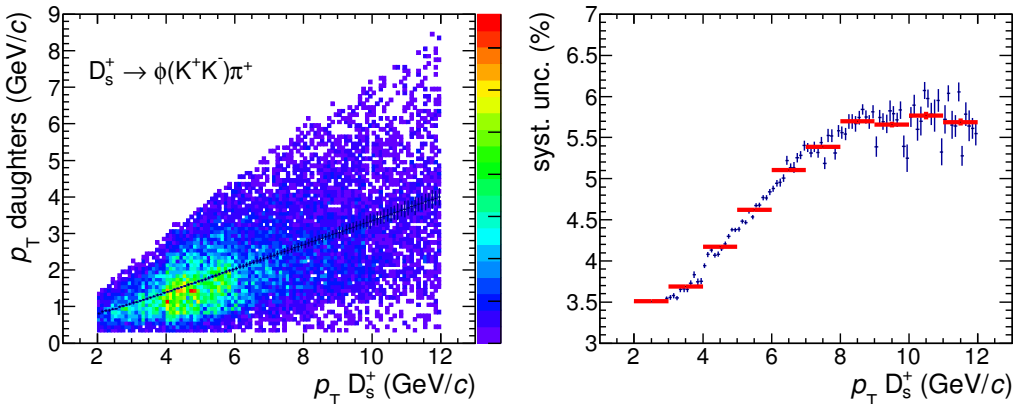

FIGURE 4.25: Left: scatter plot of daughter p_{T} versus $\mathrm{D_s}$-meson p_{T}. Right: final systematic uncertainties propagated at $\mathrm{D_s}$-meson level, after weighting for daughter kinematics, as a function of p_{T}.

4.8.5 B feed-down

The systematic uncertainty on the feed-down contribution, i.e. $\mathrm{D_s}$ mesons originating from beauty-hadron decays in the raw yield, was estimated by varying the p_{T}-differential cross section of feed-down D mesons within the theoretical uncertainties of the FONLL calculation. The procedure for the variation of the b-quark mass, of the perturbative scales and of the parton distribution functions is described in [123]. The factorisation and renormalisation scales, μ_{F} and μ_{R}, were made to vary independently in the ranges $0.5 < \mu_{\mathrm{F}}/m_{\mathrm{t}} < 2$, $0.5 < \mu_{\mathrm{R}}/m_{\mathrm{t}} < 2$, with the constraint $0.5 < \mu_{\mathrm{F}}/\mu_{\mathrm{R}} < 2$, where $m_{\mathrm{t}} = \sqrt{p_{\mathrm{T}}^2 + m_{\mathrm{c}}^2}$. The mass of the c and b quarks were varied within $1.3 < m_{\mathrm{c}} < 1.7$ GeV/c^2 and $4.5 < m_{\mathrm{b}} < 5$ GeV/c^2, respectively. The uncertainties on the fragmentation fractions of b quarks into B mesons quoted in the

PDG were kept into account. The uncertainty related to the B decay kinematics was neglected, after verifying that the difference resulting from using the PYTHIA [243] decayer instead of EvtGen [192] is negligible with respect to the FONLL B-meson cross-section uncertainty. Previous D-meson analyses in ALICE [19, 45, 54] used to compare two different methods to correct for the beauty feed-down component and include their difference in the systematic uncertainty. The first method, used to give the central value for $f_{\rm prompt}$, is the one presented in Eq. 4.4 and needs as inputs the measured $D_s^{\pm}$ raw yields, the FONLL predictions of B-meson cross-sections and the selection efficiency for feed-down D mesons. The alternative method takes as inputs FONLL predictions for both feed-down and prompt D mesons and their respective Monte Carlo efficiencies, as follows:

$$f'_{\rm prompt} = \left(1 + \frac{(\mathrm{Acc} \times \epsilon)_{\rm feed-down}}{(\mathrm{Acc} \times \epsilon)_{\rm prompt}} \cdot \frac{\left(\frac{\mathrm{d}^2\sigma}{\mathrm{d}y\,\mathrm{d}p_{\rm T}}\right)^{\rm FONLL}_{\rm feed-down}}{\left(\frac{\mathrm{d}^2\sigma}{\mathrm{d}y\,\mathrm{d}p_{\rm T}}\right)^{\rm FONLL}_{\rm prompt}} \right)^{-1} . \tag{4.5}$$

The use of this alternative approach has been reconsidered after a review of currently available measurements of beauty and charmed meson cross-sections at the LHC was carried out. The measurements were compared to FONLL predictions for heavy-flavoured hadrons for the specific centre-of-mass energy and rapidity interval. In Fig. 4.26, the B^+-, B^0-, B_s^0-meson and Λ_b-baryon cross sections measured by CMS in pp collisions at $\sqrt{s} = 7$ TeV [181, 128, 131, 129], in the rapidity interval $|y| < 2.4$, are compared to FONLL predictions. The latter were rescaled for the fragmentation fractions of b quark into b hadrons from PDG [214], which provides the production fractions of b hadrons in hadronic Z decays. The measurements lay within FONLL uncertainty bands in the case of non-strange B mesons. A worse agreement for FONLL is found to B_s^0-meson and Λ_b-baryon cross sections. In Fig. 4.27, measurements of B^+-, B_s^0-meson and Λ_b-baryon cross sections from LHCb in pp collisions at $\sqrt{s} = 7$ TeV at forward rapidity $2.0 < y < 4.5$ are shown [6, 10]. FONLL predictions were scaled by the fragmentation fraction values of b quarks into b hadrons measured by LHCb in the rapidity interval $2.0 < y < 4.5$ [5]. The LHCb measurements in pp collisions indicate an enhancement of baryon production from b-quark fragmentation at forward rapidity with respect to the value quoted by the PDG [214]. The values from LHCb are in agreement with the measurements of the b-quark fragmentation fraction in $p\bar{p}$ collisions at Tevatron reviewed in [214]. In Tab. 4.4, the fragmentation fractions of beauty quarks at Z resonance and in $p\bar{p}$ collisions are summarised:

b hadron	fraction at Z [%]	fraction at $p\bar{p}$
B^+, B^0	40.7 ± 0.7	34.4 ± 2.1
B_s	10.0 ± 0.8	11.5 ± 1.3
b baryons	8.5 ± 1.1	19.7 ± 4.6

TABLE 4.4: Fragmentation fractions of b quarks into weakly-decaying b-hadron species in $Z \to b\bar{b}$ decay, in $p\bar{p}$ collisions at $\sqrt{s} = 1.96$ TeV [214].

In the top left panel of Fig. 4.27 the comparison between LHCb B^+-meson cross section and the FONLL calculations shows a good agreement. Also the Λ_b-baryon cross section (top-right panel) is well described by FONLL, provided that the value of $f(b \to \Lambda_b)$ measured in pp or $p\bar{p}$ collisions is used. This supports the evidence

for non-universality of hadronisation fractions in the two different environment of pp ($p\bar{p}$) collisions and in Z decay. A better agreement is found for LHCb B_s^0-meson

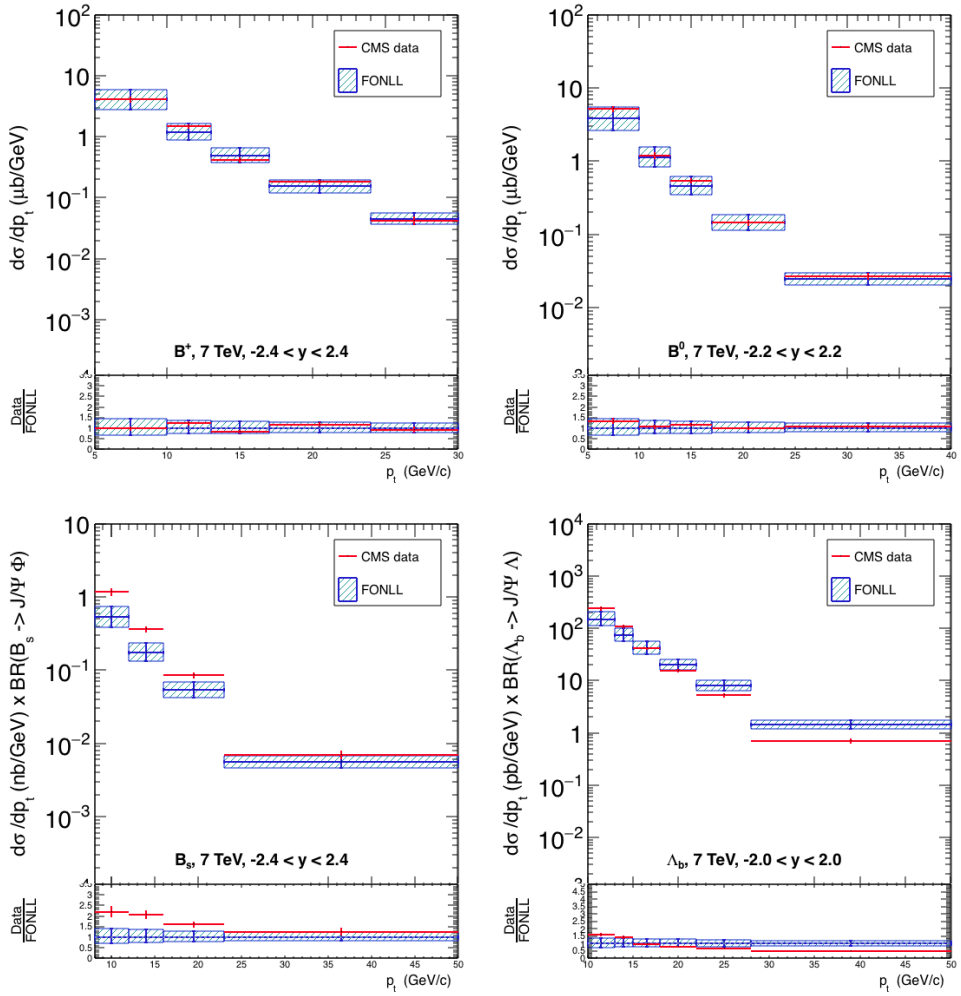

FIGURE 4.26: B^+-, B^0-, B_s-meson and Λ_b-baryon differential cross-sections (red points) as a function of p_T measured by CMS in pp collisions at $\sqrt{s} = 7$ TeV at mid-rapidity [181, 128, 131, 129] compared to FONLL predictions [120, 119] at the same energy (blue boxes).

cross-section with FONLL calculations (bottom left panel), measured in a wider p_T range than CMS. The CMS and LHCb B_s^0-meson cross-sections in $8 < p_T < 50$ GeV/c are shown in the bottom right panel as a function of y, together with FONLL predictions in the two different rapidity intervals. For the CMS data, two cases are reported, one obtained using the 2015 PDG [210] value for BR($B_s \to J/\psi\ \phi$) = $(1.40 \pm 0.04)\times10^{-3}$, the other obtained using the 2010 PDG [209] value BR = $(1.08 \pm 0.09)\times10^{-3}$, referenced in the CMS paper. The agreement of FONLL to the measurements is good at forward rapidity and also at mid-rapidity when the updated value of BR($B_s \to J/\psi\ \phi$) is used. In Fig. 4.28 the cross-section of J/ψ-meson from beauty-hadron decays in pp collisions at $\sqrt{s} = 7$ TeV measured by LHCb [7] and the D^+-, D^0-, D^{*+}-meson cross-sections in pp collisions at $\sqrt{s} = 7$ TeV by ALICE [19] are presented. For J/ψ mesons from beauty decays, FONLL provides a good description of the data (note that this holds also for data at $\sqrt{s} = 8$ TeV [8]). The D-meson results show that the measurements systematically lay on the upper

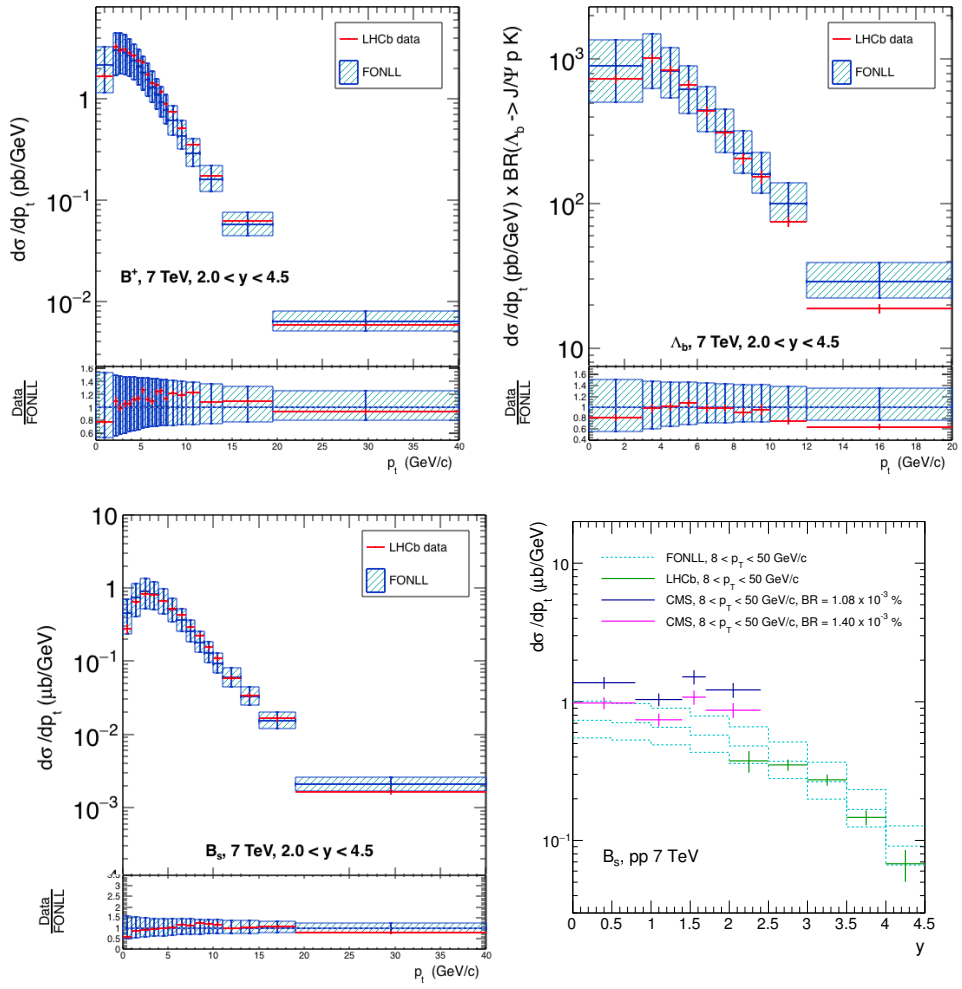

FIGURE 4.27: B^+, Λ_b and B_s^0 differential cross-sections (red points) measured by LHCb in pp collisions at $\sqrt{s} = 7$ TeV at $2 < y < 4.5$ compared to FONLL predictions at the same energy (blue boxes) [6, 10]. In the bottom right panel, B_s^0-meson differential cross-section as a function of y from LHCb is compared to same measurements from CMS at mid-rapidity ($8 < p_T < 50$ GeV/c) and to FONLL predictions [120, 119] in the full rapidity range.

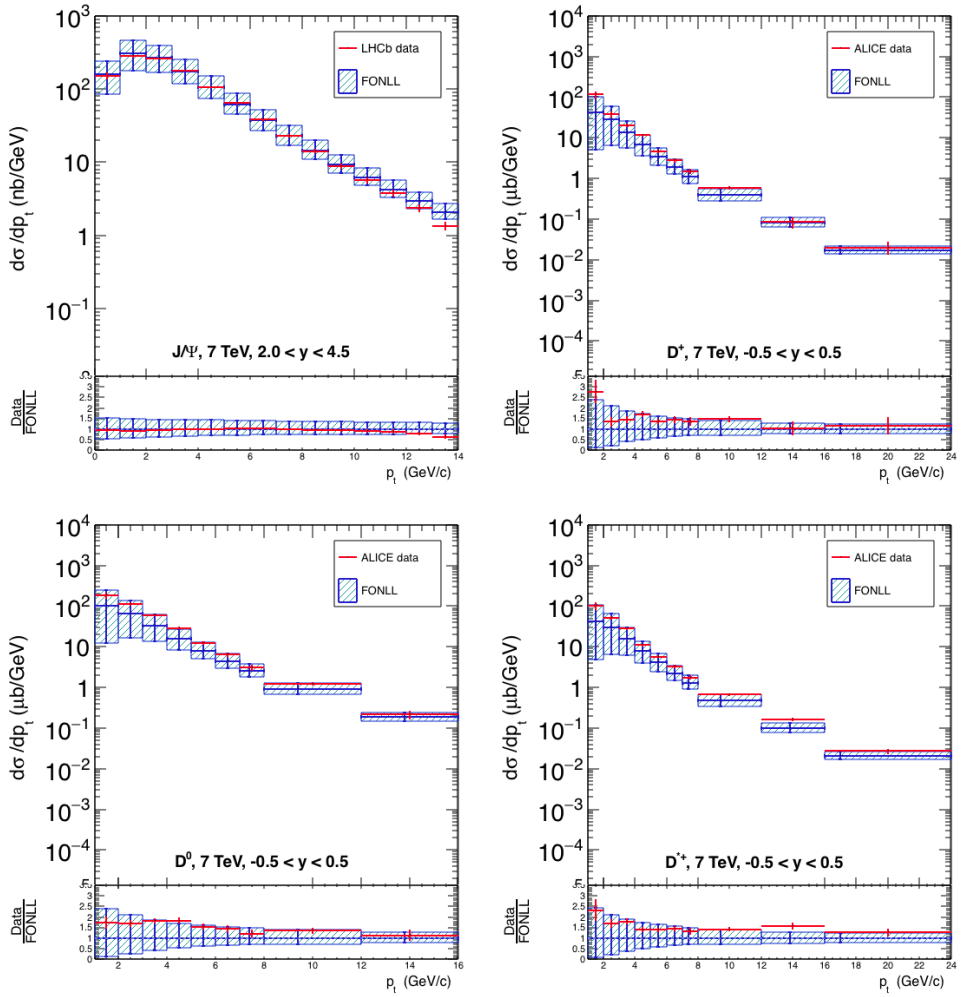

FIGURE 4.28: J/ψ from b-hadron decays (from LHCb, $2 < y < 4.5$ [7]), D^+, D^0 and D^{*+}-meson (from ALICE, mid-rapidity [19]) differential cross-sections (red points) as a function of p_T in pp collisions at $\sqrt{s} = 7$ TeV compared to FONLL predictions [120, 119] at the same energy (blue boxes).

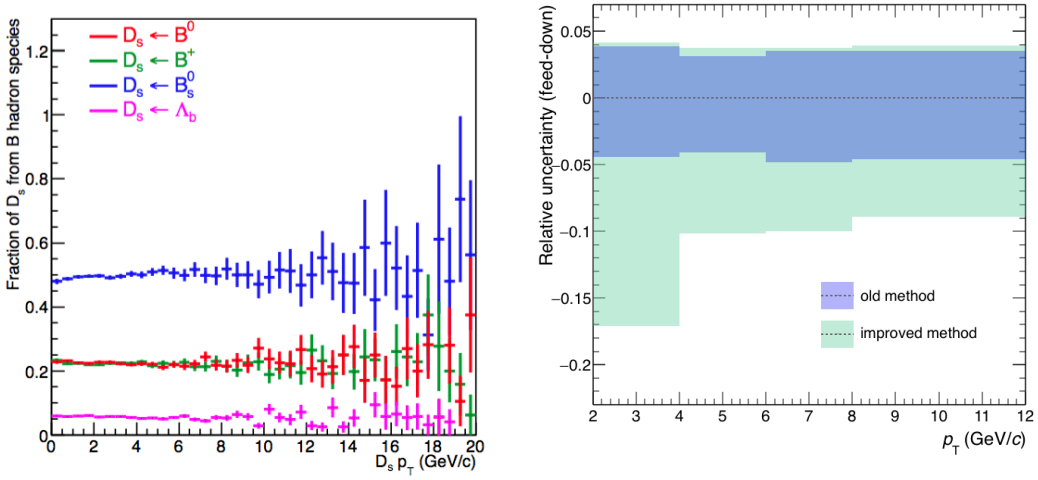

FIGURE 4.29: Left: fraction of D_s originating from decays of different species of beauty hadrons. Right: comparison of systematic uncertainties on beauty feed-down component subtraction with the old and the new procedure.

edge of FONLL uncertainty band, thus charm production being underestimated by the FONLL calculation with the central values of charm mass ($m_c = 1.5\,\mathrm{GeV}/c$) and of factorisation and renormalisation scales.
Considering that:

- FONLL provides a good description of B^+- and B^0-meson cross-sections at $\sqrt{s} = 7$ TeV at both mid- and forward rapidity and of the cross-section of J/ψ from beauty-hadron decays at forward rapidity at $\sqrt{s} = 7$, 8 TeV;
- FONLL provides a good description also for the B_s^0-meson cross-section at forward rapidity where data are available in a wider p_T range than at mid-rapidity. FONLL also describes Λ_b-baryon cross-section, provided the usage of the $f(b \to \Lambda_b)$ measured in pp collisions;

the calculation of f_{prompt} with the method in Eq. 4.4 is then fully justified. Indeed, as Fig. 4.29 (left) shows, around half of B feed-down D_s originates from B^0- and B^+-meson decays and half from B_s^0-meson decays, which are all described by FONLL calculations. The sum of the contributions to the D_s yield shown in Fig. 4.29 (left) is unity. The method in Eq. 4.5, instead, would suffer from the fact that FONLL underestimates charm production at LHC energies. It is reasonable to conclude that, on the basis of the current measurements, Eq. 4.5 could introduce a bias if used to correct for the beauty feed-down component, thus artificially enhancing the systematic uncertainty. In Fig. 4.29 (right) the comparison of the relative (low and high) systematic uncertainties on the D_s cross-section, due to the beauty feed-down subtraction, show that the lower uncertainties are reduced by a factor 2-3, depending on p_T, with the improved procedure with respect to the old one. The low uncertainty bars result the most affected by the reduction since the estimate of the prompt fraction with Eq. 4.5 is systematically lower than that with Eq. 4.4, because FONLL calculations underestimate charm production at LHC.

4.8.6 Generated p_{T} shape

The influence of the shape of the generated $\mathrm{D_s}$ p_{T} spectrum used in Monte Carlo simulations on the efficiency calculated in the p_{T} intervals used in the measurement was also evaluated. To estimate this contribution, the efficiencies computed with the $\mathrm{D_s}$ p_{T} shape from PYTHIA with Perugia-0 tune were compared to the ones obtained with that from FONLL calculations. This resulted in a systematic effect on the $\mathrm{D_s}$ efficiency of $\sim 3\%$ in the two lowest p_{T} intervals and of $\sim 2\%$ at higher transverse momenta.

	p_{T} interval (GeV/c)			
	2–4	4–6	6–8	8–12
Raw yield extraction	5%	5%	5%	5%
Topol. sel. efficiency	7%	7%	7%	7%
Tracking efficiency	5%	5.5%	6%	6%
PID efficiency	7%	7%	7%	7%
MC p_{T} shape	3%	3%	2%	2%
Feed-down from B	$^{+4.1\%}_{-4.6\%}$	$^{+3.7\%}_{-4.7\%}$	$^{+3.8\%}_{-4.8\%}$	$^{+4.0\%}_{-4.8\%}$
Luminosity	3.5%			
BR	3.5%			

TABLE 4.5: Relative systematic uncertainties on the p_{T}-differential production cross section of prompt $\mathrm{D_s}$ mesons.

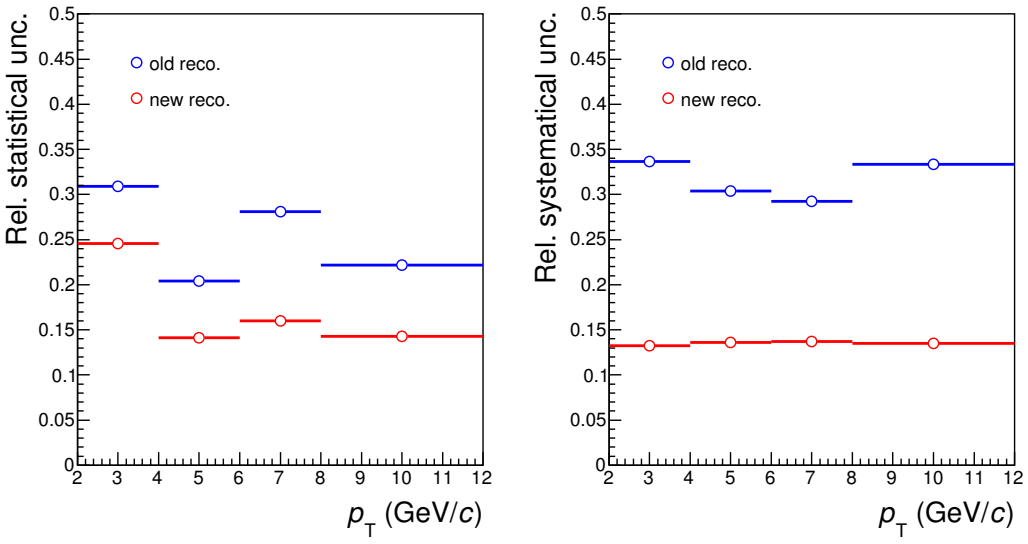

FIGURE 4.30: Comparison of statistical and global systematic uncertainty on $\mathrm{D_s^+}$-meson cross section in the new analysis [43] and in the publication based on the old reconstruction.

The values of the systematic uncertainties estimated according to the procedures discussed above are summarised in Table 4.5. The $\mathrm{D_s^+}$-meson production cross-section normalisation has also a further normalisation uncertainty due to the 3.5% uncertainty on the luminosity [28] and to the uncertainty on the branching ratio of the considered decay channel (2.27 ± 0.08 %). The systematic uncertainty on the luminosity originates from the uncertainty in the determination of the cross section of the

minimum-bias trigger that was measured by means of the van der Meer scan technique [203]. In Fig. 4.30 the values of statistical and global systematic uncertainties of D_s-meson cross-section are shown as a function of p_T and compared to values from the analysis of previous reconstruction of this sample. The statistical uncertainties are reduced due to a 20% larger integrated luminosity of the sample. The improvement of a factor of 1.5-2 in the total uncertainty originates from a revision of the treatment of the different sources, which is now more more data-driven.

4.9 Results

4.9.1 D_s^+ p_T-differential cross section

The p_T-differential cross section for prompt D_s production in $|y| < 0.5$ is shown in Fig. 4.31 [43]. The error bars represent the statistical uncertainties, while the systematic uncertainties are shown as boxes around the data points. The symbols are positioned horizontally at the centre of each p_T interval, with the horizontal bars representing the width of the p_T interval. The results are consistent within uncertainties with those reported in the previous publication on charmed-meson cross sections in pp collisions at $\sqrt{s} = 7$ TeV [19, 26], as can be seen in Fig. 4.32, but the total uncertainties (sum in quadrature of statistical and systematic errors) are reduced by a factor 1.5-2, depending on the the p_T interval. The measured p_T-differential cross section is also compared with results from perturbative QCD calculations with the GM-VFNS [189, 187, 188] and leading-order (LO) k_T-factorisation [197] approaches. The results of these calculations, performed in the same p_T intervals of the measurement, are shown as filled boxes spanning the theoretical uncertainties and a solid line representing the values obtained with the central values of the pQCD parameters. The theoretical uncertainties are estimated in the two frameworks by varying the renormalisation

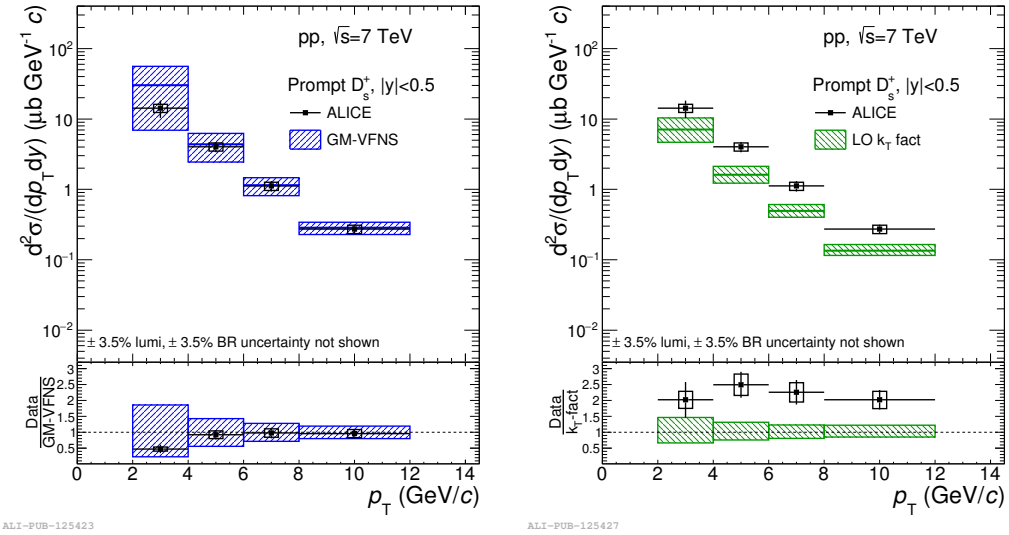

FIGURE 4.31: p_T-differential production cross section of prompt D_s^+ mesons with $|y| < 0.5$ in the interval $2 < p_T < 12$ GeV/c, in pp collisions at $\sqrt{s} = 7$ TeV [43]. The cross section is compared to two pQCD calculations: GM-VFNS [188] (left panel) and a leading order (LO) calculation based on k_T-factorisation [197] (right panel).

and factorisation scales. In k_{T}-factorisation calculations also the effect of the charm-quark mass uncertainty is considered. In the GM-VFNS calculations, the CTEQ6.6 PDFs [225] were used. The LO k_{T}-factorisation calculations were performed with an updated set of unintegrated gluon-distribution functions computed from the recent MMHT2014-LO PDFs [169]. The GM-VFNS calculations describe the data within uncertainties for $p_{\mathrm{T}} > 4$ GeV/c, while in the interval $2 < p_{\mathrm{T}} < 4$ GeV/c the predictions overestimate the measured production cross sections. The central value of the LO k_{T}-factorisation predictions lies systematically below the data.

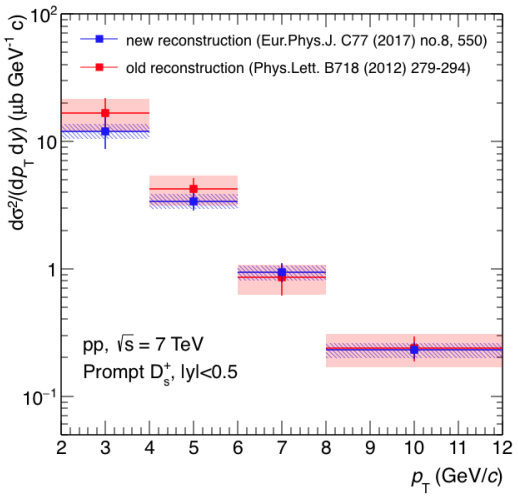

FIGURE 4.32: Comparison of p_{T}-differential production cross section of prompt $\mathrm{D_s^+}$ mesons in pp collisions at $\sqrt{s} = 7$ TeV, $|y| < 0.5$, with the first [26] and second [43] reconstruction.

4.9.2 p_{T}-differential D-meson ratios

The ratios of the p_{T}-differential cross sections of $\mathrm{D^0}$, $\mathrm{D^+}$, $\mathrm{D^{*+}}$ and $\mathrm{D_s}$ mesons are reported in Fig. 4.33 [43]. In the evaluation of the systematic uncertainties on these ratios, the sources of correlated and uncorrelated systematic effects were treated separately. In particular, the contributions of the yield extraction and cut efficiency were considered as uncorrelated among the mesons, while those of feed-down from beauty-hadron decays and tracking efficiency were treated as fully correlated among the different D-meson species. The measured D-meson ratios do not show a significant p_{T} dependence within the experimental uncertainties, thus suggesting a small difference between the fragmentation functions of charm quarks to pseudoscalar ($\mathrm{D^0}$, $\mathrm{D^+}$ and $\mathrm{D_s^+}$) and vector ($\mathrm{D^{*+}}$) mesons and to strange and non-strange mesons. The data are compared to the ratios of the D-meson cross sections from FONLL (only for $\mathrm{D^0}$, $\mathrm{D^+}$ and $\mathrm{D^{*+}}$ mesons), GM-VFNS and LO k_{T}-factorisation pQCD calculations. The ratios of the theoretical predictions were computed assuming their uncertainties to be fully correlated among the D-meson species, which results in an almost complete cancellation of the uncertainties in the ratio. Note that in all these pQCD calculations, the relative abundances of the different D-meson species are not predicted by the theory, but the fragmentation fractions, $f(\mathrm{c} \to \mathrm{D})$, are taken from the experimental

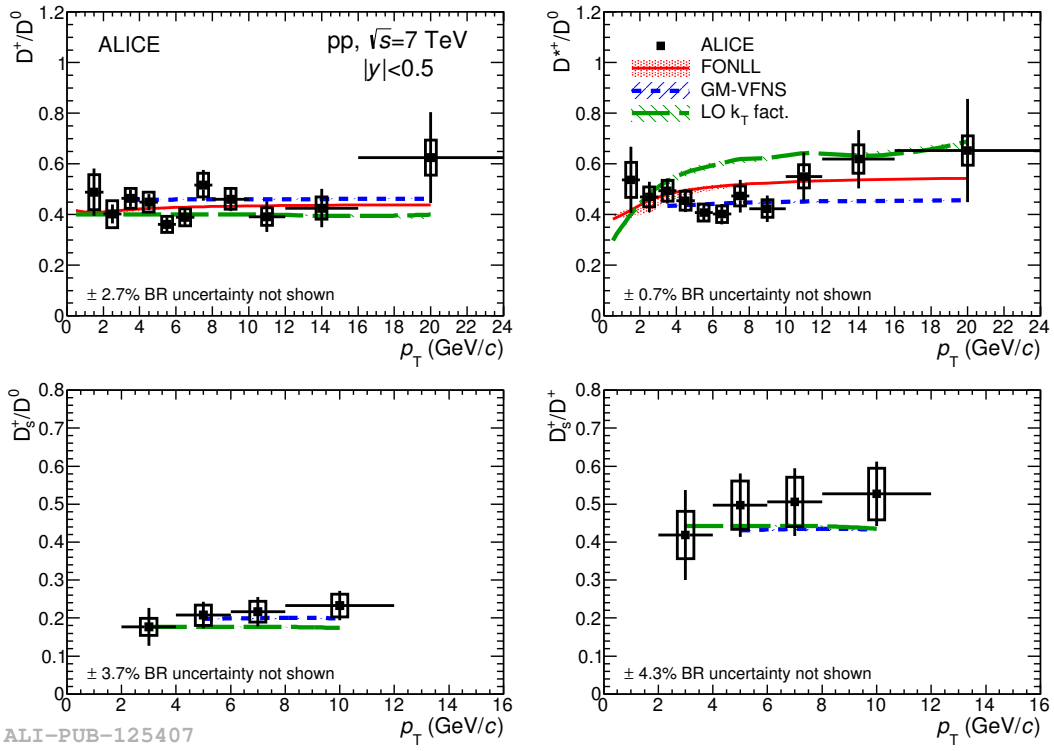

FIGURE 4.33: Ratios of D-meson production cross sections as a function of p_{T} [43]. Predictions from FONLL, GM-VFNS and LO k_{T}-factorisation calculations are also shown. For the pQCD calculations the line shows the ratio of the central values of the theoretical cross sections, while the shaded area is defined by the ratios computed from the upper and lower limits of the theoretical uncertainty band.

measurements [186, 123, 121, 197, 96, 161]. In the FONLL and GM-VFNS frameworks, the p_{T} dependence of the ratios of the D-meson production cross sections arises from the different fragmentation functions used to model the transfer of energy from the charm quark to a specific D-meson species [121, 186, 190], and from the different contributions from decays of higher excited states. The parton fragmentation models used in the calculations provide an adequate description of the measured data. In the LO k_{T}-factorisation calculations, the same fragmentation function (Peterson [216]) is used for D^0, D^+ and D_s^+ mesons, resulting in the same shape of the p_{T} distributions of these three meson species, while the fragmentation functions for vector mesons from Ref. [111] are used for D^{*+} mesons [197].

4.9.3 p_{T}-integrated D_s^+ cross section

The visible cross section of prompt D_s^+ mesons, obtained by integrating the p_{T}-differential cross section in the measured p_{T} range, is reported in Table 4.6. The

	Kinematic range	Visible cross section (μb)
D_s^+	$2 < p_{\mathrm{T}} < 12$ GeV/c	$40 \pm 8(\mathrm{stat}) \pm 5(\mathrm{syst}) \pm 1(\mathrm{lumi}) \pm 1(\mathrm{BR})$

TABLE 4.6: Visible production cross sections of prompt D_s^+ mesons in $|y| < 0.5$ in pp collisions at $\sqrt{s} = 7$ TeV.

systematic uncertainty was defined by propagating the yield extraction uncertainties as uncorrelated among the four $p_{\rm T}$ intervals of the measurements and all the other uncertainties as correlated.

The production cross section per unit of rapidity, $\mathrm{d}\sigma/\mathrm{d}y$, at mid-rapidity was computed by extrapolating the visible cross section to the full $p_{\rm T}$ range. The extrapolation factor was defined as the ratio between the total production cross section in $|y| < 0.5$ and that in the experimentally covered phase space, both of them calculated with the FONLL central parameters. Since for $\mathrm{D_s^+}$ mesons a FONLL prediction is not available, the central value of the extrapolation factor was computed from the prediction based on the $p_{\rm T}$-differential cross section of charm quarks from FONLL, the fractions $f(\mathrm{c} \to \mathrm{D_s^+})$ and $f(\mathrm{c} \to \mathrm{D_s^{*+}})$ from ALEPH [96], and the fragmentation functions from [111], which have one parameter, r, that was set to 0.1 as done in FONLL [121]. The $\mathrm{D_s^{*+}}$ mesons produced in the c-quark fragmentation were made to decay with PYTHIA and the resulting $\mathrm{D_s^+}$ mesons were summed to the primary ones to obtain the prompt yield. The systematic uncertainty on the extrapolation factor was estimated by considering the contributions due to i) the uncertainties on the CTEQ6.6 PDFs [225] and ii) the variation of the charm-quark mass and the renormalisation and factorisation scales in the FONLL calculation, as proposed in [123]. An additional contribution to the systematic uncertainty was assigned based on the envelope of the results obtained using the FONLL $p_{\rm T}$-differential cross sections of $\mathrm{D^0}$, $\mathrm{D^+}$ and $\mathrm{D^{*+}}$ mesons to compute the $\mathrm{D_s^+}$ extrapolation factor. The resulting values for the extrapolation factor and for the prompt $\mathrm{D_s^+}$-meson production cross section per unit of rapidity $\mathrm{d}\sigma/\mathrm{d}y$ are reported in Table 4.7.

	Extr. factor to $p_{\rm T} > 0$	$\mathrm{d}\sigma/\mathrm{d}y\,\vert_{\vert y\vert<0.5}$ (μb)
$\mathrm{D_s}$	$2.23^{+0.71}_{-0.65}$	$89 \pm 18(\mathrm{stat}) \pm 11(\mathrm{syst}) \pm \ \ 3(\mathrm{lumi}) \pm 3(\mathrm{BR})^{+28}_{-26}(\mathrm{extrap})$

TABLE 4.7: Production cross sections of prompt $\mathrm{D_s^+}$ mesons in $|y| < 0.5$ and full $p_{\rm T}$ range in pp collisions at $\sqrt{s} = 7$ TeV.

4.9.4 $p_{\rm T}$-integrated D-meson ratios

The $\mathrm{D_s^+}$ and non-strange D-meson integrated cross-sections values, in Tab. 4.6 and in [43] respectively, were used to compute the ratios of the $p_{\rm T}$-integrated D-meson production cross sections, which are reported in Table 4.8. The systematic uncertainties on the ratios were computed taking into account the sources correlated and uncorrelated among the different D-meson species as described in Sec. 4.9.2. The measured ratios are compatible within uncertainties with the results at $\sqrt{s} = 2.76$ TeV [27] and with the measurements of the LHCb collaboration at forward rapidity ($2.0 < y < 4.5$) at three different collision energies $\sqrt{s} = 5$, 7 and 13 TeV [9, 12, 11]. The measured $p_{\rm T}$-integrated production ratios are also compatible with the charm-quark fragmentation fractions $f(\mathrm{c} \to \mathrm{D})$ measured in $\mathrm{e^+e^-}$ collisions from the compilation in [161]. These results indicate that the fragmentation fractions of charm quarks into different D-meson species do not substantially vary with rapidity, collision energy and colliding system.

	Kinematic range	Production cross section ratio
$\sigma(D^+)/\sigma(D^0)$	$1 < p_T < 24$ GeV/c	$0.45 \pm 0.04(\text{stat}) \pm 0.05(\text{syst}) \pm 0.01(\text{BR})$
$\sigma(D^{*+})/\sigma(D^0)$	$1 < p_T < 24$ GeV/c	$0.52 \pm 0.07(\text{stat}) \pm 0.05(\text{syst}) \pm 0.01(\text{BR})$
$\sigma(D_s)/\sigma(D^0)$	$2 < p_T < 12$ GeV/c	$0.19 \pm 0.04(\text{stat}) \pm 0.02(\text{syst}) \pm 0.01(\text{BR})$
$\sigma(D_s)/\sigma(D^+)$	$2 < p_T < 12$ GeV/c	$0.45 \pm 0.09(\text{stat}) \pm 0.06(\text{syst}) \pm 0.02(\text{BR})$

TABLE 4.8: Ratios of the measured p_T-integrated cross sections of prompt D mesons in $|y| < 0.5$ in pp collisions at $\sqrt{s} = 7$ TeV.

Chapter 5

$\mathrm{D_S^+}$ production in Pb-Pb collisions at $\sqrt{s} = 5.02$ TeV

In this Chapter the measurements of the p_{T}-differential yield, the nuclear modification factor and the elliptic flow of $\mathrm{D_s^+}$ mesons in Pb-Pb collisions at $\sqrt{s_{\mathrm{NN}}} = 5.02$ TeV will be presented. Data were collected during the LHC Run 2 in 2015 and recorded with a minimum-bias interaction trigger that required coincident signals in both scintillator arrays of the V0 detector. Events produced by the interaction of the beams with residual gas in the vacuum pipe were rejected offline using the V0 and the ZDC timing information. Only events with a reconstructed primary vertex within ±10 cm from the centre of the ITS detector along the beam line were analysed. The centrality classes used in the analysis, the corresponding average nuclear overlap functions $\langle T_{\mathrm{AA}} \rangle$ [127] and the number of events (N_{events}) in each class are summarised in Table 5.1. The corresponding integrated luminosity is $L_{\mathrm{int}} = 13.04 \pm 0.4\ \mu\mathrm{b}^{-1}$.

Centrality class	$\langle T_{\mathrm{AA}} \rangle$ (mb^{-1})	N_{events}
0–10%	23.4 ± 0.8	10.4×10^6
30–50%	3.76 ± 0.13	20.8×10^6
60–80%	0.417 ± 0.026	20.8×10^6

TABLE 5.1: Average nuclear overlap function and number of events for the three centrality classes used in the analysis.

For sake of clarity, I will start with the description of p_{T}-differential yields and R_{AA} analyses and move to the analysis of elliptic flow in the second part of the Chapter. The results of the measurements will be discussed together in Sec. 5.7.

5.1 $\mathrm{D_s^+}$ p_{T}-differential yields

5.1.1 Signal extraction

$\mathrm{D_s^\pm}$ mesons in Pb-Pb collisions were reconstructed and selected with the same strategy adopted in the analysis of pp collisions (see Sec. 4.2). The differences with respect to the analysis performed in proton-proton collisions are due to the much larger combinatorial background that is a consequence of the very high particle multiplicity in heavy-ion collisions. In particular, in the Pb-Pb analysis, stricter selections on the tracks used to build the $\mathrm{D_s^\pm}$ candidates and on the geometrical selections on the displaced decay vertex topology were applied. The stricter selections on the decay tracks contributed also to reduce the computing resources needed to build and store the candidates.

In Tables 5.2, 5.3 and 5.4, the topological selections applied in the 0-10%, 30-50% and 60-80% centrality classes to extract the raw yields in different p_T intervals are reported. Tighter cuts are needed for most central events due the larger amount of background. To give an idea, there are $\sim 260 \cdot 10^9$ D_s candidates for the 10.4M events in the 0-10% centrality class after a first loose filtering selection, i.e. before the optimised topological selection. This number reduces to $\sim$ 113M candidates after the selection cuts.

The PID selection is the same used in the analysis of pp collisions and is described in Sec. 4.5. It considers a track to be compatible with the kaon or pion hypothesis if both its dE/dx and time-of-flight are within 3σ from the expected values. Tracks without a TOF signal (mostly at low momentum) are identified using only the TPC information and requiring a 2σ compatibility with the expected dE/dx. This selection was used for $p_T < 8\,\mathrm{GeV}/c$ in the 0-10% and 30-50% centrality classes. and for the most peripheral 60-80% class at all p_T. For the high p_T regions in the 0-10% and 30-50% classes, the looser PID selection introduced in Sec. 4.8.3 was applied since it provided good values of statistical significance of the extracted yields.

p_T (GeV/c)/variable	[4,6]	[6,8]	[8,12]	[12,16]
Decay length (μm)	>500	>500	>400	>400
Decay length XY (μm)	>500	>500	>400	>400
Norm Decay length XY	>9.0	>9.0	>6.0	>8.0
Cosine pointing	>0.995	>0.99	>0.98	>0.99
Cosine pointing XY	>0.995	>0.99	>0.98	>0.99
σ_{vertex} (cm)	<0.025	<0.030	<0.025	<0.025
ΔM (MeV/c^2)	<6.0	<5.0	<4.0	<4.0
$\cos\theta^*(\pi)$	<0.80	<1.00	<0.80	<0.90
$\lvert\cos^3\theta'(\mathrm{K})\rvert$	>0.20	>0.10	>0.20	>0.10
Norm. IP residual	<1.0	<2.0	<2.0	<2.5

TABLE 5.2: List of the topological selections applied for the D_s analysis in 0-10% centrality class.

p_T (GeV/c)/variable	[4,6]	[6,8]	[8,12]	[12,16]
Decay length (μm)	>500	>500	>500	>400
Decay length XY (μm)	>500	>500	>500	>300
Norm Decay length XY	>8.0	>7.0	>6.0	>5.0
Cosine pointing	>0.99	>0.98	>0.98	>0.98
Cosine pointing XY	>0.99	>0.98	>0.98	>0.98
σ_{vertex} (cm)	<0.020	<0.02	<0.025	<0.020
ΔM (MeV/c^2)	<5.0	<5.0	<5.0	<5.0
$\cos\theta^*(\pi)$	<0.70	<0.85	<0.85	<0.75
$\lvert\cos^3\theta'(\mathrm{K})\rvert$	>0.15	>0.10	>0.15	>0.00
Norm. IP residual	<1.5	<2.5	<2.5	<2.5

TABLE 5.3: List of the topological selections applied for the D_s analysis in 30-50% centrality class.

p_T (GeV/c)/variable	[2,4]	[4,6]	[6,8]	[8,12]	[12,16]
Decay length (μm)	>300	>400	>400	>500	>400
Decay length XY (μm)	>300	>400	>400	>500	>400
Norm Decay length XY	>7.0	>6.0	>8.0	>4.0	>1.0
Cosine pointing	>0.99	>0.98	>0.98	>0.97	>0.995
Cosine pointing XY	>0.99	>0.98	>0.98	>0.97	>0.995
σ_{vertex} (cm)	<0.030	<0.030	<0.025	<0.015	<0.030
ΔM (MeV/c^2)	<5.0	<10.0	<7.0	<10.0	<5.0
$\cos\theta^*(\pi)$	<0.70	<0.80	<1.00	<1.00	<1.00
$\lvert\cos^3\theta'(\mathrm{K})\rvert$	>0.05	>0.00	>0.00	>0.00	>0.00
Norm. IP residual	<3.0	<3.0	<3.0	<5.0	<2.5

TABLE 5.4: List of the topological selections applied for the D_s analysis in 60-80% centrality class.

The D_s signal in the 0-10% and 30-50% centrality classes was extracted in four p_T intervals in the transverse momentum region $4 < p_T < 16\,\mathrm{GeV}/c$, while the lower limit was extended down to 2 GeV/c for the 60-80% class. Figures 5.1, 5.2 and 5.3 show the signal extraction from fits to the invariant-mass histograms, in the analysed p_T intervals for the 0-10%, 30-50% and 60-80% centrality classes respectively. The distributions were fitted with two Gaussian functions to model the D_s peak and that of $D^+ \to K^+K^-\pi^+$ decays, with BR = (0.264±0.011%), which gives rise to a bump in the background shape around 1.870 GeV/c^2. The position and width of the Gaussian function used to fit the D^+ peak were fixed respectively to the D^+ invariant mass from PDG and to the value of the width from the simulations. An exponential function was used to model the background. The $D_s^\pm$ raw yield (sum of particles and anti-particles) is defined as the integral of the Gaussian function after subtracting the background calculated from the background fit function. The values of raw yields, statistical significance and signal over background are reported in Tab. 5.5 for the analysed p_T intervals and in the three centrality classes. In Fig. 5.4 the values of the Gaussian mean and width of D_s peak line shape are compared to the values obtained from the simulation, as a function of p_T, in the three considered centrality classes.

p_T (GeV/c)	0-10%			30-50%			60-80%		
	Raw yield	Signif	S/B	Raw yield	Signif	S/B	Raw yield	Signif	S/B
[2,4]	-	-	-	-	-	-	42 ± 12	3.6	0.47
[4,6]	175 ± 32	5.4	0.20	141 ± 26	6.0	0.35	113 ± 17	6.6	0.63
[6,8]	195 ± 36	5.1	0.16	162 ± 30	5.9	0.28	33 ± 7	5.1	3.08
[8,12]	137 ± 28	5.1	0.23	137 ± 18	8.0	0.86	40 ± 7	5.5	2.95
[12,16]	40 ± 8	5.1	1.90	56 ± 11	5.8	1.57	16 ± 5	3.3	2.10

TABLE 5.5: D_s raw yields (sum of particles and anti-particles), statistical significance and signal over background per p_T interval for the three analysed centrality classes.

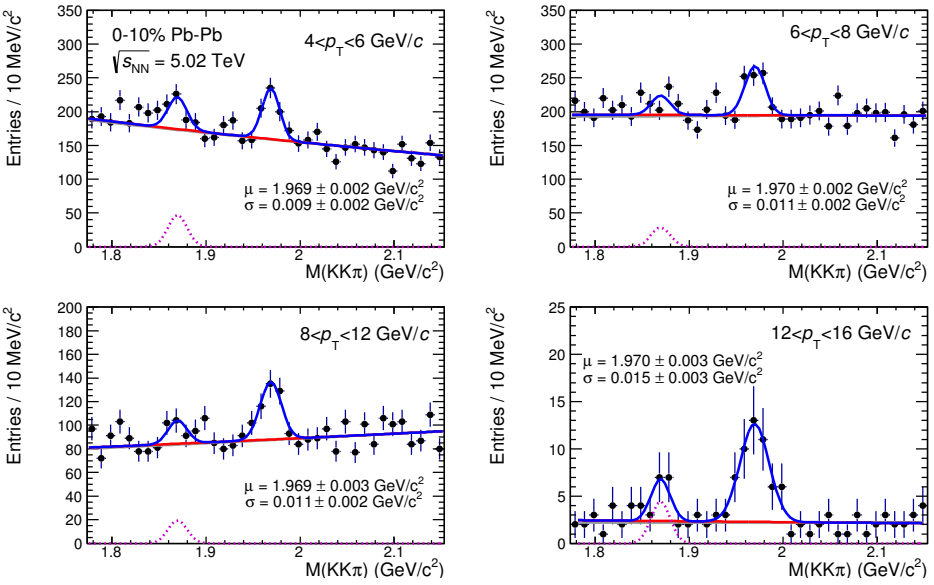

FIGURE 5.1: Fits to the invariant-mass distribution of $D_s^+ \to K^+K^-\pi^+$ candidates (and charge conjugates) in the four p_T intervals between $4 < p_T < 16\,\mathrm{GeV}/c$ in the 0-10% centrality class.

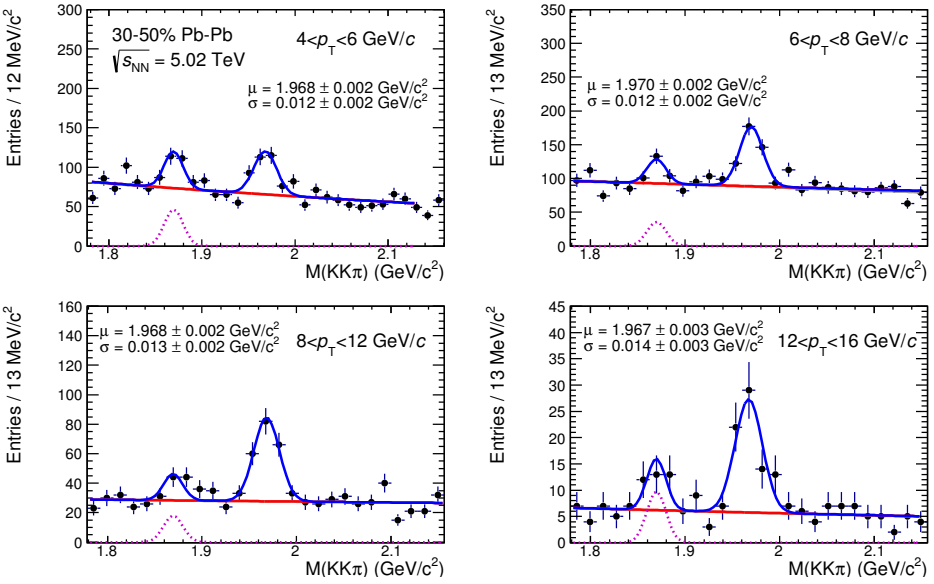

FIGURE 5.2: Fits to the invariant-mass distribution of $D_s^+ \to K^+K^-\pi^+$ candidates (and charge conjugates) in the four p_T intervals between $4 < p_T < 16\,\mathrm{GeV}/c$ in the 30-50% centrality class.

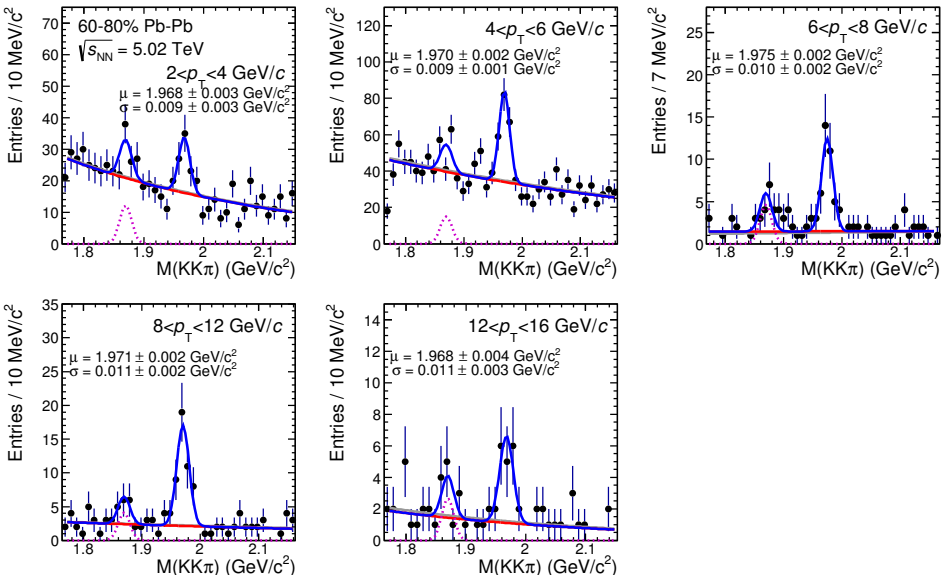

FIGURE 5.3: Fits to the invariant-mass distribution of $\mathrm{D_s^+} \to \mathrm{K^+K^-}\pi^+$ candidates (and charge conjugates) in the five p_T intervals between $2 < p_\mathrm{T} < 16\,\mathrm{GeV}/c$ in the 60-80% centrality class.

5.1.2 Corrections

The $\mathrm{D_s^\pm}$-meson raw yields were corrected in order to obtain the p_T-differential yields of prompt $\mathrm{D_s^+}$ mesons:

$$\left.\frac{\mathrm{d}N^{\mathrm{D_s^+}}}{\mathrm{d}p_\mathrm{T}}\right|_{|y|<0.5} = \frac{f_\mathrm{prompt}(p_\mathrm{T}) \cdot \frac{1}{2} N_\mathrm{raw}^{\mathrm{D_s^\pm}}(p_\mathrm{T})\Big|_{|y|<y_\mathrm{fid}}}{\Delta p_\mathrm{T} \cdot C_{\Delta y} \cdot (\mathrm{Acc} \times \epsilon)_\mathrm{prompt}(p_\mathrm{T}) \cdot \mathrm{BR} \cdot N_\mathrm{events}} \,. \tag{5.1}$$

The difference with respect to Eq. 4.3 is that the raw yields $N_\mathrm{raw}^{\mathrm{D_s^\pm}}$ were divided by the number of events (N_events), to obtain a $\mathrm{d}N^{\mathrm{D_s^+}}/\mathrm{d}p_\mathrm{T}$, instead of the integrated luminosity, used in Eq. 4.3 to obtain a $\mathrm{d}\sigma^{\mathrm{D_s^+}}/\mathrm{d}p_\mathrm{T}$. The raw yields $N_\mathrm{raw}^{\mathrm{D_s^\pm}}$ were also divided by a factor of two to obtain the charge-averaged (particle and antiparticle) yields. To correct for the contribution of feed-down from B-meson decays, the raw yields were multiplied by the fraction of promptly produced D mesons, f_prompt. Furthermore, they were divided by the product of prompt D-meson acceptance and efficiency $(\mathrm{Acc} \times \epsilon)_\mathrm{prompt}$, by the branching ratio BR of the decay channel and by the transverse momentum interval width (Δp_T). The rapidity acceptance correction factor $C_{\Delta y} = 2y_\mathrm{fid}(p_\mathrm{T})$ was calculated as described in Sec. 4.7.

The correction for acceptance and efficiency $(\mathrm{Acc} \times \epsilon)_\mathrm{prompt}$ was determined using Monte Carlo simulations with a detailed description of the detector and its response, based on the GEANT3 transport package [115]. The underlying Pb–Pb events at $\sqrt{s_\mathrm{NN}} = 5.02$ TeV were simulated using the HIJING v1.383 generator [255] and D-meson signals were added with the PYTHIA v6.421 generator [243] with Perugia-2011 tune. Each simulated PYTHIA event contained a $\mathrm{c\overline{c}}$ or $\mathrm{b\overline{b}}$ pair. Only the particles originating from the fragmentation of c ($\bar{c}$) and b ($\bar{b}$) quarks were injected in the event. D mesons were forced to decay into the hadronic channels of interest for the analysis. The number of $c\bar{c}$ pairs added to each Pb-Pb event was adjusted according

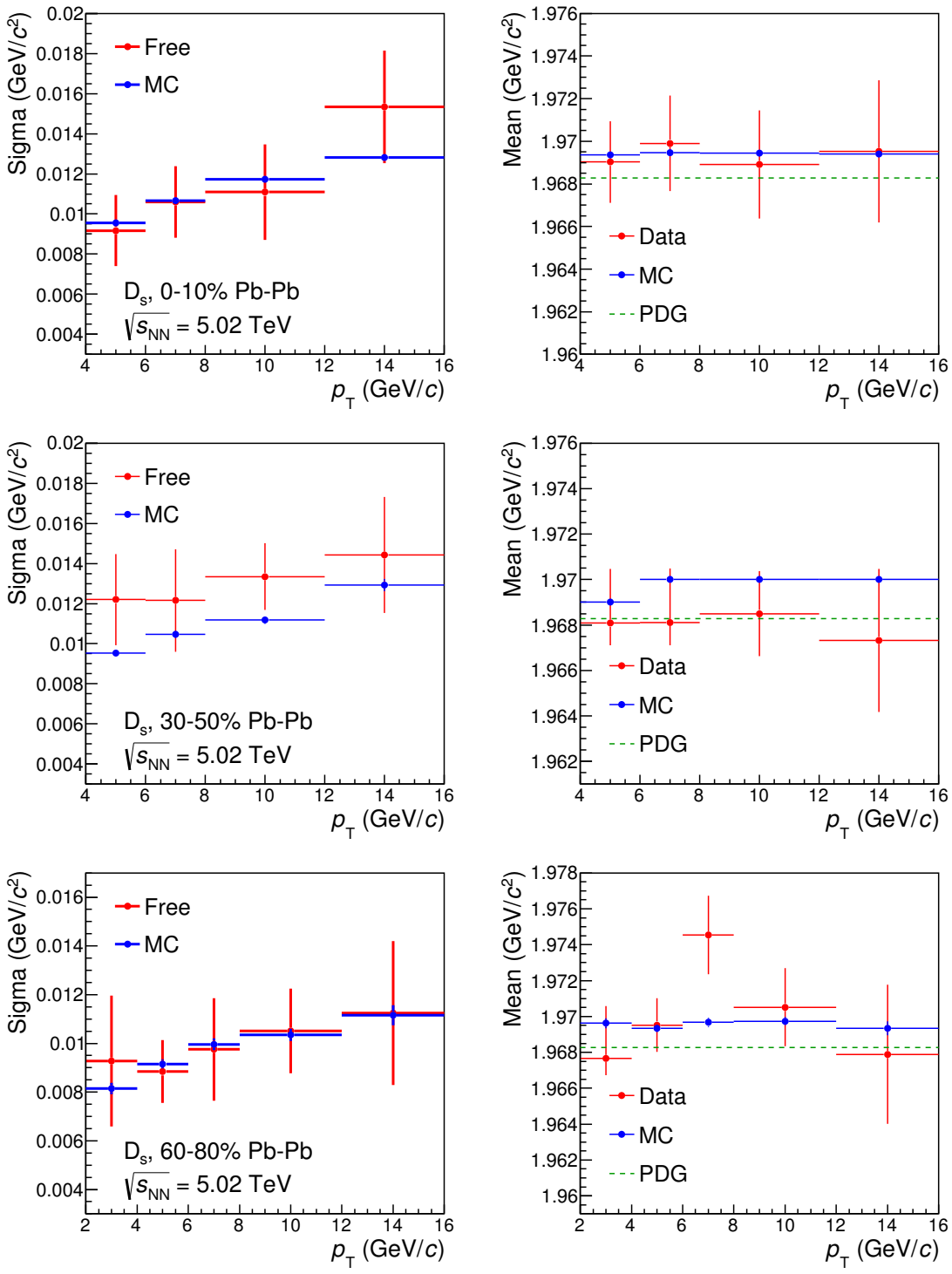

FIGURE 5.4: Gaussian width (left) and mean (right) of the D_s signal peak and as a function of p_T: values in data (red) are compared to values in MC (blue). For the peak position, also the PDG value of D_s^+ meson mass (green) is shown.

to the Pb-Pb collision centrality. The efficiencies were evaluated in a centrality class corresponding to the one used in data in terms of charged particle multiplicity in the mid-rapidity region, hence of the detector occupancy. In the most central event

class, the generated p_T distribution of D_s mesons was tuned utilising a re-weighting procedure in order to match the shape measured for D^0 mesons in finer p_T intervals. In the other two centrality classes, where an analysis of D^0-meson yield in finer p_T intervals was not possible, the simulated D_s-meson p_T distribution was weighted to match the shape given by fixed-order next-to-leading-log perturbative QCD calculations (FONLL) [120, 119] multiplied by the $R_{AA}(p_T)$ of D mesons computed using the BAMPS model for semi-central collisions [251, 153, 252]. Figure 5.5 shows the acceptance-times-efficiency corrections for prompt and feed-down D_s mesons in the three centrality classes. Some of the topological selections (decay length, normalised decay length and their projections on the transverse plane) tend to reject less feed-down due to the larger decay length with respect to the prompt D mesons. Other topological cuts, like the one on the normalised track-impact parameter residual,

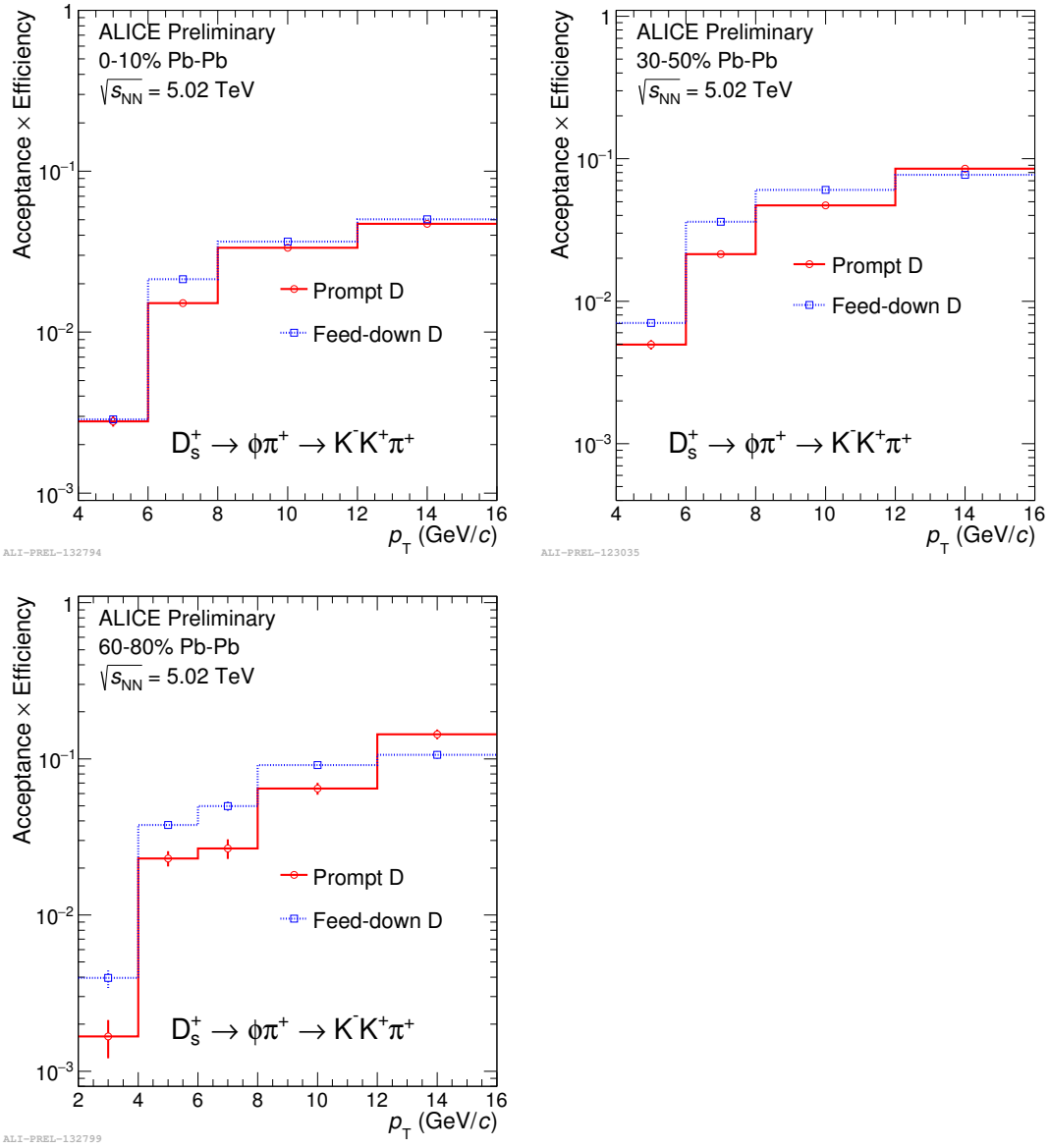

FIGURE 5.5: Acceptance times efficiency for D_s mesons in the three centrality classes, as a function of p_T, for prompt (red) and feed-down (blue) components.

are more effective in rejecting the feed-down component, allowing higher prompt efficiencies at high p_T. The reconstruction and selection efficiencies for prompt and feed-down D_s mesons in Pb-Pb collisions are smaller than the results in pp collisions up to a factor of 3 as a consequence of the tighter topological selections applied.

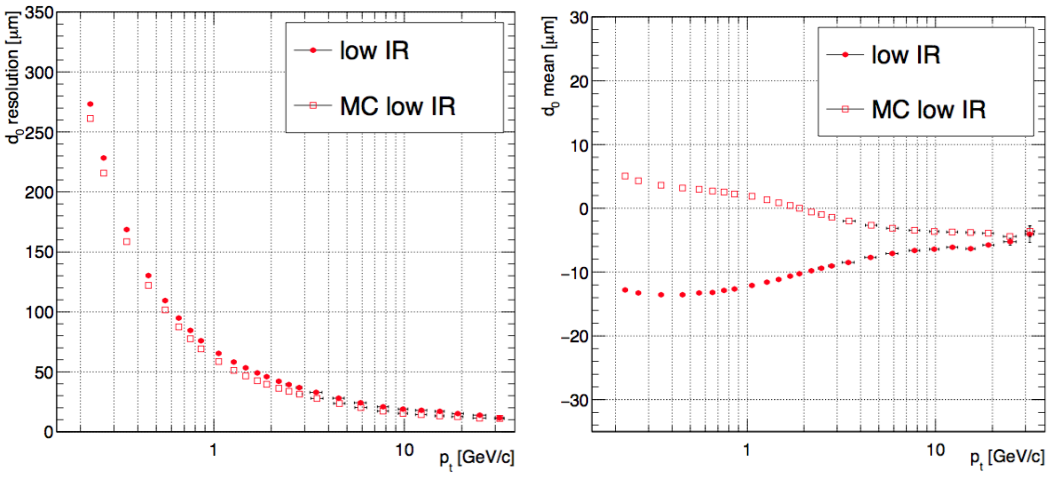

FIGURE 5.6: Impact parameter resolution in the transverse plane (left) and mean value (right) in 2015 Pb-Pb data taking at $\sqrt{s_{NN}} = 5.02$ TeV for low interaction rate runs compared to Monte Carlo simulations.

Figure 5.6 shows the resolution of the impact parameter of reconstructed tracks in the transverse plane (d_0^{xy}), for low interaction rate runs (frequency of collisions $<$ 2kHz) in data and in simulations. The values of the resolution are obtained via a fit to the distributions of d_0^{xy} of charged tracks, in the different p_T intervals. The histograms are fitted by a function consisting of a sum of a Gaussian, to describe the d_0^{xy} of primary particles, and an exponential function for the tails of the distribution, whose main contributors are secondary tracks, that have larger impact parameter values. The position of the Gaussian function should be compatible to 0 if no biases are present, while the width is the resolution on the impact parameter values, which depends on the transverse momentum of the tracks. The values of the impact parameter resolution in data are not fully reproduced in the simulations (see Fig. 5.6, left panel). Furthermore, the impact parameter distribution is shifted to negative values by up to 10-15 micron at low p_T and decreasing to 5-10 micron at high p_T. The shift depends on the azimuthal angle and is not described in the MC (Fig. 5.6, right panel). The information on detector alignment used in the reconstruction of the Pb-Pb sample dates back to early 2015. The observed bias in the simulation has a dependence on the B field polarity and on the time. This suggests that the bias originates from a residual misalignment in the simulation that slightly varies as a function of time. Furthermore, a minor part of the shift is caused by the presence of three SPD modules which were not included in the detector alignment. In order to reduce possible systematic effects arising from these discrepancies between data and simulations, a tuning procedure of the Monte Carlo output was developed. The impact parameter resolution measured in data was reproduced in MC by applying to the tracks of the simulated sample a scaling of the residuals $d_0^{true} - d_0^{reco}$ according to the data-to-MC ratio of the impact parameter resolutions. A shift of d_0^{reco} was also applied to correct for the different bias in MC and in data. The covariance matrix of the track was also

updated after the corrections, in order not to introduce biases at the level of topological variables based on standardised quantities such as the normalised decay length.

The f_prompt factor, which corrects for the contribution of D mesons from B-meson decays in the measured raw yield in each p_T interval, was obtained following the procedure described in Sec 4.7.2. The expression for f_prompt reads:

$$f_\mathrm{prompt} = 1 - \frac{N_\mathrm{raw}^{\mathrm{D\ feed\text{-}down}}}{N_\mathrm{raw}^\mathrm{D}} = 1 - R_\mathrm{AA}^{\mathrm{feed-down}} \cdot \langle T_\mathrm{AA} \rangle \left(\frac{\mathrm{d}^2\sigma}{\mathrm{d}p_\mathrm{T}\mathrm{d}y} \right)_\mathrm{feed\text{-}down}^\mathrm{FONLL} \cdot \frac{(\mathrm{Acc} \times \epsilon)_\mathrm{feed\text{-}down} \cdot \Delta y \Delta p_\mathrm{T} \cdot \mathrm{BR} \cdot L_\mathrm{int}}{N^{\mathrm{D}+\overline{\mathrm{D}},\mathrm{raw}}/2} \,. \tag{5.2}$$

The difference with respect to Eq. 4.4 is that the beauty-hadron production cross section from FONLL pQCD calculations in pp collisions at $\sqrt{s} = 5.02$ TeV [123] is multiplied by the average nuclear overlap function $\langle T_\mathrm{AA} \rangle$ of the corresponding centrality class. In addition, a hypothesis on the nuclear modification factor of feed-down $\mathrm{D_s}$ mesons, $R_\mathrm{AA}^\mathrm{feed\text{-}down}$, was introduced to account for the different modification of beauty and charm production in Pb-Pb collisions. The resulting sample of feed-down $\mathrm{D_s}$ mesons is composed of two contributions: about 50% of the feed-down originates from $\mathrm{B_s^0}$-meson decays, while the remaining 50% comes from decays of non-strange B mesons ($\mathrm{B^0}$ and $\mathrm{B^+}$) (see Fig. 4.29 left). To determine the central value of f_prompt in the 0-10% and 30-50% centrality classes, it was assumed that the nuclear modification factors of feed-down and prompt $\mathrm{D_s}$ mesons were equal ($R_\mathrm{AA}^\mathrm{feed\text{-}down} = R_\mathrm{AA}^\mathrm{prompt}$). The resulting feed-down contribution is about 10%, depending on the p_T interval, as it is shown in Fig. 5.18. To determine the systematic uncertainty, the hypothesis

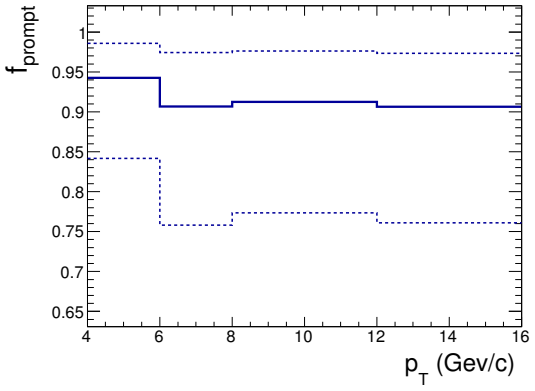

FIGURE 5.7: Prompt fraction of $\mathrm{D_s}$ yield in the 0-10% centrality class as a function of p_T. The dashed lines indicate the uncertainties on f_prompt from FONLL scales and $R_\mathrm{AA}^\mathrm{feed\text{-}down}$ hypothesis.

was varied in the range $1/3 < R_\mathrm{AA}^\mathrm{feed\text{-}down}/R_\mathrm{AA}^\mathrm{prompt} < 3$, as discussed in detail in Section 5.2. It should be noted that the central value and the range of the hypothesis on $R_\mathrm{AA}^\mathrm{feed\text{-}down}/R_\mathrm{AA}^\mathrm{prompt}$ differ from those used for non-strange D mesons in Refs. [222, 58]. The central hypothesis of $R_\mathrm{AA}^\mathrm{feed\text{-}down}/R_\mathrm{AA}^\mathrm{prompt}$ for non-strange D mesons is set at 2 due to the comparison of the R_AA of prompt D mesons at $\sqrt{s_\mathrm{NN}} = 2.76$ TeV [48] with that of J/ψ from B-meson decays [183] measured in the CMS experiment (see Sec. 2.4.4), that indicates that charmed hadrons with $p_\mathrm{T} > 8\,\mathrm{GeV}/c$ are more suppressed than

beauty hadrons in semi-peripheral and central Pb-Pb collisions relative to binary scaled pp collisions. The hypothesis for D_s meson accounts for the possible recombination in the charm and beauty sectors. The contribution of coalescence of charm quarks should enhance the R_{AA} of D_s with respect to that of non-strange D mesons. If recombination does not occur for beauty quarks, the suppression of D_s could result similar to that of B^0, B^+ and B_s^0 mesons. If, on the other hand, recombination plays a role for beauty, the hypothesis on $R_{AA}^{\text{feed-down}}$ accounts for a possible enhancement of the ratio of B_s^0 over non-strange B mesons [171] and for the large fraction of feed-down D_s mesons originating from non-strange B-meson decays. For the peripheral class 60–80%, in which the medium effects are milder, also the difference between charm and beauty mesons is assumed to be reduced: the value $R_{AA}^{\text{feed-down}} = 1.3 \cdot R_{AA}^{\text{prompt}}$ was used for all D-meson species and the range of the hypothesis to estimate the uncertainty was reduced to $0.9 < R_{AA}^{\text{feed-down}}/R_{AA}^{\text{prompt}} < 1.3$.

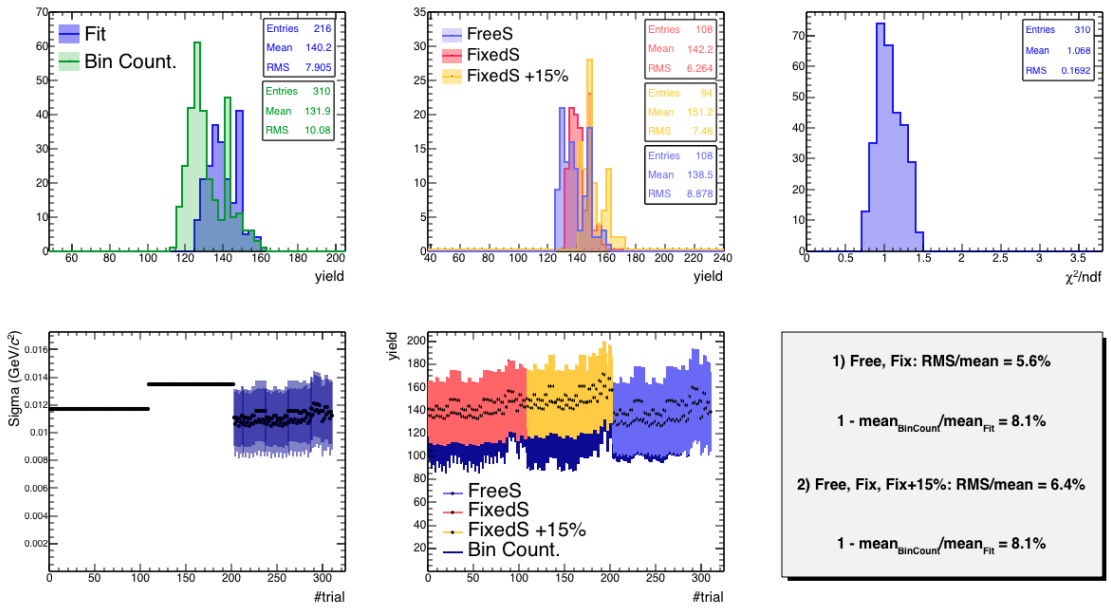

FIGURE 5.8: Output of multiple-trial fits to D_s invariant-mass distributions in the p_T intervals 8-12 GeV/c, for the 0-10% centrality class.

5.2 Systematic uncertainty on corrected dN/dp_T

Most of the sources of systematic uncertainty considered for the analysis of the corrected yields and the methods used to estimate them were already described in Sec. 4.8. Hence in the next sections I will concentrate on the differences with respect to the pp analysis.

5.2.1 Yield extraction systematics

The estimate of the systematic uncertainty on the yield extraction was based on the multiple-trial fit approach described in Sec. 4.8.1 (it is the first approach of the two presented there). Figure 5.8 shows an example of the multiple trial fit procedure on the invariant-mass distribution in the interval $8 < p_T < 12$ GeV/c, for the 0-10%

centrality class. The panels of the figure show, starting from top left plot: (i) the raw yield distributions from the multiple trials, with the histograms obtained via fit and bin counting shown in different colours. The histograms include the cases in which the Gaussian width of the $\mathrm{D_s}$ signal function was left as free parameter in the fit or was fixed to its MC value; (ii) the distributions of raw yields from multiple trials via fit, distinguishing the cases in which the Gaussian width of the $\mathrm{D_s}$ signal function was left as free parameter in the fit, or was fixed to its MC value or fixed to MC value +15% (where 15% is the average underestimate of the width value in MC with respect to data in some p_{T} intervals); (iii) the distribution of the reduced χ^2 of the fits; (iv) the Gaussian width of the peak as a function of the trial number; (v) the raw yield distribution as a function of the trial number; (vi) a panel reporting the Gaussian RMS value (used as estimator of the systematic uncertainty) of the yield distribution in two cases: 1) considering the yields extracted from the fits with the Gaussian sigma left as free parameter in the fit or fixed to its MC values, 2) considering the cases with sigma free, fixed to MC and fixed to MC +15%. The systematic uncertainty was estimated from the RMS of the distribution of yields via fit considering value 1). For those p_{T} intervals where the value of the Gaussian width in simulation underestimates that in data, it was verified that the value 2) of the RMS (i.e. considering also the case of sigma fixed to MC values +15%) was in agreement with the assigned value for the systematic uncertainty. It was also verified that the difference between the mean values of the yield distributions from fit and from bin counting methods was contained within the RMS value quoted as systematic uncertainty (the value is also reported in panel (vi)). The final assigned uncertainties range from 5% to 10% depending on p_{T} and centrality class and are reported in Tab. 5.6.

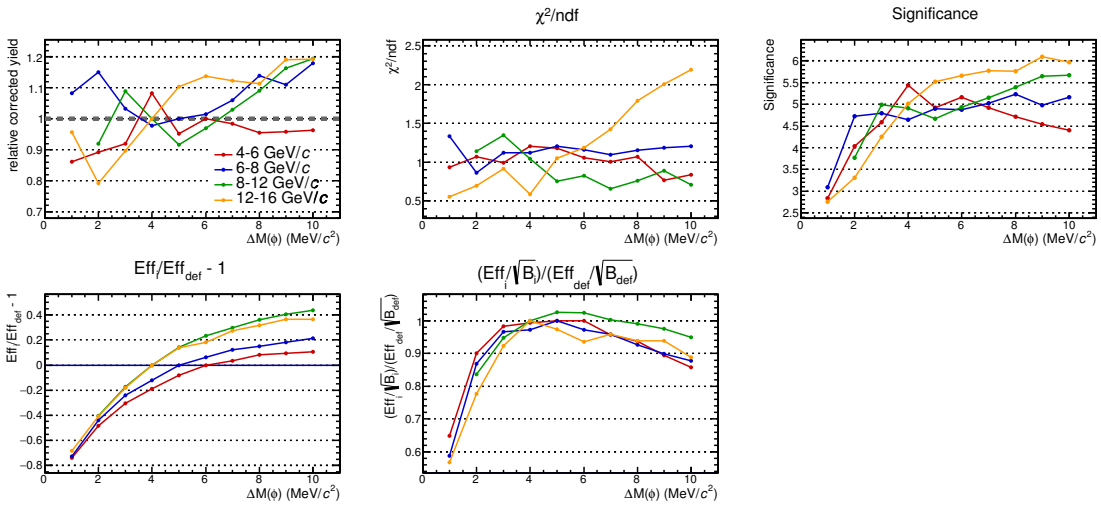

FIGURE 5.9: Distribution of the $\mathrm{D_s}$ relative corrected yields in the 0-10% centrality class, obtained varying the selection on the invariant mass of the reconstructed K^+K^- pair (top left panel). The other panels report the values of reduced χ^2, significance, selection efficiency, selection efficiency divided by the to square root of the background counts.

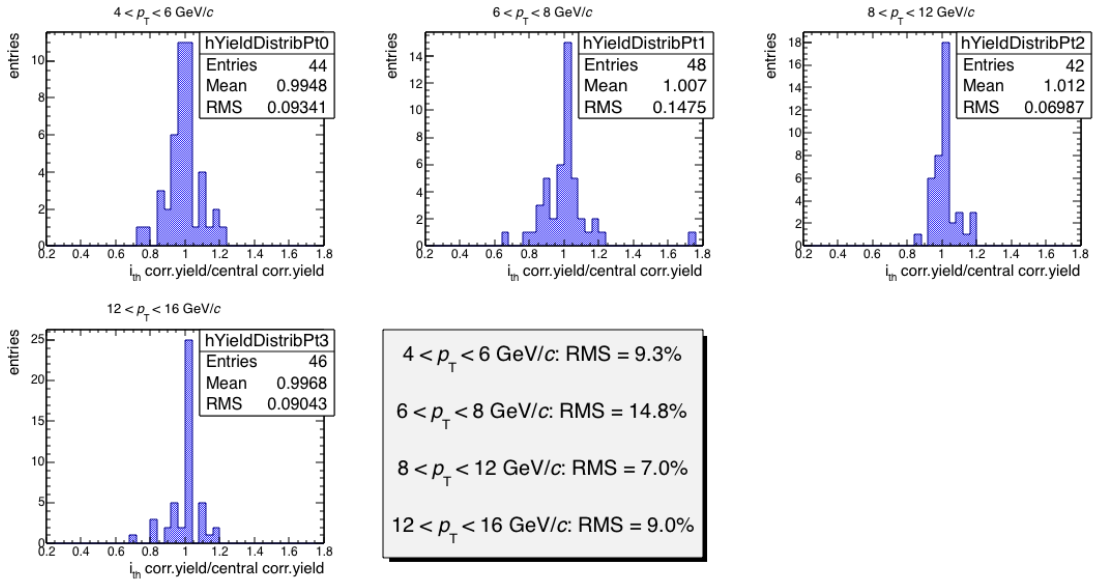

FIGURE 5.10: Distribution of D_s corrected yields in the 0-10% centrality class, from the variation of the selection criteria (on the topological variables and on the invariant mass of the reconstructed K^+K^+ pair) with respect to the default value.

5.2.2 Selection efficiency

The systematic uncertainty on the efficiency of the D_s selection was studied via cut variation procedures, similarly to what done for pp collisions (see Sec. 4.8.2). A systematic scan from looser to tighter cuts was done on a variable-per-variable basis, extracting the raw yields, correcting them with the corresponding efficiency, comparing the corrected yields to those obtained with a reference set of cuts and looking for possible trends/biases of the corrected yield as a function of the cut strength. The study was done using as reference set of cuts the one used to provide the central values of the yields. A selection on the basis of the χ^2/ndf (< 2.5) of the invariant-mass fits and the statistical significance (> 2) of the signal was applied to reject the sets of cuts that were not showing a robust determination of the raw yield. An example of the scan performed on the cut on the reconstructed K^+K^- invariant-mass pair is shown in Fig. 5.9. The top-left panel shows the ratios of the corrected yields (at a specific cut value) to that obtained with the default cut, in different colours for the different p_T intervals. Some systematic deviations from unity of this ratio are visible when the selection on this variable is released with respect to the default cut ($\Delta M <$ 4-6 MeV/c^2 depending on the p_T interval). This behaviour could be due to a systematic effect originating, e.g., from a different p_T resolutions in data and in MC, as well as to a less-reliable extraction of the raw yield in the cases of low S/B ratios with loose selections. The statistical significance (top-right panel) of the signal and the reduced χ^2 (middle-top panel) as a function of the cut value were also considered. The relative variation of the selection efficiencies with respect to that with default set of cuts is shown in the bottom-left panel. Finally, in the bottom-middle panel the ratio of the selection efficiency to the square root of background counts in the interval within 3σ around the peak complements the information from the statistical significance, and it is less affected by possible fluctuations of the signal. Since the values of the reduced χ^2 and of the statistical significance do not allow to reject any set of cuts shown in

Fig. 5.9, the corrected yields associated to the different cuts tested (from the study of ΔM and of all the other topological variables) were collected, for each p_{T} interval, into a global distribution. The RMS value of this distribution provides, in each p_{T} interval, an estimate for the systematic uncertainty. Figure 5.10 shows an example of these final distributions for the 0-10% centrality class, in the four analysed p_{T} intervals. The values of the RMS of the Gaussian distributions are reported in the last panel.

5.2.3 PID selection efficiency

To estimate the systematic uncertainty due to PID efficiency, two particle identification selections (a tighter one, discussed in Sec. 4.5, and a looser, in Sec. 4.8.3) were compared. Figure 5.11 shows, as an example for 0-10% centrality class, the ratio of the corrected yields with looser and tighter PID selections. Due to the large error bars, it is difficult to asses whether the points are affected by a systematic effect or they are dominated by statistical fluctuations. For this reason, an alternative approach of a per-track estimate of the PID systematic was followed. The idea is to select samples of kaon and pion tracks in data and MC.

The difference in the efficiencies for a given Nσ cut (on dE/dx or time-of-flight signal) in data and MC will constitute a p_{T}-dependent per-track systematics for each species.

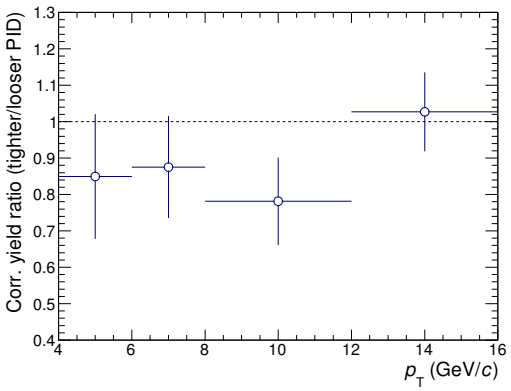

FIGURE 5.11: Ratio of $\mathrm{D_s}$ corrected yield in 0–10% centrality class with tighter-to-looser PID selections.

Pions from $\mathrm{V^0}$ decays were selected using the optimised cuts used in [237]. The term $\mathrm{V^0}$ accounts for the V-shaped track topology of the daughters and 0 stands for the decay of neutral particles. In Fig. 5.12 the Monte Carlo Nσ distributions for the dE/dx of pions in TPC are shown for different p_{T} intervals, from 0.2 to 10 GeV/c. The Nσ distributions of pions (in green) selected utilising the MC truth are compared to the those of tracks passing the selection as pions from $\mathrm{V^0}$ decays (in blue). A peak centred at N$\sigma = 0$ is the dominant contribution for both track samples. A second population (less that 1% of the total) is visible at the right of the peak at low p_{T} in the in the Nσ distribution of pion candidate tracks from $\mathrm{V^0}$ decays. This second population is present also in the Nσ distribution obtained from data and shown in Fig. 5.13 and it is likely a contamination from electrons passing the pion selection criteria. For this reason, only the left side of the peak will be used to study the systematic uncertainty. A part from this small contamination, we conclude that the utilised selections provide a pure enough sample of pions. In Fig. 5.13, the

Nσ distributions in data (blue) are compared to the distributions of true MC pions (green), in the different p_T intervals. Finally, the efficiencies of the Nσ selection in data and in MC are obtained by integrating the corresponding distributions (blue and green distributions in Fig. 5.13) within 1σ, 2σ or 3σ, and normalising these values to the integral of the distributions within 5σ. It was verified that enlarging the number of σ from 5 to 10 at the denominator of the efficiency does not affect the final results. The systematic uncertainty is defined as the relative difference between the efficiencies of the Nσ selection in data and in MC. The same procedure was carried out with the Nσ distributions of the time-of-flight signals for the pions from V^0 decays, to estimate the systematic uncertainty on pion identification with TOF. To obtain the uncertainty on kaon identification in TPC, a tight cut on the PID signal in TOF, requiring the signal to be within N$\sigma < 0.25\sigma$ from the kaon expectation value, was applied. The black curve in Fig. 5.14 shows the Nσ distribution for the dE/dx of simulated tracks that satisfy this selection. Contaminations from other particle species are still present and they are shown in different colours in Fig. 5.14. The black curve was fitted in a region around N$\sigma = 0$ with a Gaussian shape to extract the kaon contribution. The ranges of the fits are set, for each p_T interval, to exclude the regions more affected by contamination from other species. In Fig. 5.15, the distribution of Nσ for dE/dx in data is displayed. The Monte Carlo templates for true kaons (yellow filled histograms) are superimposed to the data distributions, only for visualisation purposes, but they are not used in the fits. The distribution of candidate kaons from the data was fitted with a Gaussian function in the Nσ-axis range previously tuned on the simulation, to extract the kaon distribution, in each p_T interval.
The values of the data-to-MC ratios of the efficiencies estimated with this procedure are shown in Fig 5.16, as a function of p_T, for cuts at 1, 2 and 3σ on the PID signals. Since it is not possible to select a pure sample of kaons to compare the TOF Nσ distributions, an assumption for the systematic uncertainty on kaon identification with the TOF is needed. The same uncertainty estimated for pion identification with TOF is assigned also to kaon identification, based on the observation that the systematic uncertainties on pion and kaon identification with the TPC are similar. The p_T-dependent per-track systematics can be propagated to the D_s-meson level, via the kinematics of the daughter tracks. This was done by assigning to the D_s daughter tracks a PID uncertainty which depends on their p_T. The PID uncertainties of the three daughter tracks were assumed to be fully correlated and were summed linearly. The correlation between the p_T of the daughter track and that of D_s mesons is shown in the left panel of Fig. 5.17. The final values of the systematic uncertainties are around 3% for the tighter (Sec. 4.5) PID selection, utilised for D_s at low p_T in the 0-10% and 30-50% classes and at all p_T in 60-80% (see Fig. 5.17), and are negligible for the looser PID selection, used at high p_T in the 0-10% and 30-50% classes (Sec. 4.8.3).

5.2.4 Generated p_T shape

The systematic effect on the efficiency due to a possible difference between the real and simulated D_s-meson transverse momentum distributions was estimated by using alternative D_s-meson p_T distributions. In particular, the p_T distributions from FONLL calculations with and without hot-medium effects parametrised based on the R_{AA} in central collisions from the TAMU [170] model and in semi-central collisions from BAMPS [250] model were used in this study. The values assigned as systematic uncertainty are reported in Tab. 5.6 for the three centrality classes.

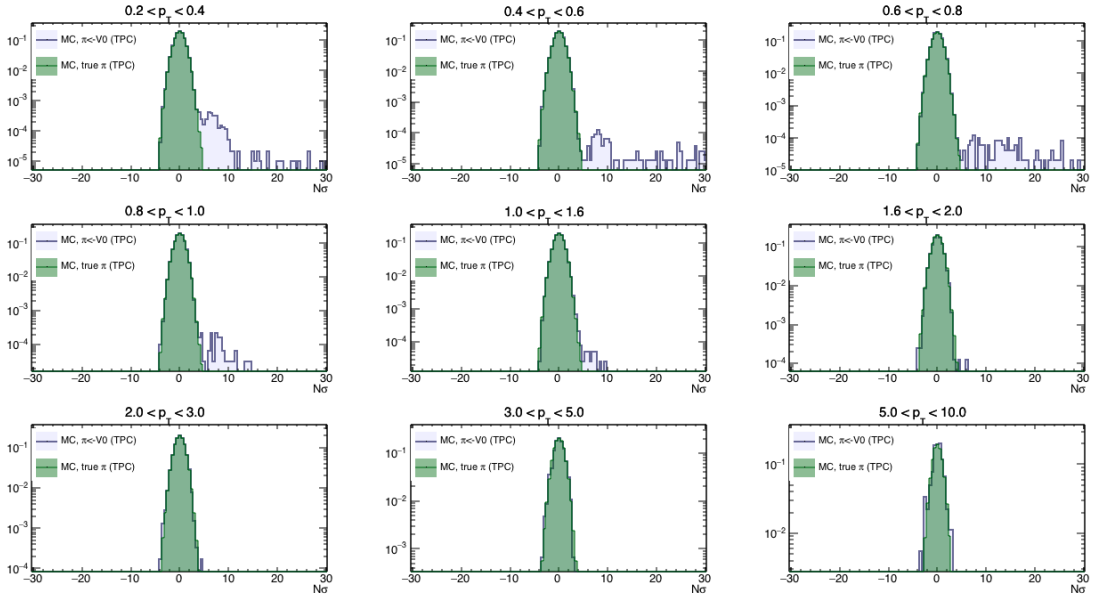

FIGURE 5.12: Nσ distribution of dE/dx signal in TPC for pions in Monte Carlo. In green pions selected by PDG code, in blue tracks passing the selection for pions from V^0 decays.

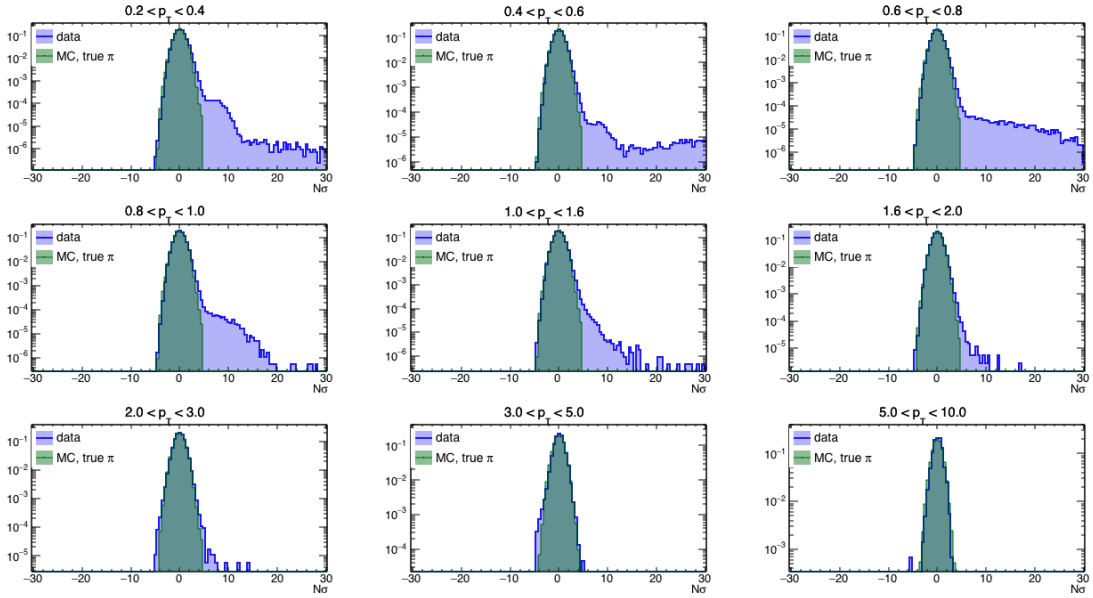

FIGURE 5.13: Nσ distribution of dE/dx signal in TPC for pions in data (blue) and Monte Carlo (green)

5.2.5 Feed-down subtraction

The systematic uncertainty on the correction for the contribution of feed-down from B-meson decays was estimated by varying i) the p_{T}-differential B-meson cross section in the FONLL calculation within the theoretical uncertainties (that originate from variations of b-quark mass, perturbative scales and from uncertainties on the parton distribution functions [123]), ii) the variation of the hypothesis on $R_{\mathrm{AA}}^{\mathrm{feed-down}}/R_{\mathrm{AA}}^{\mathrm{prompt}}$. Several theoretical models predict that charm quarks lose more energy in the medium than beauty quarks. As a consequence, the nuclear modification factor of B mesons should be larger than that of D mesons and hence the ratio $\mathrm{R}_{\mathrm{AA}}^{\mathrm{feed-down}}/\mathrm{R}_{\mathrm{AA}}^{\mathrm{prompt}}$ should

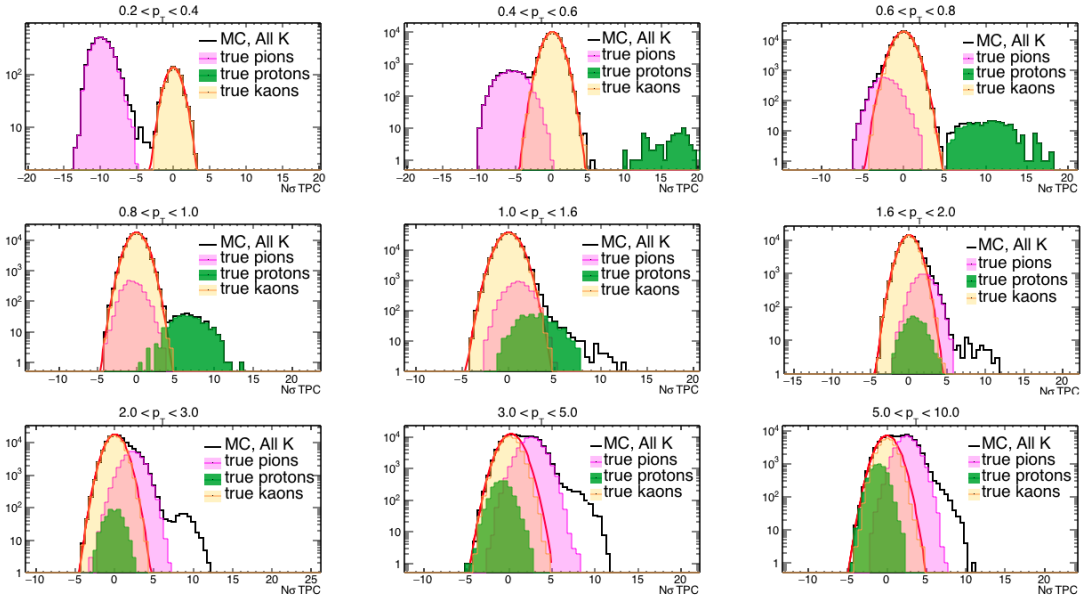

FIGURE 5.14: Nσ distribution of dE/dx signal in TPC for tracks from the Monte Carlo simulation that pass the selections in TOF as kaons (black curve). In yellow, contribution from true kaons, in magenta from pions and in green from protons. The fit to extract the kaon component from the inclusive distribution is shown in red.

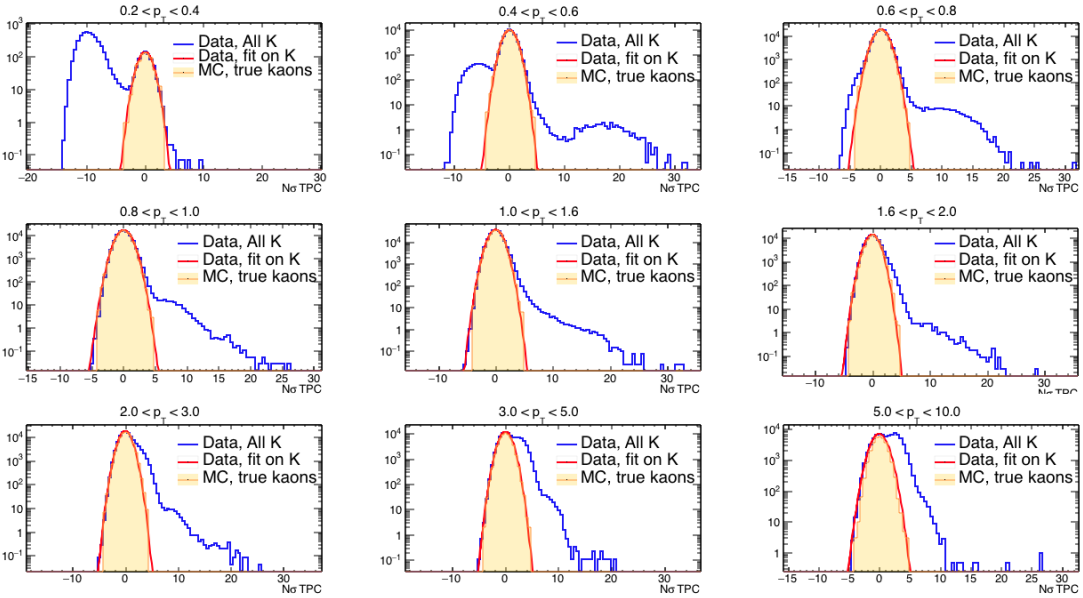

FIGURE 5.15: Nσ distribution of dE/dx signal in TPC for kaons selected based on TOF information in data. The distribution of true kaons form the Monte Carlo is shown in yellow. The fit to extract the kaon component from the inclusive distribution is shown in red.

be larger than unity. This assumption was confirmed by the comparison of the $R_{\rm AA}$ of prompt D mesons at $\sqrt{s_{\rm NN}} = 2.76$ TeV [48] with that of J/ψ from B-meson decays [183] measured by the CMS experiment (see Sec. 2.4.4). If recombination plays a role in the charm hadronisation, however, the ratio $\mathrm{R}_{\rm AA}^{\rm feed-down}/\mathrm{R}_{\rm AA}^{\rm prompt}$ could assume values less than unity. The ratio of the nuclear modification factors of feed-down and prompt $\mathrm{D_s}$ mesons was therefore varied in the range $\frac{1}{3} < R_{\rm AA}^{\rm feed-down}/R_{\rm AA}^{\rm prompt} < 3$, in

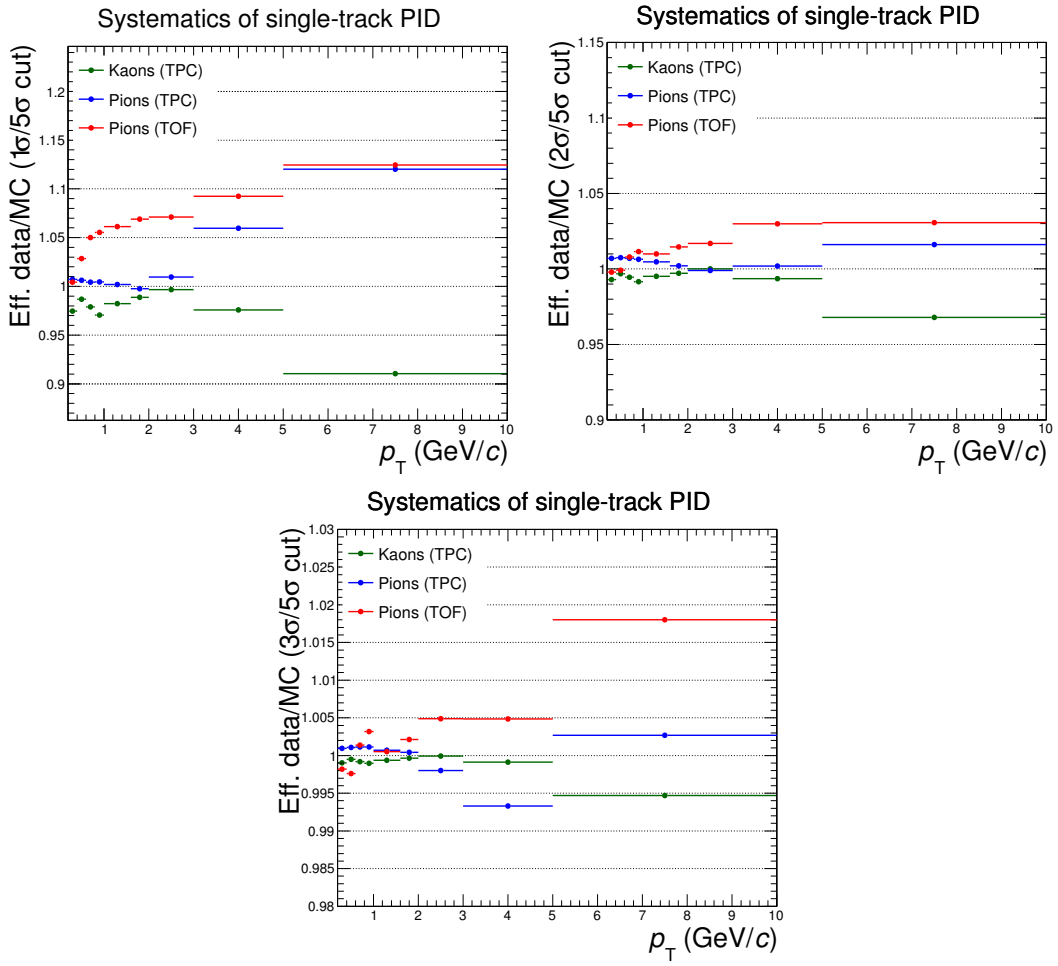

FIGURE 5.16: Ratios of Nσ selection efficiencies in data and MC for kaons and pions in TPC and TOF in different colours, as a function of p_{T}, for 1σ (top left), 2σ (top right) and 3σ (bottom) selection, normalised to a 5σ cut.

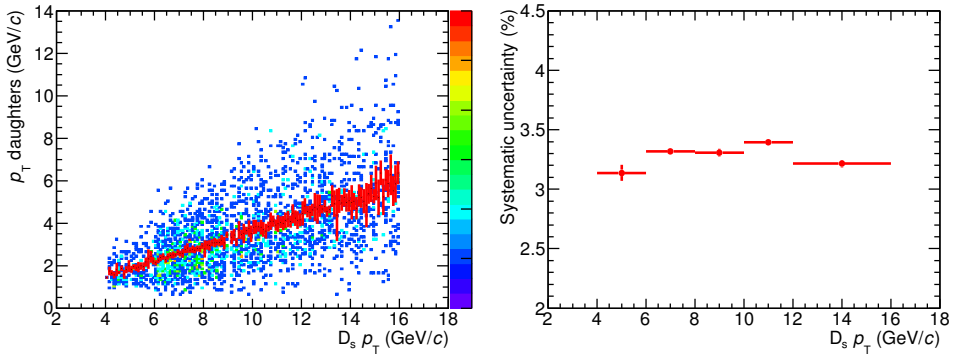

FIGURE 5.17: Left: scatter plot of $\mathrm{D_s}$ daughter p_{T} as a function of $\mathrm{D_s}$ meson p_{T}. Right: systematic uncertainty on the tighter PID selection used for $\mathrm{D_s}$ meson as a function of $\mathrm{D_s}$ p_{T}.

the 0-10% and 30-50% centrality classes. The relative variation of prompt $\mathrm{D_s^+}$ yield is presented as a function of the hypothesis on $R_{\mathrm{AA}}^{\mathrm{feed-down}}/R_{\mathrm{AA}}^{\mathrm{prompt}}$ in Fig. 5.18 for the 0-10% centrality class. respectively. The range was limited to $1 < R_{\mathrm{AA}}^{\mathrm{feed-down}}/R_{\mathrm{AA}}^{\mathrm{prompt}} <$

1.6 for the centrality class 60-80%, as anticipated in Sec. 5.1.2, due to the milder medium effects.

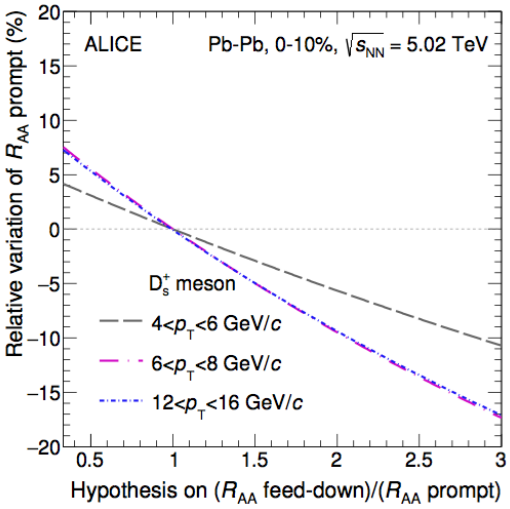

FIGURE 5.18: Relative variation of of prompt D_s^+ yield in the 0-10% centrality class as a function of the hypothesis on $R_{\rm AA}^{\rm feed\text{-}down}/R_{\rm AA}^{\rm prompt}$.

5.2.6 Track reconstruction efficiency

The procedure to estimate the systematic uncertainty due to tracking efficiency was discussed in Sec. 4.8.4. The per-track uncertainty quoted to account for track-quality selection efficiencies based on a cut variation approach is 1.5% in the 10% most central events and 1% in 30-50% and 60-80% centrality classes. The systematic uncertainty on the ITS-TPC track-matching efficiency was estimated by comparing its values in data and simulations after correcting for the different contribution of secondary particles, according to the procedure described in Sec. 4.8.4. In Pb-Pb, some discrepancies are observed in the systematic uncertainties (up to 4%, for $2 < p_{\rm T} < 4\,{\rm GeV}/c$) if the request of a point in SPD is applied or not on the tracks used to fill the $\rm DCA_{xy}$ distribution. The two approaches have different pros and cons.

- The extraction of the primary and secondary fractions from the fit to $\rm DCA_{xy}$ distribution of tracks with a point in SPD is more robust thanks to the better resolution on the track parameters as compared to the TPC-only tracks. However, the request of the ITS point requires to introduce a correction factor to the fraction of primary tracks from fit. The latter is in fact the fraction of primary tracks in the ITS. Since the matching efficiency is normalised to the number of tracks reconstructed in the TPC, we need to rescale the fraction of primary tracks in the ITS to the fraction of primary tracks in the TPC. This factor is extracted from MC and it relies on the hypothesis that the simulation reproduces well the data for what concerns the dependence of the relative abundance of primary tracks on the radial distance from the beam axis.

- In the case of fit without the request of hit in the SPD, the $\rm DCA_{xy}$ resolution is worse. However, the fits can be performed with acceptable quality and we do not need the correction factor of the first case. Neverthless, primary and secondary tracks with different impact parameter resolutions are mixed in this case. This means that the $\rm DCA_{xy}$ distributions are filled with tracks that may

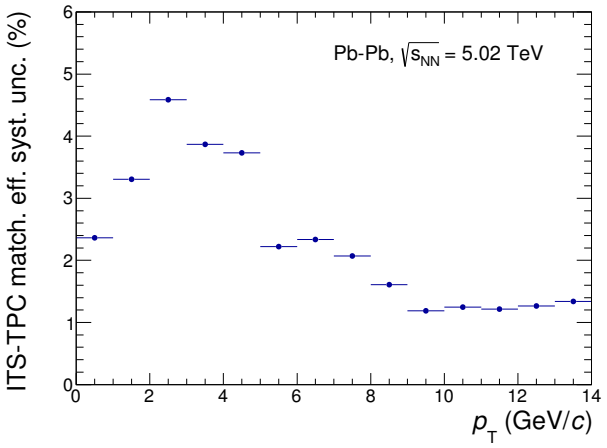

FIGURE 5.19: Systematic uncertainty on ITS-TPC track-matching efficiency in Pb-Pb at $\sqrt{s_{\rm NN}} = 5.02$ TeV as a function of $p_{\rm T}$ of the track.

have a point in the SPD (optimal resolution) and tracks that may not have it (worse resolution). This second approach assumes that the templates from the simulation and utilised in the fit have the correct mixture of tracks.

The observed discrepancy in the results between the two approaches may be due to: (i) a less precise estimate of the fraction of primary tracks due to worse $\rm DCA_{xy}$ resolution (in the case of not requiring the SPD point) or to (ii) mixtures of tracks in the MC templates which do not reproduce those in data (in the case of not requiring the SPD point), as well as to (iii) a non valid assumption on the MC-based correction factor (in case in which the SPD point is required). For this reason, the systematic uncertainty on the ITS-TPC matching efficiency for the single track was assigned by averaging the two results, and the resulting plot is shown in Fig. 5.19.

The values of the systematic uncertainties on the $\rm D_s$-meson corrected yields are summarised in Tab. 5.6, in the $p_{\rm T}$ intervals considered in the analysis. The uncertainties on the fraction of the hadronic cross section used in the Glauber fit to determine the centrality are shown as well in the Table.

5.3 Nuclear modification factor in Pb-Pb collisions

The nuclear modification factor $R_{\rm AA}$ of prompt $\rm D_s^+$ mesons was defined as follows:

$$R_{\rm AA}(p_{\rm T}) = \frac{1}{\langle T_{\rm AA}\rangle}\frac{{\rm d}N_{\rm AA}/{\rm d}p_{\rm T}}{{\rm d}\sigma_{\rm pp}/{\rm d}p_{\rm T}}, \tag{5.3}$$

where ${\rm d}N_{\rm AA}/{\rm d}p_{\rm T}$ is the $p_{\rm T}$-differential yield of prompt $\rm D_s^+$ mesons of Eq. 5.1, $\langle T_{\rm AA}\rangle$ is the average nuclear overlap function for the considered centrality class and ${\rm d}\sigma_{\rm pp}/{\rm d}p_{\rm T}$ is the $\rm D_s^+$ $p_{\rm T}$-differential cross section in pp collisions at $\sqrt{s} = 5.02$ TeV.

5.4 Systematic uncertainty on the $R_{\rm AA}$

The systematic uncertainty on the $R_{\rm AA}$ measurement was computed by combining the uncertainties on the $\rm D_s$-meson yield in Pb-Pb collisions described in Sec. 5.2 and

0–10% centrality class					
p_T interval (GeV/c)	2–4	4–6	6–8	8–12	12–16
Yield extraction	-	6%	6%	6%	6%
Tracking efficiency	-	11%	11.5%	11.5%	10%
PID efficiency	-	3%	3%	0%	0%
Cut efficiency	-	10%	10%	10%	10%
MC p_T shape	-	7%	2%	1%	0%
Feed-down (FONLL scales)	-	$^{+2.2\%}_{-2.9\%}$	$^{+3.5\%}_{-4.6\%}$	$^{+3.1\%}_{-3.9\%}$	$^{+3.1\%}_{-3.7\%}$
Feed-down ($R_{AA}^{\text{feed-down}}$ hypothesis)	-	$^{+4.0\%}_{-10.3\%}$	$^{+6.6\%}_{-15.7\%}$	$^{+6.3\%}_{-14.7\%}$	$^{+6.7\%}_{-15.6\%}$
Centrality limit	0.1%				
Branching ratio	3.5%				
Total	-	$^{+20.7\%}_{-22.8\%}$	$^{+18.6\%}_{-23.6\%}$	$^{+17.9\%}_{-22.5\%}$	$^{+17.1\%}_{-22.3\%}$
30–50% centrality class					
p_T interval (GeV/c)	2–4	4–6	6–8	8–12	12–16
Yield extraction	-	9%	7%	6%	5%
Tracking efficiency	-	11%	11.5%	11.5%	10%
PID efficiency	-	3%	3%	0%	0%
Cut efficiency	-	15%	15%	10%	10%
MC p_T shape	-	4%	1%	2%	1%
Feed-down (FONLL scales)	-	$^{+3.3\%}_{-4.2\%}$	$^{+4.5\%}_{-5.8\%}$	$^{+3.5\%}_{-4.5\%}$	$^{+2.5\%}_{-3.0\%}$
Feed-down ($R_{AA}^{\text{feed-down}}$ hypothesis)	-	$^{+5.5\%}_{-13.4\%}$	$^{+7.8\%}_{-18.1\%}$	$^{+7.2\%}_{-16.8\%}$	$^{+5.6\%}_{-13.8\%}$
Centrality limit	0.1%				
Branching ratio	3.5%				
Total	-	$^{+20.7\%}_{-24.8\%}$	$^{+24.5\%}_{-29.6\%}$	$^{+16.3\%}_{-22.4\%}$	$^{+14.7\%}_{-19.5\%}$
60–80% centrality class					
p_T interval (GeV/c)	2–4	4–6	6–8	8–12	12–16
Yield extraction	10%	6%	6%	5%	5%
Tracking efficiency	11%	11%	11.5%	11.5%	10%
PID efficiency	3%	3%	3%	3%	3%
Cut efficiency	14%	10%	12%	10%	12%
MC p_T shape	6%	2%	2%	1%	1%
Feed-down (FONLL scales)	$^{+7.2\%}_{-8.5\%}$	$^{+4.5\%}_{-6.0\%}$	$^{+6.2\%}_{-8.0\%}$	$^{+5.2\%}_{-6.6\%}$	$^{+2.9\%}_{-3.4\%}$
Feed-down ($R_{AA}^{\text{feed-down}}$ hypothesis)	$^{+3.4\%}_{-3.1\%}$	$^{+2.6\%}_{-2.6\%}$	$^{+3.6\%}_{-3.4\%}$	$^{+3.3\%}_{-3.1\%}$	$^{+2.0\%}_{-1.9\%}$
Centrality limit	0.1%				
Branching ratio	3.5%				
Total	$^{+28.4\%}_{-28.7\%}$	$^{+18.3\%}_{-18.7\%}$	$^{+21.4\%}_{-22.0\%}$	$^{+18.0\%}_{-18.4\%}$	$^{+17.7\%}_{-17.7\%}$

TABLE 5.6: Relative systematic uncertainties on the p_T-differential yields of D_s in the 0-10%, 30-50% and 60-80% centrality classes.

those on the pp reference cross-section. The systematic uncertainty on the feed-down subtraction deriving from the variation of the parameters of the FONLL calculation was considered to be correlated between the Pb–Pb and pp measurements and therefore canceled in the ratio to obtain the R_{AA}. All the other sources of systematic uncertainties were treated as uncorrelated. An additional source of systematic uncertainty originates from the uncertainty on the $\langle T_{AA} \rangle$ used in the R_{AA} calculation. The systematic uncertainties on the R_{AA} measurements are summarised in Tab. 5.7.

5.4.1 Proton-proton reference

The $p_{\rm T}$-differential cross section of prompt $\rm D_s^+$ mesons with $|y| < 0.5$ in pp collisions at $\sqrt{s} = 5.02$ TeV, used as reference for the nuclear modification factor, was obtained by scaling the measurement at $\sqrt{s} = 7$ TeV described in Chapter 4 [43] to $\sqrt{s} = 5.02$ TeV with FONLL calculations [123]. This measurement reaches up to 12 GeV/c for $\rm D_s$ mesons. In particular, the value of the cross section measured at $\sqrt{s} = 7$ TeV at central rapidity $|y| < 0.5$ was scaled in each $p_{\rm T}$ interval by the ratio of the FONLL predictions at the two energies in the same rapidity region as follows:

$$\sigma^{5.02\rm TeV}_{\rm scaled}(p_{\rm T}) = \frac{\sigma^{5.02\rm TeV}_{\rm FONLL}(p_{\rm T})}{\sigma^{7\rm TeV}_{\rm FONLL}(p_{\rm T})}\sigma^{7\rm TeV}_{\rm meas}(p_{\rm T}). \tag{5.4}$$

Since FONLL does not have a specific prediction for $\rm D_s^+$ mesons, the cross sections of the D-meson admixture (70% of $\rm D^0$ and 30% of $\rm D^+$) were used for the scaling. The uncertainty on the pp reference has two contributions. The first one is the uncertainty on the measured $p_{\rm T}$-differential $\rm D_s^+$-meson cross section at $\sqrt{s} = 7$ TeV. The second contribution is the $p_{\rm T}$-dependent scaling factor from $\sqrt{s} = 7$ TeV to $\sqrt{s} = 5.02$ TeV, determined by varying the FONLL parameters (charm-quark mass, factorisation and renormalisation scales) as described in Sec. 4.8.5 and in [93]. The values of these parameters were varied coherently at the two energies. The scaling factor and its uncertainties from FONLL calculations are shown in Fig. 5.20. In the interval $12 < p_{\rm T} < 16$ GeV/c, where the pp reference is missing, the FONLL cross section of the D-meson admixture at $\sqrt{s} = 5.02$ TeV was used as a reference. The latter was rescaled to match the data points of the $\rm D_s^+$ cross section at $\sqrt{s} = 5.02$ TeV (after the $\sqrt{s}$-rescaling) in the $p_{\rm T}$ interval $2 < p_{\rm T} < 12\,\rm GeV/\mathit{c}$, providing in this way a reference value for $\rm D_s^+$ cross section in $12 < p_{\rm T} < 16\,\rm GeV/\mathit{c}$. The procedure is

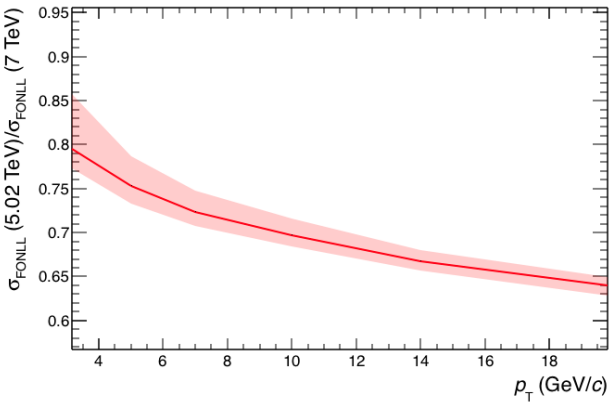

FIGURE 5.20: Scaling factor obtained for cross sections of prompt $\rm D_s^+$ mesons in pp collisions, from $\sqrt{s} = 7$ TeV to $\sqrt{s} = 5.02$ TeV, as a function of $p_{\rm T}$. The red line corresponds to the result used as central value for the correction; the uncertainty bands are obtained from variation of FONLL perturbative parameters.

described in Ref. [58]. The total systematic uncertainty on the $p_{\rm T}$-extrapolated cross section is about $^{+29}_{-42}$% for $\rm D_s$ in the $p_{\rm T}$ interval 12–16 GeV/c.

5.4.2 Normalisation

The uncertainties on the R_{AA} normalisation are the quadratic sum of (i) the normalisation uncertainty on the integrated luminosity used for the measurement of the D_s^+ cross section in pp collisions (3.5%), (ii) the uncertainty on $\langle T_{AA} \rangle$, which ranges from 3.3% to 6.2% depending on the centrality, and (iii) the uncertainty on the fraction of the hadronic cross section used in the Glauber fit to determine the centrality ($< 0.1\%$, 2% and 3% for the 0–10%, 30–50% and 60–80% centrality classes, respectively) [58], while the branching ratio uncertainty cancels out in the ratio.

0–10% centrality class					
p_T interval (GeV/c)	2–4	4–6	6–8	8–12	12–16
Data syst. AA	-	20.1%	17.0%	16.5%	15.5%
Data syst. pp + $\sqrt{s}$-scaling	-	$^{+13.2\%}_{-13.7\%}$	$^{+12.9\%}_{-13.2\%}$	$^{+12.9\%}_{-13.0\%}$	$^{+29.3\%}_{-42.3\%}$
Feed-down (FONLL scales)	-	$^{+1.2\%}_{-0.9\%}$	$^{+0.2\%}_{-0.1\%}$	$^{+0.7\%}_{-0.4\%}$	$^{+3.1\%}_{-3.7\%}$
Feed-down ($R_{AA}^{feed-down}$ hypothesis)	-	$^{+3.9\%}_{-10.2\%}$	$^{+6.6\%}_{-15.6\%}$	$^{+6.1\%}_{-14.7\%}$	$^{+6.5\%}_{-15.6\%}$
Normalisation	4.8%				
Total	-	$^{+24.4\%}_{-26.5\%}$	$^{+22.4\%}_{-26.6\%}$	$^{+21.8\%}_{-25.7\%}$	$^{+34.0\%}_{-47.8\%}$
30–50% centrality class					
p_T interval (GeV/c)	2–4	4–6	6–8	8–12	12–16
Data syst. AA	-	24.0%	22.7%	14.2%	13.4%
Data syst. pp + $\sqrt{s}$-scaling	-	$^{+13.2\%}_{-13.7\%}$	$^{+12.9\%}_{-13.2\%}$	$^{+12.9\%}_{-13.0\%}$	$^{+29.3\%}_{-42.3\%}$
Feed-down (FONLL scales)	-	$^{+0.1\%}_{-0.1\%}$	$^{+1.0\%}_{-1.0\%}$	$^{+0.1\%}_{-0.1\%}$	$^{+2.5\%}_{-3.0\%}$
Feed-down ($R_{AA}^{feed-down}$ hypothesis)	-	$^{+5.5\%}_{-13.3\%}$	$^{+7.8\%}_{-18.0\%}$	$^{+7.1\%}_{-16.7\%}$	$^{+5.6\%}_{-13.8\%}$
Normalisation	4.9%				
Total	-	$^{+28.0\%}_{-30.7\%}$	$^{+27.3\%}_{-31.9\%}$	$^{+20.4\%}_{-25.5\%}$	$^{+32.8\%}_{-46.6\%}$
60–80% centrality class					
p_T interval (GeV/c)	2–4	4–6	6–8	8–12	12–16
Data syst. AA	27.2%	17.6%	20.2%	16.9%	17.3%
Data syst. pp + $\sqrt{s}$-scaling	$^{+12.9\%}_{-14.5\%}$	$^{+13.2\%}_{-13.7\%}$	$^{+12.9\%}_{-13.2\%}$	$^{+12.9\%}_{-13.0\%}$	$^{+29.3\%}_{-42.3\%}$
Feed-down (FONLL scales)	$^{+3.3\%}_{-4.2\%}$	$^{+1.4\%}_{-2.0\%}$	$^{+2.5\%}_{-3.4\%}$	$^{+1.6\%}_{-2.1\%}$	$^{+2.9\%}_{-3.4\%}$
Feed-down ($R_{AA}^{feed-down}$ hypothesis)	$^{+3.4\%}_{-3.1\%}$	$^{+2.6\%}_{-2.5\%}$	$^{+3.6\%}_{-3.3\%}$	$^{+3.3\%}_{-3.1\%}$	$^{+2.0\%}_{-1.9\%}$
Normalisation	6.7%				
Total	$^{+30.5\%}_{-31.1\%}$	$^{+22.2\%}_{-22.5\%}$	$^{+24.4\%}_{-24.6\%}$	$^{+21.6\%}_{-21.7\%}$	$^{+34.2\%}_{-45.9\%}$

TABLE 5.7: Relative systematic uncertainties on the R_{AA} of D_s in the 0-10%, 30-50% and 60-80% centrality classes.

5.5 D_s elliptic flow

In this section, the first measurement of the v_2 of prompt D_s mesons in Pb-Pb collisions at $\sqrt{s_{NN}} = 5.02$ TeV is reported. The analysis was carried out for the 30-50% centrality class, because it is the centrality interval where the elliptic flow reaches its maximum value [47].

5.5.1 Event characterisation: event plane

The measurement of the azimuthal anisotropy of charm and beauty hadrons with respect to the symmetry plane of the collision can provide important information on the properties of the QGP medium and the interactions between heavy quarks and the medium. The p_{T}-differential azimuthal distribution of produced particles can be described by a Fourier series:

$$\frac{\mathrm{d}^2N}{\mathrm{d}\varphi \mathrm{d}p_{\mathrm{T}}} = \frac{\mathrm{d}N}{2\pi \mathrm{d}p_{\mathrm{T}}}\Big[1 + 2\sum_{n=1}^{\infty} v_n(p_{\mathrm{T}}) \cos n(\varphi - \Psi_n^{\mathrm{RP}})\Big], \tag{5.5}$$

where v_n are the Fourier coefficients, that can be evaluated as $v_n = \langle \cos n(\varphi - \Psi_n^{\mathrm{RP}})\rangle$ and $\langle\rangle$ indicates an average over all particles in all events, with their azimuthal angle φ in a given rapidity and p_{T} momentum at a fixed centrality. In Eq. 5.5, Ψ_n^{RP} is the initial-state spatial plane of symmetry (reaction plane) of the n^{th} harmonic defined by the geometrical distribution of the nucleons participating in the collision. The symmetry plane Ψ_n^{RP} of a given n^{th} harmonic is estimated event-by-event from the azimuthal distribution of the produced particles via the n^{th}-harmonic event-plane angle, ψ_n. For a given harmonic n, one constructs the two-dimensional event-plane vector $\vec{Q}_n$:

$$\vec{Q}_n = \begin{pmatrix} Q_{n,x} \\ Q_{n,y} \end{pmatrix} = \begin{pmatrix} \sum_{i=0}^{N} w_i \cos(n\varphi_i) \\ \sum_{i=0}^{N} w_i \sin(n\varphi_i) \end{pmatrix}. \tag{5.6}$$

The sums run over all reconstructed tracks in the case of the TPC, or over the scintillator tiles of the V0 detector. The angle φ_i is the azimuthal emission angle of the the i^{th} particle or the azimuthal coordinate of the centre of the i^{th} detector element, respectively. For TPC tracks the weight w_i can be unity or a specific function of p_{T}, useful to enhance the contribution of particle with large flow, improving the resolution on the event plane. For segmented detectors, w_i is the amplitude of the signal measured in the i^{th} detector element. The observed plane angle of the n^{th} harmonic is given by the orientation of $\vec{Q}_n$:

$$\psi_n = \frac{1}{n}\tan^{-1}\left(\frac{Q_{n,y}}{Q_{n,x}}\right). \tag{5.7}$$

Due to the finite number of detected particles, the angular resolution on the reaction plane Ψ_n^{RP} is limited and can be estimated for the n^{th} harmonic as:

$$R_n = \langle \cos[n(\psi_n - \Psi_n^{\mathrm{RP}})]\rangle, \tag{5.8}$$

where the angle brackets denote an average over a large event sample. The resolution term must be used to correct the Fourier coefficients as:

$$v_n' = \frac{v_n}{R_n}. \tag{5.9}$$

It can be demonstrated that the the event plane resolution correction factor can be expressed as [221]:

$$\left\langle \cos[km\left(\psi_m - \Psi_n^{\mathrm{RP}}\right)]\right\rangle = \sqrt{\frac{\pi}{8}}\chi_m \cdot \mathrm{e}^{-\chi_m^2/4} \cdot I_{(k-1)/2}(\chi_m^2/4) + I_{(k+1)/2}(\chi_m^2/4), \tag{5.10}$$

where the equation has been written in terms of km instead of n, $\chi_m = v_m/\sigma = v_m\sqrt{2N}$ (N is the multiplicity) is the variable concerning the resolution, I_ν is the

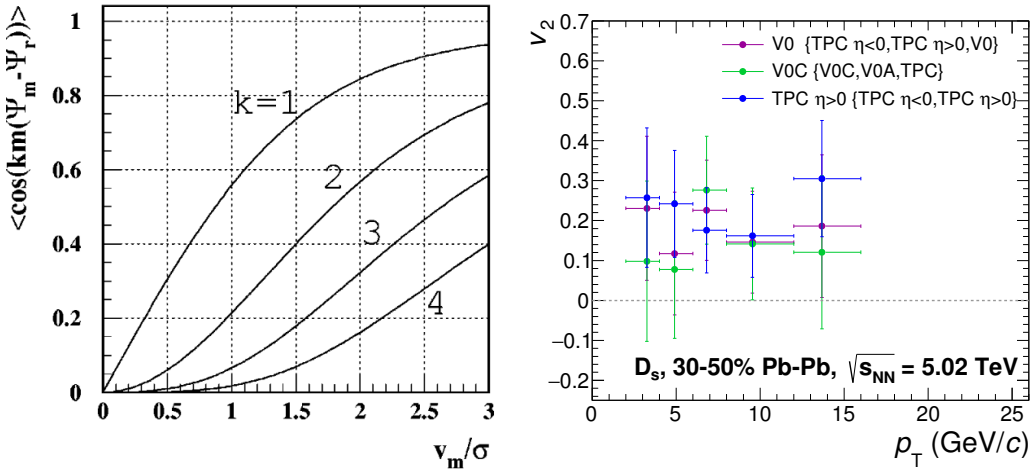

FIGURE 5.21: Left: the event plane resolution for the n^{th} ($n = km$, according the conventions of Eq. (5.10)) harmonic of the particle distribution with respect to the m^{th} harmonic plane, as a function of χ_m [221]. Right: D_s v_2 calculated with different detector configurations.

Bessel function of order ν and k is an integer number that accounts for the fact that the event plane of m^{th} order can be used to compute all Fourier harmonics that are multiples of m (i.e. km). The resolution correction factor from Eq. 5.10 is drawn in Fig. 5.21 (left) as a function of χ_m, for different values of k. The mean cosine values are less than one, thus the correction always increases the Fourier coefficients. To estimate the event plane resolution, the correlations of the event planes determined from different samples of tracks, or different detectors are exploited. If the full sample of tracks can be divided into two independent sub-samples a and b, with same multiplicity and rapidity coverage, the following relation holds for the correlations between the two independent sub-sets and the true event plane:

$$\langle \cos[n(\psi_n^a - \psi_n^b))] \rangle = \langle \cos[n(\psi_n^a - \Psi_n^{\text{RP}})] \rangle \langle \cos[n(\psi_n^b - \Psi_n^{\text{RP}})] \rangle. \tag{5.11}$$

Since, given the conditions above, the resolution of each sub-sets is expected to be the same, their resolution can be obtained once the correlation between the two samples is known:

$$R_{n,sub} = \langle \cos[n(\psi_n^a - \Psi_n^{\text{RP}})] \rangle = \sqrt{\langle \cos[n(\psi_n^a - \psi_n^b)] \rangle}. \tag{5.12}$$

If the two sub-events are not equal or have different rapidity coverage, at least three sub-samples are needed to determine the event-plane resolution in each of them. In this case, the resolution of the first sub-set a is determined as:

$$\langle \cos[n(\psi_n^a - \Psi_n^{\text{RP}})] \rangle = \sqrt{\frac{\langle \cos[n(\psi_n^a - \psi_n^c)] \rangle \langle \cos[n(\psi_n^a - \psi_n^b)] \rangle}{\langle \cos[n(\psi_n^b - \psi_n^c)] \rangle}}. \tag{5.13}$$

5.5.2 Event plane measurement and corrections

The azimuthal angle of the $\vec{Q}_2$ vector in Eq. 5.6:

$$\psi_2 = \frac{1}{2} \tan^{-1}\left(\frac{Q_{2,y}}{Q_{2,x}}\right) \tag{5.14}$$

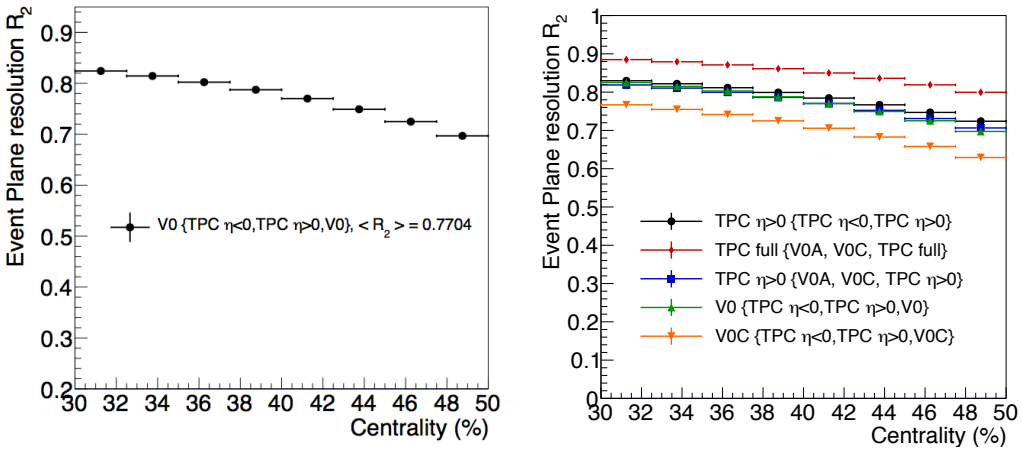

FIGURE 5.22: R_2 resolution as a function of centrality estimated with default configuration (left panel) and with 5 different detector configurations (right) for the 30–50% centrality class.

is called event plane angle and it is an estimate of the second harmonic symmetry plane Ψ_2. The event plane method was used to measure the D_s meson Fourier coefficient v_2 (elliptic flow) in this analysis. The determination of the event plane in ALICE can be performed using either the tracks reconstructed in the TPC, which has a uniform azimuthal coverage in the central rapidity region, or the V0 detectors, located at forward ($2.8 < \eta < 5.1$) and backward ($-3.7 < \eta < -1.7$) pseudo-rapidity. In this analysis the event plane was obtained from the signals produced by the charged particles in the eight azimuthal sectors of each V0 array. The current uncertainties on the v_2 values do not allow to appreciate different non-flow contributions, i.e. correlations not induced by the collective expansion but rather by particle decays and jet production, which can be exploited by using different detector configurations for the event plane measurement. In this way in fact, it is possible to introduce different rapidity gaps between the tracks used for the event plane measurement and the D meson reconstruction. As an example, the right panel of Fig. 5.21 shows the v_2 of D_s meson measured with the following detector configurations:

1. event plane measured with V0, resolution R_2 with three sub-samples: TPC tracks with $\eta < 0$ and $\eta > 0$, V0;

2. event plane measured with V0C, resolution R_2 with three sub-samples: V0C, V0A, full TPC;

3. event plane measured with TPC tracks with $\eta > 0$, resolution R_2 with the event planes from the two samples with same resolution: TPC tracks with $\eta < 0$ and $\eta > 0$.

Even though the current statistical uncertainties do no allow to discriminate among these three options, the separation of at least 0.9 units of pseudo-rapidity ($|\Delta\eta| > 0.9$) between the D mesons (reconstructed in the TPC) and the particles (detected with V0) used in the ψ_2 calculation was preferred, because it suppresses non-flow contributions in the v_2 measurement with respect to the measurement of the event plane considering tracks in the same pseudo-rapidity region of the D meson candidates (TPC event planes). Since the V0s sub-detectors cover different rapidity regions and measure different multiplicities, the three events technique was used to compute the

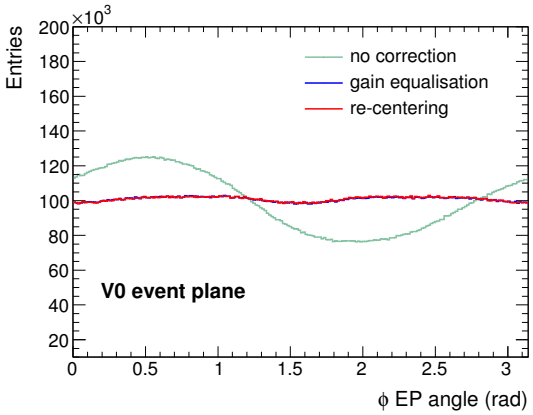

FIGURE 5.23: Event-plane angle distributions obtained with the V0 detector without corrections and after gain equalisation, re-centering and alignment corrections.

event plane resolution. The three event planes needed to calculate the resolution were computed with the V0 detector itself and the positive and negative η regions of the TPC. In the 30-50% centrality class, the resolution decreases from ≈ 0.83 to ≈ 0.70 with increasing centrality percentile and the average resolution correction factor is $R_2 = 0.77045 \pm 0.00007$ (see left panel of Fig. 5.22). Other detector configurations have been tested in order to compare the resolution and check the consistency of the different results obtained:

1. event plane measured with TPC tracks with $\eta > 0$, resolution R_2 with the event planes from the two samples with same resolution: TPC tracks with $\eta < 0$ and $\eta > 0$;

2. event plane measured with TPC tracks with $\eta > 0$, resolution R_2 with three sub-samples: V0A, V0C, TPC region at $\eta > 0$;

3. event plane measured with full TPC, resolution R_2 with three sub-samples: V0A, V0C, full TPC;

4. event plane measured with V0C, resolution R_2 with three sub-samples: V0C, TPC regions at $\eta < 0$ and $\eta > 0$.

The best resolution is obtained considering configuration 3, while the worst resolution using configuration 4, due to the limited acceptance of the C-side of the V0 detector (see right panel of Fig. 5.22). The resolution obtained with full V0 for the event plane measurement (default configuration) and the resolutions obtained with configurations 1 or 2 are very similar.

The distribution of the event plane angles recorded by an ideal detector is completely flat, since there is not a preferred direction for the Ψ_n^{RP} angle. Effects of non-uniformity of the detector performance and tracking efficiency (in the case of the TPC) can generate a non-flat distribution of the event plane angle. For this purpose, a gain equalisation of individual V0 detector channels was applied, correcting the raw amplitudes M_c as: $M'_c = M_c/\langle M_c \rangle$, where $\langle M_c \rangle$ is the average amplitude of the V0 channels in intervals of z vertex and V0A(C) multiplicity. A re-centering of the distributions of the components of $\vec{Q}_n$ vector (X_n, Y_n) can also be applied, by

subtracting the ($\langle X_n \rangle$, $\langle Y_n \rangle$) values averaged over all events:

$$\begin{aligned} X'_n &= X_n - \langle X_n \rangle, \\ Y'_n &= Y_n - \langle Y_n \rangle. \end{aligned} \tag{5.15}$$

Further corrections can be introduced but, as shown in the right panel of Fig. 5.23, already the re-centering procedure, applied after the gain equalisation, does not provide a substantial improvement. The $\vec{Q}_n$ vector was normalised to the multiplicity M of the event to reduce the sensitivity to multiplicity fluctuations.

5.5.3 Event-plane based methods for v_2 extraction

The basic principle in flow analysis is to quantify the azimuthal anisotropies via Fourier coefficients obtained through a decomposition of the azimuthal distributions of reconstructed particles in a Fourier series (see Eq. 5.5). The v_2 coefficient of D mesons can be obtained by integrating Eq. 5.5 in two $\Delta\varphi$ intervals and including a correction for the resolution. In the analysis presented here, the sample of candidates was divided in two $\Delta\varphi = \varphi_{\rm D} - \psi_n$ regions: the *in-plane* and the *out-of-plane* regions. We define the in-plane region (centred on the event plane) as the region $\left(-\frac{\pi}{4}, \frac{\pi}{4}\right] \cup \left(\frac{3\pi}{4}, \frac{5\pi}{4}\right]$ and the out-of-plane as $\left(\frac{\pi}{4}, \frac{3\pi}{4}\right] \cup \left(\frac{5\pi}{4}, \frac{7\pi}{4}\right]$. In each $\Delta\varphi$ interval the D_s yield is extracted via an invariant-mass fit. Resolving Eq. 5.5 for the number of D_s measured in the in-plane and out-of-plane regions separately we obtain:

$$\begin{aligned} N_{\text{in-plane}} &= k \int_{\text{in-plane}} 1 + 2v_2 \cos(2\Delta\varphi) d\Delta\varphi = k' \cdot (\pi + 4v_2) \\ N_{\text{out-plane}} &= k \int_{\text{out-plane}} 1 + 2v_2 \cos(2\Delta\varphi) d\Delta\varphi = k' \cdot (\pi - 4v_2), \end{aligned} \tag{5.16}$$

and therefore it is possible to compute v_2 from the relative difference between the number of D_s mesons observed in-plane and out-of-plane:

$$v_2 = \frac{1}{R_2} \frac{\pi}{4} \frac{N_{\text{in-plane}} - N_{\text{out-plane}}}{N_{\text{in-plane}} + N_{\text{out-plane}}}. \tag{5.17}$$

The contribution of all odd harmonics, as well as v_4 and v_8, to the v_2 value induce the same average contribution to $N_{\text{in-plane}}$ and $N_{\text{out-of-plane}}$ due to symmetry, and therefore they do not affect v_2 calculated with Eq. 5.17. The contribution of v_6, v_{10} and higher harmonics is assumed to be negligible based on the values measured for light-flavour hadrons [13, 2]. The factor $\frac{1}{R_2}$ in Eq. 5.17 is the correction for the finite resolution in the estimate of the symmetry plane Ψ_2 via the event plane ψ_2. Simulations showed that the D-meson reconstruction and selection efficiencies do not depend on $\Delta\varphi$ [18], therefore Eq. 5.17 can be applied using the D-meson raw yields, without an efficiency correction.

5.5.4 In- and out-of-plane signal extraction

The topological selections used for the selection of $D_s^{\pm}$ candidates in the 30-50% centrality class are very similar to those reported in Table 5.3 for the φ-integrated yields in the same centrality class. Only the selections on NDL_{xy}, σ_{vertex}, ΔM and $|\cos^3\theta'(\text{K})|$ were slightly released in some $p_{\rm T}$ intervals. The invariant-mass distributions were analysed separately for $D_s^{\pm}$ candidates in the in-plane and out-of-plane $\Delta\varphi$ intervals, with the event plane determined with the V0 in the 30-50% centrality class. To extract the $D_s^{\pm}$ raw yield, the invariant mass distribution was fitted using a two

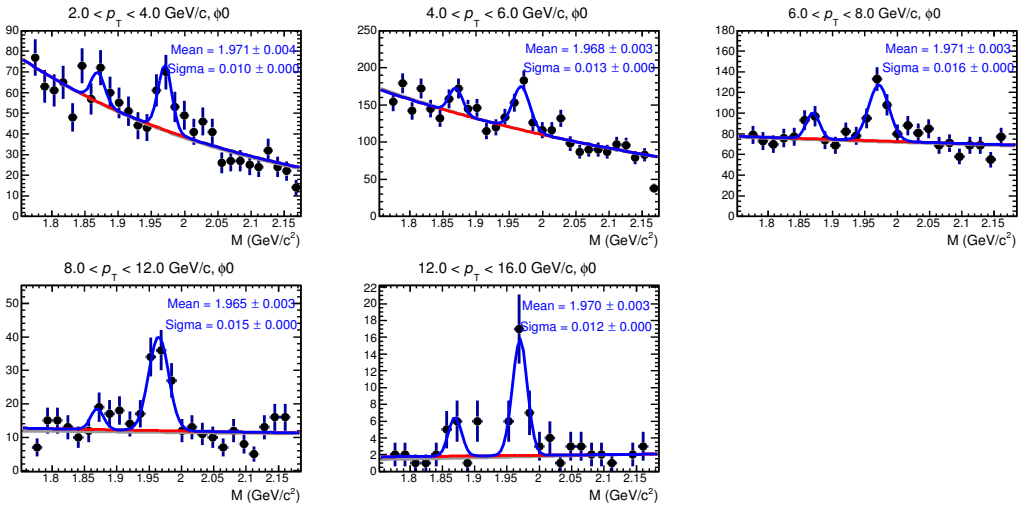

FIGURE 5.24: $D_s^{\pm}$ in-plane invariant-mass distributions in the analysed p_T intervals.

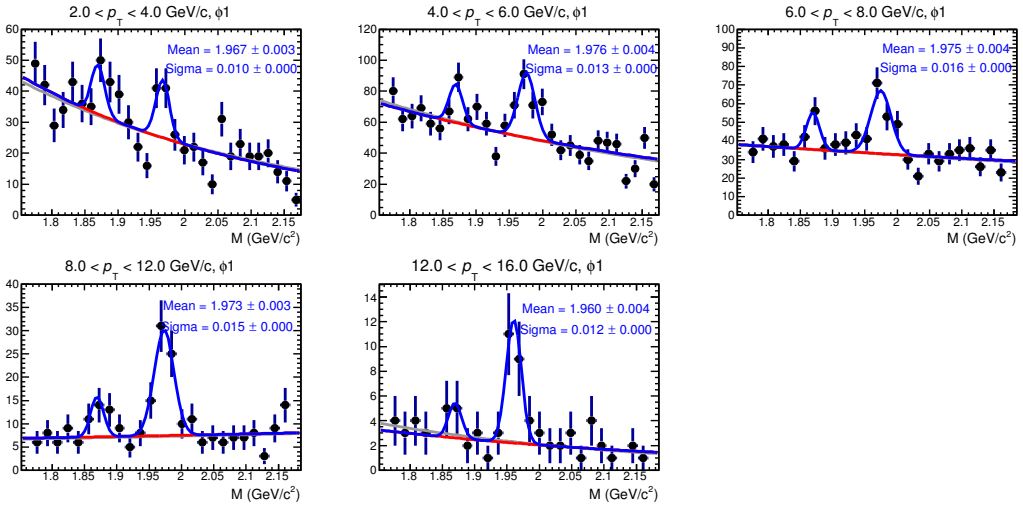

FIGURE 5.25: $D_s^{\pm}$ out-of-plane invariant-mass distributions in the analysed p_T intervals.

Gaussian functions to model the $D_s^{\pm}$ peak and the contribution of the $D^+ \to K^+K^-\pi^+$ and an exponential shape to model the background. The mean and the width of the Gaussians were fixed to those obtained from a fit to the invariant-mass distribution integrated over $\Delta\varphi$, where the signal has higher statistical significance. The position and width of the Gaussian function used to fit the D^+ peak were fixed respectively to the D^+ invariant mass from PDG and to the value of the width from the simulations. The yields in the two φ regions were extracted in five p_T intervals between 2 and 16 GeV/c. Figures 5.24 and 5.25 show, respectively, the fits to the in-plane and out-of-plane invariant-mass distributions for the five analysed p_T intervals between $2 < p_T < 16\,\mathrm{GeV}/c$. Figure 5.26 shows the values of Gaussian means and widths for the in-/out-of-plane and the φ-integrated extracted yields. The values of the extracted raw yields and the signal-over-background ratios for the in-plane and out-of-plane invariant-mass fits are reported in Table 5.8.

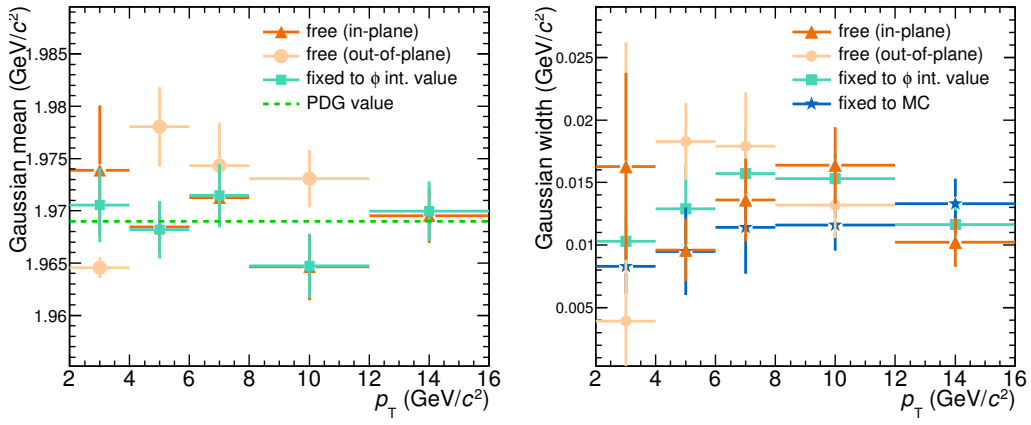

FIGURE 5.26: Position (left) and widths (right) of the Gaussian peak in the D_s candidate invariant-mass fits for φ-integrated, in-plane and out-of-plane samples. In the left panel, the value of D_s mass from PDG is also shown (dashed green line).

p_T (GeV/c)	In-plane		Out-of-plane	
	raw yield	S/B	raw yield	S/B
2-4	58 ± 14	0.31	34 ± 11	0.31
4-6	135 ± 24	0.21	97 ± 18	0.35
6-8	134 ± 21	0.31	83 ± 15	0.43
8-12	70 ± 11	0.99	57 ± 10	1.36
12-16	25 ± 6	3.00	18 ± 5	1.89

TABLE 5.8: $D_s^{\pm}$ raw yields and signal-over-background ratios in the different p_T intervals and $\Delta\varphi$ regions.

5.5.5 B feed-down subtraction

The measured $D_s^{\pm}$ meson raw yield includes a contribution (of about 90%) from prompt D_s mesons and a contribution from beauty feed-down. Considering that v_2 is an additive quantity, the measured v_2 is therefore given by:

$$v_2^{\rm obs} = f_{\rm prompt} v_2^{\rm promptD} + (1 - f_{\rm prompt}) v_2^{\rm feed-down}. \tag{5.18}$$

The value of $f_{\rm prompt}$ is estimated via Eq. 5.2 using FONLL calculations for B meson cross sections, the B→D decay kinematics from the EvtGen package and the Monte Carlo efficiencies for feed-down D mesons and a hypothesis for the $R_{\rm AA}^{\rm feed-down}$, which is the same used for $R_{\rm AA}$ analyses and discussed in Sec. 5.1.2. To calculate $v_2^{\rm prompt}$, a hypothesis on $v_2^{\rm feed\text{-}down}$ is used. The measured v_2 of non-prompt J/ψ [183] and the available model calculations [69, 252, 162] suggest that $0 < v_2^{\rm feed\text{-}down} < v_2^{\rm prompt}$. The lower limit, $v_2^{\rm feed-down} = 0$, corresponds to the extreme assumption case in which:

- at low p_T, where v_2 is determined by collective flow, b quarks do not take part in the collective expansion and hence do not contribute to the observed D-meson anisotropy;
- at high p_T, where v_2 is determined by energy loss, due to different path lengths for quarks emitted in-plane and out-of-plane, b quarks are not affected by the

medium.

The upper limit, $v_2^{\text{feed-down}} = v_2^{\text{prompt}}$, implies that:

- at low p_T, b quarks are flowing as c quarks;
- at high p_T, b and c quarks lose same amount of energy interacting with the medium (i.e. no effect due to the different quark mass).

Assuming a uniform probability distribution of $v_2^{\text{feed-down}}$ in this interval, the central value for v_2^{prompt} is calculated considering:

$$v_2^{\text{feed-down}} = v_2^{\text{prompt}}/2, \tag{5.19}$$

thus:

$$v_2^{\text{prompt}} = 2\, v_2^{\text{obs}}/(1 + f_{\text{prompt}}). \tag{5.20}$$

5.6 Systematic uncertainties on v_2

The main sources of systematic uncertainty affecting the measurement of v_2 are related to:

- signal extraction from the invariant-mass distributions;
- centrality dependence of the resolution term R_2;
- non-flow effects;
- B feed-down subtraction;

5.6.1 Yield extraction systematics

The systematic uncertainty on the yield extraction was estimated by testing different fit configurations. Fits were performed by varying: (i) background fit functions (exponential, first and second order polynomial functions), (ii) lower and upper limits in the fit, (iii) Gaussian peak widths free or fixed to the value extracted from the φ-integrated distribution. Furthermore, the yield was defined by counting the histogram entries in the invariant-mass region of the signal, after subtracting the background contribution estimated from a fit to the side bands. The distributions of residuals between the i^{th} trial and the reference v_2 value, $v_2^{trial} - v_2^{ref}$, were obtained in each p_T interval and are shown in Fig. 5.27. The systematic uncertainty was assigned considering both the shift with respect to zero and the RMS of the residual distributions. The absolute values of this uncertainty range from 0.015 to 0.070 for D_s mesons, depending on the p_T interval.

5.6.2 Event Plane resolution

The event-plane resolution correction factor R_2 depends on the collision centrality [18]. The left-hand panel of Fig. 5.22 shows the resolution R_2 of the event plane determined from the V0 detector as a function of the centrality in the interval 30-50%. The resolution was computed using three sub-events, i.e. the V0 and the TPC tracks in two different η intervals, with and without the introduction of a pseudo-rapidity gap between the two considered TPC regions. The value of resolution used in Eq. 5.17 was computed assuming a uniform distribution of the D-meson yield within the 30-50% centrality class. To estimate the systematic uncertainty, this value was compared

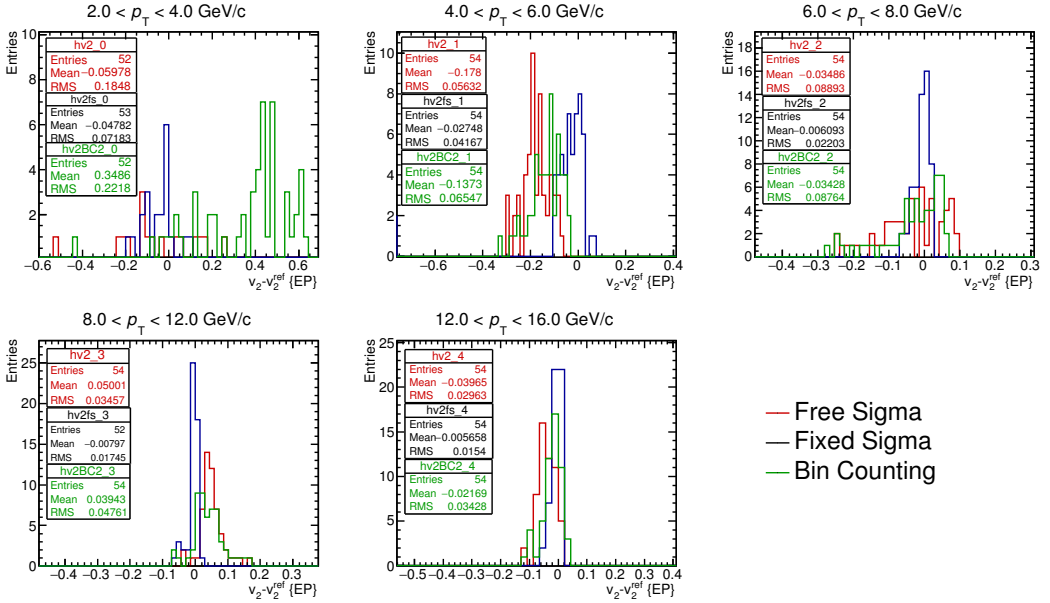

FIGURE 5.27: Residual distributions of v_2 values from multiple-trial procedure for in-plane and out-of-plane yield extraction and default v_2 values. The three distributions refer to yield extraction via fit with Gaussian width left as free parameter (red), fixed to the values from the φ-integrated distribution (black) and to extraction via bin counting method (green).

with those obtained from two alternative approaches based on weighted averages of the R_2 values in narrow centrality intervals, using as weights either the measured D^0-meson yields or the number of nucleon-nucleon collisions from the Glauber model. A systematic uncertainty of 2% on R_2 was estimated from this study.

5.6.3 Non-flow contributions

In order to estimate a possible bias in the R_2 correction factor due to non-flow correlations among the three event planes (computed with the V0 and the TPC tracks in two different η intervals) used for the resolution estimates, the resolution was re-computed introducing a pseudo-rapidity gap between the TPC sub-events. In particular it was considered an eta gap of 0.1 and 0.2 units between the samples of the TPC tracks with positive/negative eta. The left panel of Fig. 5.28 shows the comparison of the event plane resolution as a function of centrality computed without η gap (default), with an η gap of 0.1 units, with an η gap 0.2 units. In the latter case the resolution was also computed applying per-track p_{T} weights in the calculation of the $\vec{Q}_2$ vector with the tracks reconstructed in the TPC. In the right panel of Fig. 5.28 the corresponding relative variation of the event plane resolution is shown and the effect integrated over the 30-50% centrality class is reported in the legend. Considering this observation, an additional 1% systematic uncertainty on the determination of the event plane resolution was assigned.

5.6.4 Feed down systematics

The systematic uncertainty on v_2^{prompt} due to the subtraction of the feed-down contribution is estimated by varying the central value of $v_2^{\text{feed-down}} = v_2^{\mathrm{prompt}}/2$ by $\pm v_2^{\mathrm{prompt}}/\sqrt{12}$, corresponding to ± 1 RMS of a uniform distribution in $(0, v_2^{\mathrm{prompt}})$.

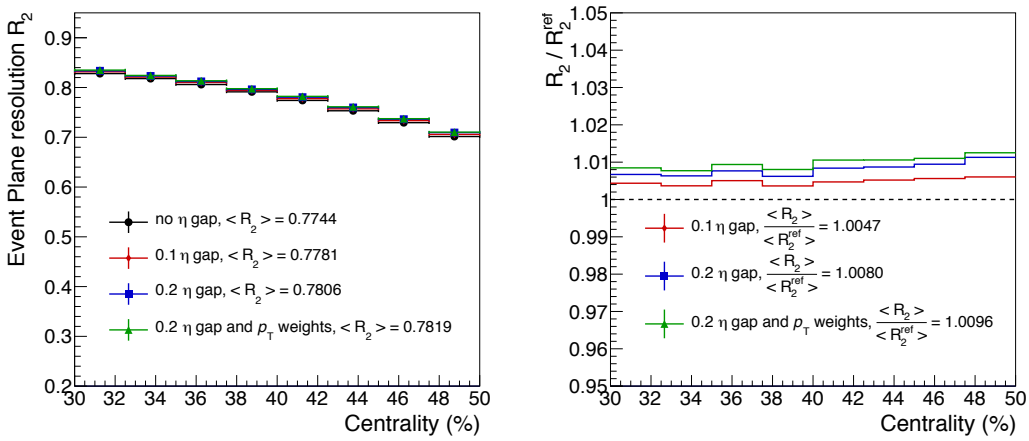

FIGURE 5.28: Event plane resolution as a function of centrality (left) estimated introducing an η gap between the sub-events computed using the TPC tracks and the corresponding relative variation with respect to the default configuration (right).

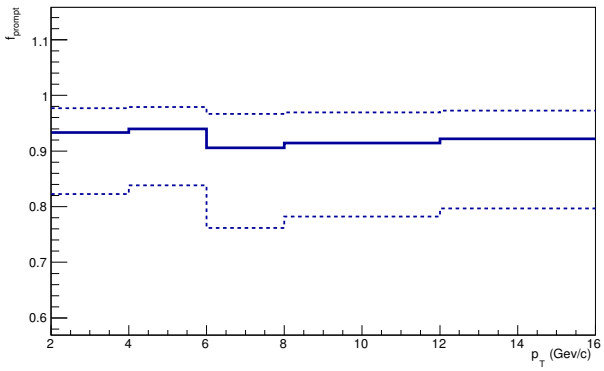

FIGURE 5.29: Values of prompt fraction for D_s mesons in the 30-50% centrality class.

The value of $v_2^{\rm prompt}$ is computed as:

$$v_2^{\rm prompt} = v_2^{\rm obs}/f_{\rm prompt} - (1 - f_{\rm prompt})/f_{\rm prompt} v_2^{\rm feed-down}. \quad (5.21)$$

The maximum and minimum values of $v_2^{\rm prompt}$ were obtained using respectively the minimum and the maximum values of $v_2^{\rm feed-down}$ and $f_{\rm prompt}$. The uncertainty on $f_{\rm prompt}$ is obtained from the variation of the renormalisation and factorisation scales and of the charm quark mass in the FONLL calculation, and from the variation of the $R_{\rm AA}^{\rm feed\text{-}down}$ hypothesis in $\frac{1}{3} < R_{\rm AA}^{\rm feed\text{-}down}/R_{\rm AA}^{\rm prompt} < 3$ [54]. The values of $f_{\rm prompt}$ of $\rm D_s$ mesons are shown in Fig. 5.29 and the error bars include the contributions of the FONLL scales variations and of the variation of the $R_{\rm AA}$ hypothesis. The value of the absolute systematic uncertainty on v_2 due to the correction of the feed-down contribution, which includes also the variation of the hypothesis on $v_2^{\rm feed-down}$, ranges from 0.001 to 0.030 depending on the $p_{\rm T}$ interval.

5.7 Results

The transverse-momentum distributions $\mathrm{d}N/\mathrm{d}p_{\rm T}$ of prompt $\rm D_s^+$ mesons in Pb-Pb collisions at $\sqrt{s_{\rm NN}} = 5.02$ TeV are shown in Fig. 5.30 for the 0-10%, 30-50% and 60-80% centrality classes [222]. They are compared to the corresponding cross-section in pp collisions at the same centre-of-mass energy multiplied by the $\langle T_{\rm AA} \rangle$ of the considered centrality class. The vertical bars represent the statistical uncertainties, the empty boxes the systematic uncertainties from the data analysis, and the shaded boxes the systematic uncertainty due to the subtraction of the feed-down from B-hadron decays. The uncertainty on the branching ratios is quoted separately. The points of the $\mathrm{d}N/\mathrm{d}p_{\rm T}$ in Pb-Pb collisions have empty markers in the interval $12 < p_{\rm T} < 16\,\mathrm{GeV}/c$, because they are obtained with the $p_{\rm T}$-rescaled reference. The $\rm D_s$ yields in Pb-Pb collisions show a suppression relative to the pp reference yields in the 0-10% and 30-50%. The suppression increases with increasing centrality percentile and with the transverse momentum.

The production yields of the different D-meson species were studied by computing the ratios of the $\mathrm{d}N/\mathrm{d}p_{\rm T}$ of $\rm D^0$, $\rm D^+$ and $\rm D_s$ mesons in Pb-Pb collisions and comparing them to those measured in pp collisions at $\sqrt{s} = 7$ TeV. The results for the $\rm D_s/D^0$ and $\rm D_s/D^+$ ratios are shown in the top panels of Fig. 5.31. For comparison, the ratios of non-strange D-meson yields ($\rm D^+/D^0$, $\rm D^{*+}/D^0$) are shown in the bottom panels. The $\rm D^+/D^0$ and $\rm D^{*+}/D^0$ ratios are compatible in Pb-Pb and pp collisions, indicating no significant modification of their relative abundances. In the ratios involving the charmed strange $\rm D_s$ meson a hint of difference is observed. The central values of the $\rm D_s/D^0$ and $\rm D_s/D^+$ ratios are larger in Pb-Pb than in pp collisions, in all three centrality classes, however no strong conclusion can be drawn because the measurements in the two systems are compatible within about one standard deviation of the combined statistical and systematic uncertainties. It is also worth noting that the measurements in Pb-Pb collisions at $\sqrt{s_{\rm NN}} = 5.02$ TeV reported here are more precise than the ones at $\sqrt{s_{\rm NN}} = 2.76$ TeV of Ref. [54], thanks to the larger data sample in the semi-peripheral classes and the improvements in the analysis.

The magnitude of the suppression observed in the $\mathrm{d}N/\mathrm{d}p_{\rm T}$ in Pb-Pb relative to pp collisions can be estimated by looking at the nuclear modification factor presented in Fig. 5.32 [222]. The $R_{\rm AA}$ of prompt $\rm D_s^+$ mesons is shown, for the three different centrality classes, and it is compared to the average $R_{\rm AA}$ of non-strange D mesons.

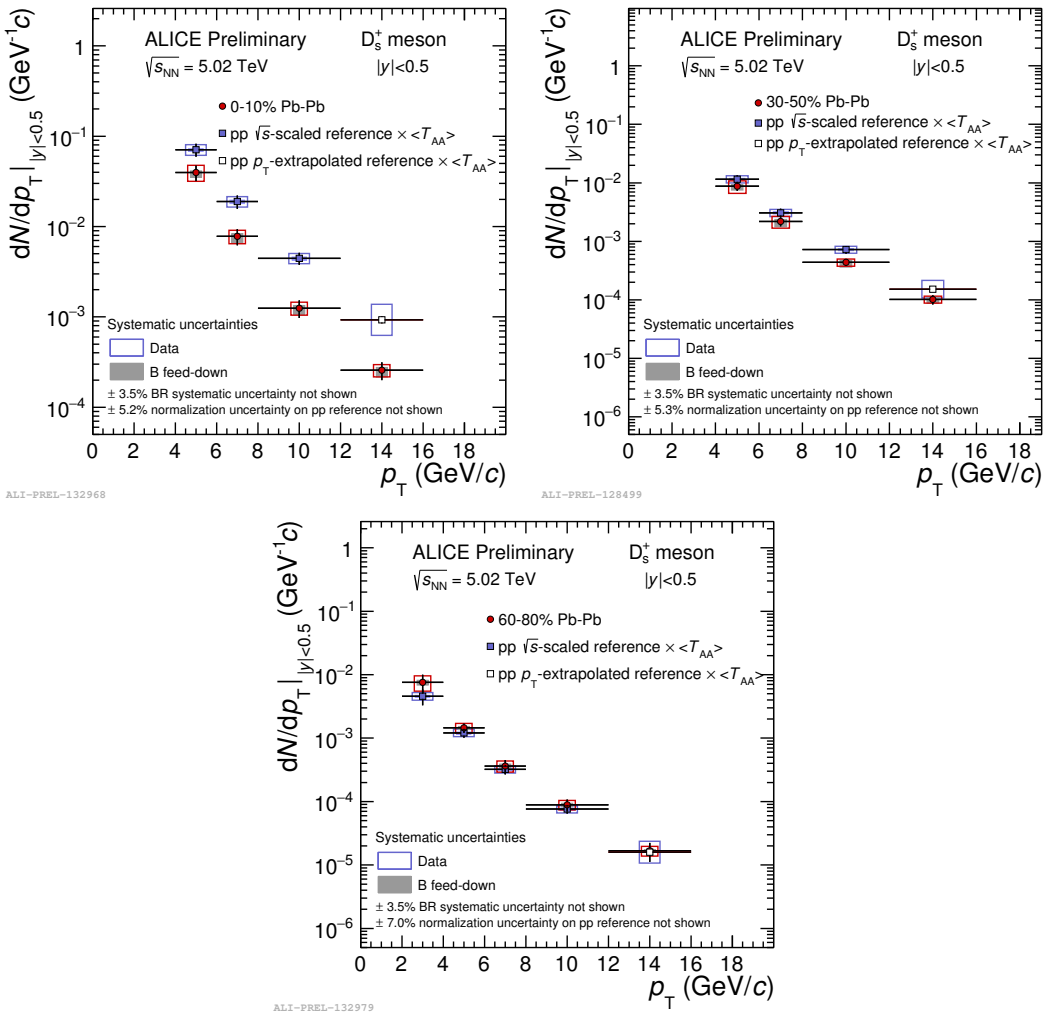

FIGURE 5.30: Transverse momentum distributions $\mathrm{d}N/\mathrm{d}p_\mathrm{T}$ of prompt $\mathrm{D_s}$ meson in the 0–10%, 30–50% and 60–80% centrality classes in Pb–Pb collisions at $\sqrt{s_\mathrm{NN}} = 5.02$ TeV [222].

The $\mathrm{D_s^+}$ nuclear modification factors in the 0–10% and 30–50% centrality classes show a suppression that is maximal at $p_\mathrm{T} = 6$–10 GeV/c, where a reduction of the yields by a factor of about 3 and 1.5 with respect to the binary-scaled pp reference is observed in the two centrality classes, respectively. The average R_AA in the 60–80% centrality class is compatible with unity, without a pronounced dependence on p_T. The central values of the R_AA of $\mathrm{D_s}$ mesons are larger than those of non-strange D mesons but the differences between the strange and non-strange D-meson R_AA are of about one standard deviation of the combined statistical and systematic uncertainties, as in the case of the ratios shown in Fig. 5.31. Therefore, no strong conclusion can be drawn on the predicted difference of $\mathrm{D_s}$ and non-strange D-meson nuclear modification factor in presence of hadronisation via charm quark recombination in the QGP.

In Fig. 5.33, the non-strange and strange D-meson R_AA are compared with the PHSD [245] and TAMU [170] models that provide a calculation for both observables. A larger R_AA of $\mathrm{D_s}$ mesons as compared to non-strange D mesons is expected in the two models, in particular for $p_\mathrm{T} < 5$ GeV/c. Both the calculations are based on heavy-flavour transport with the Langevin approach. In TAMU the interactions

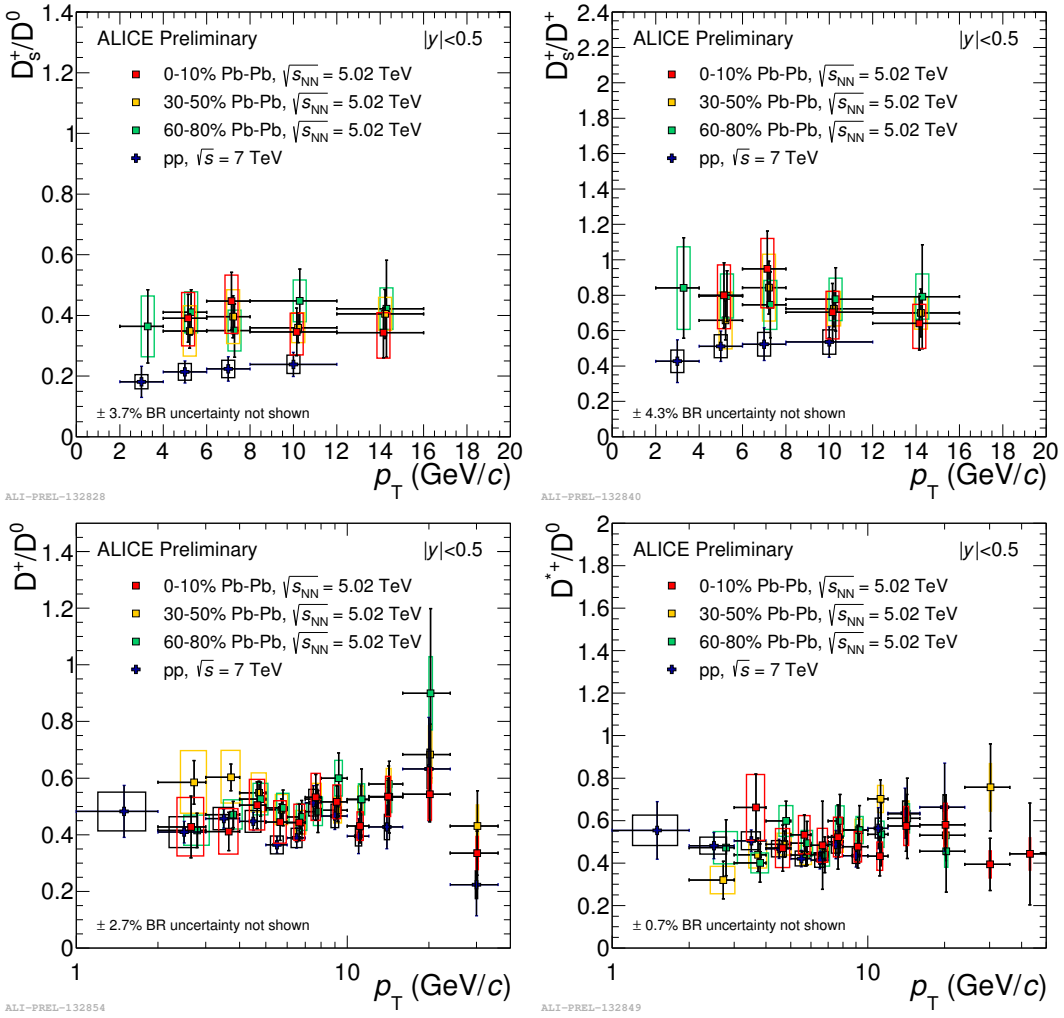

FIGURE 5.31: Ratio of prompt D-meson yields as a function of p_{T} [222]. Statistical (bars) and systematic (boxes) uncertainties are shown.

of the charm quarks with the medium include only collisional (i.e. elastic) processes, while in PHSD [245] also energy loss from medium-induced gluon radiation is considered, in addition to collisional processes. In the models, the enhancement of $\mathrm{D_s}$ R_{AA} with respect to that of non-strange D mesons at low p_{T} is induced by charm-quark recombination with strange quarks in the QGP. It is interesting to note that the TAMU model (see Fig. 5.33) predicts a larger effect than the PHSD model and this is due to the fact that in TAMU the enhancement of strange-quark production in heavy-ion relative to pp collisions is considered. The central values of the measured R_{AA} of strange and non-strange D mesons differ also at $p_{\mathrm{T}} \approx 10$ GeV/c, although the present experimental uncertainties prevent us from drawing a firm conclusion. This difference is absent in the PHSD model. In the TAMU model the difference becomes smaller at $p_{\mathrm{T}} > 10\,\mathrm{GeV}/c$, because the fragmentation mechanism (universal in pp and Pb-Pb) dominates in this region and leads to similar R_{AA} for D and $\mathrm{D_s}$ mesons. The small residual splitting in TAMU model at $p_{\mathrm{T}} > 10\,\mathrm{GeV}/c$ is induced by an extra suppression of D mesons due to interactions in the hadronic phase, which are expected to be small for $\mathrm{D_s}$ mesons [173] and neglected in the calculations.

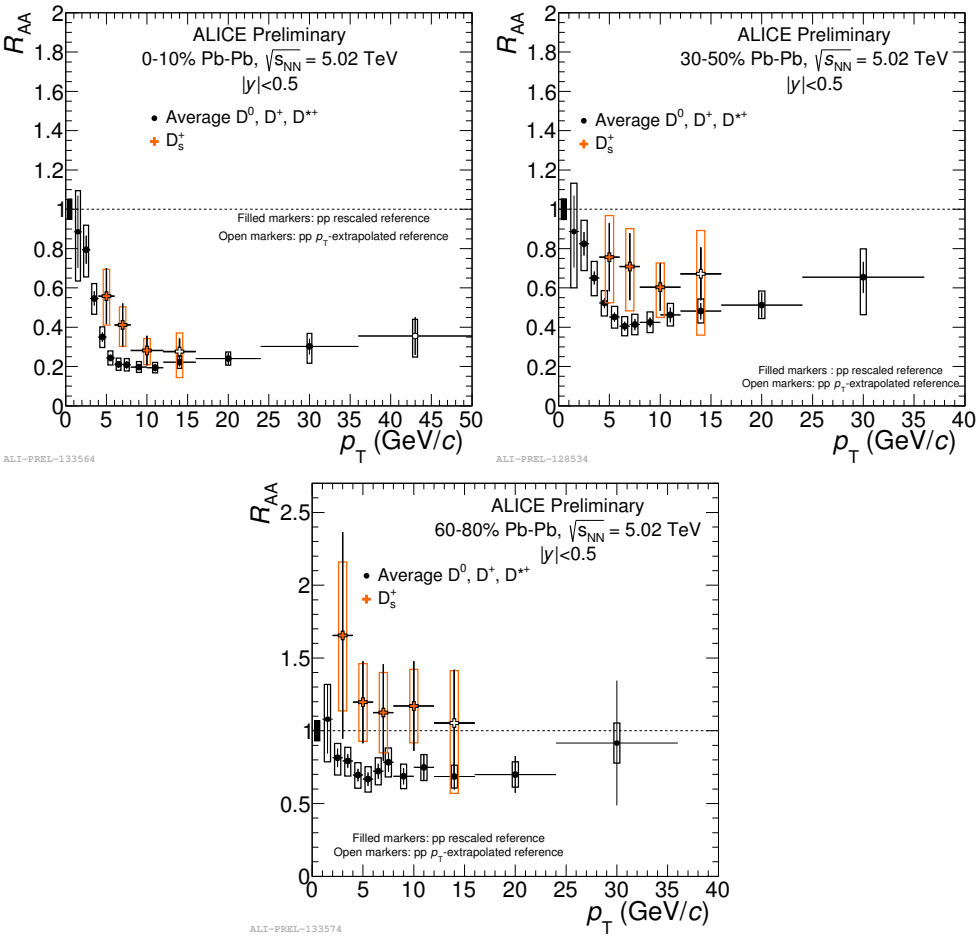

FIGURE 5.32: R_{AA} of prompt D_s^+ mesons compared with the average R_{AA} of D^0, D^+ and D^{*+} mesons for the 0–10%, 30–50% and 60–80% [222]. Statistical (bars), systematic (empty boxes), and normalisation (shaded box) uncertainties are shown.

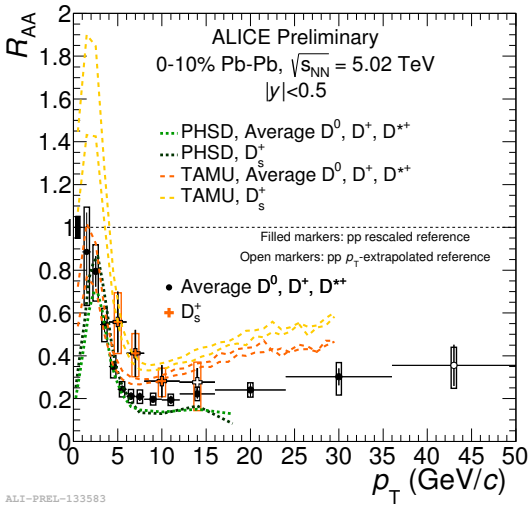

FIGURE 5.33: Average R_{AA} of D^0, D^+ and D^{*+} mesons and R_{AA} of D_s mesons in the 0–10% centrality class [222] compared with the PHSD [245] and TAMU [170] model calculations.

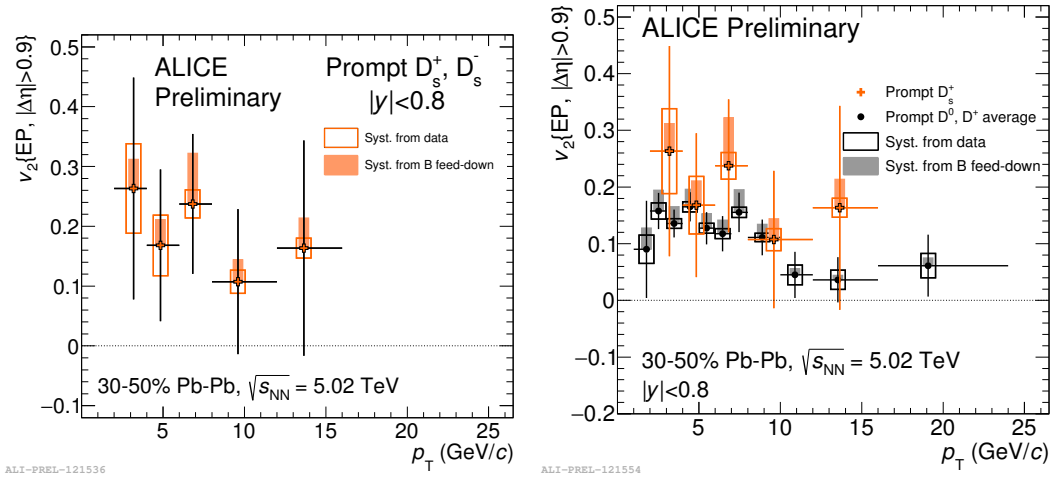

FIGURE 5.34: Elliptic flow v_2 as a function of p_T for prompt D_s mesons and their charge conjugates for Pb–Pb collisions at $\sqrt{s_{NN}} = 5.02$ TeV in the centrality class 30-50% [41]. Right: comparison with average non-strange D meson v_2 as a function of p_T, for the 30-50% centrality class in Pb-Pb collisions [41].

The v_2 of prompt D_s mesons in the 30–50% centrality class is shown as a function of p_T in Fig. 5.34 [41]. The symbols are positioned at the average p_T of the reconstructed D_s mesons in the considered p_T interval. This $\langle p_T \rangle$ value was determined as the average of the p_T distribution of candidates in the signal invariant-mass region, after subtracting the contribution of the background candidates estimated from the side bands. The average v_2 of D_s meson in the intervals $2 < p_T < 8$ GeV/c is $\langle v_2 \rangle = (0.226^{+0.138}_{-0.088})$, where the uncertainty was calculated using quadratic error propagation for the statistical and uncorrelated systematic uncertainties (signal extraction) and linear propagation for the correlated systematic uncertainties (R_2 and feed-down correction). The average v_2 of D_s is positive with a significance of $2.6\,\sigma$ of its uncertainty. The v_2 of D_s mesons is compared to the average v_2 of D^0, D^+ and D^{*+} as a function of p_T in the right panel of Fig. 5.34. The v_2 of D_s and non-strange D mesons are found to be compatible within uncertainties [41].

In Fig. 5.35, the measured v_2 is compared to theoretical calculations. Both TAMU and PHSD predict similar v_2 for strange and non-strange D mesons. In the TAMU model, the small difference between v_2 of D_s and that of non-strange D mesons is due to the fact that the D_s spectra freeze out after hadronisation, while D mesons couple to the hadronic medium, and this further enhances their v_2 by 30%. Therefore, the v_2 splitting between non-strange D and D_s mesons is also a promising measure of the transport properties of the hadronic phase, although the current uncertainties do not allow to draw strong conclusions. The TAMU model describes the magnitude of the elliptic flow, but fails in reproducing the shape, probably due to the missing radiative term for the energy loss. Larger statistical samples are essential to reduce the current uncertainties and will allow firmer constraints on the models via simultaneous comparison of R_{AA} and elliptic flow v_2 measurements.

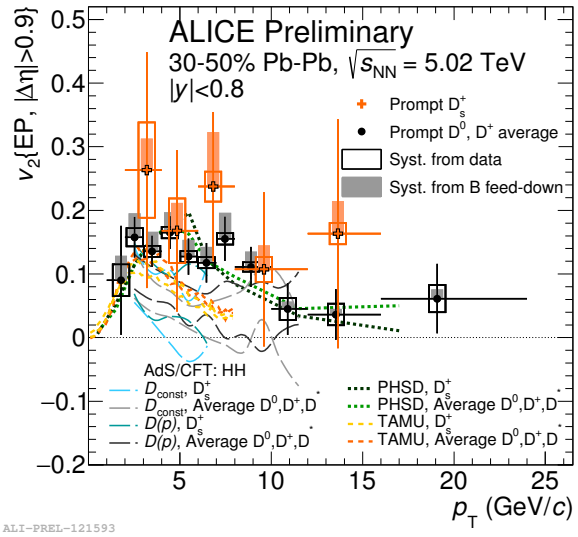

FIGURE 5.35: v_2 of D_s mesons for Pb-Pb collisions at $\sqrt{s_{NN}} = 5.02$ TeV in the 30-50% centrality class [41] compared with the PHSD [245] and TAMU [170] model calculations.

5.8 Discussion and perspectives

In the previous sections, the measurements of D_s^+-meson dN/dp_T and R_{AA} in the 0-10%, 30-50% and 60-80% centrality classes and of D_s^+-meson v_2 in the 30-50% class in Pb-Pb collisions at $\sqrt{s_{NN}} = 5.02$ TeV were presented. The measurement of D_s^+ production can provide insight into charm-quark hadronisation in presence of a QGP. According to theoretical models, a significant fraction of charm quarks could undergo hadronisation via in-medium coalescence at intermediate and low momentum [164]. Furthermore, an enhancement of strangeness production with respect to pp collisions was long suggested as a possible signal of QGP formation [227]. Strange and multi-strange hadron enhancement was observed from SPS to LHC energy, showing a dependence on the strangeness content of the particles and also on the collision centrality [52, 89, 20, 35]. The possibility of coalescence of charm quarks with the medium constituents, together with the observed strangeness enhancement, is predicted to lead to a larger relative abundance of D_s mesons compared to non-strange D mesons when going from pp to Pb-Pb collisions [173].

The central values of the measured ratios of D_s^+ to non-strange D meson yields in Pb-Pb collisions, for all the centrality classes, are higher than those in pp collisions, although the results in Pb-Pb and pp interactions are compatible within 1σ of the combined statistical and systematic uncertainty. The magnitude of the suppression observed in the D_s^+ yield in Pb-Pb relative to pp collisions was estimated via the nuclear modification factor. The central values of the D_s^+ R_{AA} are larger than those of non-strange D mesons but compatible within uncertainties. The D_s^+ R_{AA} is minimum at $p_T = 6$–10 GeV/c in the 0-10% centrality class, where the yields are suppressed by a factor of about 3 with respect to the binary-scaled pp reference. The measured suppression of D_s mesons can be described by models that include interaction of charm quarks with an hydrodynamically expanding QGP via collisional (and radiative) processes and in-medium coalescence of charm quarks with thermalised light quarks of the bulk. However, the current uncertainties do not allow to discriminate among

different models and, in particular, different hadronisation mechanisms. To conclude about the predicted enhancement of the D_s^+ yield relative to non-strange D mesons in heavy-ion collisions and about the centrality dependence of D_s^+ R_{AA}, the uncertainties need to be reduced. The elliptic flow of D_s^+ meson was measured for the first time. The average v_2 of D_s^+ mesons is positive within 2.6σ of the combined statistical and systematic uncertainty in the interval $2 < p_T < 8\,\mathrm{GeV}/c$. This together with the results on v_2 of D^0, D^+ and D^{*+} indicates that low-momentum charm quarks take part in the collective motion of the QGP and that interactions with the medium constituents as well as recombination of charm and light quarks contribute to the observed elliptic flow. The comparison of the v_2 of D_s^+ and non-strange D mesons is also a expected to be sensitive to the properties of the medium during the hadronic phase [170], although possible effects are not appreciable with the current statistical sample.

The measurements will benefit from the larger data sample that will be collected in the Pb-Pb run at $\sqrt{s_{NN}} = 5.02$ TeV in 2018. A sample of more than 100M central collisions could be recorded by ALICE. This will allow to reduce the statistical uncertainty on the D_s^+ yield in Pb-Pb from $\sim 20\%$ (current) to $\sim 6\%$ in the p_T interval $4 < p_T < 6\,\mathrm{GeV}/c$. Furthermore, with the recent pp run at the same centre-of-mass energy of Pb-Pb sample, the $\sqrt{s}$-scaling of the pp cross section will not be anymore necessary. The contribution to the systematic uncertainty from the $\sqrt{s}$-scaling is currently $\sim 4\%$ in $4 < p_T < 6\,\mathrm{GeV}/c$.

A further improvement in the precision of the measurements will be achieved with the data samples that will be collected in the Run 3, after 2020. A completely new Inner Tracking System will be constructed for LHC Run 3. The new detector will consists of seven layers of Monolithic Active Pixel Sensors and it will improve the impact parameter resolution σ_{d0} over the full p_T range, providing $\sigma_{d0} < 50\,\mu\mathrm{m}$ at $p_T = 0.4\,\mathrm{GeV}/c$. The resolution of the new ITS will provide an increase of the S/B by a factor larger than 2 at low p_T as compared to the current ITS, thanks to the improved resolution on primary and secondary vertex reconstruction. In addition, a larger integrated luminosity will be collected during the Run 3, reaching 10 nb^{-1} for Pb-Pb collisions. Hence, the Run 3 data samples are expected to allow us to draw firm conclusions about in-medium charm quark hadronisation and energy loss.

Chapter 6

$\mathrm{D_S^+}$ production in p-Pb collisions at $\sqrt{s} = 5.02$ TeV as a function of multiplicity

In this Chapter the measurement of the ratios of $\mathrm{D_s^+}$-meson yield to that of the non-strange $\mathrm{D^+}$ meson is presented as a function of the primary charged-particle multiplicity produced in p-Pb collisions at $\sqrt{s_{\mathrm{NN}}} = 5.02$ TeV and compared to results from pp collisions at $\sqrt{s} = 7$ TeV [43] and Pb-Pb interactions at $\sqrt{s_{\mathrm{NN}}} = 5.02$ TeV [222]. A primary charged particle is a charged particle with mean proper lifetime τ larger than 1 cm, which is either produced directly in the interaction or from decay of particles with $\tau < 1$ cm/c. In presence of a medium composed of deconfined quarks and gluons, a modification of the hadronisation mechanisms is expected due to the possible formation of hadrons via coalescence of charm quarks with other quarks from the medium during the deconfined phase or at the phase boundary [163, 164, 82, 173]. This coalescence mechanism competes with fragmentation. The enhancement of strange quark abundance in the QGP (see Sec. 1.5.3) could affect the production of charmed hadrons if the dominant mechanism for D-meson formation at low and intermediate momenta is in-medium recombination. In particular, the relative yield of $\mathrm{D_s}$ mesons with respect to non-strange charmed mesons at low p_{T} is predicted to be enhanced in nucleus-nucleus collisions as compared to pp interactions [84, 191, 172]. The measurements of $\mathrm{D_s^+/D^0}$ and $\mathrm{D_s^+/D^+}$ ratios in Pb-Pb collisions presented in Chapter 5 indicate higher values in Pb-Pb than in pp collisions, although the values are compatible within 1σ of the combined statistical and systematic uncertainties. Given the observed increase of strange particle production with increasing particle multiplicity in pp and p-Pb collisions [35, 57, 52], which reaches yields compatible with those observed in Pb-Pb collisions at similar multiplicities, the possible hadronisation via coalescence could result in an enhancement of the relative yield of $\mathrm{D_s^+}$ meson with respect to non-strange D mesons in high multiplicity p-Pb collisions.

6.1 Event selection

The analysis was performed on the data sample of p-Pb collisions at $\sqrt{s_{\mathrm{NN}}} = 5.02$ TeV collected in 2016. Events were recorded with a minimum-bias (MB) interaction trigger that required coincident signals in both scintillator arrays of the V0 detector. The V0 timing information was used together with that from the ZDCs for offline rejection of events produced by the interaction of the beams with residual gas in the vacuum pipe. The MB trigger was estimated to be sensitive to about 96.4% of the p-Pb inelastic cross section. For the data sample analysed here, the probability of event pile-up in the same bunch crossing was below 0.5% per triggered p-Pb event.

The remaining undetected pile-up is negligible in the present analysis. An algorithm to detect multiple interaction vertices was used to reduce the pileup contribution. An event was rejected if a second interaction vertex was found. Only events with a primary vertex reconstructed within ±10 cm from the centre of the detector along the beam line were considered. The number of events passing these selection criteria was about 6×10^8. This number is larger by a factor of ∼6 with respect to the number of events analysed with the p-Pb sample collected in 2013 [34, 46, 45] where, due to the limited statistics, the measurement of D_s production in multiplicity classes was not possible. The corresponding integrated luminosity of the current sample is $L_{\rm int} = N_{\rm MB}/\sigma_{\rm MB} = 292 \pm 11\ \mu{\rm b}^{-1}$, where $\sigma_{\rm MB} = 2.09$ b is the MB-trigger cross section measured via a van der Meer scan, with negligible statistical uncertainty and a systematic uncertainty of 3.7% [29]. During the p-Pb data taking, the beam energies were 4 TeV for protons and 1.58 TeV per nucleon for lead nuclei. With this beam configuration, the nucleon-nucleon centre-of-mass system moves in rapidity by $\Delta y_{\rm cms} = 0.465$ in the direction of the proton beam. The D-meson analyses were performed in the laboratory-frame interval $|y_{\rm lab}| < 0.5$, which leads to a shifted centre-of-mass rapidity coverage of $-0.96 < y_{\rm cms} < 0.04$.

During the p-Pb data taking, two different detector clusters were used to collect data, depending on the availability of the SDD detector in the readout. Consequently, the respective reconstructions have different detector configurations and their $p_{\rm T}$ resolution may differ. It was verified that the width and the position of the D-meson signal peaks were compatible in the two reconstructions, as a function of $p_{\rm T}$.The two samples were hence merged and used in the analysis in order to maximise the statistics.

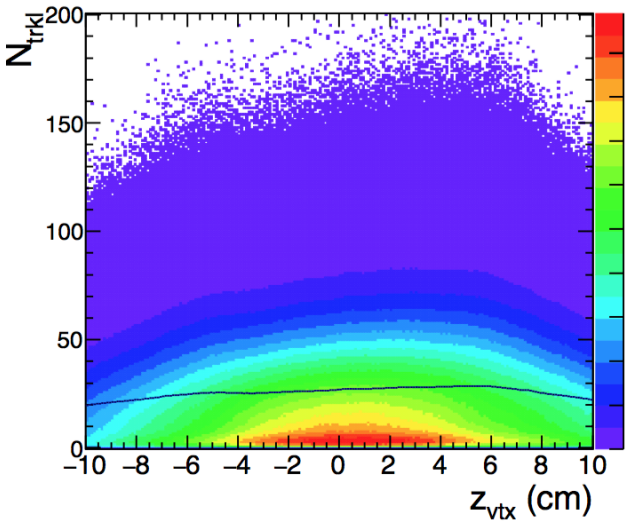

FIGURE 6.1: $N_{\rm trkl}$ distribution as a function of the $z_{\rm vtx}$ coordinate.

6.2 Equalisation of $N_{\rm tracklets}$ distribution as a function of $z_{\rm vtx}$

The ratios of D_s^+ /D^+ yields were studied as a function the charged-particle multiplicity in different $p_{\rm T}$ intervals. The multiplicity estimator used for this analysis was based on the number of tracklets reconstructed in the SPD within a pseudo-rapidity

range of $|\eta| < 1$. A tracklet in the SPD is obtained by joining space points on the two SPD layers and it is required to point to the reconstructed primary vertex. In Fig. 6.1, the distribution of the number of tracklets ($N_{\rm trkl}$) in $|\eta| < 1$ as a function of the z coordinate of the vertex ($z_{\rm vtx}$) is shown. The average number of tracklets $< N_{\rm trkl} >$ as a function of $z_{\rm vtx}$ is also shown in the plots. The trend of $< N_{\rm trkl} >$ as a function of $z_{\rm vtx}$ is related to the SPD geometrical acceptance, which does not cover the range $-1 < \eta < 1$ for collisions with $|z_{\rm vtx}| > 5-6$ cm. Therefore, lower $< N_{\rm trkl} >$ values towards $|z_{\rm vtx}| \sim 10$ cm are due to the finite acceptance of the SPD layers. The modification of the number of active SPD modules during the data acquisition affects also the number of reconstructed tracklets. For this reason, the distribution of $< N_{\rm trkl} >$ as a function of $z_{\rm vtx}$ and as a function of the time during the data taking needs to be equalised in order to consistently define the $N_{\rm trkl}$ intervals in which the analysis is performed. Otherwise, a given $N_{\rm trkl}$ interval would correspond to different real charged particle multiplicities, depending on $z_{\rm vtx}$ or data taking time. To this purpose, the average profile of $N_{\rm trkl}$ as a function of $z_{\rm vtx}$ was analysed on a run-by-run basis over the full period, to evaluate the stability of $< N_{\rm trkl} >$ versus $z_{\rm vtx}$ as a function of time. Four bunches of runs were defined corresponding to different SPD configurations on the A-side of the detector and showing up to ∼10% difference in the $< N_{\rm trkl} >$ values at positive values of $z_{\rm vtx}$. Fig. 6.2 (left) shows the ratios of the $N_{\rm trkl}$ profiles of the run groups 1, 2 and 3 to group 4, which is the one with the lowest average tracklet multiplicity. The equalisation of $< N_{\rm trkl} >$ as a function of $z_{\rm vtx}$ was applied on an event-by-event basis on each of the four groups of runs separately. The $< N_{\rm trkl} >$ value that was used as the absolute reference multiplicity value was defined as the maximum of $< N_{\rm trkl} >$ value as a function of $z_{\rm vtx}$ and time, resulting $N_{\rm trkl}^{\rm ref} = 29.2$. The number $N_{\rm trkl}^{\rm raw}$ of reconstructed tracklets in each event is corrected by using a Poissonian term as follows:

$$N_{\rm trkl}^{\rm corr} = N_{\rm trkl}^{\rm raw} + {\rm Pois}(\Delta N), \tag{6.1}$$

where:

$$\Delta N = \Big(\frac{N_{\rm trkl}^{\rm ref}}{\langle N(z_{\rm vtx}) \rangle} - 1 \Big) \cdot N_{\rm trkl}^{\rm raw}. \tag{6.2}$$

The reference multiplicity value $N_{\rm trkl}^{\rm ref}$ was chosen as the maximum value of the $< N_{\rm trkl} >$ distribution, in order to assure that ΔN follows a Poissonian distribution. The average $< N_{\rm trkl} >$ profiles of the four bunches of runs after the $z_{\rm vtx}$ equalisation are shown in the right panel of Fig. 6.2. They were fitted with a pol1 function in order to check the flatness of the distribution. The slope of the fit function resulted compatible with zero validating the efficiency of the correction procedure.

6.3 Raw-yield extraction

The $\rm D_s^{\pm}$ signal was extracted in five $p_{\rm T}$ intervals from 2 to 16 GeV/c, in three different classes of $N_{\rm trkl}^{\rm corr}$: $[1, 40)$, $[40, 70)$, $[70, 200]$ tracklets, corrected for SPD acceptance effects described in Sec. 6.2. The intervals were chosen in order to have sufficient statistics for the $\rm D_s$-meson yield extraction. They contain, in the order, 26.7%, 45.3% and 28% of total number of events. The $\rm D_s^+ \to K^+K^-\pi^+$ candidates were built from triplets of tracks as described in Chapter 4 and they were selected by applying cuts on the displaced vertex topology, the invariant mass of the $\rm K^+K^-$ pair and the dE/dx and time of flight of the decay tracks. The $\rm D_s^{\pm}$ raw yield was extracted via fits to the invariant-mass distributions of candidates passing the selection criteria described

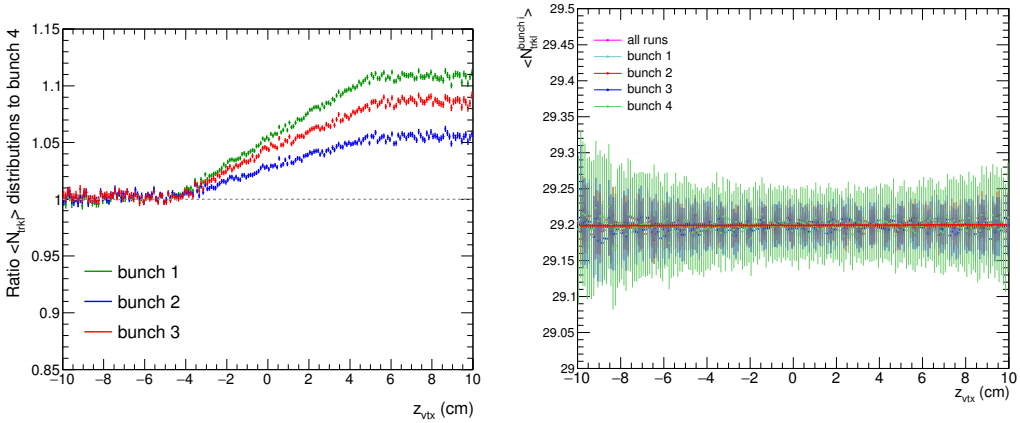

FIGURE 6.2: Left: ratio of $< N_{\rm trkl} >$ distributions of run groups 1, 2 and 3 to group 4 in different colours, as a function of $z_{\rm vtx}$. Right: $< N_{\rm trkl} >$ distributions as a function of $z_{\rm vtx}$ for the four groups of runs in different colours, after equalisation over $z_{\rm vtx}$.

above. The fit function is composed of two Gaussians to model the D_s peak and the $D^+ \to K^+K^-\pi^+$ decay contribution, which give rise to a peak around 1.88 MeV/c^2, and an exponential function to describe the background. The position and width of the Gaussian function used to fit the D^+ peak were fixed respectively to the D^+ invariant mass from PDG and to the value of the width from the simulations. The cuts were tuned in each $p_{\rm T}$ interval to have good statistical significance of the extracted yields and are summarised in Tab. 6.1. The same selection criteria were used in the three multiplicity classes. The particle identification selection is described in Sec. 4.5. It considers a track to be compatible with the kaon or pion hypothesis if both its dE/dx and time of flight are within 3σ from the expected values. Tracks without a TOF signal (mostly at low momentum) are identified using only the TPC information and requiring a 2σ compatibility with the expected dE/dx. Fig. 6.3, 6.4 and 6.5 show

D_s selections	$p_{\rm T}$ interval (GeV/c)				
	2–4	4–6	6–8	8–12	12–16
Decay length (μm)	>300	>350	>350	>400	>400
Decay length XY (μm)	>0	>200	>200	>200	>200
Norm Decay length XY	>2.0	>0.0	>2.0	>2.0	>2.0
Cosine pointing	>0.94	>0.95	>0.95	>0.97	>0.97
σ_{vertex} (cm)	<0.02	<0.03	<0.03	<0.06	<0.06
ΔM (MeV/c^2)	<8.0	<10.0	<4.5	<9.0	<9.0
$\cos\theta^*(\pi)$	<1.0	<1.0	<1.0	<0.95	<0.95
$\lvert\cos^3\theta'(\mathrm{K})\rvert$	>0.10	>0.05	>0.05	>0.05	>0.05
Norm. IP residual	<2.5	<2.0	<2.0	<2.0	<2.0

TABLE 6.1: Selection criteria used for D_s candidates in the five transverse momentum intervals considered for the three $N_{\rm trkl}$ classes.

the invariant-mass fits performed in the five $p_{\rm T}$ intervals, for the three multiplicity classes. To avoid fluctuations, the D_s peak widths were fixed to the values obtained from the multiplicity-integrated sample of simulated $D_s^+ \to K^+K^-\pi^+$ decays. To this purpose, it was verified that the width of the D_s peak in the simulation and in data does not depend on the multiplicity intervals, as it can be seen in Fig. 6.6, in the left

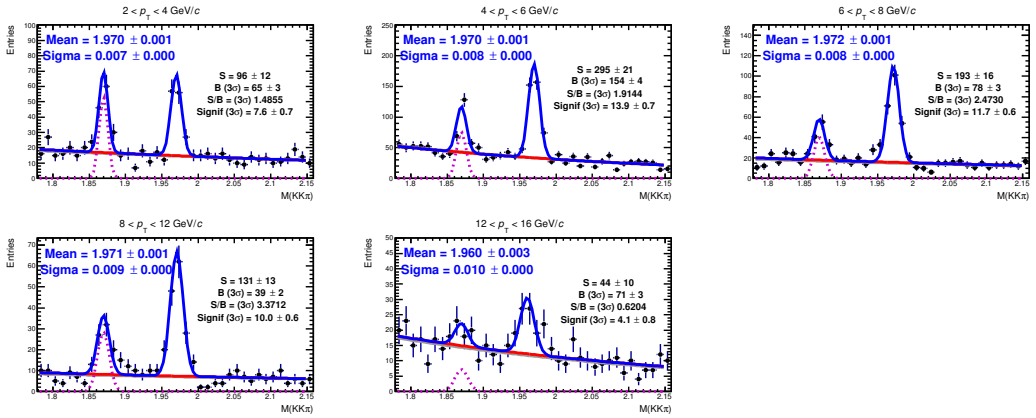

FIGURE 6.3: D_s^+ candidate (and charge conjugates) invariant-mass spectra, in five p_T intervals from $2 < p_T < 16$ GeV/c, in the $1 \leq N_{trkl} < 40$ multiplicity interval.

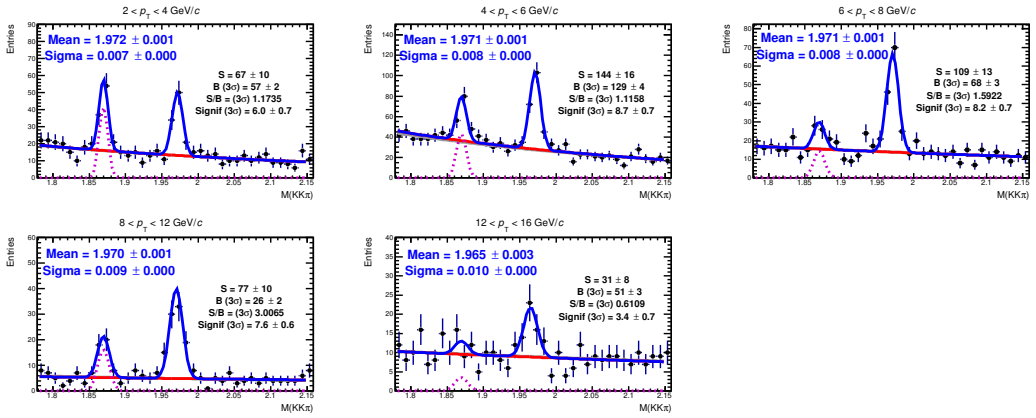

FIGURE 6.4: D_s^+ candidate (and charge conjugates) invariant-mass spectra, in five p_T intervals from $2 < p_T < 16$ GeV/c, in the $40 \leq N_{trkl} < 70$ multiplicity interval.

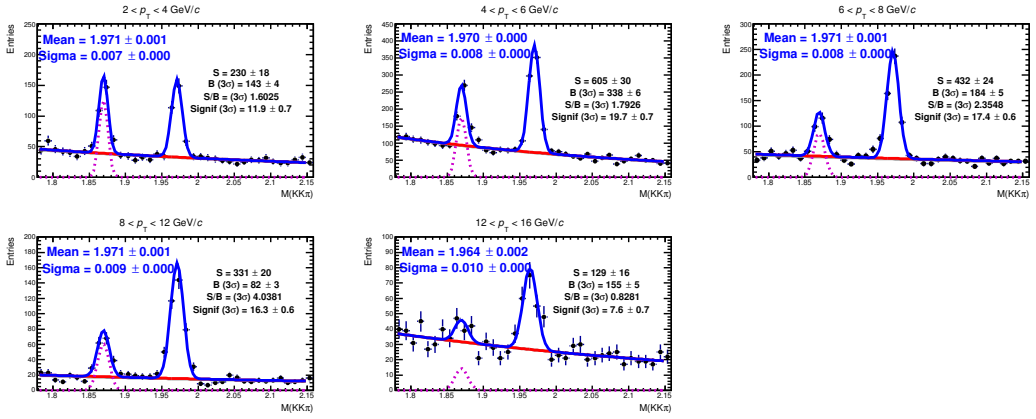

FIGURE 6.5: D_s^+ candidate (and charge conjugates) invariant-mass spectra, in five p_T intervals from $2 < p_T < 16$ GeV/c, in the $70 \leq N_{trkl} \leq 200$ multiplicity interval.

and right panels, respectively. In Fig. 6.7 the Gaussian peak positions in data for the three intervals of $N_{\rm trkl}$ are compared to the values of the widths extracted from the fit on the distribution integrated over multiplicity in data and in the simulation and to the PDG value.

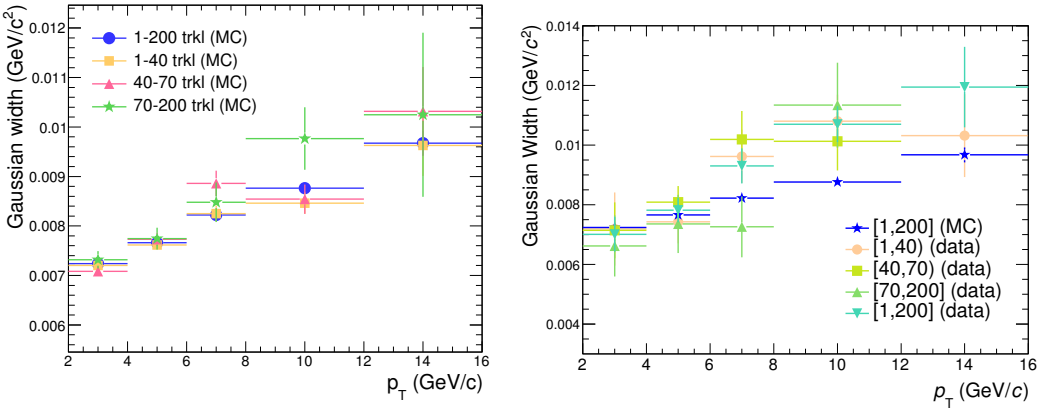

FIGURE 6.6: D_s peak widths as a function of p_T, obtained from the fits to the invariant-mass distributions in the three $N_{\rm trkl}$ intervals in simulations (left) and in data (right) compared to the widths extracted from the fit in the sample integrated over multiplicity.

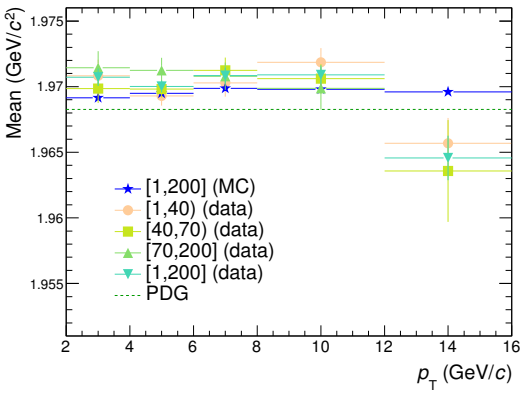

FIGURE 6.7: D_s peak position obtained from the fits to the invariant mass distribution in the three intervals of $N_{\rm trkl}$ in data compared to the data and simulations integrated over multiplicity.

6.4 Corrections

The D_s^+/D^+ ratios in the multiplicity class i and the p_T interval j were calculated as:

$$\frac{(\mathrm{d}^2N_{\mathrm{D_s^+}}/\mathrm{d}p_\mathrm{T}\mathrm{d}y)}{(\mathrm{d}^2N_{\mathrm{D^+}}/\mathrm{d}p_\mathrm{T}\mathrm{d}y)}\Big|_i = \frac{Y^{i,j}_{\mathrm{D_s^+}} f^{i,j}_{\mathrm{prompt,D_s^+}}/(\mathrm{Acc}\times\epsilon)^{i,j}_{\mathrm{promptD_s^+}}}{Y^{i,j}_{\mathrm{D^+}} f^{i,j}_{\mathrm{prompt,D^+}}/(\mathrm{Acc}\times\epsilon)^{i,j}_{\mathrm{promptD^+}}} \cdot \frac{\mathrm{BR}(\mathrm{D_s^+}\to\mathrm{K^+K^-\pi^+})}{\mathrm{BR}(\mathrm{D^+}\to\mathrm{K^-\pi^+\pi^+})}, \tag{6.3}$$

where $Y^{i,j}_{\rm D}$ is the extracted yield of D_s^+ and D^+, which is corrected for the prompt fraction $f^{i,j}_{\rm prompt}$, for the acceptance-times-efficiency term $(\mathrm{Acc}\times\epsilon)^{i,j}$ and for the branching

ratio BR of the decay channel, which is different for D_s^+ and D^+.

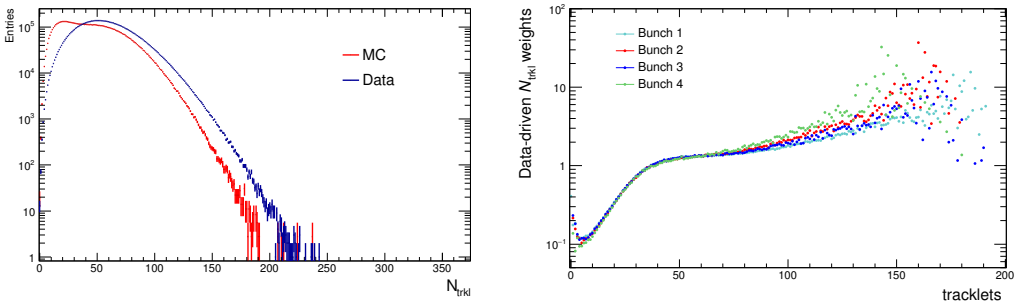

FIGURE 6.8: Left: tracklets distribution in data and in MC in different colours. Right: data-driven weights used to correct the efficiencies as a function of the tracklet multiplicity, for the four groups of runs in different colours.

The acceptance-times-efficiency term was obtained via Monte Carlo simulations using PYTHIA v6.4.21 [243] with Perugia-2011 tuning as event generator. A HIJING [255] p-Pb event is added as underlying event to the PYTHIA one in a fraction of events corresponding to the probability of having $N_{\rm coll} > 1$ in the Glauber MC simulations of p-Pb collisions. Particles were transported through the detectors using the GEANT3 package [115]. Fig. 6.8 (left) shows the distributions of the number of SPD tracklets $N_{\rm trkl}$ in $|\eta| < 1$ in data and simulation. The events selected to fill the distributions were required to have at least a $D^0 \to K^-\pi^+$ meson candidate passing the selection criteria, with the invariant mass compatible within 3σ to the D^0 mass from PDG (σ being the width of $D^0 \to K^-\pi^+$ invariant-mass peak). The choice of D^0 meson was made in order to study the multiplicity distribution of events with charm production which differ from that of minimum bias events. Measurements in pp collisions [68] show that the events with charm production have on average higher multiplicity than minimum-bias collisions. In particular, among the different D-meson species, the $D^0 \to K^-\pi^+$ decays were used in this study because of their large abundance and high signal-to-background ratio. The distributions in Fig. 6.8 (left) are shown before the correction for the $z_{\rm vtx}$ equalisation. It is evident that the $N_{\rm trkl}$ distributions in data and MC are different. For this reason, since the selection efficiency depends on multiplicity, the calculation of (Acc $\times$ ϵ) from the simulation was done with with data-driven multiplicity weights. These multiplicity weights were extracted separately for each of the four groups of runs discussed in Sec. 6.2, corresponding to different SPD configurations. The weights were defined as the ratios of the multiplicity distribution in data and in the simulations, and their distributions as a function of the $N_{\rm trkl}$ multiplicity are shown in Fig. 6.8 (right), in different colours for the fours groups of runs. The ratios of the weights from the four groups of runs to the ones integrated over all runs is shown in Fig. 6.9. Furthermore, the simulated $N_{\rm trkl}$ distribution does not reach the highest $N_{\rm trkl}$ values observed in data. However, it was verified that the selection efficiency of D_s mesons does not depend on the tracklet multiplicity for $N_{\rm trkl} > 20$, as it is shown in Fig. 6.10 (left). Hence, the different maximum $N_{\rm trkl}$ values in data and MC does not introduce a bias. The efficiencies were re-weighted separately for each of the three intervals of tracklets in which the analysis was performed, using the procedure discussed above and considering the respective $N_{\rm trkl}^{\rm corr}$ distributions in data to calculate the weights. The re-weighted acceptance-times-efficiency values for the three $N_{\rm trkl}$ classes are presented in the right panel of

Fig. 6.10 as a function of $N_{\rm trkl}$, for the five analysed $p_{\rm T}$ intervals in different colours. As shown in this figure, the efficiency is almost flat as a function of the event multiplicity.

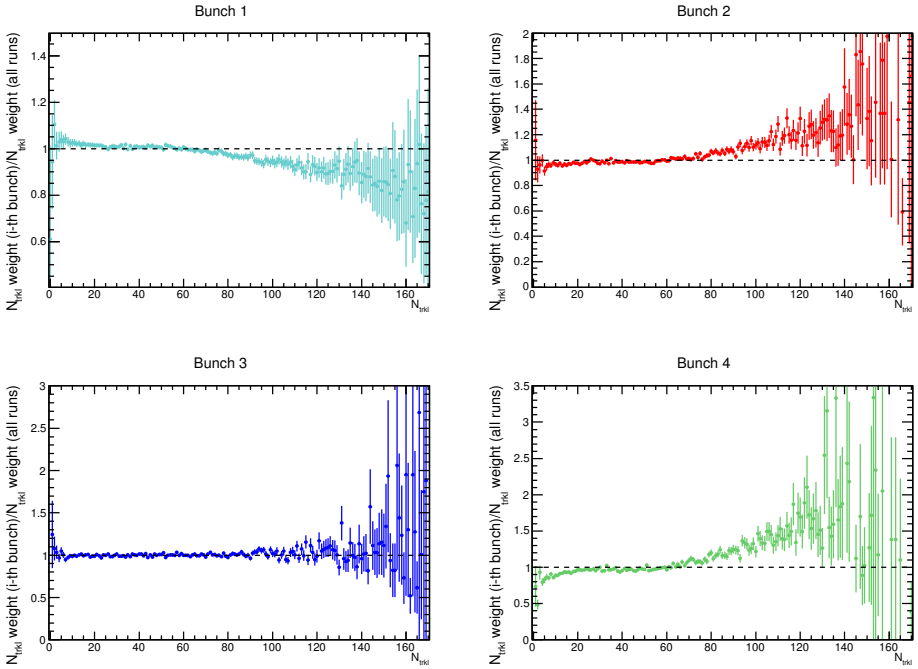

FIGURE 6.9: Ratios of multiplicity weights for each of the four groups of runs to the weights computed for the full sample.

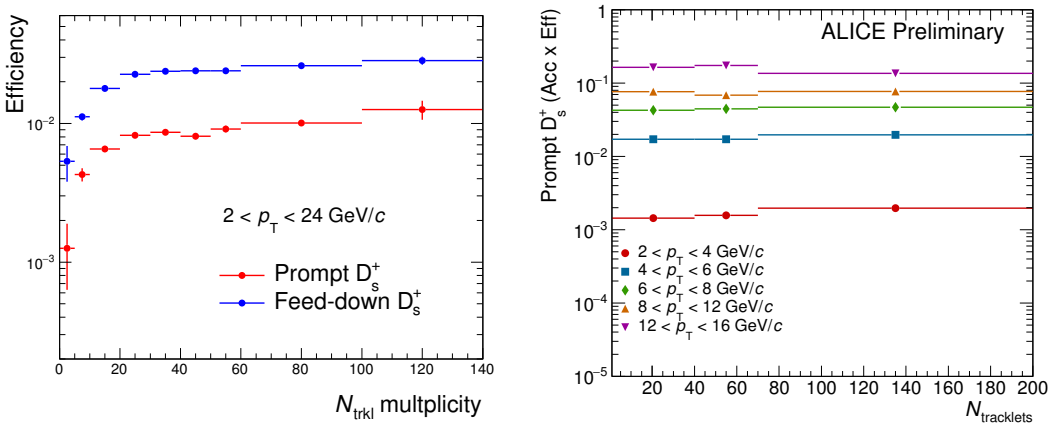

FIGURE 6.10: Left: D_s efficiency as a function of the tracklet multiplicity in fine intervals of $N_{\rm trkl}$, for prompt (in red) and feed-down (in blue) D_s^+. Right: D_s efficiency as a function of the tracklet multiplicity for the three $N_{\rm trkl}^{\rm corr}$ intervals used in the analysis, for the five $p_{\rm T}$ intervals in different colours. The dashed lines represent the uncertainty band on $f_{\rm prompt}$.

For the subtraction of the B feed-down contribution to the raw yields, the FONLL-based method described in Eq. 5.2 was used. It was assumed that the fractions of prompt D_s^+ and D^+ do not depend on the multiplicity and therefore the prompt

fractions computed in the multiplicity-integrated samples were used for all the $N_{\rm trkl}$ classes. This hypothesis is supported by the results obtained for the D-meson nuclear modification factor analysis in different centrality classes [223], where the fractions of prompt D mesons in the 0-10% and 60-100% centrality classes and in the minimum-bias sample were found to be compatible. In Eq. 5.2, a hypothesis on $R_{\rm AA}^{\rm feed-down}$ was applied to account for different modification of beauty and charm production in Pb-Pb collisions. In a similar way, for the calculation of $f_{\rm prompt}$ in the minimum-bias p-Pb sample, the assumption of $R_{\rm pPb}^{\rm feed-down} = R_{\rm pPb}^{\rm prompt}$ was done, for both $\rm D_s$ and $\rm D^+$ mesons. This hypothesis was varied between $0.9 < R_{\rm pPb}^{\rm feed-down}/R_{\rm pPb}^{\rm prompt} < 1.3$ for the assignment of the systematic uncertainty. The resulting $f_{\rm prompt}$ for $\rm D_s^+$ mesons selected according to the criteria reported in Tab. 6.1 is shown in Fig 6.11 as a function of $p_{\rm T}$.

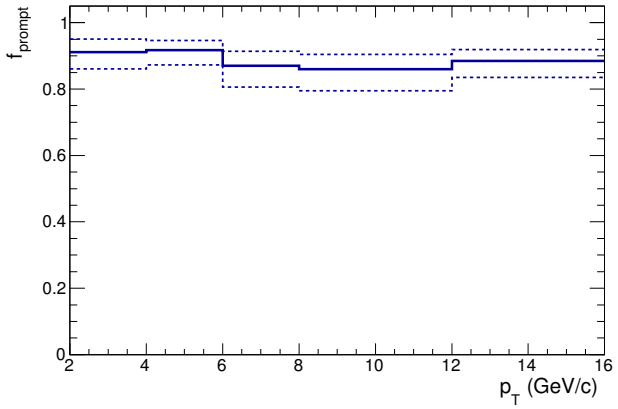

FIGURE 6.11: Fraction of prompt $\rm D_s$ in the $p_{\rm T}$ intervals considered for the analysis.

6.5 Systematic uncertainties

Most of the sources of systematic uncertainty and the methodology for their evaluation are the same that were discussed in Chapters 4 and 5 for the pp and Pb-Pb analyses. They are the systematics on the yield extraction, on the efficiency (including $\rm D_s$ meson selection, track reconstruction and particle identification) and on the generated D-meson $p_{\rm T}$ shape. The systematic uncertainty on the yield extraction was estimated via a multiple trial approach by varying the configuration of the fit parameters and by comparing the extracted yields with those using a bin counting method, as discussed in Sec. 4.8.1 and 5.2.1. The systematic uncertainty on the selection efficiency was estimated by varying the topological selections applied on $\rm D_s$ candidates and testing the stability of the corrected yields in each $p_{\rm T}$ interval (see Sec. 4.8.2 and 5.2.2). The systematic uncertainty on the particle identification was assigned by comparing the corrected yields with the looser and tighter PID selections introduced in Sec. 4.5 and 4.8.3. The systematic uncertainty on the tracking efficiency was estimated by the comparison of the efficiency in data and in simulation, after the data-driven re-weighting of the fraction of primary tracks in the simulation (see Sec. 4.8.4). The systematic uncertainty due to the generated $\rm D_s$-meson $p_{\rm T}$ shape was estimated by considering different input distributions (PYTHIA, FONLL) and was found to be negligible. As regards the systematic uncertainty on the calculation of the prompt fraction, the hypothesis on the $R_{\rm pPb}$ of feed-down D mesons was varied

in the range $0.9 < R_{\rm pPb}^{\rm feed-down}/R_{\rm pPb}^{\rm prompt} < 1.3$. The error bars on $f_{\rm prompt}$ shown in Fig. 6.11 include the contribution of the variation of the hypothesis on $R_{\rm pPb}^{\rm feed-down}$ as well as of the variation of factorisation and renormalisation scales and charm quark mass in FONLL. All the values of the assigned systematic uncertainties are reported in Tab. 6.2 as a function of $p_{\rm T}$, for the three multiplicity classes.

An additional source of systematic uncertainty, which is specific of this analysis, is the one related to the re-weighting procedure of the efficiencies. Since the simulated $N_{\rm trkl}$ distribution does not reproduce the distribution in data, a correction was introduced to re-weight the D_s-meson efficiencies in each of the three $N_{\rm trkl}^{\rm corr}$ intervals, as described in Sec. 6.4. The data-driven weights used for the central value of the efficiencies were obtained from events that have at least a D^0-meson candidate passing the selections, with invariant mass compatible within 3σ to D^0 mass from PDG, as mentioned in Sec. 6.4. To estimate the systematic uncertainty on this procedure, the efficiencies were corrected with weights from events that have at least a D^0-meson candidate, with no further request on its invariant mass. The two multiplicity dependent weights obtained in the two cases are shown in Fig. 6.12 for the four groups of runs. Fig. 6.13 shows the ratios of the efficiencies re-weighted with these two options for the multiplicity weights, for the three intervals on $N_{\rm trkl}^{\rm corr}$ used in the analysis. A 1% systematic uncertainty was assigned based on the difference between the re-weighted efficiencies.

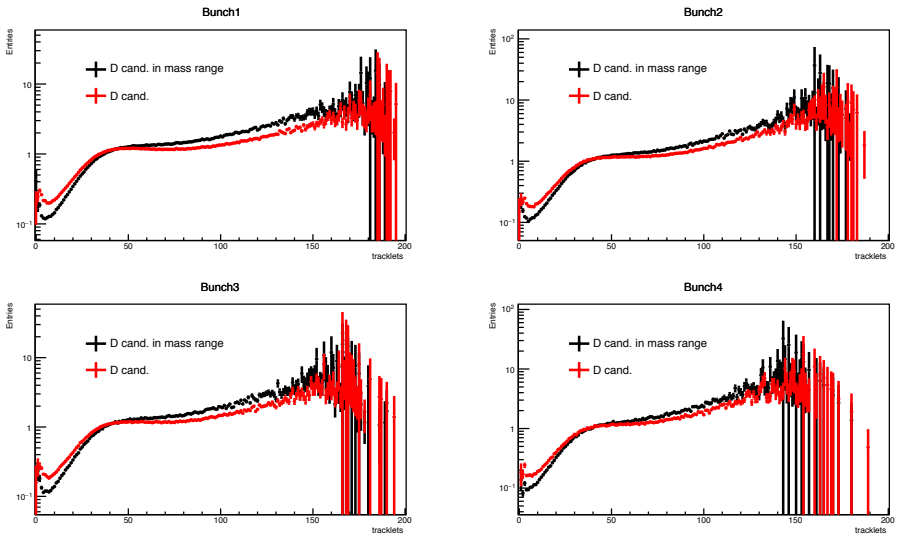

FIGURE 6.12: Comparison of the $N_{\rm trkl}$ weights obtained from events with at least a D^0 candidate and from events with at least a D^0 candidate in the D^0 mass range (default).

The same sources of systematic uncertainties were considered also for the D^+ meson. In the calculation of the D_s/D^+ yield ratios, the following sources of systematic uncertainties were considered as uncorrelated:

- raw-yield extraction;
- selection efficiency;
- PID selection efficiency;

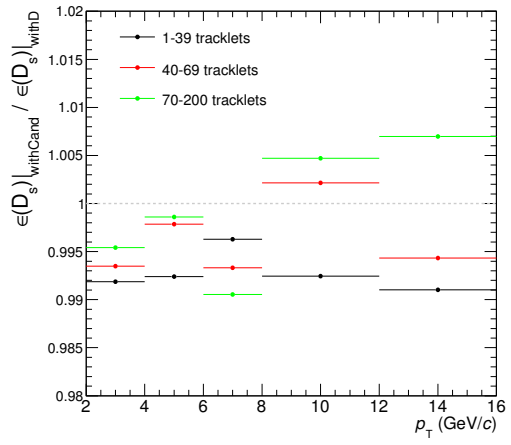

FIGURE 6.13: Ratio between the efficiency re-weighted with the two options considered for the $N_{\rm trkl}$-dependent weights: events with at least a D^0 candidate and events with at least a D^0 candidate in the D^0 mass range (default).

- hypothesis on $R_{\rm pPb}^{feed-down}$ for the feed-down D meson subtraction;

while these other sources:

- efficiency correction with data-driven weights;
- tracking efficiency;
- variation of FONLL scales for the feed-down D meson subtraction;

were considered as fully correlated between D_s^+ and D^+ yields.

6.6 Conversion of $N_{\rm trkl}$ to primary charged particles

The conversion of the number of tracklets in $|\eta| < 1$ to the average multiplicity of primary charged particles ($N_{\rm ch}$) in the same η range was performed using a Monte Carlo production with the EPOS-LHC generator [144]. The distribution of the reconstructed $N_{\rm trkl}$ as a function of the number of $N_{\rm ch}$ in the simulation, which is shown in Fig. 6.14 (left), was considered to this purpose. The 2D correlation was re-weighted with the $N_{\rm trkl}$ weights obtained as the ratio of the $N_{\rm trkl}$ distributions in data and in simulation as described in Sec. 6.4, to adapt the tracklet distribution from the simulation to that of the data. The $N_{\rm trkl}$ distributions were obtained with the request of at least a D^0 candidate in the D^0 mass range. The profile of the correlation was fitted with a linear function with two parameters $N_{\rm trkl} = {\rm a} + {\rm b}N_{\rm ch}$. The parameters were found to be: ${\rm a} = (-0.3 \pm 0.1)$ and ${\rm b} = (0.900 \pm 0.002)$. The profile-to-fit ratio is presented in Fig. 6.14 (right panel). The fitted function was used to extract the central value of $< N_{\rm ch} >$ from the average $< N_{\rm trkl} >$ value in each class.

To estimate the systematic uncertainties on the evaluation of the average $< N_{\rm ch} >$ values in the considered $N_{\rm trkl}$ intervals, three different checks have been performed.

1. To test the dependence of the correction factor on the event generator, the correlation between $N_{\rm trkl}$ to $N_{\rm ch}$ with a different event generator (DPMJET [229])

D_s syst. unc. (%)	p_T interval (GeV/c)				
$1 \leq N_{trkl} < 40$	2–4	4–6	6–8	8–12	12–16
Yield extraction	4	4	3	3	9
Selection efficiency	14	9	8	8	7
PID efficiency	2	2	2	2	2
Tracking efficiency	4	4	4	4	4
MC p_T-shape	negl	negl	negl	negl	negl
Feed-down	$^{+3}_{-4}$	$^{+3}_{-4}$	$^{+3}_{-4}$	$^{+3}_{-4}$	$^{+5}_{-5}$
Multiplicity weights	1	1	1	1	1
$40 \leq N_{trkl} < 70$	2–4	4–6	6–8	8–12	12–16
Yield extraction	3	3	4	5	12
Selection efficiency	14	9	8	8	7
PID efficiency	2	2	2	2	2
Tracking efficiency	4	4	4	4	4
MC p_T-shape	negl	negl	negl	negl	negl
Feed-down	$^{+3}_{-4}$	$^{+3}_{-4}$	$^{+3}_{-4}$	$^{+3}_{-4}$	$^{+5}_{-5}$
Multiplicity weights	1	1	1	1	1
$70 \leq N_{trkl} < 200$	2–3	4–6	6–8	8–12	12–16
Yield extraction	4	4	4	4	10
Selection efficiency	14	9	8	8	7
PID efficiency	2	2	2	2	2
Tracking efficiency	4	4	4	4	4
MC p_T-shape	negl	negl	negl	negl	negl
Feed-down	$^{+3}_{-4}$	$^{+3}_{-4}$	$^{+3}_{-4}$	$^{+3}_{-4}$	$^{+5}_{-5}$
Multiplicity weights	1	1	1	1	1

TABLE 6.2: Systematic uncertainties on D_s yield used in the D_s/D^+ versus multiplicity measurement.

was considered. The correlation between N_{trkl} to N_{ch} can in fact be sensitive to the relative abundance of different particle species produced by the event generator. The comparison of the average $< N_{ch} >$ in the three N_{trkl} intervals used in the analysis from the EPOS and DPMJET generators is presented in Fig. 6.15. The difference, which is 2% in all N_{trkl} intervals, was assigned as systematic uncertainty.

2. To test deviations from the linear correlation which were observed in particular at low and high multiplicity (right panel of Fig. 6.14), a different method to compute $< N_{ch} >$ was considered. The average $< N_{ch} >$ was extracted by considering the N_{ch} intervals used in the analysis as shown in Fig. 6.16. In Fig. 6.17 (left) the comparison of the $< N_{ch} >$ values obtained with this methods are compared to the ones computed with the linear fit. The difference is $< 3\%$ in all N_{trkl} intervals and is assigned as systematic uncertainty.

3. To estimate the dependence on the shape of the multiplicity distribution, the conversion factor from N_{trkl} to N_{ch} was recalculated: (i) without the data-driven N_{trkl} weights and (ii) applying the N_{trkl} weights obtained considering all the events that pass the physics selection, without requirements on the D^0 candidate. The comparison of $< N_{ch} >$ values from these tests to the default one, obtained with the weights extracted from events with D^0 candidates in the D^0 mass range, is shown in Fig. 6.17 (right). The assigned systematics are $5\%, 0\%, 3\%$ in the $[1, 40), [40, 70), [70, 200]$ N_{trkl} intervals respectively.

The three sources of uncertainties were considered as uncorrelated and their contributions were summed in quadrature. The final values of $< N_{ch} >$ in $|\eta| < 1$ and the

associated systematic uncertainties are reported in Tab. 6.3 and shown in Fig. 6.18. These values were then divided by the width of the considered η range, $\Delta\eta = 2$, to obtain $\langle {\rm d}N_{\rm ch}/{\rm d}\eta\rangle|_{|\eta|<0.5}$.

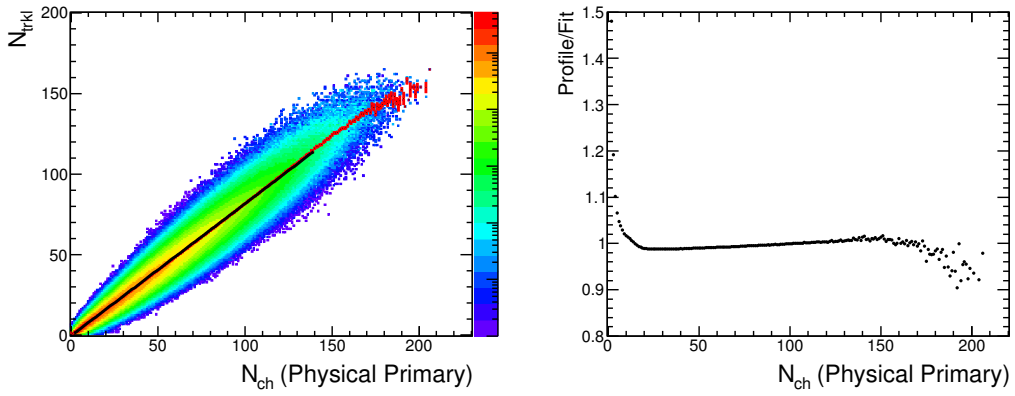

FIGURE 6.14: Left: distribution of number of SPD tracklets $N_{\rm trkl}$ versus number of generated charged particles $N_{\rm ch}$ obtained from simulations with the EPOS-LHC generator. The profile of the correlation (red markers) is fit with a linear function (black line). Right: ratio of the profile of $N_{\rm trkl}$ versus $N_{\rm ch}$ distribution to the fit result.

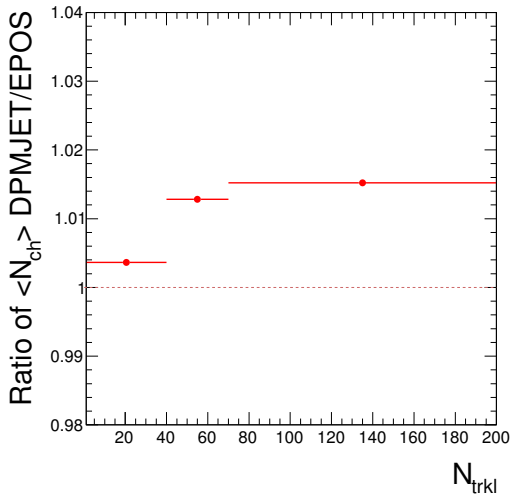

FIGURE 6.15: Ratio of $< N_{\rm ch} >$ values in the considered multiplicity classes obtained with EPOS-LHC and DPMJET generators.

$< N_{\rm ch} >$	$N_{\rm trkl}$ weights (%)	Lin. corr. $N_{\rm trkl}$-$N_{\rm ch}$ (%)	Ev. generator (%)
21.6	6.9	2.6	0.4
63.1	0.7	0.1	1.3
102.7	2.5	2.9	1.5

TABLE 6.3: $< N_{\rm ch} >$ values and related systematic uncertainties in each of the three $N_{\rm trkl}$ multiplicity intervals.

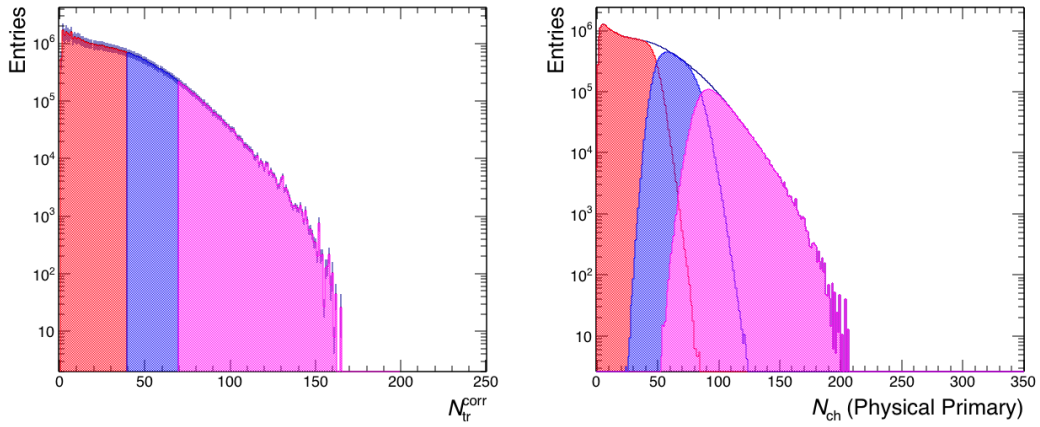

FIGURE 6.16: Left: N_{trkl}^{corr} distributions for the three multiplicity classes from simulations with EPOS-LHC. Right: N_{ch} distributions in the three multiplicity classes.

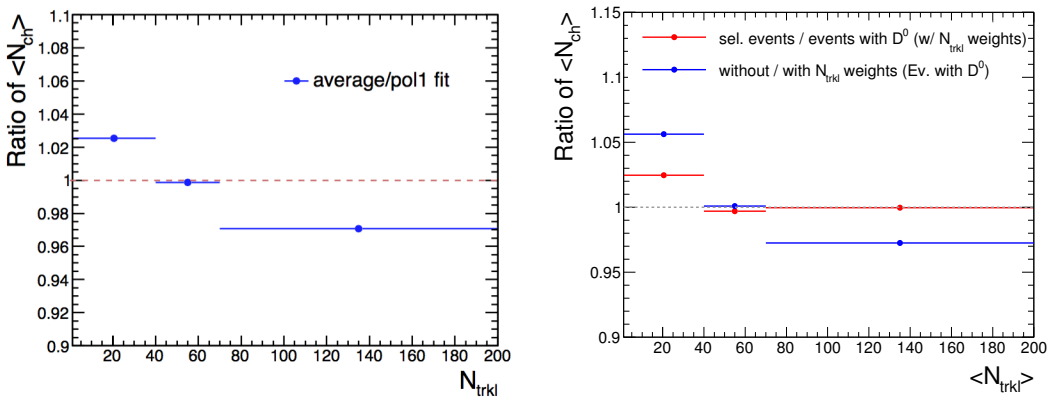

FIGURE 6.17: Left: ratio of $< N_{ch} >$ values obtained as average of the N_{ch} distributions in the N_{trkl} intervals to those obtained from the linear fit to the N_{trkl}-N_{ch} correlation. Right: ratios of $< N_{ch} >$ values obtained with different data-driven weights.

6.7 Results

The ratios of D_s/D^+-meson yields are shown in Fig. 6.19 as a function of the average number of primary charged particles per unity of pseudo-rapidity, in five p_T intervals from 2 to 16 GeV/c. The ratios measured in pp collisions at $\sqrt{s}$ =7 TeV [43] and in Pb-Pb collisions at $\sqrt{s_{NN}}$ = 5.02 TeV [222] (for the 0-10%, 30-50% and 60-100% centrality classes), which were presented in Chap. 4 and 5 are also reported in the figure. A hint for an enhanced D_s/D^+ ratio in Pb-Pb collisions was discussed in Chap. 5 and could result from a significant contribution of recombination mechanism in charm-quark hadronisation in the QGP. The data point in Fig. 6.19 could provide further insight on the multiplicity dependence of this possible enhancement also in the smaller systems, such as those produced in p-Pb collisions. The measured D_s/D^+ ratios in p-Pb collisions in the different multiplicity and p_T intervals are found to be compatible within uncertainties. To test for possible presence of non-flat trends as a function of multiplicity, the measured points were fitted with a linear function to quantify their slope. The results of the fit are shown in Fig. 6.20 and were obtained

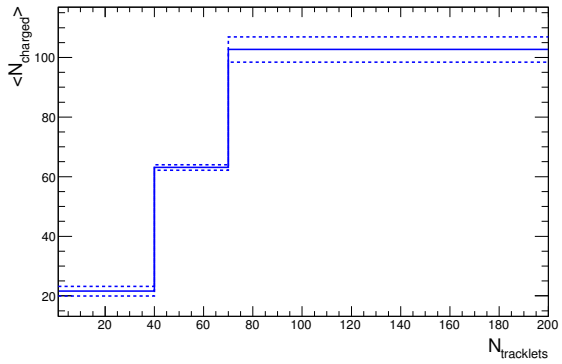

FIGURE 6.18: Average N_{ch} values in $|\eta| < 1$ for the considered multiplicity classes. The lower and higher dashed lines represent the systematic uncertainties.

considering only the statistical uncertainties. The reason for this choice is that, even without including the systematic uncertainties, the slopes from the linear fit on the pp, p-Pb and Pb-Pb points were found to be different from zero no more than 1σ of the slope parameter error between 2 and 8 GeV/c. If the fit is performed on pp and p-Pb measurements only (blue lines in Fig. 6.20), the slopes differ from zero within 1σ in the p_{T} intervals between $4 < p_{\mathrm{T}} < 6\,\mathrm{GeV}/c$ and $6 < p_{\mathrm{T}} < 8\,\mathrm{GeV}/c$.

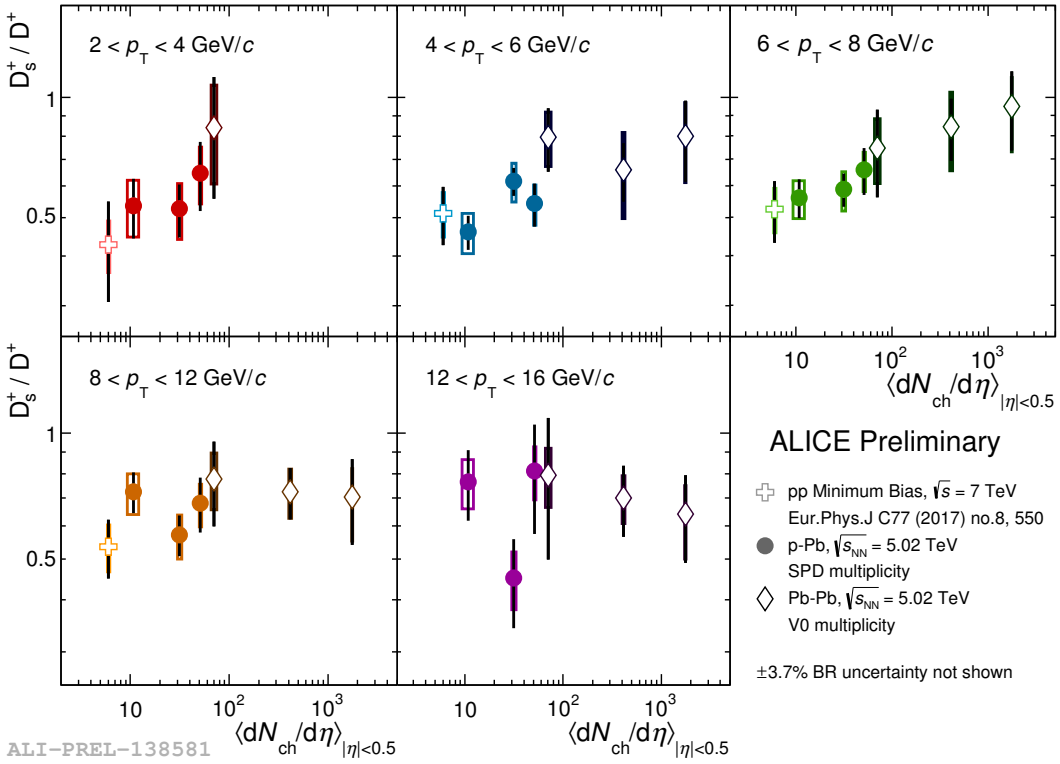

FIGURE 6.19: $\mathrm{D_s/D^+}$-meson yield ratios as a function of the multiplicity of primary charged particles in $|\eta| < 0.5$, in the five p_{T} intervals from 2 to 16 GeV/c.

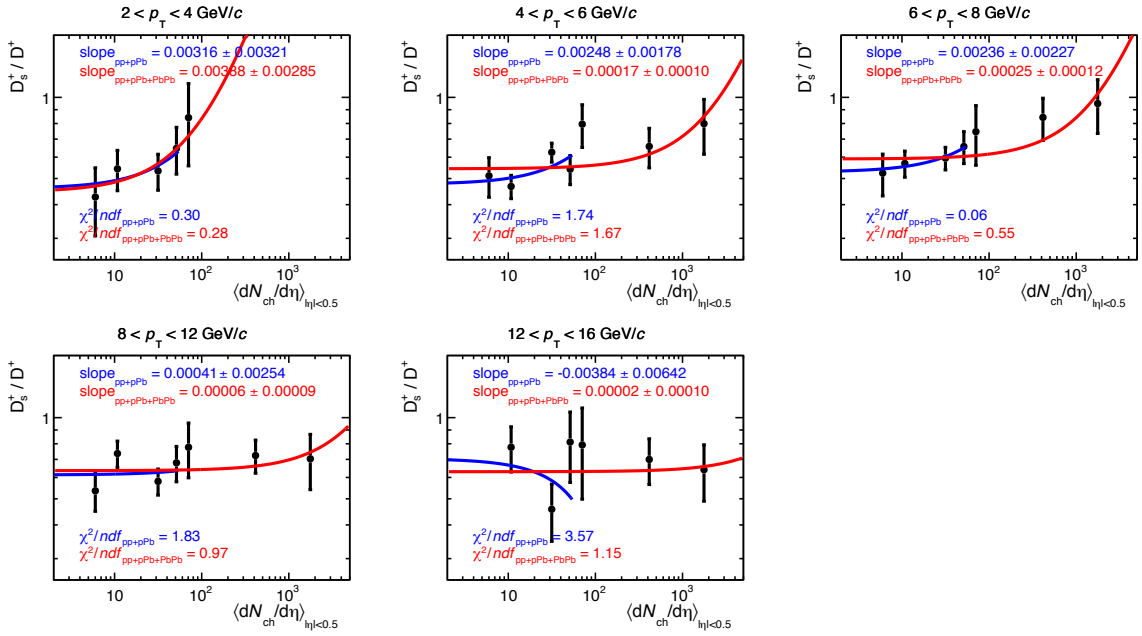

FIGURE 6.20: Linear fit to D_s/D^+ ratios as a function of the multiplicity of primary charged particles, in the different p_T intervals from 2 to 16 GeV/c. The slope parameter of the linear function is reported in each pad, for the fits made only on the pp and p-Pb points (blue lines) or on all the pp, p-Pb and Pb-Pb points (red lines). Only statistical uncertainties are considered in the fit.

6.8 Discussion and perspectives

An hint for an enhancement of the ratios D_s^+/D^0 and D_s^+/D^+ in Pb-Pb collisions at $\sqrt{s_{NN}} = 5.02$ TeV relative to the values measured in pp collisions was discussed in Chap. 5. The measured ratios are described by models including charm-quark hadronisation via recombination in the QGP. As discussed in Chap. 1, several experimental results from high-multiplicity pp collisions and p-Pb collisions at the LHC resemble effects observed in Pb-Pb collisions: long-range rapidity correlations, azimuthal anisotropies v_n ... It is not clear yet which is the physics behind these observations, for which explanations based on a hydrodynamical expansion of the system created in the collision and also on the formation of droplets of QGP in small systems were proposed [167, 261, 193, 146, 235]. The measurement of ratios of D_s^+ and D^+ yields as a function of multiplicity, presented in this Chapter is a test for the possible contribution of recombination to charm quark hadronisation also in small systems, such as those produced in high multiplicity pp and p-Pb collisions. Although intriguing, the current measurement of D_s^+/D^+ as a function of the multiplicity in p-Pb collisions does not allow to draw firm conclusions due to the large statistical and systematic uncertainties.

The precision of this measurement will be improved using the larger data samples of p-Pb collisions that will be collected during the LHC Run 3. Fig. 6.21 shows the estimate for the relative statistical uncertainty of D_s yield in p-Pb collisions at $\sqrt{s_{NN}} = 5.5$ TeV estimated for Run 3 in the full multiplicity range, and compared to Run 2 preliminary results [224]. During LHC Run 3, a sample about 150 times larger than the current one could be recorded, providing a reduction of the statistical

uncertainties by a factor larger than 10. The estimates in Fig. 6.21 in the transverse momentum range $p_{\rm T} > 2\,{\rm GeV}/c$ (full red markers) were obtained by rescaling the statistical uncertainty on the $\rm D_s$ yields measured with the current sample to the statistics expected for Run 3. The statistical uncertainties are expected to be 1% or less for $p_{\rm T} > 2\,{\rm GeV}/c$. For the low-$p_{\rm T}$ region, the estimates were obtained from an analysis of $\rm D_s^+$ production without secondary vertex reconstruction (open red symbols). Since the $\rm D_s$-meson decay topology cannot be efficiently resolved at low $p_{\rm T}$ due to the insufficient resolution of the track impact parameter and the small Lorentz boost, the selections based on the secondary-vertex topology were not applied. Since it is impossible to have a measurement of the $\rm D_s^\pm$ signal from the data sample of p-Pb collisions collected in Run 2 due to the large amount of background at $p_{\rm T} < 2\,{\rm GeV}/c$, the raw signal per event was estimated from pQCD calculations as:

$$S_{\rm D_s^+}\big|_{\rm p-Pb,5TeV} = \langle {\rm T_{pA}^{0-100\%}} \rangle \, \sigma_{\rm FONLL}^{\rm D^0,pp,5TeV} \, \frac{{\rm d}N^{\rm Ds^+,pp7TeV}/{\rm d}p_{\rm T}}{{\rm d}N^{\rm D^0,pp7TeV}/{\rm d}p_{\rm T}} \times ({\rm Acc}\times\epsilon)_{\rm D_s^+}^{\rm p-Pb,5TeV} \times 2\,{\rm BR}({\rm D_s^+ \to K^+K^-\pi^+})\,, \tag{6.4}$$

where $\sigma_{\rm FONLL}^{\rm D^0,pp,5TeV}$ is the FONLL cross-section for $\rm D^0$ meson production at $\sqrt{s_{\rm NN}} = 5$ TeV, which was rescaled to $\rm D_s^+$ cross section with the ratio of the $\rm D_s^+$ and $\rm D^0$ yields measured in pp collisions at $\sqrt{s} = 7$ TeV (see Chap. 4). This ratio was found to be ~ 0.2 in the transverse momentum interval $2 < p_{\rm T} < 12\,{\rm GeV}/c$ and assumed to be constant at $p_{\rm T} < 2\,{\rm GeV}/c$. Results of $\rm D_s^+/D^0$ ratio in p-Pb collisions at $\sqrt{s_{\rm NN}} = 5.02$ TeV [224] are compatible with those in pp collisions. The cross-section was then rescaled by the average nuclear overlap function $\langle {\rm T_{pA}^{0-100\%}} \rangle$ in p-Pb collisions at $\sqrt{s_{\rm NN}} = 5$ TeV and by the product of the acceptance and efficiency, $({\rm Acc}\times\epsilon)_{\rm D_s^+}^{\rm p-Pb,5TeV}$, calculated from the simulations. In the calculation of the $({\rm Acc}\times\epsilon)$, only the selections on $\cos\theta^*(\pi)$, $|\cos^3\theta'({\rm K})|$ and on the invariant mass of the reconstructed $\rm K^+K^-$ pair were used. Finally, the yield was multiplied by the branching ratio of the $\rm D_s^+ \to K^+K^-\pi^+$ decay. The factor 2 accounts for the fact that both particles and antiparticles contributes to the raw yield. The per-event background contribution was obtained from data by integrating the function used to model the background in the fits to the $\rm D_s$ candidate invariant-mass distributions obtained with the same selections used for the efficiencies. The integral was performed in an interval of 3σ around the $\rm D_s$ mass, where σ is the Gaussian width of a fit to the $\rm D_s$ invariant-mass distribution from the simulations. The estimates for the signal and the background were combined into a statistical significance. The relative uncertainty on the signal can be obtained from the significance: $\delta S/S \sim 1/{\rm significance}$. The statistical uncertainty was finally scaled by the number of events that could be recorded in Run 3.

The upgrade ITS that will be installed after Run 2 will allow to further improve the statistical uncertainty with respect to the estimates discussed above, thanks to its improved resolution on primary and secondary vertex reconstruction, which will provide a better separation between signal and background candidates. This will pave the way to measure with sufficient precision the $\rm D_s^+$ production as a function of the multiplicity in small systems and to assess how the charm hadronisation evolves from pp to Pb-Pb collisions.

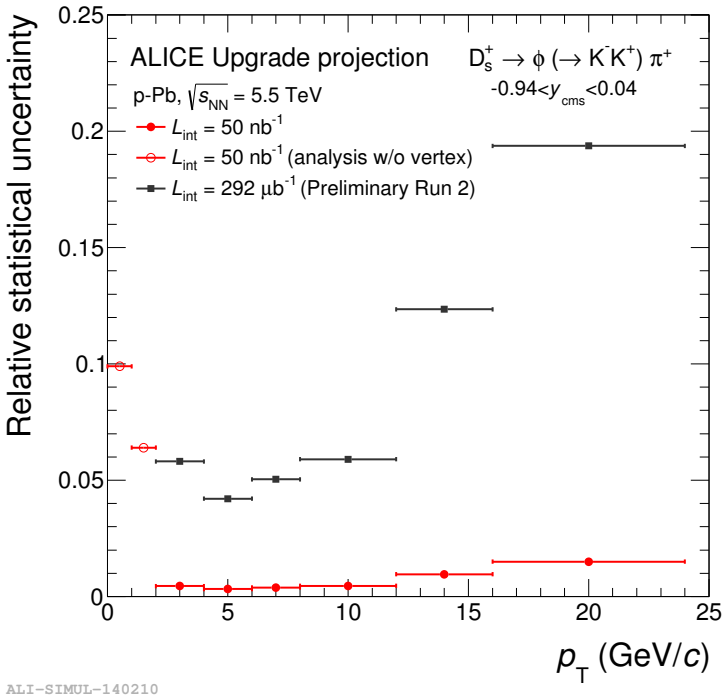

FIGURE 6.21: Relative statistical uncertainty on D_s yield in p-Pb collisions at 5.5 TeV estimated for Run 3, compared with Run 2 preliminary results [224]. Full red symbols: estimates obtained by scaling the statistical uncertainty from the current preliminary results (analysis performed utilising geometrical selections on the displaced decay vertex topology). Open red symbols: estimates assuming an analysis without decay vertex reconstruction.

Chapter 7

Conclusions

This thesis presented the measurements of $\mathrm{D_s^+}$ meson production in pp, p-Pb and Pb-Pb collisions. The analysis was performed via the reconstruction of the displaced-vertex decay topology $\mathrm{D_s^+ \to K^+K^-\pi^+}$ at mid-rapidity with the ALICE detector.

In comparison to previous ALICE publications based on the same data sample of pp collisions at $\sqrt{s} = 7$ TeV, the present results have total uncertainties reduced by a factor of about two thanks to improvement in the reconstruction and detector alignments and to several optimisation in the analysis procedure. The $\mathrm{D_s^+}$ p_{T}-differential cross section was measured in the transverse-momentum interval $2 < p_{\mathrm{T}} < 12\,\mathrm{GeV}/c$ and was found to be well described by perturbative QCD calculations.

The $\mathrm{D_s^+}$ nuclear modification factor R_{AA} was measured in central, semi-peripheral and peripheral Pb-Pb collisions at $\sqrt{s_{\mathrm{NN}}} = 5.02$ TeV in the p_{T} range $4 < p_{\mathrm{T}} < 16\,\mathrm{GeV}/c$. This observable is sensitive to the interactions of charm quarks with the Quark-Gluon Plasma medium formed in the collision. The obtained results indicate a substantial modification of the $\mathrm{D_s^+}$ meson p_{T} distribution as compared to pp collisions with a maximum suppression of the $\mathrm{D_s}$ yield at $p_{\mathrm{T}} \sim 6 - 10\,\mathrm{GeV}/c$, for the 10% most central Pb-Pb collisions, suggesting a significant energy loss of the charm quark inside the hot and dense medium. The central values of the R_{AA} of $\mathrm{D_s^+}$ mesons are larger than those of non-strange D mesons. This would support the hypothesis that a fraction of the charm quarks hadronises via recombination with lighter quarks from the medium. However, the current uncertainties need to be reduced to draw firmer conclusions. For the first time, the anisotropies in the $\mathrm{D_s^+}$ azimuthal distribution were studied in semi-central Pb-Pb collisions. In particular, the elliptic flow v_2 of $\mathrm{D_s^+}$ mesons was measured, showing positive values in the p_{T} interval $2 < p_{\mathrm{T}} < 8\,\mathrm{GeV}/c$. A positive v_2 indicates that charm quarks take part in the collective motion of the QGP.

Finally, a first measurement of the relative production yields of $\mathrm{D_s^+}$ and $\mathrm{D^+}$ mesons as a function of multiplicity in p-Pb collisions $\sqrt{s_{\mathrm{NN}}} = 5.02$ TeV was performed. This measurement is particularly interesting after the observation of an increasing yield of strange particles relative to pions with increasing particle multiplicity in pp and p-Pb collisions, reaching values compatible with those observed in Pb-Pb collisions at similar multiplicities. Even though an intriguing trend of the $\mathrm{D_s^+/D^+}$ yield ratio is observed from pp to Pb-Pb collisions at low p_{T}, the large statistical and systematic uncertainties do not allow to conclude on the possible role of hadronisation via recombination in the smaller systems created in pp and p-Pb collisions. The larger data samples that will be collected during LHC Run 3 will allow to assess about the $\mathrm{D_s}$ production as a function of multiplicity and more in general about charm quark in-medium hadronisation.

Acknowledgements

I would like to thank my supervisors, Francesco Prino and Stefania Beolè, and also Elena Bruna for their constant support during these years of PhD, for the fruitful discussions with them and for the incredible amount of things they taught me. I really want to thank them also for all the opportunities that they gave me. I would like to thank Dr. Ralf Averbeck and Dr. Patrick Robbe, who accepted to read my thesis. A big thank goes to everyone in the Torino group: Stefania, Massimo, Mario, Luciano, Yasser, Max, Luca, Stefano, Matteo, Fabrizio and Ivan, and in particular to Cristina, for this year at CERN. It was a pleasure for me to be part of this group!
A special thanks goes to my family and to Alessio, that support me every day.

Bibliography

[1] Georges Aad et al. "Measurement of charged-particle spectra in Pb+Pb collisions at $\sqrt{s_{\mathrm{NN}}} = 2.76$ TeV with the ATLAS detector at the LHC". In: *JHEP* 09 (2015), p. 050. DOI: 10.1007/JHEP09(2015)050. arXiv: 1504.04337 [hep-ex].

[2] Georges Aad et al. "Measurement of the azimuthal anisotropy for charged particle production in $\sqrt{s_{NN}} = 2.76$ TeV lead-lead collisions with the ATLAS detector". In: *Phys. Rev.* C86 (2012), p. 014907. DOI: 10.1103/PhysRevC.86.014907. arXiv: 1203.3087 [hep-ex].

[3] Georges Aad et al. "Measurement of the distributions of event-by-event flow harmonics in lead-lead collisions at = 2.76 TeV with the ATLAS detector at the LHC". In: *JHEP* 11 (2013), p. 183. DOI: 10.1007/JHEP11(2013)183. arXiv: 1305.2942 [hep-ex].

[4] Georges Aad et al. "Measurements of the Nuclear Modification Factor for Jets in Pb+Pb Collisions at $\sqrt{s_{\mathrm{NN}}} = 2.76$ TeV with the ATLAS Detector". In: *Phys. Rev. Lett.* 114.7 (2015), p. 072302. DOI: 10.1103/PhysRevLett.114.072302. arXiv: 1411.2357 [hep-ex].

[5] R. Aaij et al. "Measurement of b-hadron production fractions in 7 TeV pp collisions". In: *Phys. Rev.* D85 (2012), p. 032008. DOI: 10.1103/PhysRevD.85.032008. arXiv: 1111.2357 [hep-ex].

[6] R Aaij et al. "Measurement of B meson production cross-sections in proton-proton collisions at $\sqrt{s} = 7$ TeV". In: *JHEP* 08 (2013), p. 117. DOI: 10.1007/JHEP08(2013)117. arXiv: 1306.3663 [hep-ex].

[7] R. Aaij et al. "Measurement of J/ψ production in pp collisions at $\sqrt{s} = 7$ TeV". In: *Eur. Phys. J.* C71 (2011), p. 1645. DOI: 10.1140/epjc/s10052-011-1645-y. arXiv: 1103.0423 [hep-ex].

[8] R Aaij et al. "Production of J/psi and Upsilon mesons in pp collisions at sqrt(s) = 8 TeV". In: *JHEP* 06 (2013), p. 064. DOI: 10.1007/JHEP06(2013)064. arXiv: 1304.6977 [hep-ex].

[9] R Aaij et al. "Prompt charm production in pp collisions at $\sqrt{s} = 7$ TeV". In: *Nucl. Phys.* B871 (2013), pp. 1–20. DOI: 10.1016/j.nuclphysb.2013.02.010. arXiv: 1302.2864 [hep-ex].

[10] R. Aaij et al. "Study of the production of Λ_b^0 and $\overline{B}^0$ hadrons in pp collisions and first measurement of the $\Lambda_b^0 \to J/\psi p K^-$ branching fraction". In: *Chin. Phys.* C40.1 (2016), p. 011001. DOI: 10.1088/1674-1137/40/1/011001. arXiv: 1509.00292 [hep-ex].

[11] Roel Aaij et al. "Measurements of prompt charm production cross-sections in pp collisions at $\sqrt{s} = 13$ TeV". In: *JHEP* 03 (2016). [Erratum: *JHEP* **09** (2016) 013], p. 159. DOI: 10.1007/JHEP03(2016)159. arXiv: 1510.01707 [hep-ex].

[12] Roel Aaij et al. "Measurements of prompt charm production cross-sections in pp collisions at $\sqrt{s} = 5\,\text{TeV}$". In: (2016). arXiv: 1610.02230 [hep-ex].

[13] K. Aamodt et al. "Harmonic decomposition of two-particle angular correlations in Pb-Pb collisions at $\sqrt{s_{NN}} = 2.76$ TeV". In: *Phys. Lett.* B708 (2012), pp. 249–264. DOI: 10.1016/j.physletb.2012.01.060. arXiv: 1109.2501 [nucl-ex].

[14] K. Aamodt et al. "The ALICE experiment at the CERN LHC". In: *JINST* 3 (2008), S08002. DOI: 10.1088/1748-0221/3/08/S08002.

[15] K. Aamodt et al. "Two-pion Bose-Einstein correlations in central Pb-Pb collisions at $\sqrt{s_{NN}} = 2.76$ TeV". In: *Phys. Lett.* B696 (2011), pp. 328–337. DOI: 10.1016/j.physletb.2010.12.053. arXiv: 1012.4035 [nucl-ex].

[16] Kenneth Aamodt et al. "Centrality dependence of the charged-particle multiplicity density at mid-rapidity in Pb-Pb collisions at $\sqrt{s_{NN}} = 2.76$ TeV". In: *Phys. Rev. Lett.* 106 (2011), p. 032301. DOI: 10.1103/PhysRevLett.106.032301. arXiv: 1012.1657 [nucl-ex].

[17] G. Abbiendi et al. "Inclusive analysis of the b quark fragmentation function in Z decays at LEP". In: *Eur. Phys. J.* C29 (2003), pp. 463–478. DOI: 10.1140/epjc/s2003-01229-x. arXiv: hep-ex/0210031 [hep-ex].

[18] B. Abelev et al. "Azimuthal anisotropy of D meson production in Pb-Pb collisions at $\sqrt{s_{\text{NN}}} = 2.76$ TeV". In: *Phys. Rev.* C90 (2014), p. 034904. DOI: 10.1103/PhysRevC.90.034904. arXiv: 1405.2001 [nucl-ex].

[19] B. Abelev et al. "Measurement of charm production at central rapidity in proton-proton collisions at $\sqrt{s} = 7$ TeV". In: *JHEP* 01 (2012), p. 128. DOI: 10.1007/JHEP01(2012)128. arXiv: 1111.1553 [hep-ex].

[20] B. I. Abelev et al. "Enhanced strange baryon production in Au + Au collisions compared to p + p at s(NN)**(1/2) = 200-GeV". In: *Phys. Rev.* C77 (2008), p. 044908. DOI: 10.1103/PhysRevC.77.044908. arXiv: 0705.2511 [nucl-ex].

[21] B. I. Abelev et al. "Three-particle coincidence of the long range pseudorapidity correlation in high energy nucleus-nucleus collisions". In: *Phys. Rev. Lett.* 105 (2010), p. 022301. DOI: 10.1103/PhysRevLett.105.022301. arXiv: 0912.3977 [hep-ex].

[22] B. I. Abelev et al. "Transverse momentum and centrality dependence of high-p_{T} non-photonic electron suppression in Au+Au collisions at $\sqrt{s_{\text{NN}}} = 200\,\text{GeV}$". In: *Phys. Rev. Lett.* 98 (2007). [Erratum: Phys. Rev. Lett.106,159902(2011)], p. 192301. DOI: 10.1103/PhysRevLett.106.159902,10.1103/PhysRevLett.98.192301. arXiv: nucl-ex/0607012 [nucl-ex].

[23] Betty Abelev et al. "Centrality Dependence of Charged Particle Production at Large Transverse Momentum in Pb–Pb Collisions at $\sqrt{s_{\text{NN}}} = 2.76$ TeV". In: *Phys. Lett.* B720 (2013), pp. 52–62. DOI: 10.1016/j.physletb.2013.01.051. arXiv: 1208.2711 [hep-ex].

[24] Betty Abelev et al. "Centrality dependence of pi, K, p production in Pb-Pb collisions at $\sqrt{s_{\text{NN}}} = 2.76$ TeV". In: *Phys. Rev.* C88 (2013), p. 044910. DOI: 10.1103/PhysRevC.88.044910. arXiv: 1303.0737 [hep-ex].

[25] Betty Abelev et al. "Centrality determination of Pb-Pb collisions at $\sqrt{s_{NN}} = 2.76$ TeV with ALICE". In: *Phys. Rev.* C88.4 (2013), p. 044909. DOI: 10.1103/PhysRevC.88.044909. arXiv: 1301.4361 [nucl-ex].

[26] Betty Abelev et al. "D_s^+ meson production at central rapidity in proton–proton collisions at $\sqrt{s} = 7$ TeV". In: *Phys. Lett.* B718 (2012), pp. 279–294. DOI: 10.1016/j.physletb.2012.10.049. arXiv: 1208.1948 [hep-ex].

[27] Betty Abelev et al. "Measurement of charm production at central rapidity in proton-proton collisions at $\sqrt{s} = 2.76$ TeV". In: *JHEP* 07 (2012), p. 191. DOI: 10.1007/JHEP07(2012)191. arXiv: 1205.4007 [hep-ex].

[28] Betty Abelev et al. "Measurement of inelastic, single- and double-diffraction cross sections in proton–proton collisions at the LHC with ALICE". In: *Eur. Phys. J.* C73.6 (2013), p. 2456. DOI: 10.1140/epjc/s10052-013-2456-0. arXiv: 1208.4968 [hep-ex].

[29] Betty Abelev et al. "Measurement of visible cross sections in proton-lead collisions at $\sqrt{s_{\rm NN}} = 5.02$ TeV in van der Meer scans with the ALICE detector". In: *JINST* 9.11 (2014), P11003. DOI: 10.1088/1748-0221/9/11/P11003. arXiv: 1405.1849 [nucl-ex].

[30] Betty Abelev et al. "Pion, Kaon, and Proton Production in Central Pb–Pb Collisions at $\sqrt{s_{NN}} = 2.76$ TeV". In: *Phys. Rev. Lett.* 109 (2012), p. 252301. DOI: 10.1103/PhysRevLett.109.252301. arXiv: 1208.1974 [hep-ex].

[31] Betty Abelev et al. "Production of muons from heavy flavour decays at forward rapidity in pp and Pb-Pb collisions at $\sqrt{s_{NN}} = 2.76$ TeV". In: *Phys. Rev. Lett.* 109 (2012), p. 112301. DOI: 10.1103/PhysRevLett.109.112301. arXiv: 1205.6443 [hep-ex].

[32] Betty Abelev et al. "Pseudorapidity density of charged particles in p + Pb collisions at $\sqrt{s_{NN}} = 5.02$ TeV". In: *Phys. Rev. Lett.* 110.3 (2013), p. 032301. DOI: 10.1103/PhysRevLett.110.032301. arXiv: 1210.3615 [nucl-ex].

[33] Betty Bezverkhny Abelev et al. "Centrality, rapidity and transverse momentum dependence of J/ψ suppression in Pb-Pb collisions at $\sqrt{s_{\rm NN}}$=2.76 TeV". In: *Phys. Lett.* B734 (2014), pp. 314–327. DOI: 10.1016/j.physletb.2014.05.064. arXiv: 1311.0214 [nucl-ex].

[34] Betty Bezverkhny Abelev et al. "Measurement of prompt D-meson production in $p - Pb$ collisions at $\sqrt{s_{NN}} = 5.02$ TeV". In: *Phys. Rev. Lett.* 113.23 (2014), p. 232301. DOI: 10.1103/PhysRevLett.113.232301. arXiv: 1405.3452 [nucl-ex].

[35] Betty Bezverkhny Abelev et al. "Multiplicity Dependence of Pion, Kaon, Proton and Lambda Production in p-Pb Collisions at $\sqrt{s_{NN}} = 5.02$ TeV". In: *Phys. Lett.* B728 (2014), pp. 25–38. DOI: 10.1016/j.physletb.2013.11.020. arXiv: 1307.6796 [nucl-ex].

[36] Betty Bezverkhny Abelev et al. "Performance of the ALICE Experiment at the CERN LHC". In: *Int. J. Mod. Phys.* A29 (2014), p. 1430044. DOI: 10.1142/S0217751X14300440. arXiv: 1402.4476 [nucl-ex].

[37] Betty Bezverkhny Abelev et al. "Production of charged pions, kaons and protons at large transverse momenta in pp and PbPb collisions at $\sqrt{s_{\rm NN}}$ =2.76 TeV". In: *Phys. Lett.* B736 (2014), pp. 196–207. DOI: 10.1016/j.physletb.2014.07.011. arXiv: 1401.1250 [nucl-ex].

[38] B.I. Abelev et al. "Enhanced strange baryon production in Au + Au collisions compared to p + p at $\sqrt{s_{\rm NN}} = 200$ GeV". In: *Phys.Rev.* C77 (2008), p. 044908. DOI: 10.1103/PhysRevC.77.044908. arXiv: 0705.2511 [nucl-ex].

[39] B.I. Abelev et al. "Systematic Measurements of Identified Particle Spectra in pp, d+Au and Au+Au Collisions from STAR". In: *Phys.Rev.* C79 (2009), p. 034909. DOI: 10.1103/PhysRevC.79.034909. arXiv: 0808.2041 [nucl-ex].

[40] M. C. Abreu et al. "Evidence for deconfinement of quarks and gluons from the J / psi suppression pattern measured in Pb + Pb collisions at the CERN SPS". In: *Phys. Lett.* B477 (2000), pp. 28–36. DOI: 10.1016/S0370-2693(00)00237-9.

[41] Shreyasi Acharya et al. "D-meson azimuthal anisotropy in mid-central Pb-Pb collisions at $\sqrt{s_{\rm NN}} = 5.02$ TeV". In: (2017). arXiv: 1707.01005 [nucl-ex].

[42] Shreyasi Acharya et al. "J/ψ elliptic flow in Pb-Pb collisions at $\sqrt{s_{\rm NN}} = 5.02$ TeV". In: (2017). arXiv: 1709.05260 [nucl-ex].

[43] Shreyasi Acharya et al. "Measurement of D-meson production at mid-rapidity in pp collisions at $\sqrt{s} = 7$ TeV". In: *Eur. Phys. J.* C77.8 (2017), p. 550. DOI: 10.1140/epjc/s10052-017-5090-4. arXiv: 1702.00766 [hep-ex].

[44] Shreyasi Acharya et al. "Production of muons from heavy-flavour hadron decays in p-Pb collisions at $\sqrt{s_{\rm NN}} = \mathbf{5.02}$ TeV". In: *Phys. Lett.* B770 (2017), pp. 459–472. DOI: 10.1016/j.physletb.2017.03.049. arXiv: 1702.01479 [nucl-ex].

[45] J. Adam et al. "D-meson prouction in p–Pb collisions at $\sqrt{s_{\rm NN}} = 5.02$ TeV and in pp collisions at $\sqrt{s} = 7$ TeV". In: (2016). arXiv: 1605.07569 [nucl-ex].

[46] J. Adam et al. "Measurement of D-meson production versus multiplicity in p-Pb collisions at $\sqrt{s_{\rm NN}} = 5.02$ TeV". In: *JHEP* 08 (2016), p. 078. DOI: 10.1007/JHEP08(2016)078. arXiv: 1602.07240 [nucl-ex].

[47] Jaroslav Adam et al. "Anisotropic flow of charged particles in Pb-Pb collisions at $\sqrt{s_{\rm NN}} = 5.02$ TeV". In: *Phys. Rev. Lett.* 116.13 (2016), p. 132302. DOI: 10.1103/PhysRevLett.116.132302. arXiv: 1602.01119 [nucl-ex].

[48] Jaroslav Adam et al. "Centrality dependence of high-p$_T$ D meson suppression in Pb-Pb collisions at $\sqrt{s_{\rm NN}} = 2.76$ TeV". In: *JHEP* 11 (2015). [Addendum: JHEP06,032(2017)], p. 205. DOI: 10.1007/JHEP11(2015)205, 10.1007/JHEP06(2017)032. arXiv: 1506.06604 [nucl-ex].

[49] Jaroslav Adam et al. "Centrality dependence of the charged-particle multiplicity density at midrapidity in Pb-Pb collisions at $\sqrt{s_{\rm NN}} = 5.02$ TeV". In: *Phys. Rev. Lett.* 116.22 (2016), p. 222302. DOI: 10.1103/PhysRevLett.116.222302. arXiv: 1512.06104 [nucl-ex].

[50] Jaroslav Adam et al. "Charged-particle multiplicities in protonproton collisions at $\sqrt{s} = 0.9$ to 8 TeV". In: *Eur. Phys. J.* C77.1 (2017), p. 33. DOI: 10.1140/epjc/s10052-016-4571-1. arXiv: 1509.07541 [nucl-ex].

[51] Jaroslav Adam et al. "Determination of the event collision time with the ALICE detector at the LHC". In: *Eur. Phys. J. Plus* 132.2 (2017), p. 99. DOI: 10.1140/epjp/i2017-11279-1. arXiv: 1610.03055 [physics.ins-det].

[52] Jaroslav Adam et al. "Enhanced production of multi-strange hadrons in high-multiplicity proton-proton collisions". In: *Nature Phys.* 13 (2017), pp. 535–539. DOI: 10.1038/nphys4111. arXiv: 1606.07424 [nucl-ex].

[53] Jaroslav Adam et al. "J/ψ suppression at forward rapidity in Pb-Pb collisions at $\sqrt{s_{\rm NN}} = 5.02$ TeV". In: *Phys. Lett.* B766 (2017), pp. 212–224. DOI: 10.1016/j.physletb.2016.12.064. arXiv: 1606.08197 [nucl-ex].

[54] Jaroslav Adam et al. "Measurement of D_s^+ production and nuclear modification factor in Pb-Pb collisions at $\sqrt{s_{NN}} = 2.76$ TeV". In: *JHEP* 03 (2016), p. 082. DOI: 10.1007/JHEP03(2016)082. arXiv: 1509.07287 [nucl-ex].

[55] Jaroslav Adam et al. "Measurement of electrons from beauty-hadron decays in p-Pb collisions at $\sqrt{s_{NN}} = 5.02$ TeV and Pb-Pb collisions at $\sqrt{s_{NN}} = 2.76$ TeV". In: *JHEP* 07 (2017), p. 052. DOI: 10.1007/JHEP07(2017)052. arXiv: 1609.03898 [nucl-ex].

[56] Jaroslav Adam et al. "Measurement of the production of high-p_T electrons from heavy-flavour hadron decays in Pb-Pb collisions at $\sqrt{s_{NN}} = 2.76$ TeV". In: *Phys. Lett.* B771 (2017), pp. 467–481. DOI: 10.1016/j.physletb.2017.05.060. arXiv: 1609.07104 [nucl-ex].

[57] Jaroslav Adam et al. "Multi-strange baryon production in p-Pb collisions at $\sqrt{s_{NN}} = 5.02$ TeV". In: *Phys. Lett.* B758 (2016), pp. 389–401. DOI: 10.1016/j.physletb.2016.05.027. arXiv: 1512.07227 [nucl-ex].

[58] Jaroslav Adam et al. "Transverse momentum dependence of D-meson production in Pb-Pb collisions at $\sqrt{s_{NN}} = 2.76$ TeV". In: *JHEP* 03 (2016), p. 081. DOI: 10.1007/JHEP03(2016)081. arXiv: 1509.06888 [nucl-ex].

[59] L. Adamczyk et al. "Observation of D0 Meson Nuclear Modifications in Au+Au Collisions at $\sqrt{s_{NN}} = 200$ GeV". In: *Phys. Rev. Lett.* 113.14 (2014), p. 142301. DOI: 10.1103/PhysRevLett.113.142301. arXiv: 1404.6185 [nucl-ex].

[60] J. Adams et al. "Transverse momentum and collision energy dependence of high p(T) hadron suppression in Au+Au collisions at ultrarelativistic energies". In: *Phys. Rev. Lett.* 91 (2003), p. 172302. DOI: 10.1103/PhysRevLett.91.172302. arXiv: nucl-ex/0305015 [nucl-ex].

[61] A. Adare et al. "J/ψ Production vs Centrality, Transverse Momentum, and Rapidity in Au+Au Collisions at $\sqrt{s_{NN}} = 200$ GeV". In: *Phys. Rev. Lett.* 98 (2007), p. 232301. DOI: 10.1103/PhysRevLett.98.232301. arXiv: nucl-ex/0611020 [nucl-ex].

[62] A. Adare et al. "J/ψ suppression at forward rapidity in Au+Au collisions at $\sqrt{s_{NN}} = 200$ GeV". In: *Phys. Rev.* C84 (2011), p. 054912. DOI: 10.1103/PhysRevC.84.054912. arXiv: 1103.6269 [nucl-ex].

[63] A. Adare et al. "Measurements of Higher-Order Flow Harmonics in Au+Au Collisions at $\sqrt{s_{NN}} = 200$ GeV". In: *Phys. Rev. Lett.* 107 (2011), p. 252301. DOI: 10.1103/PhysRevLett.107.252301. arXiv: 1105.3928 [nucl-ex].

[64] A. Adare et al. "Neutral pion production with respect to centrality and reaction plane in Au+Au collisions at $\sqrt{s_{NN}}$=200 GeV". In: *Phys. Rev.* C87.3 (2013), p. 034911. DOI: 10.1103/PhysRevC.87.034911. arXiv: 1208.2254 [nucl-ex].

[65] S.V. Afanasiev et al. "Energy dependence of pion and kaon production in central Pb + Pb collisions". In: *Phys.Rev.* C66 (2002), p. 054902. DOI: 10.1103/PhysRevC.66.054902. arXiv: nucl-ex/0205002 [nucl-ex].

[66] M. M. Aggarwal et al. "Transverse mass distributions of neutral pions from Pb-208 induced reactions at 158-A-GeV". In: *Eur. Phys. J.* C23 (2002), pp. 225–236. DOI: 10.1007/s100520100886. arXiv: nucl-ex/0108006 [nucl-ex].

[67] S. Agostinelli et al. "GEANT4: A Simulation toolkit". In: *Nucl. Instrum. Meth.* A506 (2003), pp. 250–303. DOI: 10.1016/S0168-9002(03)01368-8.

[68] M. Aguilar-Benitez et al. "Comparative Properties of 400-GeV/c Proton - Proton Interactions With and Without Charm Production". In: *Z. Phys.* C41 (1988), p. 191. DOI: 10.1007/BF01566916.

[69] J. Aichelin, P. B. Gossiaux, and T. Gousset. "Radiative and Collisional Energy Loss of Heavy Quarks in Deconfined Matter". In: *Acta Phys. Polon.* B43 (2012), pp. 655–662. DOI: 10.5506/APhysPolB.43.655. arXiv: 1201.4192 [nucl-th].

[70] Dellacasa at al. *ALICE time projection chamber: Technical Design Report*. Technical Design Report ALICE. Geneva: CERN, 2000. URL: https://cds.cern.ch/record/451098.

[71] Javier L. Albacete, Adrian Dumitru, and Yasushi Nara. "CGC initial conditions at RHIC and LHC". In: *J. Phys. Conf. Ser.* 316 (2011), p. 012011. DOI: 10.1088/1742-6596/316/1/012011. arXiv: 1106.0978 [nucl-th].

[72] *ALICE Inner Tracking System (ITS): Technical Design Report*. Technical Design Report ALICE. Geneva: CERN, 1999. URL: https://cds.cern.ch/record/391175.

[73] C. Alt et al. "Directed and elliptic flow of charged pions and protons in Pb + Pb collisions at 40-A-GeV and 158-A-GeV". In: *Phys. Rev.* C68 (2003), p. 034903. DOI: 10.1103/PhysRevC.68.034903. arXiv: nucl-ex/0303001 [nucl-ex].

[74] C. Alt et al. "Energy dependence of Λ and Ξ production in central Pb+Pb collisions at 20A, 30A, 40A, 80A, and 158A GeV measured at the CERN Super Proton Synchrotron". In: *Phys.Rev.* C78 (2008), p. 034918. DOI: 10.1103/PhysRevC.78.034918. arXiv: 0804.3770 [nucl-ex].

[75] C. Alt et al. "High Transverse Momentum Hadron Spectra at s(NN)**(1/2) = 17.3-GeV, in Pb+Pb and p+p Collisions, Measured by CERN-NA49". In: *Phys. Rev.* C77 (2008), p. 034906. DOI: 10.1103/PhysRevC.77.034906. arXiv: 0711.0547 [nucl-ex].

[76] Guido Altarelli and G. Parisi. "Asymptotic Freedom in Parton Language". In: *Nucl. Phys.* B126 (1977), pp. 298–318. DOI: 10.1016/0550-3213(77)90384-4.

[77] B. Alver and G. Roland. "Collision geometry fluctuations and triangular flow in heavy-ion collisions". In: *Phys. Rev.* C81 (2010). [Erratum: Phys. Rev.C82,039903(2010)], p. 054905. DOI: 10.1103/PhysRevC.82.039903,10.1103/PhysRevC.81.054905. arXiv: 1003.0194 [nucl-th].

[78] B. Alver et al. "High transverse momentum triggered correlations over a large pseudorapidity acceptance in Au+Au collisions at s(NN)**1/2 = 200 GeV". In: *Phys. Rev. Lett.* 104 (2010), p. 062301. DOI: 10.1103/PhysRevLett.104.062301. arXiv: 0903.2811 [nucl-ex].

[79] B. Alver et al. "System size dependence of cluster properties from two-particle angular correlations in Cu+Cu and Au+Au collisions at s(NN)**(1/2) = 200-GeV". In: *Phys. Rev.* C81 (2010), p. 024904. DOI: 10.1103/PhysRevC.81.024904. arXiv: 0812.1172 [nucl-ex].

[80] Burak Han Alver et al. "Triangular flow in hydrodynamics and transport theory". In: *Phys. Rev.* C82 (2010), p. 034913. DOI: 10.1103/PhysRevC.82.034913. arXiv: 1007.5469 [nucl-th].

[81] A. Andronic, P. Braun-Munzinger, and J. Stachel. "Thermal hadron production in relativistic nuclear collisions: The Hadron mass spectrum, the horn, and the QCD phase transition". In: *Phys. Lett.* B673 (2009). [Erratum: Phys. Lett.B678,516(2009)], pp. 142–145. DOI: 10.1016/j.physletb.2009.02.014, 10.1016/j.physletb.2009.06.021. arXiv: 0812.1186 [nucl-th].

[82] A. Andronic et al. "Charmonium and open charm production in nuclear collisions at SPS/FAIR energies and the possible influence of a hot hadronic medium". In: *Phys. Lett.* B659 (2008), pp. 149–155. DOI: 10.1016/j.physletb.2007.10.064. arXiv: 0708.1488 [nucl-th].

[83] A. Andronic et al. "Heavy-flavour and quarkonium production in the LHC era: from protonproton to heavy-ion collisions". In: *Eur. Phys. J.* C76.3 (2016), p. 107. DOI: 10.1140/epjc/s10052-015-3819-5. arXiv: 1506.03981 [nucl-ex].

[84] A. Andronic et al. "Statistical hadronization of charm in heavy ion collisions at SPS, RHIC and LHC". In: *Phys.Lett.* B571 (2003), pp. 36–44. DOI: 10.1016/j.physletb.2003.07.066. arXiv: nucl-th/0303036 [nucl-th].

[85] Anton Andronic. "An overview of the experimental study of quark-gluon matter in high-energy nucleus-nucleus collisions". In: *Int. J. Mod. Phys.* A29 (2014), p. 1430047. DOI: 10.1142/S0217751X14300476. arXiv: 1407.5003 [nucl-ex].

[86] F. Antinori et al. "Enhancement of hyperon production at central rapidity in 158-A-GeV/c Pb-Pb collisions". In: *J.Phys.* G32 (2006), pp. 427–442. DOI: 10.1088/0954-3899/32/4/003. arXiv: nucl-ex/0601021 [nucl-ex].

[87] F Antinori et al. "Strangeness enhancements at central rapidity in 40 A GeV/c Pb-Pb collisions". In: *J.Phys.* G37 (2010), p. 045105. DOI: 10.1088/0954-3899/37/4/045105. arXiv: 1001.1884 [nucl-ex].

[88] H. Appelshauser et al. "Baryon stopping and charged particle distributions in central Pb + Pb collisions at 158-GeV per nucleon". In: *Phys. Rev. Lett.* 82 (1999), pp. 2471–2475. DOI: 10.1103/PhysRevLett.82.2471. arXiv: nucl-ex/9810014 [nucl-ex].

[89] H. Appelshauser et al. "Xi and anti-xi production in 158-GeV / nucleon Pb + Pb collisions". In: *Phys. Lett.* B444 (1998), pp. 523–530. DOI: 10.1016/S0370-2693(98)01399-9. arXiv: nucl-ex/9810005 [nucl-ex].

[90] Nestor Armesto, Carlos A. Salgado, and Urs Achim Wiedemann. "Relating high-energy lepton-hadron, proton-nucleus and nucleus-nucleus collisions through geometric scaling". In: *Phys. Rev. Lett.* 94 (2005), p. 022002. DOI: 10.1103/PhysRevLett.94.022002. arXiv: hep-ph/0407018 [hep-ph].

[91] R. Arnaldi et al. "Evidence for radial flow of thermal dileptons in high-energy nuclear collisions". In: *Phys. Rev. Lett.* 100 (2008), p. 022302. DOI: 10.1103/PhysRevLett.100.022302. arXiv: 0711.1816 [nucl-ex].

[92] J. J. Aubert et al. "The ratio of the nucleon structure functions $F2_n$ for iron and deuterium". In: *Phys. Lett.* 123B (1983), pp. 275–278. DOI: 10.1016/0370-2693(83)90437-9.

[93] R. Averbeck et al. "Reference Heavy Flavour Cross Sections in pp Collisions at $\sqrt{s} = 2.76$ TeV, using a pQCD-Driven $\sqrt{s}$-Scaling of ALICE Measurements at $\sqrt{s} = 7$ TeV". In: (2011). arXiv: 1107.3243 [hep-ph].

[94] R. Baier. "Jet quenching". In: *Nucl. Phys.* A715 (2003), pp. 209–218. DOI: 10.1016/S0375-9474(02)01429-X. arXiv: hep-ph/0209038 [hep-ph].

[95] R. Baier et al. "Radiative energy loss and p(T) broadening of high-energy partons in nuclei". In: *Nucl. Phys.* B484 (1997), pp. 265–282. DOI: 10.1016/S0550-3213(96)00581-0. arXiv: hep-ph/9608322 [hep-ph].

[96] R. Barate et al. "Study of charm production in Z decays". In: *Eur. Phys. J.* C16 (2000), pp. 597–611. DOI: 10.1007/s100520000421. arXiv: hep-ex/9909032 [hep-ex].

[97] F. Becattini et al. "Centrality dependence of hadronization and chemical freeze-out conditions in heavy ion collisions at $\sqrt{s_{NN}} = 2.76$ TeV". In: *Phys. Rev.* C90.5 (2014), p. 054907. DOI: 10.1103/PhysRevC.90.054907. arXiv: 1405.0710 [nucl-th].

[98] Francesco Becattini et al. "Hadron Formation in Relativistic Nuclear Collisions and the QCD Phase Diagram". In: *Phys. Rev. Lett.* 111 (2013), p. 082302. DOI: 10.1103/PhysRevLett.111.082302. arXiv: 1212.2431 [nucl-th].

[99] Rene Bellwied et al. "Is there a flavor hierarchy in the deconfinement transition of QCD?" In: *Phys. Rev. Lett.* 111 (2013), p. 202302. DOI: 10.1103/PhysRevLett.111.202302. arXiv: 1305.6297 [hep-lat].

[100] A. Beraudo et al. "Heavy flavors in heavy-ion collisions: quenching, flow and correlations". In: *Eur. Phys. J.* C75.3 (2015), p. 121. DOI: 10.1140/epjc/s10052-015-3336-6. arXiv: 1410.6082 [hep-ph].

[101] Andrea Beraudo et al. "Heavy-flavour production in high-energy d-Au and p-Pb collisions". In: *JHEP* 03 (2016), p. 123. DOI: 10.1007/JHEP03(2016)123. arXiv: 1512.05186 [hep-ph].

[102] R. A. Bertens. "Anisotropic flow of inclusive and identified particles in Pb–Pb collisions at $\sqrt{s_{\mathrm{NN}}} = 5.02$ TeV". In: (2017). arXiv: 1704.03028 [nucl-ex].

[103] F. Beutler et al. "The Canonical partition function for relativistic hadron gases". In: *Eur. Phys. J.* C67 (2010), pp. 439–444. DOI: 10.1140/epjc/s10052-010-1309-3. arXiv: 0910.1697 [hep-ph].

[104] R. S. Bhalerao, N. Borghini, and J. Y. Ollitrault. "Genuine collective flow from Lee-Yang zeroes". In: *Phys. Lett.* B580 (2004), pp. 157–162. DOI: 10.1016/j.physletb.2003.11.056. arXiv: nucl-th/0307018 [nucl-th].

[105] Ante Bilandzic, Raimond Snellings, and Sergei Voloshin. "Flow analysis with cumulants: Direct calculations". In: *Phys. Rev.* C83 (2011), p. 044913. DOI: 10.1103/PhysRevC.83.044913. arXiv: 1010.0233 [nucl-ex].

[106] J. D. Bjorken. "Highly Relativistic Nucleus Nucleus Collisions: The Central Rapidity Region". In: *Phys. Rev.* D27 (1983), pp. 140–151. DOI: 10.1103/PhysRevD.27.140.

[107] J. D. Bjorken. "Highly Relativistic Nucleus-Nucleus Collisions: The Central Rapidity Region". In: *Phys. Rev.* D27 (1983), pp. 140–151. DOI: 10.1103/PhysRevD.27.140.

[108] Walter Blum, Luigi Rolandi, and Werner Riegler. *Particle detection with drift chambers*. Particle Acceleration and Detection. 2008. ISBN: 9783540766834, 9783540766841. DOI: 10.1007/978-3-540-76684-1. URL: http://www.springer.com/physics/elementary/book/978-3-540-76683-4.

[109] Szabolcs Borsanyi et al. "The QCD equation of state with dynamical quarks". In: *JHEP* 11 (2010), p. 077. DOI: 10.1007/JHEP11(2010)077. arXiv: 1007.2580 [hep-lat].

[110] Piotr Boek and Wojciech Broniowski. "Hydrodynamic approach to p-Pb". In: *Nucl. Phys.* A926 (2014), pp. 16–23. DOI: 10.1016/j.nuclphysa.2014.04.004. arXiv: 1401.2367 [nucl-th].

[111] Eric Braaten et al. "Perturbative QCD fragmentation functions as a model for heavy quark fragmentation". In: *Phys. Rev.* D51 (1995), pp. 4819–4829. DOI: 10.1103/PhysRevD.51.4819. arXiv: hep-ph/9409316 [hep-ph].

[112] P. Braun-Munzinger. "Quarkonium production in ultra-relativistic nuclear collisions: Suppression versus enhancement". In: *J. Phys.* G34 (2007), S471–478. DOI: 10.1088/0954-3899/34/8/S36. arXiv: nucl-th/0701093 [NUCL-TH].

[113] Peter Braun-Munzinger, Krzysztof Redlich, and Johanna Stachel. "Particle production in heavy ion collisions". In: (2003). DOI: 10.1142/9789812795533_0008. arXiv: nucl-th/0304013 [nucl-th].

[114] R. Brun and F. Rademakers. "ROOT: An object oriented data analysis framework". In: *Nucl. Instrum. Meth.* A389 (1997), pp. 81–86. DOI: 10.1016/S0168-9002(97)00048-X.

[115] Rene' Brun et al. *GEANT Detector Description and Simulation Tool*. Tech. rep. CERN, 1994. URL: http://cds.cern.ch/record/1082634.

[116] Ren Brun et al. *GEANT: Detector Description and Simulation Tool; Oct 1994*. CERN Program Library. Long Writeup W5013. Geneva: CERN, 1993. URL: http://cds.cern.ch/record/1082634.

[117] Karen M. Burke et al. "Extracting the jet transport coefficient from jet quenching in high-energy heavy-ion collisions". In: *Phys. Rev.* C90.1 (2014), p. 014909. DOI: 10.1103/PhysRevC.90.014909. arXiv: 1312.5003 [nucl-th].

[118] Adam Bzdak et al. "Initial state geometry and the role of hydrodynamics in proton-proton, proton-nucleus and deuteron-nucleus collisions". In: *Phys. Rev.* C87.6 (2013), p. 064906. DOI: 10.1103/PhysRevC.87.064906. arXiv: 1304.3403 [nucl-th].

[119] Matteo Cacciari, Stefano Frixione, and Paolo Nason. "The p(T) spectrum in heavy flavor photoproduction". In: *JHEP* 03 (2001), p. 006. DOI: 10.1088/1126-6708/2001/03/006. arXiv: hep-ph/0102134 [hep-ph].

[120] Matteo Cacciari, Mario Greco, and Paolo Nason. "The P(T) spectrum in heavy flavor hadroproduction". In: *JHEP* 05 (1998), p. 007. DOI: 10.1088/1126-6708/1998/05/007. arXiv: hep-ph/9803400 [hep-ph].

[121] Matteo Cacciari and Paolo Nason. "Charm cross-sections for the Tevatron Run II". In: *JHEP* 09 (2003), p. 006. DOI: 10.1088/1126-6708/2003/09/006. arXiv: hep-ph/0306212 [hep-ph].

[122] Matteo Cacciari, Paolo Nason, and Carlo Oleari. "A Study of heavy flavored meson fragmentation functions in e+ e- annihilation". In: *JHEP* 04 (2006), p. 006. DOI: 10.1088/1126-6708/2006/04/006. arXiv: hep-ph/0510032 [hep-ph].

[123] Matteo Cacciari et al. "Theoretical predictions for charm and bottom production at the LHC". In: *JHEP* 10 (2012), p. 137. DOI: 10.1007/JHEP10(2012)137. arXiv: 1205.6344 [hep-ph].

[124] Shanshan Cao, Guang-You Qin, and Steffen A. Bass. "Heavy-quark dynamics and hadronization in ultrarelativistic heavy-ion collisions: Collisional versus radiative energy loss". In: *Phys. Rev.* C88 (2013), p. 044907. DOI: 10.1103/PhysRevC.88.044907. arXiv: 1308.0617 [nucl-th].

[125] Shanshan Cao et al. "Heavy and light flavor jet quenching at RHIC and LHC energies". In: (2017). arXiv: 1703.00822 [nucl-th].

[126] M. Caselle et al. "String effects in Polyakov loop correlators". In: *Nucl. Phys. Proc. Suppl.* 119 (2003). [,499(2002)], pp. 499–501. DOI: 10.1016/S0920-5632(03)01595-0. arXiv: hep-lat/0210023 [hep-lat].

[127] *Centrality dependence of the charged-particle multiplicity density at midrapidity in Pb-Pb collisions at $\sqrt{s_{\mathrm{NN}}}$ = 5.02 TeV*. Tech. rep. ALICE-PUBLIC-2015-008. 2015. URL: https://cds.cern.ch/record/2118084.

[128] Serguei Chatrchyan et al. "Measurement of the B^0 production cross section in pp Collisions at $\sqrt{s} = 7$ TeV". In: *Phys. Rev. Lett.* 106 (2011), p. 252001. DOI: 10.1103/PhysRevLett.106.252001. arXiv: 1104.2892 [hep-ex].

[129] Serguei Chatrchyan et al. "Measurement of the Λ_b cross section and the $\bar{\Lambda}_b$ to Λ_b ratio with $J/\Psi\Lambda$ decays in pp collisions at $\sqrt{s} = 7$ TeV". In: *Phys. Lett.* B714 (2012), pp. 136–157. DOI: 10.1016/j.physletb.2012.05.063. arXiv: 1205.0594 [hep-ex].

[130] Serguei Chatrchyan et al. "Measurement of the pseudorapidity and centrality dependence of the transverse energy density in PbPb collisions at $\sqrt{s_{NN}} = 2.76$ TeV". In: *Phys. Rev. Lett.* 109 (2012), p. 152303. DOI: 10.1103/PhysRevLett.109.152303. arXiv: 1205.2488 [nucl-ex].

[131] Serguei Chatrchyan et al. "Measurement of the Strange B Meson Production Cross Section with J/Psi ϕ Decays in pp Collisions at $\sqrt{s} = 7$ TeV". In: *Phys. Rev.* D84 (2011), p. 052008. DOI: 10.1103/PhysRevD.84.052008. arXiv: 1106.4048 [hep-ex].

[132] Serguei Chatrchyan et al. "Study of high-pT charged particle suppression in PbPb compared to pp collisions at $\sqrt{s_{NN}} = 2.76$ TeV". In: *Eur. Phys. J.* C72 (2012), p. 1945. DOI: 10.1140/epjc/s10052-012-1945-x. arXiv: 1202.2554 [nucl-ex].

[133] S. Chekanov et al. "Measurement of charm fragmentation ratios and fractions in photoproduction at HERA". In: *Eur. Phys. J.* C44 (2005), pp. 351–366. DOI: 10.1140/epjc/s2005-02397-3. arXiv: hep-ex/0508019 [hep-ex].

[134] Yang-Ting Chien et al. "Jet Quenching from QCD Evolution". In: *Phys. Rev.* D93.7 (2016), p. 074030. DOI: 10.1103/PhysRevD.93.074030. arXiv: 1509.02936 [hep-ph].

[135] G. Corcella et al. "HERWIG 6: An Event generator for hadron emission reactions with interfering gluons (including supersymmetric processes)". In: *JHEP* 01 (2001), p. 010. DOI: 10.1088/1126-6708/2001/01/010. arXiv: hep-ph/0011363 [hep-ph].

[136] J. W. Cronin et al. "Production of hadrons with large transverse momentum at 200, 300, and 400 GeV". In: *Phys. Rev.* D11 (1975), pp. 3105–3123. DOI: 10.1103/PhysRevD.11.3105.

[137] S. Damjanovic et al. "First measurement of the rho spectral function in nuclear collisions". In: *Nucl. Phys.* A774 (2006), pp. 715–718. DOI: 10.1016/j.nuclphysa.2006.06.121. arXiv: nucl-ex/0510044 [nucl-ex].

[138] Wei-Tian Deng, Xin-Nian Wang, and Rong Xu. "Hadron production in p+p, p+Pb, and Pb+Pb collisions with the HIJING 2.0 model at energies available at the CERN Large Hadron Collider". In: *Phys. Rev.* C83 (2011), p. 014915. DOI: 10.1103/PhysRevC.83.014915. arXiv: 1008.1841 [hep-ph].

[139] David G. d'Enterria. "Indications of suppressed high p(T) hadron production in nucleus - nucleus collisions at CERN-SPS". In: *Phys. Lett.* B596 (2004), pp. 32–43. DOI: 10.1016/j.physletb.2004.06.071. arXiv: nucl-ex/0403055 [nucl-ex].

[140] S. Digal, P. Petreczky, and H. Satz. "Quarkonium feed down and sequential suppression". In: *Phys. Rev.* D64 (2001), p. 094015. DOI: 10.1103/PhysRevD.64.094015. arXiv: hep-ph/0106017 [hep-ph].

[141] Magdalena Djordjevic. "Heavy flavor puzzle at LHC: a serendipitous interplay of jet suppression and fragmentation". In: *Phys. Rev. Lett.* 112.4 (2014), p. 042302. DOI: 10.1103/PhysRevLett.112.042302. arXiv: 1307.4702 [nucl-th].

[142] Magdalena Djordjevic and Marko Djordjevic. "Predictions of heavy-flavor suppression at 5.1 TeV Pb+Pb collisions at the CERN Large Hadron Collider". In: *Phys. Rev.* C92.2 (2015), p. 024918. DOI: 10.1103/PhysRevC.92.024918. arXiv: 1505.04316 [nucl-th].

[143] Yuri L. Dokshitzer, Valery A. Khoze, and S. I. Troian. "On specific QCD properties of heavy quark fragmentation ('dead cone')". In: *J. Phys.* G17 (1991), pp. 1602–1604. DOI: 10.1088/0954-3899/17/10/023.

[144] H. J. Drescher et al. "Parton based Gribov-Regge theory". In: *Phys. Rept.* 350 (2001), pp. 93–289. DOI: 10.1016/S0370-1573(00)00122-8. arXiv: hep-ph/0007198 [hep-ph].

[145] Xiaojian Du and Ralf Rapp. "Sequential Regeneration of Charmonia in Heavy-Ion Collisions". In: *Nucl. Phys.* A943 (2015), pp. 147–158. DOI: 10.1016/j.nuclphysa.2015.09.006. arXiv: 1504.00670 [hep-ph].

[146] Kevin Dusling, Prithwish Tribedy, and Raju Venugopalan. "Energy dependence of the ridge in high multiplicity proton-proton collisions". In: *Phys. Rev.* D93.1 (2016), p. 014034. DOI: 10.1103/PhysRevD.93.014034. arXiv: 1509.04410 [hep-ph].

[147] K. J. Eskola, H. Paukkunen, and C. A. Salgado. "EPS09: A New Generation of NLO and LO Nuclear Parton Distribution Functions". In: *JHEP* 04 (2009), p. 065. DOI: 10.1088/1126-6708/2009/04/065. arXiv: 0902.4154 [hep-ph].

[148] Kari J. Eskola et al. "EPPS16: Nuclear parton distributions with LHC data". In: *Eur. Phys. J.* C77.3 (2017), p. 163. DOI: 10.1140/epjc/s10052-017-4725-9. arXiv: 1612.05741 [hep-ph].

[149] Christian Wolfgang Fabjan et al. "ALICE: Physics performance report, volume II". In: *J. Phys.* G32 (2006). Ed. by B Alessandro et al., pp. 1295–2040. DOI: 10.1088/0954-3899/32/10/001.

[150] Christian Wolfgang Fabjan et al. *ALICE trigger data-acquisition high-level trigger and control system: Technical Design Report*. Technical Design Report ALICE. Geneva: CERN, 2004. URL: https://cds.cern.ch/record/684651.

[151] Daniel de Florian et al. "Global Analysis of Nuclear Parton Distributions". In: *Phys. Rev.* D85 (2012), p. 074028. DOI: 10.1103/PhysRevD.85.074028. arXiv: 1112.6324 [hep-ph].

[152] Michele Floris. "Hadron yields and the phase diagram of strongly interacting matter". In: *Nucl. Phys.* A931 (2014), pp. 103–112. DOI: 10.1016/j.nuclphysa.2014.09.002. arXiv: 1408.6403 [nucl-ex].

[153] O. Fochler et al. "Jet quenching and elliptic flow at RHIC and LHC within a pQCD-based partonic transport model". In: *J.Phys.* G38 (2011), p. 124152. DOI: 10.1088/0954-3899/38/12/124152. arXiv: 1107.0130 [hep-ph].

[154] Stefano Frixione, Paolo Nason, and Giovanni Ridolfi. "A Positive-weight next-to-leading-order Monte Carlo for heavy flavour hadroproduction". In: *JHEP* 09 (2007), p. 126. DOI: 10.1088/1126-6708/2007/09/126. arXiv: 0707.3088 [hep-ph].

[155] Stefano Frixione and Bryan R. Webber. "Matching NLO QCD computations and parton shower simulations". In: *JHEP* 06 (2002), p. 029. DOI: 10.1088/1126-6708/2002/06/029. arXiv: hep-ph/0204244 [hep-ph].

[156] R. Fruhwirth. "Application of Kalman filtering to track and vertex fitting". In: *Nucl. Instrum. Meth.* A262 (1987), pp. 444–450. DOI: 10.1016/0168-9002(87)90887-4.

[157] Hirotsugu Fujii and Kazuhiro Watanabe. "Heavy quark pair production in high energy pA collisions: Open heavy flavors". In: *Nucl. Phys.* A920 (2013), pp. 78–93. DOI: 10.1016/j.nuclphysa.2013.10.006. arXiv: 1308.1258 [hep-ph].

[158] Hirotsugu Fujii and Kazuhiro Watanabe. "Nuclear modification of forward D production in pPb collisions at the LHC". In: (2017). arXiv: 1706.06728 [hep-ph].

[159] Martino Gagliardi. "Measurement of reference cross sections in pp and Pb-Pb collisions at the LHC in van der Meer scans with the ALICE detector". In: *AIP Conf. Proc.* 1422 (2012), pp. 110–116. DOI: 10.1063/1.3692205. arXiv: 1109.5369 [hep-ex].

[160] Charles Gale et al. "Event-by-event anisotropic flow in heavy-ion collisions from combined Yang-Mills and viscous fluid dynamics". In: *Phys. Rev. Lett.* 110.1 (2013), p. 012302. DOI: 10.1103/PhysRevLett.110.012302. arXiv: 1209.6330 [nucl-th].

[161] Leonid Gladilin. "Fragmentation fractions of c and b quarks into charmed hadrons at LEP". In: *Eur. Phys. J.* C75.1 (2015), p. 19. DOI: 10.1140/epjc/s10052-014-3250-3. arXiv: 1404.3888 [hep-ex].

[162] V. Greco, H. van Hees, and R. Rapp. "Heavy-quark kinetics at RHIC and LHC". In: *Nuclear physics. Proceedings, 23rd International Conference, INPC 2007, Tokyo, Japan, June 3-8, 2007*. 2007. arXiv: 0709.4452 [hep-ph]. URL: https://inspirehep.net/record/762313/files/arXiv:0709.4452.pdf.

[163] V. Greco, C. M. Ko, and P. Levai. "Parton coalescence at RHIC". In: *Phys. Rev.* C68 (2003), p. 034904. DOI: 10.1103/PhysRevC.68.034904. arXiv: nucl-th/0305024 [nucl-th].

[164] V. Greco, C. M. Ko, and R. Rapp. "Quark coalescence for charmed mesons in ultrarelativistic heavy ion collisions". In: *Phys. Lett.* B595 (2004), pp. 202–208. DOI: 10.1016/j.physletb.2004.06.064. arXiv: nucl-th/0312100 [nucl-th].

[165] Xingyu Guo et al. "Magnetic Field Effect on Charmonium Production in High Energy Nuclear Collisions". In: *Phys. Lett.* B751 (2015), pp. 215–219. DOI: 10.1016/j.physletb.2015.10.038. arXiv: 1502.04407 [hep-ph].

[166] M. Gyulassy, I. Vitev, and X. N. Wang. "High p(T) azimuthal asymmetry in noncentral A+A at RHIC". In: *Phys. Rev. Lett.* 86 (2001), pp. 2537–2540. DOI: 10.1103/PhysRevLett.86.2537. arXiv: nucl-th/0012092 [nucl-th].

[167] Miklos Gyulassy and Larry McLerran. "New forms of QCD matter discovered at RHIC". In: *Nucl. Phys.* A750 (2005), pp. 30–63. DOI: 10.1016/j.nuclphysa.2004.10.034. arXiv: nucl-th/0405013 [nucl-th].

[168] S. Hands. "The phase diagram of QCD". In: *Contemporary Physics* 42.4 (2001), pp. 209–225. DOI: 10.1080/00107510110063843.

[169] L. A. Harland-Lang et al. "Parton distributions in the LHC era: MMHT 2014 PDFs". In: *Eur. Phys. J.* C75.5 (2015), p. 204. DOI: 10.1140/epjc/s10052-015-3397-6. arXiv: 1412.3989 [hep-ph].

[170] Min He, Rainer J. Fries, and Ralf Rapp. "Heavy Flavor at the Large Hadron Collider in a Strong Coupling Approach". In: *Phys. Lett.* B735 (2014), pp. 445–450. DOI: 10.1016/j.physletb.2014.05.050. arXiv: 1401.3817 [nucl-th].

[171] Min He, Rainer J. Fries, and Ralf Rapp. "Heavy Flavor at the Large Hadron Collider in a Strong Coupling Approach". In: *Phys.Lett.* B735 (2014), pp. 445–450. DOI: 10.1016/j.physletb.2014.05.050. arXiv: 1401.3817 [nucl-th].

[172] Min He, Rainer J. Fries, and Ralf Rapp. "$\mathbf{D_s}$-Meson as Quantitative Probe of Diffusion and Hadronization in Nuclear Collisions". In: *Phys.Rev.Lett.* 110.11 (2013), p. 112301. DOI: 10.1103/PhysRevLett.110.112301. arXiv: 1204.4442 [nucl-th].

[173] Min He, Rainer J. Fries, and Ralf Rapp. "$\mathbf{D_s}$-Meson as Quantitative Probe of Diffusion and Hadronization in Nuclear Collisions". In: *Phys. Rev. Lett.* 110.11 (2013), p. 112301. DOI: 10.1103/PhysRevLett.110.112301. arXiv: 1204.4442 [nucl-th].

[174] A. Heister et al. "Study of the fragmentation of b quarks into B mesons at the Z peak". In: *Phys. Lett.* B512 (2001), pp. 30–48. DOI: 10.1016/S0370-2693(01)00690-6. arXiv: hep-ex/0106051 [hep-ex].

[175] Nicolo Jacazio. "Production of identified and unidentified charged hadrons in Pb–Pb collisions at $\sqrt{s_{\mathrm{NN}}} = 5.02$ TeV". In: (2017). arXiv: 1704.06030 [nucl-ex].

[176] Zhong-Bo Kang, Felix Ringer, and Ivan Vitev. "Effective field theory approach to open heavy flavor production in heavy-ion collisions". In: *JHEP* 03 (2017), p. 146. DOI: 10.1007/JHEP03(2017)146. arXiv: 1610.02043 [hep-ph].

[177] Zhong-Bo Kang et al. "Multiple scattering effects on heavy meson production in p+A collisions at backward rapidity". In: *Phys. Lett.* B740 (2015), pp. 23–29. DOI: 10.1016/j.physletb.2014.11.024. arXiv: 1409.2494 [hep-ph].

[178] Frithjof Karsch. "Lattice results on QCD thermodynamics". In: *Nucl. Phys.* A698 (2002), pp. 199–208. DOI: 10.1016/S0375-9474(01)01365-3. arXiv: hep-ph/0103314 [hep-ph].

[179] V. G. Kartvelishvili, A. K. Likhoded, and V. A. Petrov. "On the Fragmentation Functions of Heavy Quarks Into Hadrons". In: *Phys. Lett.* 78B (1978), pp. 615–617. DOI: 10.1016/0370-2693(78)90653-6.

[180] Vardan Khachatryan et al. "Evidence for collectivity in pp collisions at the LHC". In: *Phys. Lett.* B765 (2017), pp. 193–220. DOI: 10.1016/j.physletb.2016.12.009. arXiv: 1606.06198 [nucl-ex].

[181] Vardan Khachatryan et al. "Measurement of the B^+ Production Cross Section in pp Collisions at $\sqrt{s} = 7$ TeV". In: *Phys. Rev. Lett.* 106 (2011), p. 112001. DOI: 10.1103/PhysRevLett.106.112001. arXiv: 1101.0131 [hep-ex].

[182] Vardan Khachatryan et al. "Observation of Long-Range Near-Side Angular Correlations in Proton-Proton Collisions at the LHC". In: *JHEP* 09 (2010), p. 091. DOI: 10.1007/JHEP09(2010)091. arXiv: 1009.4122 [hep-ex].

[183] Vardan Khachatryan et al. "Suppression and azimuthal anisotropy of prompt and nonprompt J/ψ production in PbPb collisions at $\sqrt{s_{\mathrm{NN}}} = 2.76$ TeV". In: *Eur. Phys. J.* C77.4 (2017), p. 252. DOI: 10.1140/epjc/s10052-017-4781-1. arXiv: 1610.00613 [nucl-ex].

[184] Vardan Khachatryan et al. "Suppression of $\Upsilon(1S), \Upsilon(2S)$ and $\Upsilon(3S)$ production in PbPb collisions at $\sqrt{s_{\mathrm{NN}}} = 2.76$ TeV". In: *Phys. Lett.* B770 (2017), pp. 357–379. DOI: 10.1016/j.physletb.2017.04.031. arXiv: 1611.01510 [nucl-ex].

[185] Dmitri Kharzeev, Eugene Levin, and Marzia Nardi. "Color glass condensate at the LHC: Hadron multiplicities in pp, pA and AA collisions". In: *Nucl. Phys.* A747 (2005), pp. 609–629. DOI: 10.1016/j.nuclphysa.2004.10.018. arXiv: hep-ph/0408050 [hep-ph].

[186] T. Kneesch et al. "Charmed-meson fragmentation functions with finite-mass corrections". In: *Nucl. Phys.* B799 (2008), pp. 34–59. DOI: 10.1016/j.nuclphysb.2008.02.015. arXiv: 0712.0481 [hep-ph].

[187] B. A. Kniehl et al. "Collinear subtractions in hadroproduction of heavy quarks". In: *Eur. Phys. J.* C41 (2005), pp. 199–212. DOI: 10.1140/epjc/s2005-02200-7. arXiv: hep-ph/0502194 [hep-ph].

[188] B. A. Kniehl et al. "Inclusive Charmed-Meson Production at the CERN LHC". In: *Eur. Phys. J.* C72 (2012), p. 2082. DOI: 10.1140/epjc/s10052-012-2082-2. arXiv: 1202.0439 [hep-ph].

[189] B. A. Kniehl et al. "Inclusive D*+- production in p anti-p collisions with massive charm quarks". In: *Phys. Rev.* D71 (2005), p. 014018. DOI: 10.1103/PhysRevD.71.014018. arXiv: hep-ph/0410289 [hep-ph].

[190] Bernd A. Kniehl and Gustav Kramer. "Charmed-hadron fragmentation functions from CERN LEP1 revisited". In: *Phys. Rev.* D74 (2006), p. 037502. DOI: 10.1103/PhysRevD.74.037502. arXiv: hep-ph/0607306 [hep-ph].

[191] Inga Kuznetsova and Johann Rafelski. "Heavy flavor hadrons in statistical hadronization of strangeness-rich QGP". In: *Eur.Phys.J.* C51 (2007), pp. 113–133. DOI: 10.1140/epjc/s10052-007-0268-9. arXiv: hep-ph/0607203 [hep-ph].

[192] D. J. Lange. "The EvtGen particle decay simulation package". In: *Nucl. Instrum. Meth.* A462 (2001), pp. 152–155. DOI: 10.1016/S0168-9002(01)00089-4.

[193] Zi-Wei Lin et al. "A Multi-phase transport model for relativistic heavy ion collisions". In: *Phys. Rev.* C72 (2005), p. 064901. DOI: 10.1103/PhysRevC.72.064901. arXiv: nucl-th/0411110 [nucl-th].

[194] Fu-Ming Liu and Sheng-Xu Liu. "Quark-gluon plasma formation time and direct photons from heavy ion collisions". In: *Phys. Rev.* C89.3 (2014), p. 034906. DOI: 10.1103/PhysRevC.89.034906. arXiv: 1212.6587 [nucl-th].

[195] Zhi-Quan Liu et al. "Quantifying jet transport properties via large p_T hadron production". In: *Eur. Phys. J.* C76.1 (2016), p. 20. DOI: 10.1140/epjc/s10052-016-3885-3. arXiv: 1506.02840 [nucl-th].

[196] Constantin Loizides and Andreas Morsch. "Absence of jet quenching in peripheral nucleusnucleus collisions". In: *Phys. Lett.* B773 (2017), pp. 408–411. DOI: 10.1016/j.physletb.2017.09.002. arXiv: 1705.08856 [nucl-ex].

[197] Rafal Maciula and Antoni Szczurek. "Open charm production at the LHC - k_t-factorization approach". In: *Phys. Rev.* D87.9 (2013), p. 094022. DOI: 10.1103/PhysRevD.87.094022. arXiv: 1301.3033 [hep-ph].

[198] Michelangelo L. Mangano. "Two lectures on heavy quark production in hadronic collisions". In: *Proc. Int. Sch. Phys. Fermi* 137 (1998), pp. 95–137. DOI: 10.3254/978-1-61499-222-6-95. arXiv: hep-ph/9711337 [hep-ph].

[199] Michelangelo L. Mangano, Paolo Nason, and Giovanni Ridolfi. "Heavy quark correlations in hadron collisions at next-to-leading order". In: *Nucl. Phys.* B373 (1992), pp. 295–345. DOI: 10.1016/0550-3213(92)90435-E.

[200] T. Matsui and H. Satz. "J/ψ Suppression by Quark-Gluon Plasma Formation". In: *Phys. Lett.* B178 (1986), pp. 416–422. DOI: 10.1016/0370-2693(86)91404-8.

[201] "Measurement of D* meson production cross sections in pp collisions at $\sqrt{s}$ =7 TeV with the ATLAS detector". In: (2011).

[202] *Measurement of the correlation of jets with high p_T isolated prompt photons in lead-lead collisions at sqrts$_{NN}$ = 2.76 TeV with the ATLAS detector at the LHC*. Tech. rep. ATLAS-CONF-2012-121. Geneva: CERN, 2012. URL: https://cds.cern.ch/record/1473135.

[203] S van der Meer. *Calibration of the effective beam height in the ISR*. Tech. rep. CERN-ISR-PO-68-31. ISR-PO-68-31. Geneva: CERN, 1968. URL: https://cds.cern.ch/record/296752.

[204] Michael L. Miller et al. "Glauber modeling in high energy nuclear collisions". In: *Ann. Rev. Nucl. Part. Sci.* 57 (2007), pp. 205–243. DOI: 10.1146/annurev.nucl.57.090506.123020. arXiv: nucl-ex/0701025 [nucl-ex].

[205] Denes Molnar and Sergei A. Voloshin. "Elliptic flow at large transverse momenta from quark coalescence". In: *Phys. Rev. Lett.* 91 (2003), p. 092301. DOI: 10.1103/PhysRevLett.91.092301. arXiv: nucl-th/0302014 [nucl-th].

[206] Guy D. Moore and Derek Teaney. "How much do heavy quarks thermalize in a heavy ion collision?" In: *Phys. Rev.* C71 (2005), p. 064904. DOI: 10.1103/PhysRevC.71.064904. arXiv: hep-ph/0412346 [hep-ph].

[207] Berndt Muller. "Strangeness and the Quark-Gluon Plasma: Thirty Years of Discovery". In: *Acta Phys. Polon.* B43 (2012), p. 761. DOI: 10.5506/APhysPolB.43.761. arXiv: 1112.5382 [nucl-th].

[208] Marlene Nahrgang et al. "Influence of hadronic bound states above T_c on heavy-quark observables in Pb + Pb collisions at at the CERN Large Hadron Collider". In: *Phys.Rev.* C89.1 (2014), p. 014905. DOI: 10.1103/PhysRevC.89.014905. arXiv: 1305.6544 [hep-ph].

[209] K. Nakamura et al. "Review of particle physics". In: *J. Phys.* G37 (2010), p. 075021. DOI: 10.1088/0954-3899/37/7A/075021.

[210] K. A. Olive et al. "Review of Particle Physics". In: *Chin. Phys.* C38 (2014), p. 090001. DOI: 10.1088/1674-1137/38/9/090001.

[211] Jean-Yves Ollitrault. "Anisotropy as a signature of transverse collective flow". In: *Phys. Rev.* D46 (1992), pp. 229–245. DOI: 10.1103/PhysRevD.46.229.

[212] Yadav Pandit. "Beam Energy Dependence of First and Higher Order Flow Harmonics from the STAR Experiment at RHIC". In: *Nucl. Phys.* A904-905 (2013), pp. 357c–360c. DOI: 10.1016/j.nuclphysa.2013.02.023. arXiv: 1210.5315 [nucl-ex].

[213] C. Patrignani et al. "Review of Particle Physics". In: *Chin. Phys.* C40.10 (2016), p. 100001. DOI: 10.1088/1674-1137/40/10/100001.

[214] C. Patrignani et al. "Review of Particle Physics". In: *Chin. Phys.* C40.10 (2016), p. 100001. DOI: 10.1088/1674-1137/40/10/100001.

[215] Stephane Peigne and Andre Peshier. "Collisional energy loss of a fast heavy quark in a quark-gluon plasma". In: *Phys. Rev.* D77 (2008), p. 114017. DOI: 10.1103/PhysRevD.77.114017. arXiv: 0802.4364 [hep-ph].

[216] C. Peterson et al. "Scaling Violations in Inclusive e+ e- Annihilation Spectra". In: *Phys. Rev.* D27 (1983), p. 105. DOI: 10.1103/PhysRevD.27.105.

[217] P. Petreczky. "Lattice QCD at non-zero temperature". In: *J. Phys.* G39 (2012), p. 093002. DOI: 10.1088/0954-3899/39/9/093002. arXiv: 1203.5320 [hep-lat].

[218] Michal Petrn et al. "Hadron production and quark-gluon plasma hadronization in Pb-Pb collisions at $\sqrt{s_{NN}} = 2.76$ TeV". In: *Phys. Rev.* C88.3 (2013), p. 034907. DOI: 10.1103/PhysRevC.88.034907. arXiv: 1303.2098 [hep-ph].

[219] Owe Philipsen. "The QCD equation of state from the lattice". In: *Prog. Part. Nucl. Phys.* 70 (2013), pp. 55–107. DOI: 10.1016/j.ppnp.2012.09.003. arXiv: 1207.5999 [hep-lat].

[220] Robert D. Pisarski. "Phenomenology of the Chiral Phase Transition". In: *Phys. Lett.* 110B (1982), pp. 155–158. DOI: 10.1016/0370-2693(82)91025-5.

[221] Arthur M. Poskanzer and S. A. Voloshin. "Methods for analyzing anisotropic flow in relativistic nuclear collisions". In: *Phys. Rev.* C58 (1998), pp. 1671–1678. DOI: 10.1103/PhysRevC.58.1671. arXiv: nucl-ex/9805001 [nucl-ex].

[222] "Preliminary Physics Summary: Measurement of D^0, D^+, D^{*+} and D_s production in Pb-Pb collisions at $\sqrt{s_{NN}} = 5.02$ TeV". In: (2017). URL: https://cds.cern.ch/record/2265109.

[223] "Preliminary Physics Summary: Measurement of prompt D^0, D^+, D^{*+} and D_s^+ production in p-Pb collisions at $\sqrt{s_{NN}} = 5.02$ TeV". In: (2017). URL: https://cds.cern.ch/record/2272160.

[224] "Preliminary Physics Summary: Measurement of prompt D^0, D^+, D^{*+} and D_s^+ production in p-Pb collisions at $\sqrt{s_{NN}} = 5.02$ TeV". In: (2017). URL: https://cds.cern.ch/record/2272160.

[225] J. Pumplin et al. "New generation of parton distributions with uncertainties from global QCD analysis". In: *JHEP* 07 (2002), p. 012. DOI: 10.1088/1126-6708/2002/07/012. arXiv: hep-ph/0201195 [hep-ph].

[226] Guang-You Qin and Xin-Nian Wang. "Jet quenching in high-energy heavy-ion collisions". In: *Int. J. Mod. Phys.* E24.11 (2015). [,309(2016)], p. 1530014. DOI: 10.1142/S0218301315300143,10.1142/9789814663717_0007. arXiv: 1511.00790 [hep-ph].

[227] Johann Rafelski and Berndt Muller. "Strangeness Production in the Quark - Gluon Plasma". In: *Phys. Rev. Lett.* 48 (1982). [Erratum: Phys. Rev. Lett.56,2334(1986)], p. 1066. DOI: 10.1103/PhysRevLett.48.1066.

[228] Johann Rafelski and Berndt Müller. "Strangeness Production in the Quark-Gluon Plasma". In: *Phys. Rev. Lett.* 48 (16 1982), pp. 1066–1069. DOI: 10.1103/PhysRevLett.48.1066. URL: https://link.aps.org/doi/10.1103/PhysRevLett.48.1066.

[229] J. Ranft. "The Dual parton model at cosmic ray energies". In: *Phys. Rev.* D51 (1995), pp. 64–84. DOI: 10.1103/PhysRevD.51.64.

[230] Ralf Rapp. "Update on Chiral Symmetry Restoration in the Context of Dilepton Data". In: (2012). [J. Phys. Conf. Ser.420,012017(2013)]. DOI: 10.1088/1742-6596/420/1/012017. arXiv: 1210.3660 [hep-ph].

[231] P. Saiz et al. "AliEn - ALICE environment on the GRID". In: *Nucl. Instrum. Meth.* A502 (2003), pp. 437–440. DOI: 10.1016/S0168-9002(03)00462-5.

[232] Carlos A. Salgado and Urs Achim Wiedemann. "Calculating quenching weights". In: *Phys. Rev.* D68 (2003), p. 014008. DOI: 10.1103/PhysRevD.68.014008. arXiv: hep-ph/0302184 [hep-ph].

[233] Ladislav Sandor et al. "Results on hyperon production from the NA57 experiment". In: *Acta Phys. Hung.* A22 (2005), pp. 113–120. DOI: 10.1556/APH.22.2005.1-2.12. arXiv: nucl-ex/0404030 [nucl-ex].

[234] Bjoern Schenke and Soeren Schlichting. "3D glasma initial state for relativistic heavy ion collisions". In: *Phys. Rev.* C94.4 (2016), p. 044907. DOI: 10.1103/PhysRevC.94.044907. arXiv: 1605.07158 [hep-ph].

[235] Bjoern Schenke et al. "Mass ordering of spectra from fragmentation of saturated gluon states in high multiplicity proton-proton collisions". In: *Phys. Rev. Lett.* 117.16 (2016), p. 162301. DOI: 10.1103/PhysRevLett.117.162301. arXiv: 1607.02496 [hep-ph].

[236] Ekkard Schnedermann, Josef Sollfrank, and Ulrich W. Heinz. "Thermal phenomenology of hadrons from 200-A/GeV S+S collisions". In: *Phys. Rev.* C48 (1993), pp. 2462–2475. DOI: 10.1103/PhysRevC.48.2462. arXiv: nucl-th/9307020 [nucl-th].

[237] Simone Schuchmann and Harald Appelshaeuser. "Modification of K^0_s and $\Lambda(\overline{\Lambda})$ transverse momentum spectra in Pb-Pb collisions at $\sqrt{^sNN} = 2.76$ TeV with ALICE". Presented 22 Jul 2015. 2016. URL: https://cds.cern.ch/record/2102194.

[238] Jurgen Schukraft, Anthony Timmins, and Sergei A. Voloshin. "Ultra-relativistic nuclear collisions: event shape engineering". In: *Phys. Lett.* B719 (2013), pp. 394–398. DOI: 10.1016/j.physletb.2013.01.045. arXiv: 1208.4563 [nucl-ex].

[239] E. Scomparin. "J/ψ production in in-in and p^- A collisions". In: *J. Phys.* G34 (2007), S463–470. DOI: 10.1088/0954-3899/34/8/S35. arXiv: nucl-ex/0703030 [NUCL-EX].

[240] Rishi Sharma, Ivan Vitev, and Ben-Wei Zhang. "Light-cone wave function approach to open heavy flavor dynamics in QCD matter". In: *Phys. Rev.* C80 (2009), p. 054902. DOI: 10.1103/PhysRevC.80.054902. arXiv: 0904.0032 [hep-ph].

[241] Albert M Sirunyan et al. "Measurement of prompt D^0 meson azimuthal anisotropy in PbPb collisions at $\sqrt{s_{NN}} = 5.02$ TeV". In: (2017). arXiv: 1708.03497 [nucl-ex].

[242] Albert M Sirunyan et al. "Suppression of excited Upsilon states relative to the ground state in PbPb collisions at sqrt(sNN) = 5.02 TeV". In: (2017). arXiv: 1706.05984 [hep-ex].

[243] Torbjorn Sjostrand, Stephen Mrenna, and Peter Z. Skands. "PYTHIA 6.4 Physics and Manual". In: *JHEP* 05 (2006), p. 026. DOI: 10.1088/1126-6708/2006/05/026. arXiv: hep-ph/0603175 [hep-ph].

[244] Peter Zeiler Skands. "Tuning Monte Carlo Generators: The Perugia Tunes". In: *Phys. Rev.* D82 (2010), p. 074018. DOI: 10.1103/PhysRevD.82.074018. arXiv: 1005.3457 [hep-ph].

[245] Taesoo Song et al. "Charm production in Pb + Pb collisions at energies available at the CERN Large Hadron Collider". In: *Phys. Rev.* C93.3 (2016), p. 034906. DOI: 10.1103/PhysRevC.93.034906. arXiv: 1512.00891 [nucl-th].

[246] Michael Strickland. "Anisotropic Hydrodynamics: Three lectures". In: *Acta Phys. Polon.* B45.12 (2014), pp. 2355–2394. DOI: 10.5506/APhysPolB.45.2355. arXiv: 1410.5786 [nucl-th].

[247] Derek Teaney and Li Yan. "Triangularity and Dipole Asymmetry in Heavy Ion Collisions". In: *Phys. Rev.* C83 (2011), p. 064904. DOI: 10.1103/PhysRevC.83.064904. arXiv: 1010.1876 [nucl-th].

[248] Markus H. Thoma and Miklos Gyulassy. "Quark Damping and Energy Loss in the High Temperature QCD". In: *Nucl. Phys.* B351 (1991), pp. 491–506. DOI: 10.1016/S0550-3213(05)80031-8.

[249] Ahmed Tounsi and Krzysztof Redlich. "Strangeness enhancement and canonical suppression". In: (2001). arXiv: hep-ph/0111159 [hep-ph].

[250] Jan Uphoff et al. "Elastic and radiative heavy quark interactions in ultra-relativistic heavy-ion collisions". In: *J. Phys.* G42.11 (2015), p. 115106. DOI: 10.1088/0954-3899/42/11/115106. arXiv: 1408.2964 [hep-ph].

[251] Jan Uphoff et al. "Elliptic Flow and Energy Loss of Heavy Quarks in Ultra-Relativistic heavy Ion Collisions". In: *Phys. Rev.* C84 (2011), p. 024908. DOI: 10.1103/PhysRevC.84.024908. arXiv: 1104.2295 [hep-ph].

[252] Jan Uphoff et al. "Open Heavy Flavor in Pb+Pb Collisions at $\sqrt{s} = 2.76$ TeV within a Transport Model". In: *Phys. Lett.* B717 (2012), pp. 430–435. DOI: 10.1016/j.physletb.2012.09.069. arXiv: 1205.4945 [hep-ph].

[253] R. Vogt. "The A dependence of open charm and bottom production". In: *Int. J. Mod. Phys.* E12 (2003), pp. 211–270. DOI: 10.1142/S0218301303001272. arXiv: hep-ph/0111271 [hep-ph].

[254] Xin-Nian Wang. "Systematic study of high p_T hadron spectra in pp, p A and A A collisions from SPS to RHIC energies". In: *Phys. Rev.* C61 (2000), p. 064910. DOI: 10.1103/PhysRevC.61.064910. arXiv: nucl-th/9812021 [nucl-th].

[255] Xin-Nian Wang and Miklos Gyulassy. "HIJING: A Monte Carlo model for multiple jet production in p p, p A and A A collisions". In: *Phys.Rev.* D44 (1991), pp. 3501–3516. DOI: 10.1103/PhysRevD.44.3501.

[256] Xin-Nian Wang, Zheng Huang, and Ina Sarcevic. "Jet quenching in the opposite direction of a tagged photon in high-energy heavy ion collisions". In: *Phys. Rev. Lett.* 77 (1996), pp. 231–234. DOI: 10.1103/PhysRevLett.77.231. arXiv: hep-ph/9605213 [hep-ph].

[257] Kenneth G. Wilson. "The Renormalization Group and Strong Interactions". In: *Phys. Rev.* D3 (1971), p. 1818. DOI: 10.1103/PhysRevD.3.1818.

[258] Jiechen Xu, Jinfeng Liao, and Miklos Gyulassy. "Bridging Soft-Hard Transport Properties of Quark-Gluon Plasmas with CUJET3.0". In: *JHEP* 02 (2016), p. 169. DOI: 10.1007/JHEP02(2016)169. arXiv: 1508.00552 [hep-ph].

[259] Yingru Xu et al. "A data-driven analysis of the heavy quark transport coefficient". In: *Nucl. Phys.* A967 (2017), pp. 668–671. DOI: 10.1016/j.nuclphysa.2017.05.035. arXiv: 1704.07800 [nucl-th].

[260] Yingru Xu et al. "Heavy-flavor dynamics in relativistic p-Pb collisions at $\sqrt{s_{NN}} = 5.02$ TeV". In: *Nucl. Part. Phys. Proc.* 276-278 (2016), pp. 225–228. DOI: 10.1016/j.nuclphysbps.2016.05.050. arXiv: 1510.07520 [nucl-th].

[261] Zhe Xu and Carsten Greiner. "Thermalization of gluons in ultrarelativistic heavy ion collisions by including three-body interactions in a parton cascade". In: *Phys. Rev.* C71 (2005), p. 064901. DOI: 10.1103/PhysRevC.71.064901. arXiv: hep-ph/0406278 [hep-ph].

[262] Li Yan and Jean-Yves Ollitrault. "Universal fluctuation-driven eccentricities in proton-proton, proton-nucleus and nucleus-nucleus collisions". In: *Phys. Rev. Lett.* 112 (2014), p. 082301. DOI: 10.1103/PhysRevLett.112.082301. arXiv: 1312.6555 [nucl-th].

[263] Ben-Wei Zhang, Che-Ming Ko, and Wei Liu. "Thermal charm production in a quark-gluon plasma in Pb-Pb collisions at s**(1/2)(NN) = 5.5-TeV". In: *Phys. Rev.* C77 (2008), p. 024901. DOI: 10.1103/PhysRevC.77.024901. arXiv: 0709.1684 [nucl-th].

[264] Yi-Fei Zhang. "Open charm hadron measurement in p+p and Au+Au collisions at $\sqrt{s_{\rm NN}} = 200$ GeV in STAR". In: *J. Phys.* G38 (2011), p. 124142. DOI: 10.1088/0954-3899/38/12/124142. arXiv: 1106.6078 [nucl-ex].

[265] Kai Zhou et al. "Medium effects on charmonium production at ultrarelativistic energies available at the CERN Large Hadron Collider". In: *Phys. Rev.* C89.5 (2014), p. 054911. DOI: 10.1103/PhysRevC.89.054911. arXiv: 1401.5845 [nucl-th].